MODELLING OF THE REMOVAL OF MULTI-LAYER COATINGS USING HIGH PRESSURE WATER JET AND THE STUDY OF ITS MATERIAL REMOVAL MECHANISMS

IRATI SANCHEZ DUO

Thesis submitted in the fulfilment of the requirements for the degree of Doctor of Philosophy

Rolls-Royce University Technology Centre Manufacturing and On-Wing Technology

March 2023

Abstract

Aerospace coatings (e.g. Thermal Barrier Coatings (TBC), abradable coatings…) have been utilised in the industry for decades with the aim of protecting the substrate materials from the harsh environment and the elevate temperature of the engines as well as to improve their performance. However, due to the thermal mismatch between materials, coatings are damaged and in consequence spalled. As their durability is four or five times lower than the service life of the engine, these parts need to be replaced. The goal is to strip the coatings efficiently and without damaging the substrate material in order to recoat and hence reassemble them in the engine.

For this Plain Water Jet (PWJ) milling has been proposed, which is a nonconventional machining technique that benefits from the kinetic energy of the water released at high pressure. This technique erodes the target material and generates an accurate cut or milled trench with negligible processing temperatures and forces. Hence, it is ideal to remove damaged multi-layer coatings efficiently without damaging the substrate material at a controlled, clean and economical way. Nevertheless, coating removal with PWJ technology presents its challenges: each coating layers as well as the substrate have distinct mechanical properties that need to be addressed and the characteristic time dependency of the WJ machining process, makes the operation difficult to predict (e.g. jet penetration).

This research aims to develop a mathematical model that calculates the jet footprint to remove multi-material coatings efficiently using a rotational multiple plain water jet nozzle accurately. The proposed model is based on the understanding of the etching rate considering the mechanical properties of each individual material layer that compounds a coating and the energy of a PWJ system. This interaction has been obtained for any specific pressure, considering the energy variations along the height of the jet, for one or multiple jets, which follows a defined arbitrary trajectory in a 3D space, during a period of time. Subsequently, the model has been validated and the optimal milling conditions have been defined. Moreover, a software with a user’s friendly interface (UI) has been developed to easily integrate de mathematical model in an industrial environment.

Finally, to understand the effect of the high energy impact of water jet droplets on the coating materials (i.e. in this case YSZ) a water jet and high strain rate nanoindentations have been used to understand how the behaviour of 6-8YSZ changes upon different strain rates (from 10^{-3} to 10^{8} s^{-1}). This study shows that at extremely high strain rates (10^{6} - 10^{8} s^{-1}) the material suffers from a brittle-dominated failure which induces localized phase transformation even if the material is in its partially stabilized form in where limited amount of transformation toughening is expected, phenomenon that is not observed at lower strain rates (10^{-3} - 1 s^{-1}).

Keywords: Plain Water Jet technology, multi material coating removal, rotational nozzle, Thermal Barrier coatings (TBCs), Abradable coatings, Yttria Stabilized Zirconia (YSZ), high strain rate impact study, phase transformations.

Acknowledgements

As any other important journey this project was just possible thank to the help and collaboration of many colleagues but specially friends.

First of all, I would like to thank Dragos Axinte for the opportunity of doing this project as well as for his help and guidance not only during the PhD but also in the master's project. Thank you very much for introducing me to the research world.

In addition, a big thank to Zhirong Liao for your insightful ideas during the project. Furthermore, I would like to thank Cecilia, your work in the UTC is just invaluable and to Steve and Dan for the support in the experimental work.

Additionally, I would like to thank my sponsor Rolls-Royce and the industrial supervisors Rob Smith and Clive Grafton-Reed for your time and effort as well as the nmRC (Chris, Graham, Beth and Martin) for your help and expertise in the material analysis.

Moreover, I would like to thank to the sweet office people, for making the best work environment possible and for always being ready to help when needed. Oriol, Gonzalo, and Pachi, your advice and expertise has been invaluable in this project. Andrea and Dima, for being the loveliest friends, I could not ask for better people to start this project with. To Artem, Mariam, Matteo, David, Luca, Josue, Andres, Eric, Kieran and Mohamed you are just the most incredible colleagues. Also, to Monica, Nerea, Katarina, Ellie, Negar, Grazia, Amaia, Ibone, Nerea$_2$ and Reyes for making the Nottingham experience the best. I am grateful for all the game nights, R&C evenings, mountain hikes, concerts, dinners, just chatting's, to the swing-knitting-crocheting club and of course for all the innumerable climbing afternoons.

An especial mention has to be made to Floriana and Jorge, for being the best of the friends in and out of the office, I will never ever get bored of catching up with you, sober or not.

The support received from the Basque Country has also been crucial. A big hug to my dear family: to my parents (ama eta aita), my little sister Izaskun and Javis parents (Ana and Jesus) as well as my childhood sweet friends (Irati M, Izaskun, Lore, Iraide and Garazi) for always encouraging me to try my best, listening to me just rant in greyish days and making me feel that there is always going to be a place called home to go back to.

Finally, and most importantly, thank you from the bottom of my heart to the one and only, Javi. Thank you for always being there no matter what. You are just the best. Ready for the next adventure?

Eskerrik asko danori.

Table of contents

1.1. Motivation...2

1.2. Research problem..5

1.3. Objectives of the study...7

1.4. Structure of the thesis...10

2.1. Development of the efficiency of aeroengines in regard to their improvements to optimize fuel consumption..12

2.2. Most relevant coating used on the engines: materials analysis..........14

2.3. Coating removal mechanisms..25

2.4. How does a Plain Water Jet system work...32

2.5. History, development and research gaps of high pressure water jet coating removal mathematical models...36

2.6. Surface integrity analysis techniques...45

3.1. Plain Water jet milling machines...50

3.2. Sample preparation process...60

3.3. Water jet analysis..61

3.4. Material analysis techniques...62

4.1. Introduction...73

4.2. Study of the material removing nozzles..75

4.3. Mathematical model based on the calculation of the jet energy........87

4.4. Particular case: geometry of a pocket, the edge of a trench...............98

4.5. Presentation of the results: street light system...............................101

4.6. Concluding remarks..102

5.1. Introduction..105

5.2. Structure of the designed application..106

5.3. Installation of the software....118

5.4. Discussion on the software's functionality....118

5.5. Concluding remarks....120

6.1. Mathematical model validation in a controlled sample....123

6.2. Proposal of the most suitable parameters for the studied materials....135

6.3. Industrial validation in the Rolls-Royce PWJ machine....137

6.4. Understanding of the material removal mechanisms....142

6.5. Concluding remarks....146

7.1. Introduction....150

7.2. Experimental procedure: methodology and materials....153

7.3. Results on the case study....156

7.4. Discussion....162

7.5. Concluding remarks....163

8.1. Conclusions....166

8.2. Future work....173

List of figures

Figure 1: Schematic representation of Thermal Barrier Coatings, which are able to keep the substrate material at a cooler temperature compared to the environment they are in [9]. 3

Figure 2: *Schematic representation of Abradable Coatings, that enable a very close fit between a rotary an a static part and so that if the two of them touch the coating wears down providing a custom fit between parts (adapted from* [10]-[11]*).* 4

Figure 3: *Schematic representation of the deterioration of the aeroengine coating layers after years of service, due to the high temperatures and harsh environment.* 5

Figure 4: *Schematic representation of the structure of the thesis document.* 10

Figure 5: *Evolution of the engine blade over the years, highlighting the importance of its crystal structure for improving the performance* [17]. 13

Figure 6: *Schematic representation of the Thermal Barrier Coatings and their different layers as well as the temperature gradient throughout the cross section of the coated turbine blade* [18]. 15

Figure 7: *Schematic diagram showing the different phases that pure zirconia undergoes from room temperature monoclinic zirconia, moving through tetragonal at 1170 °C and cubic at 2370 °C to liquid state at 2680 °C (adapted from* [22]*).* . 16

Figure 8: *Schematic representation of monoclinic, tetragonal and cubic crystallographic structures of pure zirconia, made of zirconium and oxygen atoms* [25]. 17

Figure 9: *Phase diagram for ZrO2-Y2O3, with yttria represented in mol % (adapted from* [24]*).* 18

Figure 10: *Scanning electron microscopy (SEM) cross sections of EB-PVD columnar structure* [33], *and APS horizontal and porous splats structure.* 21

Figure 11: *Mechanical bonding that maintain the APS structure packed in place.* 22

Figure 12: *Schematic diagram that shows the collapse, showing different cracking mechanisms, of both EB-PVD and APS coatings after suffering around 240 thermal cycles* [18]. 22

Figure 13: *Schematic representation of Abradable Coatings, that enable a very close fit between a rotary an a static part and so that if the two of them touch the coating wears down providing a custom fit between parts (adapted from* [10]-[11]*).* 23

Figure 14: *Schematic representation of how aero engines degrade and get expelled during service [adapted from figure from RR].* 25

Figure 15: *Water jet distribution along the jet axis showing the velocity evolution* [63]. 35

Figure 16: *Water jet distribution along the jet axis showing the potential applications in each region* [64]. 36

Figure 17: *Scheme of the trench generated by the AWJ machining process and the forces that are interacting in the process. a) front view, b) top view* [72]. 38

Figure 18: *Example of the prediction of a trench milled, with an abrasive water jet at 1700 mm/min on an Inconel target, with less than a 5 % of error* [72]. 39

Figure 19: *a) crater and crack formed after the impact of a single water droplet in gamma titanium aluminide; b) Sequence of the water droplet when impacting a hard solid surface at a supersonic speed* [50]. 41

Figure 20: *a) Schematic representation of a droplet when impacting at supersonic speed; b) Magnification of the impact area; c) Schematic representation of the propagation of the shock wave and the spreading of the jet after breaking the droplet perimeter* [89]. 42

Figure 21: *a) Microcrystal nickel alloy that is transformed in nanocrystals after abrasive waterjet impact; b) Nanocrystal nickel allow that is maintained unchanged after abrasive waterjet impact; c) Single crystal nickel alloy that suffers a nanoscale crystallization and a packing of dislocation in the abrasive waterjet impact area. This demonstrates that the microstructure generates a great influence in the water jet machining process* [91]. 43

Figure 22: *Example of a 3D view of a water jet milled trench and scanned by a 3D surface metrology machine* [77]. 46

Figure 23: *Example of a how an SEM can be used to identify cracking and grain structure changes affecting the surface integrity, in this case the surface of a machining a Ni-superalloy chip* [96]. 47

Figure 24: *Schematic of a water jet machine system* [*Adapted from* [107]]. 51

Figure 25: *a) Three-axis micro water jet machine from* micro waterjet. *b) Ultra-high pressure pump* KMT Waterjet systems SL-V100D Plus *connected to the WJ machine to pressurise the water.* 52

Figure 26: *a) Five-axis water jet machine from Omicron. b) Ultra-high pressure pump* KMT Waterjet systems SL-V100D Plus *connected to the WJ machine to pressurise the water.* 54

Figure 27: *Close up of the distribution system of the AWJ machine in where the abrasive and water inlet as well as the slurry outlet through the needle nozzle for: a) the three-axis WJ machine, b) five-axis WJ machine.* 55

Figure 28: ***Rotational*** *a) Four jet and b) Fan nozzles.* 58

Figure 29: *Rolls-Royce PWJ machine.* 59

Figure 30: *Struers Tegra Force 5 UoN UTC polishing machine.* 60

Figure 31: *Carbon coater Quorum Q150 R ES from the nmRC.* 61

Figure 32: *Alicona G4 infinite focus and an example of the obtained results.* 63

Figure 33: *Schematic representation of the internal structure of an SEM and the description of the interaction volume of the beam with the material (adapted from* [110]*).* 65

Figure 34: *a) FEI Quanta 600 SEM and b) SEM (FEG-SEM) Jeol 7000F both from the nmRC.* 66

Figure 35: *Horiba LabRAM HR confocal Raman spectroscopy microscope from the nmRC.* 68

Figure 36: *EI Quanta 200 3D Dual Beam FIB-SEM from the nmRC.* 69

Figure 37: *Jeol 2100F TEM from the nmRC.* 70

Figure 38: *Alemnis nanoindenter from the UTC installed inside the FEI Quanta 600 SEM from the nmRC equipped with a 40 µm Ø spherical tip.* 71

Figure 39: *Schematic representation of an example of a multi-layer coating being stripped using high pressure waterjet technology with a rotational multiple plain water jet nozzle.* 75

Figure 40: *Schematic representation a jet indicating the key parameters to consider in order to model its performance (adapted from* [115]*).* 76

Figure 41: *High speed camera (IDT Y4-S2 Motion Pro) plus MM water density distribution analysis of the four jet nozzle flow at a) 100 MPa, b) 200 MPa, c) 300 MPa and 400 MPa.* 78

Figure 42: *A close-up high-speed camera image of a fan jet nozzle displaying the locations of each jet and the gaussian distribution of the water flow while taking into account the water density % colour scale.* 79

Figure 43: *High speed camera (IDT Y4-S2 Motion Pro) plus MM water density distribution analysis of the fan jet nozzle flow, both from the front and side, at a) 100 MPa, b) 200 MPa, c) 300 MPa and 400 MPa.*....................................... 80

Figure 44: *Process followed to calculate the water density distribution of the fan jet nozzle: a) first by milling the trench (3 axis WJ from UoN) in a soft material, b) then scanning (high-resolution optical 3D surface metrology system) and data analysis in MM and finally c) data post processing and fitting curve calculation in MATLAB.* 81

Figure 45: *Schematic representation of the trajectory of each individual jet of the four jet rotary nozzle and the definition of the parameters as well as the reference system in order to understand the kinematics of the nozzle head when rotating and advancing transversally.* 83

Figure 46: *Schematic representation of the trajectory of four different points through the width of the fan nozzle slot and the definition of the parameters as well as the reference system in order to understand the kinematics of the nozzle head when rotating and advancing transversally.*... 85

Figure 47: *MTATLAB graph representation of the effect that the difference in v_t (and hence the change in the absolute jet speed) provokes in the jet positioning patterns, in the four jet nozzle, while keeping the rest of the parameters constant ($v_r = -2\pi$): a) 1 m/s, b) 5 m/s, c) 25 m/s, d) 100 m/s.* 86

Figure 48: *MATLAB graph representation of the effect that the difference in v_t (and hence the change in the absolute jet speed) provokes considering different points along the jet width in the fan jet nozzle, while keeping the rest of the parameters constant ($v_r = -2\pi$): a) 1 m/s, b) 5 m/s, c) 25 m/s, d) 100 m/s.*............. 87

Figure 49: *The combination of both a) the kinematics of the jet and the b) calculation of the material specific etching rate (defined by Axinte et al. in 2010* [72]*) c) results in variable depth trench that follows the jet trajectory that depends on the nozzle absolute velocity.*... 88

Figure 50: *Comparison of the trench shape between a) a single material target that creates a continuous outline vs b) a trench made in a multimaterial target that has clear intersection between layers due to the fact that the trench shape depends in the jet as well as the material properties of the target.* 89

Figure 51: *Energy distribution of a cone shape nozzle (i.e. needle nozzle) following a Gaussian energy distribution along the jet z axis.*............................... 90

Figure 52: *Comparison of different spatial mesh sizes to define the optimal discretisation showing examples at the following points per mm: 20, 10, 5, 2.5 and 1. The mesh size of M=300 with 10 points per mm offers a good enough resolution with least compromise on the computational time.*.. 92

Figure 53: *Example of a) the energy distributed at every x, y target points of a single rotational jet nozzle that follows a linear trajectory and b) the resulting milled trench generated by such nozzle.* 94

Figure 54: *Generic representation of a cross section of a single jet multi-material trench with the definition of the coefficients (Ci, ki, i=1 ... m) of the surfaces of each material layers.*.. 95

Figure 55: *a) Effect on the difference of the SoD along the jet radius and b) a representation of a usual of real life application of coating removal in the interior of a jet casing.* 96

Figure 56: *Representation of overlapping trenches showing a) a single trench, b) multiple trenches with 120% of overlapping separation that results in no overlap and having unremoved coating stripes between trenches and c) example with multiple trenches with a 75% of overlapping separation resulting in areas with more than one pass.*.. 98

Figure 57: *Schematic drawing of a cross section of a pocket with protective coating*.. 99

Figure 58: *Schematic drawing of the different sections that compound the transition from exposed substrate (A) material to fully coated area (D).* 100

Figure 59: *Definition of the parameters that determine the geometry and dimensions of the sections of the edge of a pocket.* 100

Figure 60: *Example of street light system result representation made with the four jet rotary nozzle, 5 trenches and 75% of overlapping separation a) showing a good material removal and b) too much removal and substrate damage.* 102

Figure 61: *Example of street light system result representation made with the four jet rotary nozzle, 5 trenches and 75% of overlapping separation in the particular case of the edge of a pocket a) showing a good material removal and b) too much removal and substrate damage.* 102

Figure 62: *View of the first tab "Input parameters" of the* software and the *presentation of the navigation panel to move from tab to tab.* 106

Figure 63: *Nozzle definition segment of the Input parameters window showing the necessary parameters to characterise a) the rotational 4 jet nozzle and b) the fan jet nozzle, with their respective figures showing the meaning of each parameter.* 107

Figure 64: *View of the "Machining parameters" section for defining the machining conditions for the simulation, with a representative image of the variables.* 108

Figure 65: *Section of the "Input parameters" tab to define the type, geometry and position of the coating for the workpiece together with figures representing a) a flat surface and b) a curved surface with both options of cleaning inside or outside the ring.* 108

Figure 66: *Segment with the required variables to define the quantity of trenches to simulate a a) single trench and b) multiple trenches and their overlapping*

percentage. The two images visually represent the difference between having a single or multiple trenches and the meaning of the variables. 109

Figure 67: *Definition of the thicknesses in mm and the material coefficient value for each of the coating layers, in where the material coefficient is calculated from calibration data.* 110

Figure 68: *Definition of the trench depth that needs to be measured for the calibration.* 111

Figure 69: *Representation of tab number 2: Calibration coefficient calculator to calculate the material dependent coefficient for each layer from calibration data obtained from a single jet trench. The procedure for the calculation is also presented, together with a representative picture of the layers and the trench.* 112

Figure 70: *Example of a pop-up that appears when the user clicks on an image, with an explanatory description of what is shown in the figure.* 112

Figure 71: *Example of a button with the question mark that is located next to the variable input boxes, and the pop-up that appears with a description of the parameter.* 113

Figure 72: *Simulate button at the bottom of the "Input parameter" tab to run the calculation, and the alternative version to show when the program is running.* 113

Figure 73: *Representation of tab 3: Resultant preliminary graphs from the total energy calculation on the left and the resultant milled trench on the right, with a description of the meaning of both plots under them.* 114

Figure 74: *Representation of tab 4: Material removal results represented with the street light method to clearly identify untouched surface (blue), not fully removed coating (yellow), fully cleaned substrate (green) and damaged surface (red). The calculators to estimate the time needed to remove the coating from the two most common coated parts are also shown.* 115

Figure 75: *Representation of tab 5, calculation and results of the particular case in where the edge of the pocket is studied.* 117

Figure 76: *Tab (6) Unit converter with the units relevant to the model organized in four sections: pressure, translational speed, length and angles and rotational speed unit converters.* 118

Figure 77: *Experimental setup and description of the geometry and material details of the coating and the substrate of the trial material.*............................... 123

Figure 78: *Experimental setup showing the four jets nozzle head, the two layers coated annular component and the trajectories of the centres of the four rotational nozzles caused by a linear movement of the head.*.............................. 125

Figure 79: *Comparison of the simulated and the milled trench at a range of transversal velocities (vt): a) 1020 mm/min, b) 660 mm/min c) 60 mm/min.* 127

Figure 80: *Comparison between two example trenches one at vt = 60 mm/min, in order to ensure a full cleaning of the trench and the other at vt = 1020 mm/min to show the accuracy of the model when predicting preserved coating bits along the trench. The experimental and simulated trenches are shown, as well as EDX analysis to identify the coating layer and zones where it has not been removed.* 128

Figure 81: *Definition of the geometry of the tests samples as well as the tests set up for the small scale validation of the fan jet rotational nozzle head in pocket samples.*.. 129

Figure 82: *Study of the translational velocity comparing 100, 1000 and 4000 mm/min trenches in where the results are presented as a scan of the milled trench, modelled trench and model interpretation shown from the top view with the street light system.*.. 131

Figure 83: *Study of the pump pressure comparing 200, 250, 300 and 350 MPa trenches in where the results are presented as a scan of the milled trench, modelled*

trench and model interpretation shown from the top view with the street light system. 133

Figure 84: *Study of the separation percentage of the overlapping trenches comparing 80 and 55 % in where the results are presented as a scan of the milled trench, modelled trench and model interpretation shown from the top view with the street light system.* 134

Figure 85: *Photograph of the samples after coating removal at P: 350 MPa, vt: 4000 mm/min, vr 1500 rpm, SoD 20 mm and a) 55 % of overlapping separation between trenches and b) at 80 %.* 135

Figure 86: *Description of the Rolls-Royce water jet machine tests set up in where a) the mounted casing inside the machine is showcased as well as the WJ nozzle head, b) the attachment of the casing to the rotary base and c) the representation of the coating steeps to be removed are shown.* 139

Figure 87: *Study of the milling of the workpiece using the original parameters that Rolls-Royce uses for the process: a) modelled trench obtained from the mathematical model, b) top view representation of the modelled surface, c) picture of the cleaned surface showing the stripping lines, d) comparison of the measured and the modelled trenches with the error between them.* 140

Figure 88: *Study of the milling of the workpiece using the new proposed parameters for a controlled milling and reduce the damage of the substrate: a) modelled trench obtained from the mathematical model, b) top view representation of the modelled surface, c) picture of the cleaned surface, d) comparison of the measured and the modelled trenches with the error between them.* 141

Figure 89: *Study of the milling of the workpiece using parameters that should damage the workpiece to validate the predictability achieved using the model: a) modelled trench obtained from the mathematical model, b) top view representation of the modelled surface with the damage in red, c) picture of the cleaned surface*

with the damage induced, d) comparison of the measured and the modelled trenches, showing the damage and with the error between them... 142

Figure 90: *Visual representation of the theory of how the edge of the trenches after passing a milling trench are expected to be removed vs how it actually gets removed.*.. 144

Figure 91: *SEM pictures showing the different cracks generated on the sample after the waterjet milling: a) material removal due to a crack formation, b) example of a crack between the substrate and the bond coat, c) gap generated on the top coat of the sample due to crack and d) cracks generated between layers at the substrate-bond coat, and top coat-bond coat.* 145

Figure 92: *Pictures from the SEM and EDX analysis to compare machining parameters that leads to too much removal and as a consequence substrate damage and too little removal which implies coating left behind.*.................................... 146

Figure 93: *a) Schematic representation of a PWJ trench indicating the process parameters in the performed tests b) Waterjet density distribution along the jet – experimental results.*.. 154

Figure 94: *Schematic representation of the front and top view of the PWJ milled trench indicating Gaussian energy distribution (E) of the jet and the location of the three regions of interest. Finally, SEM images of the selected surface areas: a) E_0, b) E_{low}, c) E_{high} indicating the surface damage under mechanical impact.* 155

Figure 95: *Raman spectra from each of the three regions of interest: E_0, E_{low} and E_{high}. The analysis demonstrates $t \rightarrow m$ phase transformation phenomena in the zone of single droplet impact which is manifested by the appearance of new peaks (500-550 cm^{-1}), while in the trench, i.e. eroded, area and untouched surfaces show typical tetragonal spectra values.*... 157

Figure 96: *a) General view of the lamella in the HAADF STEM in where defects created by the process can clearly be seen in the first 500 – 600 nm from the surface. b) BF TEM images showing an acicular dislocation build up that leads to*

the initial phases of a defect. c) SADP TEM diffraction patterns obtained from a STEM image of a HSR water droplet impact lamella (E_{low}) shows residual strain in the top being released while getting deeper beneath the surface while indicating a phase change when reaching the crack. 159

Figure 97: *Transformation toughening process induced by crack propagation* [137]. 160

Figure 98: *a) Exemplary P-h diagram obtained at 10 mN/s loading and 5 mN/s unloading and a 10 s hold time that describes the diagrams parameters and the schematic representation of the deformation under a spherical tip and b) the description of the relevant.* 161

Figure 99: *a) SEM images of the indentations at 10^{-3} s-1 and 1 s^{-1} order of magnitude stain rates, b) Raman spectroscopy results of the indentation at all the analysed strain rates showing the absence of monoclinic phase.* 163

List of tables

Table 1: *Summary of the 3-axis water jet machine components and its respective parameters.* 52

Table 2: *Summary of the 5-axis water jet machine components and its respective parameters.* 53

Table 3: *Polishing steps for sample preparation for material characterization and understanding of material removal mechanisms, steps recommended from STRUERS.* 60

Table 4: *Definition of the parameters used in the run to show the app as an example.* 105

Table 5: *Definition of the parameters used in the calculation of the pocket section in the run to show the app as an example.* 116

Table 6: *Description of the properties of each of the materials used in the model validation example.* 124

Table 7: *Definition of the parameters used at Rolls-Royce WJ machine in order to prove the material removal prediction capabilities of the developed model.* 137

List of abbreviations

APS	*Air Plasma Sprayed*
AWJ	*Abrasive Water Jet*
BSE	*Backscattered electrons*
DT	*Destructive Testing*
EB-PVD	*Electron Beam Physical Vapour Deposition*
EBSD	*Electron Backscatter Diffraction*
EDX	*Energy Dispersive X-Ray*
FEM	*Finite Element Models*
FIB	*Focused Ion Beam*
MM	*Mountain Map®, commercial software*
NA	*Numerical Aperture*
NDT	*Non Destructive Testing*
nmRC	*Nanoscale and Microscale Research Centre*
PWJ	*Plain Water Jet*
RR	*Rolls-Royce*
SE	*Secondary electrons*
SEM	*Scanning Electron Microscopy*
SoD	*Stand-off distance*
TBC	*Thermal Barrier Coating*
TEM	*Transmission Electron Microscopy*
TGO	*Thermally Grown Oxide*
UI	*Users Interface*
UoN	*University of Nottingham*
WJ	*Water Jet*
WL	*Wave Length*
YSZ	*Yttria Stabilized Zirconia*

List of symbols

Chapter 4

a	Definition of a dimensional (expressed with suffix)	-
C	Relationship between the maximum cutting depth point	-
d_{m1r}	Position of the first jet in rotation	*mm*
d_{m1t}	Position vector of the first jet in translation	*mm*
d_{nozzle}	Nozzle diameter	*mm*
d^{total_m1}	Overall position vector of the firsts jet	*mm*
d_{total_mn}	Overall position vector for any given jet in the nozzle head	*mm*
$E_{dis(r)}$	Energy distribution along the radius	*J*
E_{hm}	Comparison between the received energy and the one needed to entirely remove a coating	*J*
E_{max}	Maximum energy	*J*
E_{nozzle}	Energy that is released from the jet	*J*
E_{space}	Jet energy that follows the defined trajectory	*J*
$E_{space(r,z,t)a}$	Arbitrary energy in space	*J*
g_n	Geometry of the nozzle such as the diameters and length	*Mm*
h_m	The unique thickness of each coating layer	*Mm*
j	Definition of a jet in a nozzle head	-
k	Jet cutting sensitivity of the target material (this is a constant value and is obtained by calibration data)	-
l	Characteristic length of the fluid, which in this particular case is the same as the SoD	*Mm*
m	Defined number of material layers	-
n	Number of jets in a nozzle head	-
P	Pump pressure	*MPa*
r	Radius to the centre of the jets	*mm*
Re	Reynolds number	-

r_p	Radius of the pocket	*mm*
S	Freeform surface	
t	Time	*s*
T	Trajectory of a rotary jet	*mm*
T_{thick}	total thickness /sum of the thickness of all the coating layers	*mm*
U	Etching rate	*mm/s*
v_{fluid}	Velocity of the fluid	*m/s*
v_r	Rotational velocity	*rad/s*
v_t	Translational velocity	*mm/s*
v_{total}	Overall velocity vector for any given jet in the nozzle head	*m/s*
x, y, z	Position of the jet in space	*mm*
α	Angular velocity	*rad*
β	Angle that each jet makes considering the first as reference	*rad*
γ	Angle between nozzles in a multiple jet nozzle head (in this application as using a four jet nozzle $\gamma = 90°$)	°
δ	Jet cone angle	*rad*
λ	slop angle of the pocket	*rad*
μ	Dynamic viscosity of the fluid	*mPa·s*
ρ	Density of the water	kg/m^3
σ	Variation of the jet diameter	*mm*

List of publications and deliverables

- Z. Liao, I. Sanchez, D. Xu, D. Axinte, G. Augustinavicius, and A. Wretland, "Dual-processing by abrasive waterjet machining—A method for machining and surface modification of nickel-based superalloy," J. Mater. Process. Technol., vol. 285, no. May, p. 116768, 2020.

- I. Sanchez, D. Axinte, and R. Smith, "Modelling of rotational multiple plain water jets for controlled removal of multi-material coatings," CIRP Ann., vol. 69, no. 1, pp. 309–312, 2020.

- I. Sanchez, D. Axinte, Z. Liao, O. Gavalda-Diaz and R. Smith, "The effect of high strain rate impact in Yttria Stabilized Zirconia," Materials & Design, vol. 229, 111908, May 2023.

Deliverables

- The developed model in a downable and installable format with instructions.

Chapter 1

Introduction to Plain Water jet machining for coating striping in aerospace components

The reduction of fuel consumption and the increase of the efficiency of the jet engines is proportionally related to the increase of its internal temperature. From the decade of the 1910s until the 1980s, this increment has been steady. However, since the 1990s the temperature that the gas-turbines can withstand has increased to almost the double. This has been achieved by developing new aerospace materials, improving their manufacturing processes and their protective coatings. However, when these coatings wear down they need to be replaced. This chapter describes how Plain Water Jet machining is one of the most promising technologies to remove this multi-layer coatings. The main goal is to identify the main challenges when applying this technology and develop a model to predict how the coatings are going to be removed as well as analysing what happens structurally to the water impacted material.

1.1. Motivation

Just over 100 years ago, at the 1st January 1914 the first commercial plane took off from St. Petersburg to Tampa, over the Tampa bay (Florida, USA), reducing the commute time from 12 h by rail to 23 minutes. It was a plane with a hull made of three layers of spurs and linen fabric between each layer and it was powered by a Roberts 6-cylinder, in-line, liquid-cooled, 75-horsepower engine that was capable of reaching the maximum speed of 103 km/h [1]. Since then, and especially in the last 50 years, commercial aviation has seen an exponential air traffic demand due to the research and improvement in aircraft and engine design incrementing the safety and leading to the democratization of the international air travel permitting the drop in prices. Nowadays more than one hundred thousand flights take off every day all over the world. This trend is increasing at 5% rate every year and it is predicted to continue so for the next 20 years [2], [3].

However, the transport industry is the second highest most polluting in the world just after the energy production [4]. An engine's exhaust is composed of ~70% of carbon dioxide emissions (CO_2), ~30% of water vapour (H_2O) and a remaining ~1% is composed of pollutants like nitrogen oxides (NOx), oxides of sulphur (SOx), carbon monoxide (CO), partially combusted or unburned hydrocarbons (HC), particulate matter (PM), and other trace compounds [5]. Due to this it is understandable the effort and budget implied trying to make the aeroengine cleaner and more efficient.

The reduction of carbon dioxide and pollutant emission as well as fuel consumption comes with the increase of the efficiency of the jet engines, which is proportionally related to the increase of the jet engine temperature [6]. In consequence, many efforts have been concentrated to develop engines that withstand higher temperature and pressures. However, these improvements are limited by the properties of the materials of the engine, temperatures in the combustion chamber can reach up to 1200 °C, with over 30 times the atmospheric pressure. Moreover, the inside of an engine is also a chemically harsh environment due to the fuel and moisture in the air. To continue developing the efficiency of the engine the integrity of the components must be improved or protected to withstand these conditions.

One of the first attempts of increasing the performance of the engine materials was to remove the grain boundaries of the blades, since the 1970s decade a directional solidification system has been used to manufacture single crystal engine blades [7]. The lack of grain boundaries prevents the part from failing by grains sliding under load, improving creep resistance, a key property in high temperature applications. Then, internal cooling channels were included in the blade design inside the engines in order to provide a faster cooling to these parts. Nowadays the research efforts for engine efficiency and increase of durability is focused on protecting the surface of the engine parts allowing them to work above their melting temperatures (~ 1300 °C) [8], [9] by applying Thermal Barrier Coatings (TBC) (Figure 2) or by physically improving the fit between parts thanks to abradable coatings [10] (Figure 2).

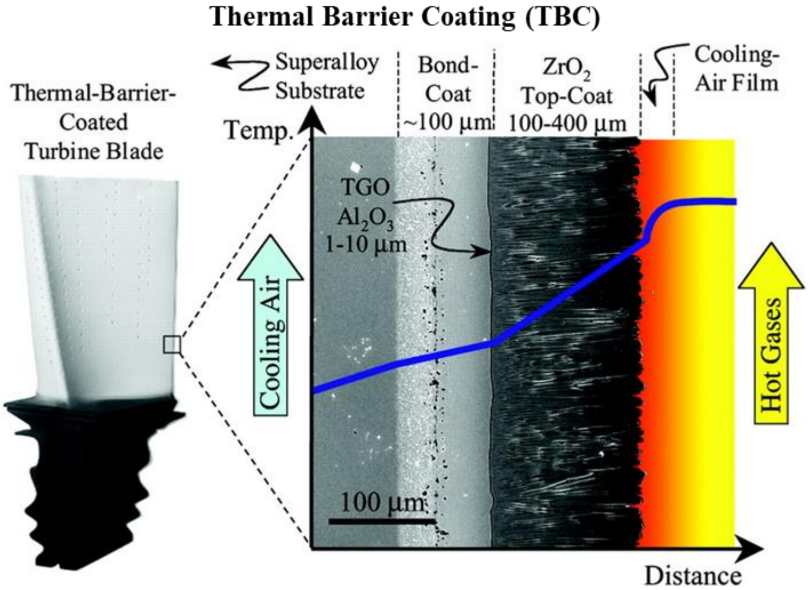

Figure 1: *Schematic representation of Thermal Barrier Coatings, which are able to keep the substrate material at a cooler temperature compared to the environment they are in* [9].

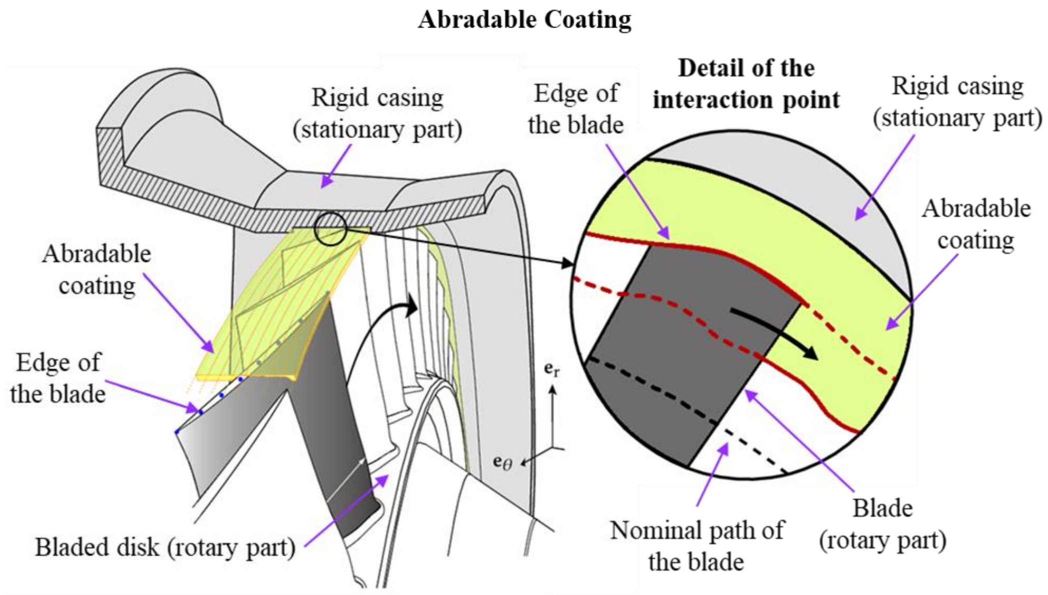

Figure 2: *Schematic representation of Abradable Coatings, that enable a very close fit between a rotary an a static part and so that if the two of them touch the coating wears down providing a custom fit between parts (adapted from* [10]-[11]*).*

Thermal Barrier Coatings (TBC) are one of the most demanding coatings present in the aero engines and they protect the base substrate from the high temperature environment, enabling the base materials to work even above their melting temperatures increasing the efficiency and durability of the engines [9]. They are built by duplex-type coatings that are formed by two main layers with different mechanical and thermal properties that compound a complex structure: a low-thermal conductivity ceramics top coat and a metallic bond coat [12]. On the other hand, abradable coatings help to reduce the leakages between parts improving the overall efficiency of the engine. The coating is applied in the stationary part and the rotor cuts through this part. In case of friction the clearance is adapted by the erosion creating a gap with the needed size. This type of coating allows having tight clearance between parts providing a minimum wear and friction heating, or components damage in case of metal-metal contact. Being easily wearable is one of their main characteristics so when the stators and rotors relative position changes due to their use, the requirements of the need of clearance changes. However, after three or four years of use, in comparison to the 20-25 years of service life of an engine, these coatings prematurely spall from the surface leaving the part exposed to the harsh environments as shown as in Figure 3. This spallation process happens due to various factors such as the thermal-expansion mismatch between the coating and the part, the oxidation of the metal and the continuous transformation of the material such as the microstructure, morphology and composition due to the harsh environment inside the engine [9].

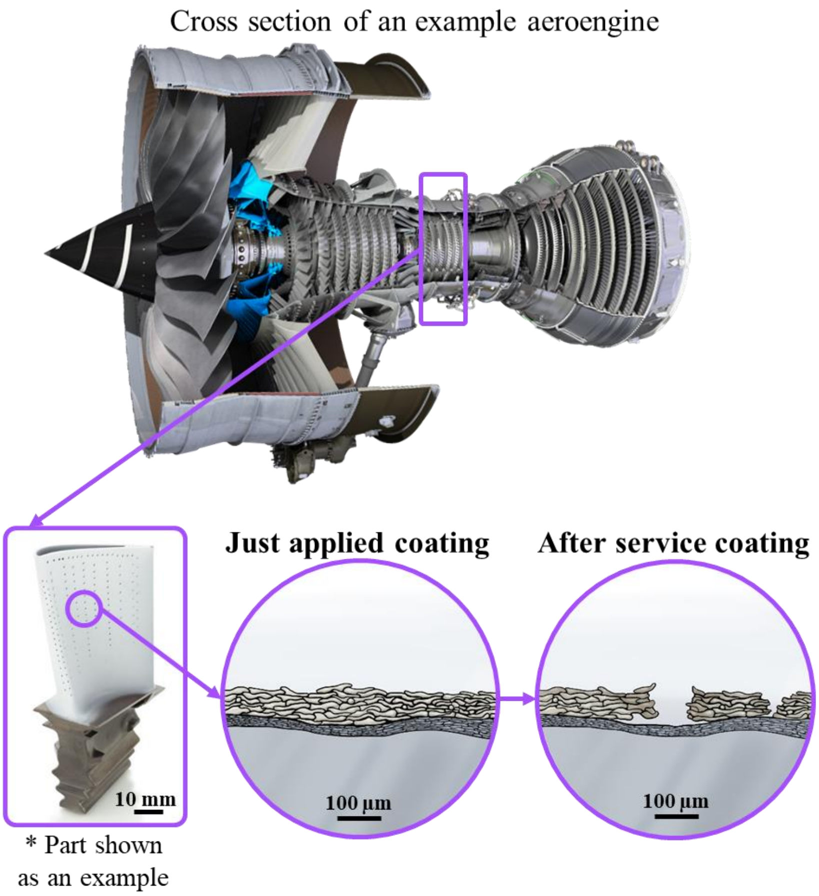

Figure 3: *Schematic representation of the deterioration of the aeroengine coating layers after years of service, due to the high temperatures and harsh environment.*

The parts where the coatings are applied are precision manufactured and hence expensive so considering that the life span of an engine is around 20-30 years the coatings have to be replace from the parts several times during their service without compromising their integrity.

1.2. Research problem

The main challenge faced when replacing a damaged coating from a part that must be accurately shaped is that first the worn-out coating has to be fully removed without damaging or altering the substrate material. These coatings have been traditionally removed by different techniques: i) submerging the parts in chemical baths so the remaining coatings could be dissolved without affecting the substrate. However, this technique is time consuming, not environmentally friendly and is hard to obtain a fully controlled process. ii) By mechanical milling, but this process requires precision manufacturing techniques and considering the complexity of the part as well as the request of maintaining the substrate untouched is an intricate process and expensive.

As an alternative, to achieve a controlled, clean and economical coating removal process Plain Water Jet (PWJ) milling has been proposed. This process is a non-conventional machining process that take advantage of the kinetic energy of the high-pressure water to remove the aerospace coatings promising to be a faster, cheaper and more accurate than other alternative methods. To upgrade the coating replacement maintenance process Rolls-Royce has suggested to develop this technology up to the level of being implemented in the production line at the end research period. The addition of hard abrasives turns the technology into a process called abrasive water jet (AWJ) that is capable of cutting virtually any kind of material, such as aerospace superalloys or even polycrystalline diamond [8], [13]. Although, the erosion power of the plain (i.e. without abrasives) waterjet (PWJ) is significantly lower, this is ideal for more “gentle” procedures such as milling, coating removal and surface cleaning.

Nevertheless, using PWJ technology for milling purposes has its own challenges. Coatings are often multi-layer, and each layer as well as the substrate have distinct mechanical properties. This means that the water jet will affect every layer differently, hence each material will respond with a different etching (i.e. material removal) rate. Moreover, the characteristic of time dependency of the WJ machining process, makes the operation difficult to predict (e.g. jet penetration), as a longer exposure to the jet will result in a proportionally higher etching rate. To cover all the surface that needs to be cleaned the jet will have to pass over some areas more than once (i.e. overlapping trenches), the second time the target material will have had already experience changes, so it would no longer be an untouched substrate making the process hard to perform accurately.

Rolls-Royce has already been using this stripping technique in their process, but it was suggested to find the most optimal way to do so. PWJ technique depends on multiple variables that involves pressurised fluids, spinning parts and the coatings that are meant to be removed are made of different layers that present various mechanical properties. Moreover, machine characteristics change from plant to plant, hence this makes it difficult to have standard parameters considering the limitations and specifications of each machine. Due to this motivations, a novel mathematical model that predicts the water jet milled trenches produced by a different water jet removal nozzles head (e.g. a four jet rotary and a fan nozzle) is proposed. This presents the innovation of considering the individual properties of the each of the multi-material layers, based on the analysis of the energy distribution of the multiple jets. This model covers any pump pressure, stand off distance (SoD), arbitrary trajectory and the overlapping of the multiple jets' footprints in curved and flat surfaces. In addition, it allows to control the depth of the jet penetration on multi-material systems to enable the damage prevention of the substrate material, while optimising the PWJ milling process to maximise the material removal rate.

To understand the effect of the impact of the high speed water jet in the target material a case study from a new perspective of analysing the effect of the high strain rate in 6-8YSZ has also been developed.

1.3. Objectives of the study

The aim of the PhD research project is to implement plain waterjet technology to remove the aerospace coatings in an effective, fast and in an economical way and ensuring no damage to the substrate underneath the coatings. After removing the coating these parts must be ready to be recoated and be installed in the engine again after ensuring their mechanical properties are still adequate. Moreover, with the aim of understanding the impact of the of a high energy water droplet against the coatings that are being removed a material analysis has been also performed. To fulfil these main tasks specific research goals have been defined, and have been listed as follow:

1) To create a foundation and understand the material removal mechanism, a mathematical model will be created to predict what will happen at the interaction between the waterjet and the coating when removing worn out aeroengine coatings. However, due to the nature of the process there are some challenges that need to be addressed:

   a. The waterjet being a commercial machine, multiple nozzles exist in the industry. Considering the width of the material to be removed being various orders of magnitude larger than a standard AWJ needle nozzle, two alternative options have been proposed that cover a wider surface area: a four jet rotary and a fan nozzle. Furthermore, the kinematics of the nozzle heads and their trajectories will need to be studied.

   b. Aero engine coatings have different layers in addition to the substrate. The coating layers have to be fully removed whereas the substrate protected. Hence, the milling depth mechanism must be very well understood. For this the material properties of each layer will be considered and implemented in the model.

   c. On some occasions, a single pass from the PWJ will not be enough to fully remove the entire coating layers but increasing its energy will not be possible without compromising the integrity of the substrate material. Due to this a jet overlapping approach will also be implemented. This presents its own challenges, as the material that will be found in the second pass will not be the same as the untouched surface, so the new initial conditions in this case will be addressed.

d. Components in an aeroengine come in different sizes and shapes, as for the versatility of the model the option of calculating the coating removal of flat and curved surfaces will be studied.

2) To facilitate the application of the mathematical model by the design of a software tool with a graphical interface, ready to be implemented in industrial scenarios at Rolls Royce manufacturing facilities. This will be accompanied by a "manual" for industry use. Thanks to this technical output the lab knowledge can be transferred and implemented into the industrial working environment.

3) To prove that the predictions obtained from the mathematical model match the reality of the PWJ removal mechanism, experiments will be done in a controlled laboratory environment. This will be done in a small scale at the laboratory from the University of Nottingham UTC, as well as in a Rolls-Royce industrial machine using a not in service real rotor case and real-life applicable parameters.

4) Finally, by the usage of advanced material science techniques and micromechanical devices the effect of the high energy water droplet impact in the coating top layer material will be studied, with the aim of further understanding the material removal mechanism at the micro- and nanoscales. This includes an assessment of the effect of the direct impact of the jet on the surface material and close up material characterisation analysis including stress strain evaluation, phase transformation analysis and defect study in the atomic scale.

1.4. Structure of the thesis

A schematic representation of the structure of the thesis is presented in Figure 4.

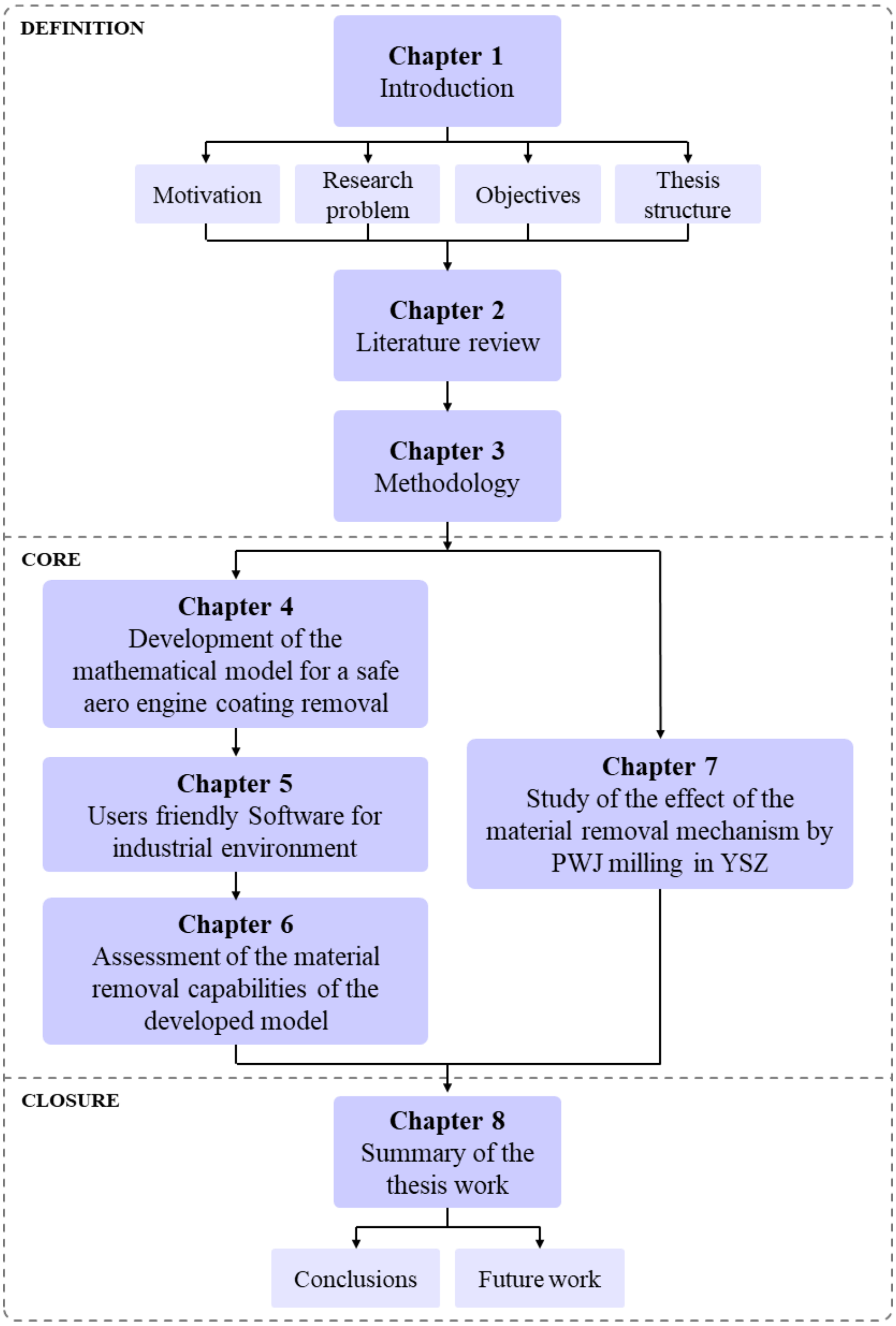

Figure 4: *Schematic representation of the structure of the thesis document.*

Chapter 2

Literature review on aerospace coatings and how to remove them

In view of the growth of Water Jet technology has seen over the last few decades there has been an extended research process in searching for new ways to implement it in different industrial applications. First, this chapter studies how the efficiency of the aeroengine evolved thanks to the improvement of the materials and manufacturing science over the decades. Then, the materials that had encourage this progress are discussed. Afterwards, the machining mechanism to replace these materials and coatings from the engine parts after they wear out during service is analysed as well as the mathematical tools that have evolve to support it. Finally, the surface integrity analysis techniques are reviewed as they are important to compare real samples to the modelled ones.

2.1. Development of the efficiency of aeroengines in regard to their improvements to optimize fuel consumption

The reduction of fuel consumption and the increase of the efficiency of the jet engines is proportionally related to the increase of the jet engine temperature [8], [14]. From the decade of the 1910s until the 1990s, the increase of this temperature has been steady and the machines were rather inefficient. However, with the growing demand for aviation and the need for more efficient engines, researchers and engineers began developing new technologies and designs to improve the performance of aero engines.

One of the major breakthroughs was the development of the turbojet engine in the 1930s and 1940s. The turbojet engine was designed to use the energy of exhaust gases to drive a turbine that would power the compressor, which would in turn compress the incoming air. This allowed for much greater power output and efficiency compared to earlier designs. The turbojet engine was quickly adopted for military aircraft and later for commercial airliners.

In the 1950s and 1960s, further improvements in aero engine technology were made with the development of the turbofan engine. These engines had a larger fan in front of the compressor, which increased the amount of air that could be compressed and also provided additional thrust. This led to further improvements in efficiency and allowed for the development of larger, more fuel-efficient aircraft.

From the 1970s to the 1990s the focus was set more in the development of new materials, and manufacturing processes of the engine components to improve elevated temperature performance rather than development of new models. As an example, grain boundaries of the blades have been removed by performing a directional solidification (see Figure 5) and allowing just a grain (i.e. a single crystal) to solidify by adjusting the chemical composition [15], [16]. The lack of grain boundaries prevents the part from failing by grains sliding under load, improving creep resistance, a key property in high temperature application [16]. These advantages and the addition of internal cooling channels in the casting process permit to increase the combustion temperature of the jet engine significantly [15]. Since the 1990s the temperature that the gas-turbines can withstand has increased to almost the double. This has been achieved by developing new aerospace materials, improving their manufacturing processes and their coatings [14].

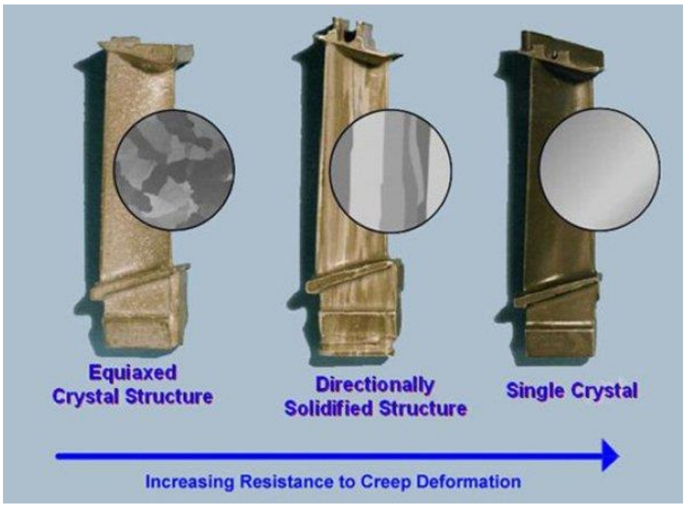

Figure 5: *Evolution of the engine blade over the years, highlighting the importance of its crystal structure for improving the performance* [17].

At the beginning of the new century, the application of aerospace coatings to improve the mechanical properties of the engine materials started to get special attention [12]. Coatings in aerospace, are used to enhance the properties of the substrate materials from the corrosion, erosion or wear caused by the hazard conditions that are held inside a gas-turbine engine:

- Thermal Barrier Coatings (TBC) are one of the most demanding coatings present in the aero engines and they protect the base substrate from the high temperature environment and enables the base materials to work even above their melting temperatures increasing the efficiency and durability of the engines [18]. They typically consist of a ceramic layer applied to the surface of the component. This layer has low thermal conductivity, which reduces the transfer of heat from the hot gas stream to the metal substrate.

- Abradable coatings are another type of coating used in aero engines and they are applied to the inner surfaces of compressor casings. They work by allowing a small amount of material to be rubbed off by the rotating blades during operation. This results in a tighter clearance between the blade tips and the casing. This leads to improved engine efficiency and reduced fuel consumption.
- Another important coating used in aero engines is erosion-resistant coatings. These coatings are applied to compressor blades and other components that are subject to erosion by airborne particles. They typically consist of a thin layer of material such as diamond-like carbon (DLC) or tungsten carbide, which provides a hard and wear-resistant surface.
- In addition, there are also anti-corrosion coatings, anti-fouling coatings, and other types of coatings used in aero engines to improve their efficiency and reliability.

2.2. Most relevant coating used on the engines: materials analysis

As mentioned, there are several types of coatings used in aero engines and each one serves its specific purpose. In this section two of the most used coatings will be further analysed from the point of view of their material properties: thermal barriers and abradable coatings.

2.2.1. Thermal Barrier Coatings (TBC)

TBCs are duplex-type coatings that are formed by two main layers with different mechanical and thermal properties that compound a complex structure: a low-thermal conductivity ceramics top coat and a metallic bond coat [12]. These coating are usually set on top of turbine blades, which are made of a substrate material that is usually a nickel or a cobalt based superalloy. Their main properties are ductility, hot corrosion and oxidation resistance, high strength at elevated temperatures and castability. In the case of the combustion chamber case components that are made of titanium alloys which also provide a good strength-to-weight ratio [18]. Figure 6 shows the described structure of the TBCs that are able to decrease the surface temperature of the base metallic superalloy in between 100 and 300 °C [18].

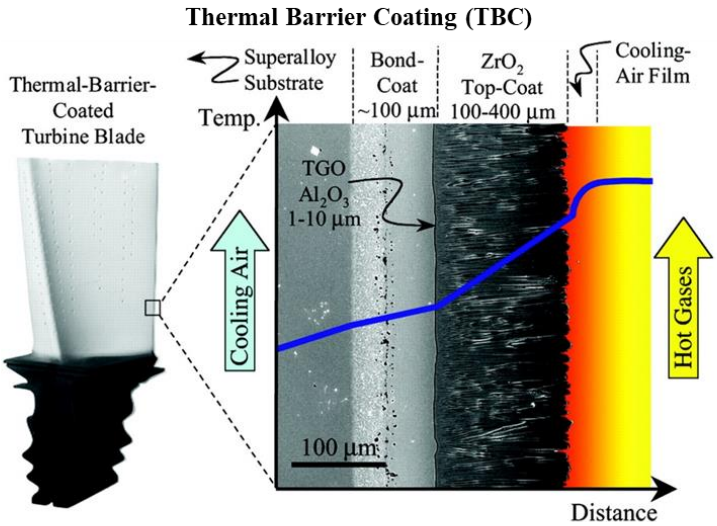

Figure 6: *Schematic representation of the Thermal Barrier Coatings and their different layers as well as the temperature gradient throughout the cross section of the coated turbine blade* [18].

The bond coat is typically made of an oxidation resistant metallic layer, NiAl or NiCrAlY alloys, of a thickness between 75 µm and 100 µm that improves the adhesion of the top coat to the substrate and helps to alleviate thermal mismatch between layers [19]. This layer frequently can reach up to 700 °C so it is unavoidable to experience some oxidation after a considerable number of thermal cycles.

The oxide layer, denominated thermally grown oxide (TGO), is an aluminium oxide (Al_2O_3) that can grow up to 10 µm. It provides a good corrosion resistance to the bond coat as it has a poor ionic diffusivity [20]. However, when the layer does not grow uniformly it can lead to an increase of the oxide layer towards the top coat decreasing its adherence [18]. Due to the growth of this oxide layer, the properties of the TBC can change with the time and during the service life [21].

The top coat layer has a thickness between 100 µm and 400 µm and is usually made of yttrium dioxide (Y_2O_3) and zirconium dioxide (ZrO_2) making Yttrium Stabilized Zirconia (YSZ) [18]. Moreover, zirconia has an elevated oxygen ion conductivity at high temperatures and due to its application process the top coat is full of interconnected porosity which leads to a fluent oxygen migration from the top coat to the bond coat contributing to the increase of the TGO layer [21], [22].

a) <u>Yttria Stabilized Zirconia (YSZ): Top layer of TBCs</u>

- <u>Phase transformations of the pure zirconia</u>

Zirconia, zirconium dioxide (ZrO_2), is one of the most used crystalline compounds in the top coat of thermal barrier coating, especially due to its high melting point of up to 2680 °C and its elevated resistance to chemical attacks. These properties make zirconia an ideal material to withstand hard and continuous thermal cycles and provide protection in hot corrosive environments [23].

However, pure zirconia shows a major limiting drawback: it suffers phase transitions due to temperature that causes property and volume changes making it unstable when facing thermal cycles [23]. The Figure 7 shows the different phases that pure zirconia undergoes from room temperature to melted liquid zirconia.

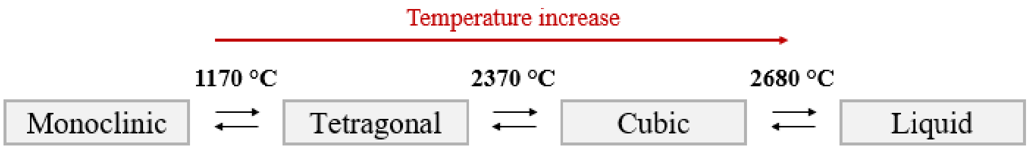

Figure 7: *Schematic diagram showing the different phases that pure zirconia undergoes from room temperature monoclinic zirconia, moving through tetragonal at 1170 °C and cubic at 2370 °C to liquid state at 2680 °C (adapted from* [22]*).*

Understanding the changes in the crystallographic structure when the phase changes happen is of vital importance for the development of the project.

Zirconium dioxide (ZrO_2) is made by zirconium atoms, which are the cation and oxygen atoms, which constitute the anion. The first phase that is formed is the cubic phase, also known as the fluorite structure, when the element is solidified just below 2680 °C. The oxygen forms a cubic sublattice structure while the zirconium atoms are packed in a face-centre cubic structure that is set around the oxygen sublattice [23].

The transition to the tetragonal structure is formed when the material is cooled down below 2370 °C and is believed to be a distortion of the fluorite structure. Zirconium atoms build a body-centre tetragonal unit and the oxygen atoms build a sublattice tetragonal cell [23].

Below 1170 °C, the zirconia undergoes a martensitic transformation to a monoclinic structure. The martensitic transformation is disrupted and suffers a volume shrinkage of up to 4% [24], which means that the coordination number drops undergoing structural instability during the transformation process in where the material suffers strain [23]. All these drawbacks make the phase change from tetragonal to monoclinic undesirable or at least known and controlled.

All the three structures of the pure ZrO_2, which are made of four Zr and eight O for the monoclinic phase and two Zr and four O for the tetragonal, are represented in Figure 8 [25].

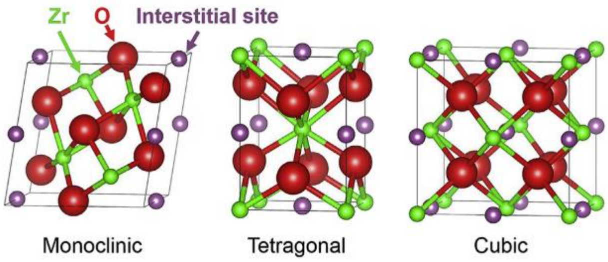

Figure 8: *Schematic representation of monoclinic, tetragonal and cubic crystallographic structures of pure zirconia, made of zirconium and oxygen atoms* [25].

- <u>Stabilization of the zirconia</u>

In order to have a further control in the phase changes, zirconia is usually stabilized adding Mg, Ca or Y to the composition. The addition of these elements will decrease the phase transition temperature making the desired state more stable. This research will be focused the yttrium stabilized zirconia (YSZ) as it is the most used one in aerospace applications due to the fact that undergoes thermal cycles really well [8]. YSZ is achieved by the addition yttrium oxide (Y_2O_3), also called yttria, to the pure zirconia (ZrO_2). The Figure 9 shows the zirconia-yttria phase diagram.

The percentage of stabilization as well as the mechanical properties of the partially stabilized zirconia will depend on the Y_2O_3 volume percentage and distribution added to the mixture. An 100 % of stabilization will be achieved at room temperature with a cubic phase. However, this is not always required nor desired as toughness decreases when incrementing the Y_2O_3 percentage [23].

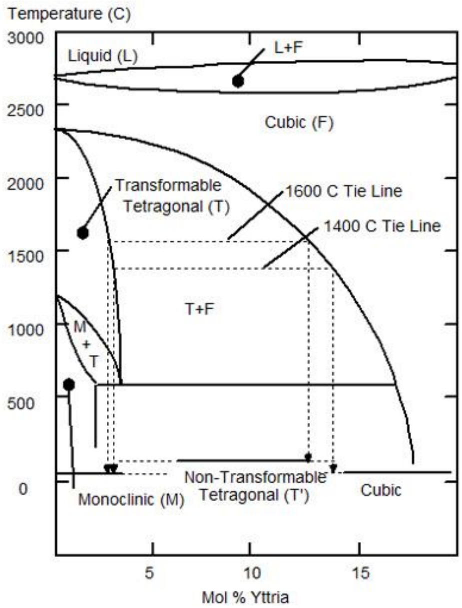

Figure 9: *Phase diagram for ZrO2-Y2O3, with yttria represented in mol % (adapted from* [24]*).*

- <u>Yttria Stabilized Zirconia properties</u>

The usual yttria mol fraction goes from 3 % up to 14 % in order to ensure a tetragonal phase all along the crevice temperature range. YSZ is a relatively low-density material (~6.4 Mg/m^3), with high hardness that is around 14 GPa making it erosion and impact resistant. It has also a low thermal conductivity of around 2.3 W/mK for a fully dense material and a high thermal expansion coefficient (11×10^{-6} $°C^{-1}$) which contributes to the stress relieve that is generated due to the thermal mismatch occasioned by the suffered thermal cycles [18]. However, the most important property of tetragonal YSZ is the elevated fracture toughness that goes between 6 to 9×10^6 $N/m^{3/2}$ [23], which begins to decrease when its close to transform to a cubic phase.

- <u>Description of phase transformation mechanism</u>

When the yttrium oxide is added to the zirconium dioxide Zr_4+ ions are randomly replaced by Y_3+ ions. Y_2O_3 and ZrO_2 have the same crystal structure but Y_3+ ions slightly larger than Zr_4+ ions and so they are able to block the structure (0.96 Å and 0.84 Å respectively), in addition, the trivalent Y_3+ ions induce O_2- oxygen vacancies in the ZrO_2 structure that is build up by Zr_4+ tetravalent ions. The introduction of oxygen vacancies reduces the fold coordination number of the zirconia from 8 to <8 at high temperature. As a result, atoms in the crystal structure are mechanically blocked (i.e. up to a degree as this phenomena increases with the increase of Y_2O_3 content) preventing the phase transition from tetragonal to monoclinic to happen [8] [26].

However, YSZ still can suffer phase transformation after extreme interactions such us prolonged thermal cycles or high-pressure. YSZ, due to its structural properties and as it is also compatible with the human body, is widely used also in biomedical applications, specially implemented to simulate the bone structure. G. Pezzotti et al. had reported, back in 2004, some issues with a hip implant made of ZrO_2 containing 3 mol % Y_2O_3. The hip suffers a strong impingement in the head part against the metallic neck attached in the femoral part, in which a transformation from tetragonal to monoclinic zirconia was observed. Raman spectroscopy was used to reported that the phase transformation from tetragonal to monoclinic as well as stress concentration where much higher in the area where the hip was in contact with the metallic femoral surface. The metastability of the YSZ lead to pain and a new surgery to replace the implant of the patient after just 3 years [27].

K. Yasuda et al. analyse a phase transformation from tetragonal to monoclinic on samples of YSZ in samples that goes from 4% to 20% mass of yttria reporting an actual phase transformation in samples with less than 8% mass of yttria after undergoing hydrothermal aging. This study demonstrates a correlation of the phase change in partially stabilized zirconia with humid atmospheres [28].

The martensitic transformation from tetragonal to monoclinic phase transformation has been widely observed. However, in parts over 8% Y_2O_3 has usually been reported happening in moisturized environments, corrosive environments, or high temperature environments. YSZ is known for its good ion (oxygen) diffusivity, which it makes sense, as the oxygen atoms are considerable smaller than the cations (Zr_4+ and Y_3+) [25], [29].

In harsh high temperature environments atom vibrations and migration is higher and the diffusion mechanism activates more easily, as diffusion is a temperature dependant phenomenon [25], [29]. Although the martensitic transformation is diffusionless, high temperature and harsh environments and their resultant diffusion mechanisms can alter the structure unlocking the stabilized atom arrangement. As a result, this new crystallographic architecture could be more likely to suffer a diffusionless martensitic transformation.

b) <u>Comparison between different application methods of Thermal Barrier Coatings (TBC) and their microstructures.</u>

The structure of the TBC will vary based on their application process. There are many techniques for coating applications, but the most common ones in aerospace industry are the followings: air plasma spray (APS) and electron beam physical vapour deposition (EB-PVD). Both of them brings up its own characteristic microstructure and hence different mechanical properties [30].

Electron beam physical vapour deposition (EB-PVD) is a coating deposition method that high-energy electron beam into the material to be deposited with the aim of evaporating them. Evaporate material gets condensate and is deposited in the desired surface [31].

APS is a thermal spray technique that is capable of applying metallic and non-metallic material on thin layers. It uses the kinetic energy of melted particles that have an approximate size of 0.1 µm to 1µm diameters [30]. It is applied by generating a direct current arc or radio frequency discharge in order to heat the display source up to 8000 K. The particle speed released from the spry can vary from 20 m/s to 500 m/s depending on their size [32]. This deposition process does not ensure the complete melt of all the droplets due to this is usual to find semi-melted particles, discontinuities and up to 30% of porosity. Both EB-PVD and APS creates a unique and characteristic microstructure shown in Figure 10.

EB-PVD **APS**

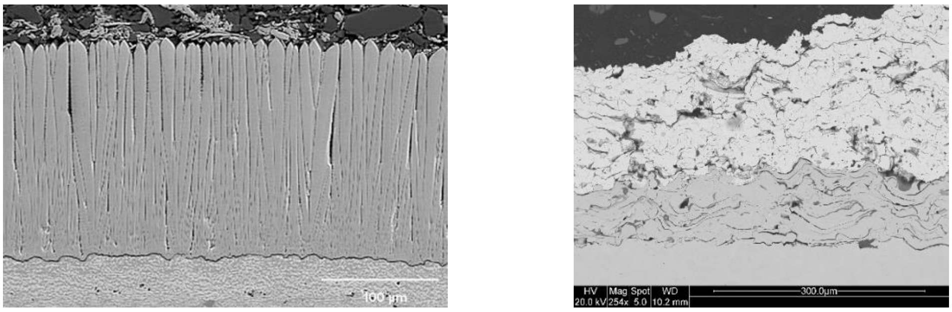

Figure 10: *Scanning electron microscopy (SEM) cross sections of EB-PVD columnar structure* [33]*, and APS horizontal and porous splats structure.*

With the EB-PVD method, a characteristic columnar structure is obtained thanks to a directional cooling which provides better insulation to the base material; hence, a directional porosity is achieved. The term "directional porosity" describes the coating structure's deliberate production of aligned pores or channels. These pores can act as channels for stress release and thermal expansion. The directed porosity makes it easier to accommodate thermal expansion and contraction when the substrate and coating are subjected to temperature variations. This lessens the chance of coating delamination or failure by reducing the accumulation of stress and strain inside the coating. The overall performance and longevity of the coated component are improved as a result, which lowers the possibility of thermal mismatch-induced failures. However, for the success of this method a vacuum environment is required which makes the process very expensive, specially to be applied in large parts [31].

On the other hand, APS coatings are built up forming a horizontal structure that is mainly bonded mechanically as it is shown in Figure 11. Even if some diffusion mechanisms are also involved in the bonding process one of the main advantages of the mechanical bonding is that splats can slide and move in order to release the residual stresses causes by thermal cycles. The obtained properties are not as good as with the EB-PVD but is much economical and easier to achieve [18] and this is why is the one that we will be using in our application.

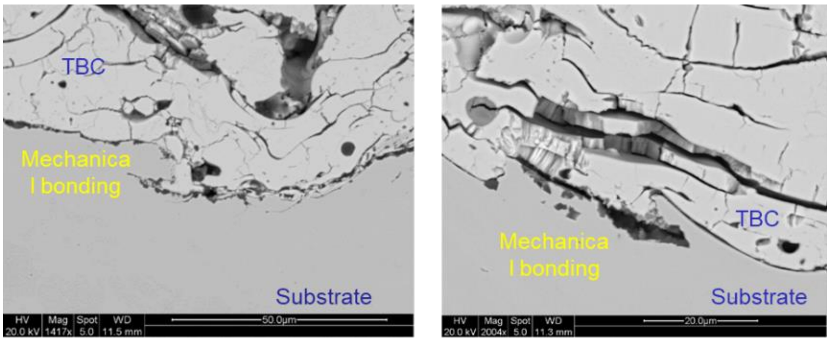

Figure 11: *Mechanical bonding that maintain the APS structure packed in place*.

However, after four or five years of service life YSZ coatings spalls out and, as shown in Figure 12, considering that the service life of an engine is of around 20 years these coatings have to be replace regularly in maintenance processes. This need led to the main objective of this project as described in the previous section: include the waterjet technology in the maintenance process of Rolls-Royce to remove and then replace these coatings.

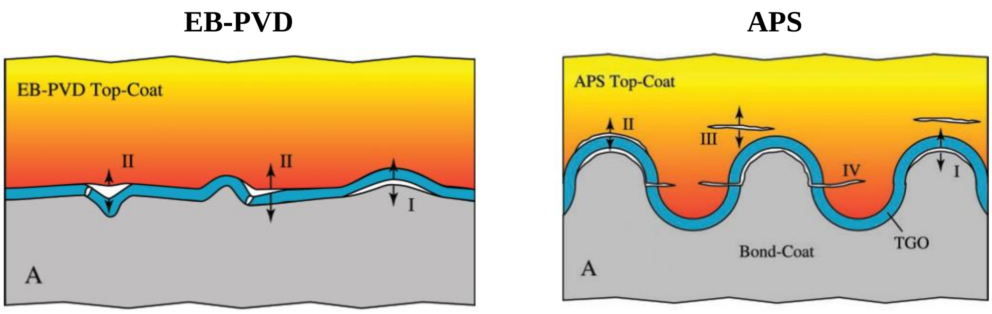

Figure 12: *Schematic diagram that shows the collapse, showing different cracking mechanisms, of both EB-PVD and APS coatings after suffering around 240 thermal cycles* [18].

2.2.2. Abradable coatings

An abradable coating is a specialized type of coating that is designed to wear away when it encounters a moving component, such as a turbine blade in an aircraft engine. The purpose of the coating is to create a tight seal between the moving and stationary parts of the engine, while minimizing friction and reducing the risk of damage to the components. They are used to reduce the gap and create a more precise seal between the blades and the casing, without causing damage or excessive wear [34], [35] (see Figure 13).

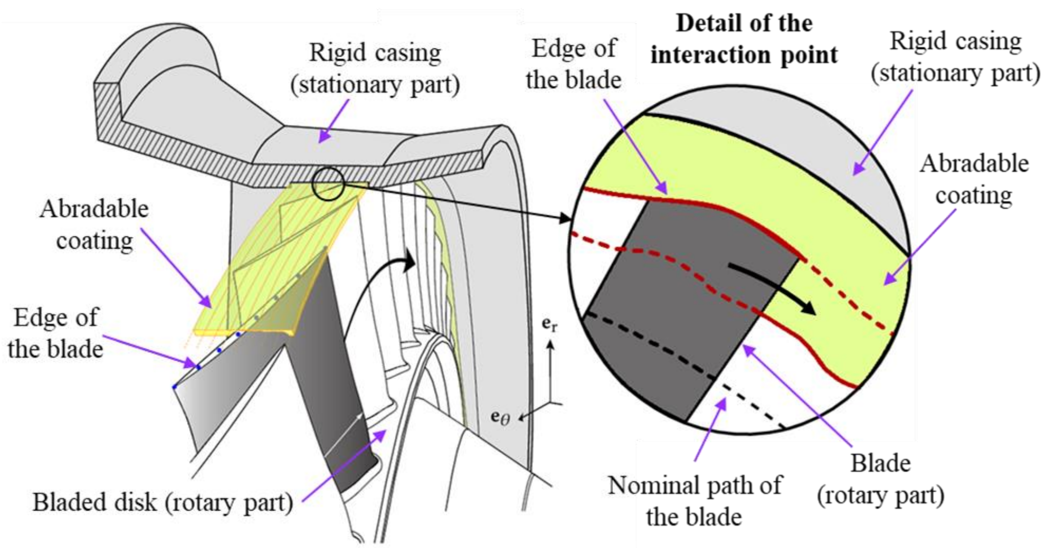

Figure 13: *Schematic representation of Abradable Coatings, that enable a very close fit between a rotary an a static part and so that if the two of them touch the coating wears down providing a custom fit between parts (adapted from* [10]-[11]*).*

Due to this they are typically located in the clearance gap between the rotating blades and the stationary casing in a gas turbine engine or in the stator vanes, to improve sealing and reduce air leakage. Specifically, they are applied to the shroud of the rotating blades and the corresponding casing of the stationary structure. The clearance gap is necessary to allow for thermal expansion of the components as they are exposed to high temperatures during operation. However, if the gap is too large, it can result in significant air leakage and reduced engine efficiency [36].

They are made from materials that have a relatively low hardness and a high level of porosity. When the coating is applied to a component, it is designed to be slightly softer than the material of the component itself. This means that when the component starts to move, the coating will wear away slowly, creating a precise and customized gap between the moving and stationary parts of the engine [37]. One of the main advantages is that they can improve the efficiency and performance of aircraft engines. By reducing the amount of air that escapes around the turbine blades, the coating can help to increase the amount of power that is generated by the engine, while reducing the amount of fuel that is required to produce that power [35].

There are usually applied by thermal spray, which involves heating a material to a molten state and then spraying it onto the surface of the component that needs to be coated (e.g. Plasma, High-velocity oxy-fuel (HVOF), Detonation gun…) [38]. Once the coating has been applied, it is usually subjected to a curing process (i.e. heat treatment or air drying) to ensure that it adheres properly to the surface of the component and has the desired properties (e.g. porosity, hardness, toughness…) [39].

2.2.3. Degradation of aeroengine coatings due to prolonged exposure to a harsh environment

TBCs degrade and expel of when exposing them to harsh conditions, as it is the inside of an engine during service, if exposed for a prolonged period of time. This can be due to many reasons such us thermal mismatch between coating and substrate [40], water vapour induced degradation, residual stresses generated crack growth, etc. [41]. When thermal barrier coatings wear off, the underlying material (i.e. the substrate) is exposed to the high temperatures and harsh conditions of the gas turbine engine environment (see Figure 14). This can lead to several issues such as, increased heat transfer, reduce engine performance, corrosion and oxidation of the substrate [18].

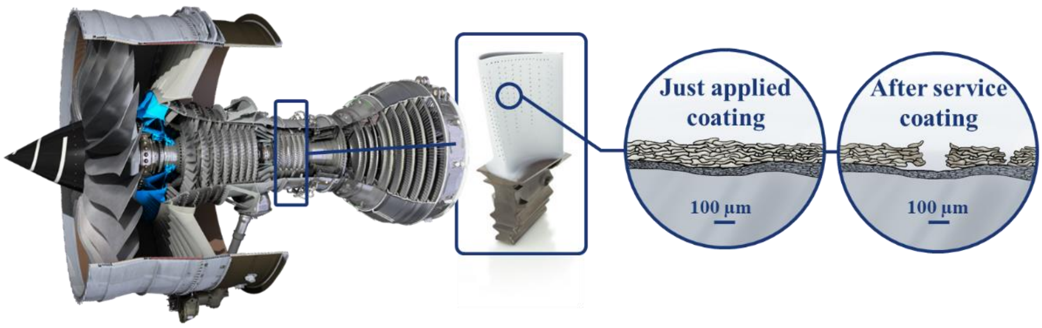

Figure 14: *Schematic representation of how aero engines degrade and get expelled during service [adapted from figure from RR].*

As for the abradable coatings, the clearance gap between the rotating blades and stationary casing in the gas turbine engine increases, which can result in a reduction in engine efficiency and performance [39]. This can cause a few problems, including increased fuel consumption, reduced power output, and increased wear on the engine components. If the gap becomes too large, it can also cause a phenomenon known as blade rub, where the rotating blades meet the stationary casing, resulting in damage to both the blades and the casing. Blade rub can be a serious issue, as it can lead to engine failure and even catastrophic damage to the aircraft [42].

To prevent these issues, it is important to regularly inspect and maintain the coatings in gas turbine engines. This may involve repairing or reapplying as necessary to ensure that the underlying material is properly protected but for this the compromised coating layer must be removed [43].

2.3. Coating removal mechanisms

Coatings on engine parts become damaged or degraded over time, due to the harsh operating conditions of the engine, such as high temperatures, high pressures, and exposure to corrosive substances or worn out due to mechanical stress and foreign object damage [40], [44]. This can lead to reduced engine performance and potentially dangerous malfunctions. Due to these coatings need to be replace by removing the worn out layer from the base part and recoating it before mounting it again in the engine [42].

The base parts can often be safely reused if they are found to be in good condition, defined by aerospace safety regulations standards, after the coating removal process [45]. To reuse parts rather than replace them with new if it is possible is more desired option due to various factors:

- It is a cost-effective option. Especially for complex geometry parts, such as turbine blades and compressor rotors. By reusing these parts, maintenance and repair costs can be significantly reduced, which can help to lower the overall cost of engine maintenance.
- Reusing parts can help to ensure that the engine retains its original performance characteristics. These parts are designed and manufactured to very precise specifications and replacing them with new parts that may have slightly different characteristics can impact engine performance. By reusing the original parts, engine performance can be maintained and optimized.
- It is a more environmentally friendly option than replacing them. Engine parts can be difficult and expensive to manufacture and replacing them with new parts can generate a significant amount of waste.

However, as a disclaimer, it is important to note that not all engine parts can be safely reused after coating removal. Some parts may become worn out or damaged beyond repair due to the stresses of engine operation and must be replaced with new parts. The decision of whether to reuse or replace a particular engine part will depend on several factors, including the type and severity of the damage, the age and condition of the part, and the requirements of the engine manufacturer and regulatory authorities such as industry norms and standards [46].

The process of removing coatings from engine parts is known as coating removal or stripping. Several methods can be used to remove coatings from engine parts, depending on the type of coating and the part's material.

The following section describes different methods used in the aerospace industry. In any of the methods applied avoiding any damage to the part being stripped is essential.

2.3.1. Classification of coating striping methods after service based on their physical process

There are different methods than can be used based on many factors (e.g. coating and substrate material, part geometry, time…) the following section develops three main methods for this purpose: mechanical, chemical and thermal coating stripping methods [46], [47].

a) Mechanical stripping methods

Mechanical stripping is a process of removing coatings from the surface of engine parts using mechanical abrasion or pressure. This method is particularly useful for removing coatings that are thick, hard, or difficult to dissolve using chemical or thermal methods.

There are several advantages to using mechanical methods for coating stripping in the aerospace industry such as controlled and precise coating removal in where consistency is easily acquired, valid for most materials (e.g. including metals, ceramics, composites, and polymers) as well as because it is an easy and accessible process. Moreover, unlike chemical stripping methods, which can be hazardous and require extensive safety precautions, mechanical stripping methods are generally safer and less toxic. They also produce less waste and are more environmentally friendly.

However, this method needs to be handled with care if not it can also cause damage to the surface of the part being stripped if not done carefully. Therefore, it is important to use the appropriate equipment, techniques and understanding of the process to ensure that the stripping process is done safely and effectively [46].

- **Sandblasting:** This is a common method that involves using a high-pressure stream of abrasive particles, such as sand or glass beads to remove the coating from the surface of the part and is particularly effective for removing thick or stubborn coatings [47].
- **Grinding:** It uses a rotating abrasive wheel that removes small amounts of material from the workpiece that is being machined. Its process in where precise shapes and tolerances can be achieved [48].
- **Shot peening:** This is a process in where small, spherical particles, typically made of steel or ceramic are bombarded into the surface of a part. The particles impact the surface, creating small dimples that help to remove the coating. Shot peening is particularly effective for removing coatings from parts that have complex geometries or that require a high degree of precision. However, it can modify the substrate material by inducing plastic deformation and compressive residual stresses [49].
- **High-pressure water jetting**: This process involves using a high-pressure stream of water to remove the coating from the surface of the part. The advantage of this method is that it is gentle enough to not damage the underlying metallic substrate, making it useful for removing coatings from delicate or sensitive parts. It is also a relatively environmentally friendly method that does not produce hazardous waste or emissions. However, water jetting may not be as effective as some of the other methods mentioned in removing certain types of coatings, such as highly adhesive or stubborn coatings. Additionally, due to all the parameters involved in the process it needs to be controlled accurately [46],[50].

b) Chemical stripping methods

Chemical stripping is a process of removing coatings from the surface of engine parts using chemical solutions. This method is particularly useful for removing coatings that are too thin (i.e. hence substrate damage is almost inevitable or difficult to remove using mechanical methods). In addition, it can be a precise and selective method with multi material components as each material type reacts differently to different acids [51], [47].

It is important to note that chemical stripping can be hazardous and requires extensive safety precautions, including the use of protective clothing, gloves, and ventilation systems. Moreover, the chemicals used in the stripping process can be toxic and require careful handling and disposal [46], [52]. This a list of most used chemical stripping methods used in the aerospace industry:

- **Acid dipping:** This involves immersing the part in an acidic solution, typically containing hydrochloric acid or sulphuric acid. The acid reacts with the coating, breaking it down and dissolving it from the surface of the part. This is an effective way to remove coatings from several materials such as including metals, ceramics, and composites [46].
- **Solvent cleaning:** This process consist on immersing the part in a solvent, such as methylene chloride, acetone, or trichloroethylene. The solvent dissolves the coating, allowing it to be wiped or rinsed away. Solvent cleaning is particularly useful for removing coatings that are difficult to dissolve in other chemicals or that are sensitive to high temperatures [46].

c) Thermal stripping methods

Thermal stripping is a process of removing coatings from engine parts using heat. It is often used to remove organic coatings such as paint or varnish that are difficult to remove using other methods. The process involves heating the part to a high temperature until the coating burns off or decomposes. It is easy to isolate a specific area that needs to be stripped and leave the rest of the part untouched which comes handy when dealing with complex geometries. However, it is a hazardous process that requires extensive safety precautions, including the use of protective clothing and equipment. It can also induce potential for damage to the part if not controlled properly leading to warping or other forms of degradation [46], [53]. Here is a summary of different methods of thermal stripping used in the aerospace industry:

- **Flame stripping:** This method involves directing a flame at the surface of the part until the coating burns off. The flame can be produced using a propane torch or other heat source. Flame stripping can be effective for removing coatings from small or simple parts, but it is not suitable for larger or more complex parts [54].
- **Fluidized bed stripping:** This method involves placing the part in a bed of heated sand or other particles. The heat from the particles causes the coating to decompose, allowing it to be removed from the surface of the part. Fluidized bed stripping is particularly useful for removing coatings from parts with complex geometries or delicate surfaces [46].
- **Induction stripping:** This method works by heating the part using electromagnetic induction. An alternating magnetic field is applied to the part, causing it to heat up and the coating to decompose. Induction stripping is particularly useful for removing coatings from parts with a high degree of precision or that are sensitive to high temperatures [46].

- **Plasma stripping:** Plasma stripping involves exposing the part to a low-pressure plasma gas, typically nitrogen or oxygen, which breaks down the coating and removes it from the surface of the part. This method is particularly useful for removing coatings that are sensitive to high temperatures or that require a high degree of precision [55].

The choice of coating removal method depends on various factors such as the type of coating, the material of the engine part, the size and complexity of the part, and the desired level of precision. However, among the methods mentioned, mechanical stripping is one of the most used methods for removing coatings from engine parts. This is because it is a relatively safe and effective method that can be used on a wide variety of materials and geometries. Additionally, it does not produce hazardous waste or emissions, making it more environmentally friendly than some other methods [46], [47].

Considering all the mechanical stripping methods available high pressure plain water jet is one of the most promising methods for coating stripping. As previously described it is a non-abrasive method, meaning it does not damage the underlying substrate. This is particularly important in the aerospace industry where the components are often made of high-performance materials that require precise tolerances and surface finishes. Moreover, it is a highly efficient method. Large surface areas can be cleaned in a relatively short amount of time, reducing downtime and increasing productivity. Additionally, the method generates very little waste, making it a relatively environmentally friendly option compared to traditional methods which can produce hazardous waste materials [46], [47].

However, it is a method that involves many parameters and it can be hard to have accurate control or full understanding of the physics involved. There have been many resources focused in researching the development of this method as it is described in the next section.

2.4. How does a Plain Water Jet system work

As described water-only or plain water jet technology is non-conventional machining technique based on the principle of using a high-pressure water jet to remove material from a workpiece, without the use of any abrasives or other cutting agents. The water jet is focused through a small orifice to create a high-velocity stream that can cut through the material [56]. The pressure of the water is typically in the range between 50 - 600 MPa, which allows it to mil a wide range of materials with control. Unlike traditional milling methods, water-only milling does not generate heat or mechanical stress, which can cause distortion, warping, or cracking of the workpiece [57].

The process of plain water jet milling involves the following steps:

1. **Pressurisation:** Water is pressurised to a high pressure of around 300 MPa using a hydraulic intensifier or a pump.
2. **Focusing:** The pressurised water is then passed through a small orifice or nozzle that reduces its diameter and increases its velocity, creating a narrow and high-velocity jet of water that is capable of cutting or milling through various materials.
3. **Machining:** The high-velocity jet of water is directed towards the material to be cut or milled, and it rapidly erodes the material by abrading and breaking apart its structure. The machining process can be further enhanced by adding abrasive particles, such as garnet of aluminium oxide or silica, to the water jet, which increases its cutting power or used as only water for controlled milling procedures.

This makes PWJ milling ideal for applications where high precision and accuracy are required [58]–[60], such as in the aerospace, medical device [61], and electronics industries. Additionally, this method if used appropriately it can be an environmentally friendly process, as it does not produce any hazardous dust, fumes, or waste materials as the water used for the process can be recirculated. Moreover, it is an efficient and non-destructive process as water jet stripping is a process that can remove coatings effectively, reducing the time required for maintenance and repair without damaging the underlying substrate. Additionally, it is precise (i.e. it is possible to achieve high accuracy), it is safe for the user and cost/effective especially for large or complex components, as it does not require the use of expensive chemicals or the disposal of hazardous waste and as it does not require any cutting tools, such as drills or saws, which can wear out over time and require frequent replacement. This can reduce maintenance costs and increase production efficiency [62].

These advantages have made water jet stripping an increasingly popular method for the removal of aerospace coatings, particularly for aircraft repainting and maintenance.

One of the most important factors to understand the impact of the high pressure water jet in the substrate is the speed of the water jet [63]. This value will be important in the future calculation of the maximum energy that will lead to the prediction of the milled trench. For this an example will be calculated with a representative PWJ pressure value: the speed of the water particles in a plain water jet at pressure of 300 MPa can be calculated using the Bernoulli's equation (1). This equation is defined by the pressure, velocity, and height of a fluid in a pipe [57]. The velocity of the water jet can be determined using the following equation:

$$v = \sqrt{2\frac{P}{\rho}} \tag{1}$$

In where:

- v is the velocity of the water jet in m/s
- P is the pressure of the water jet in Pa (300 MPa)
- ρ is the density of water in kg/m³ (assuming a temperature of 20°C, the density of water is approximately 998.2 kg/m³)

Using these values, is calculated that the theoretical velocity of the water jet particles in a plain water jet is approximately 773.7 m/s, for this specific water pressure.

However, the main reason to introduce this parameter in this section is to elaborate that this speed of the water particles in a plain jet will be affected, and hence reduced by several factors, including the condition of the equipment, the quality and type of nozzle, and the type and quality of the water used. Depending in these factors the calculated maximum jet speed will be decreased by a 10 - 40%. Here are some ways in which the functions of the system can affect the velocity of the water jet particles:

It is difficult to provide specific percentage values on how much the velocity of the water jet particles could be affected by various factors since it depends on the specific circumstances and the degree to which each factor is affecting the system [57]. However, some general examples of how different factors can affect the velocity of the water jet can be defined [57], [63]:

- **Pressure fluctuations:** Any fluctuations in the water pressure can cause the velocity of the water jet to vary. If the water pressure drops, the velocity of the water jet will decrease and vice versa. The velocity of the water jet particles are directly proportional to the pressure of the water and therefore, if the water pressure drops by 10 %, the velocity of the water jet particles will also decrease by approximately 5 %. Those pressure fluctuations can happen for example due to the variations of the pump.
- **Nozzle quality:** The quality and type of nozzle used can also affect the velocity of the water jet. A poorly designed or worn nozzle can reduce the velocity of the water jet, resulting in a slower cutting speed. A faulty nozzle can reduce the velocity of the water jet stream speed by up to 10-20% compared to a high-quality, well-designed nozzle.
- **Water quality:** The quality of the water used in the water jet machine can also affect the velocity of the jet. If the water contains impurities such as dissolved minerals or air bubbles, it can reduce the velocity and cutting performance of the water jet. The quality of the water can affect the velocity of the water jet by up to 5-10%.

- **Abrasive type and quality:** When abrasive particles are added (i.e. if they are added) to the water jet to cut harder materials, the type and quality of abrasives can also affect the velocity of the water jet. Abrasive particles that are too large or too soft might reduce the velocity of the water jet and result in a slower cutting speed by up to 10-15%.

All these factors, and others, can affect the velocity of the water jet droplets in a plain water jet, so it is important to ensure that the water jet machine is properly maintained and operated to achieve the desired cutting performance.

About its distribution it is stablished that the water pressure drops and the jet spreads with the SoD and that the jet is divided into three regions considering this pressure drop, this is clearly illustrated in Figure 15 [63] and Figure 16 [64]:

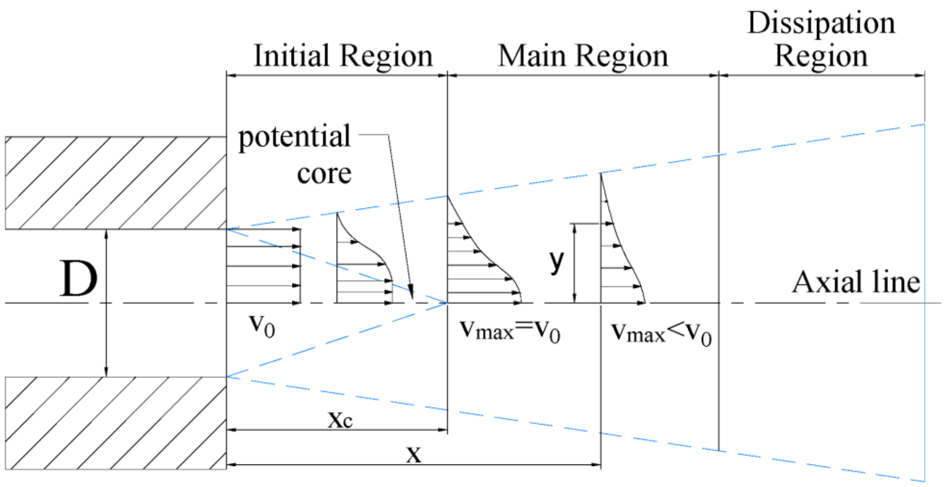

Figure 15: *Water jet distribution along the jet axis showing the velocity evolution* [63].

- **The initial region or continuous jet region**: In this section the pressure is at its highest and the jet dimeter is mainly equal to the nozzle diameter. It's the region in where the jet will have the highest energy and when using abrasives it is where the cutting takes place.
- **Main region or open jet region**: the pressure drops and the jet starts to spread at a constant angle due to friction and fluctuations. The energy of the jet here is too low for cutting but it is ideal for plain water jet milling (e.g. aerospace coating removal) as it is more controllable and it has a wider area.

- **Dissipation region o diffused jet region**: In this region the jet is too diffuse and disperse. The energy is too low for machining purposes.

During this work a study has been made using high speed camera recordings in order to understand the distribution of every nozzle that has been used at different pressure parameters.

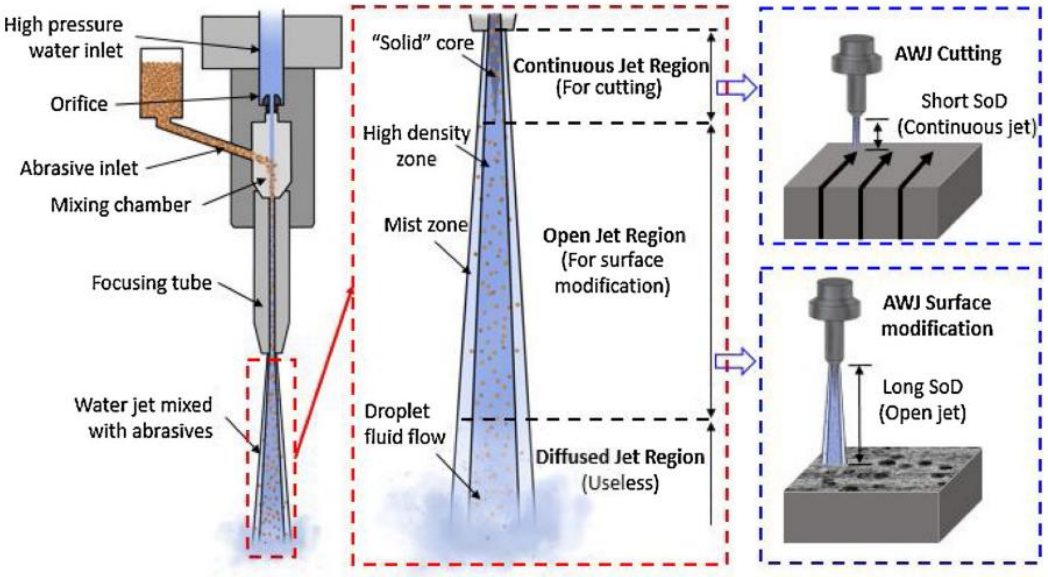

Figure 16: *Water jet distribution along the jet axis showing the potential applications in each region* [64].

2.5. History, development and research gaps of high pressure water jet coating removal mathematical models

Modelling water jet generated kerfs (i.e. U shape slot machined, in this case, by Water Jet milling) can be a challenging task due to the complexity of the physical processes involved [57], [62]. Some of the challenges that researchers face when modelling water jet generated kerfs include:

- **Non-uniformity of the jet:** The water jet is not uniform in its velocity and pressure, and its properties can vary along the length of the jet. This can result in variations in the kerf geometry and surface roughness, making it challenging to accurately predict the kerf geometry.
- **Material removal mechanisms:** The water jet cuts through the workpiece by a combination of erosion, impact, and fracture. These material removal

mechanisms can vary depending on the material being cut, the pressure and flow rate of the jet, and other factors, making it challenging to accurately model the material removal process.

- **Abrasive particles:** In abrasive water jet cutting, the water jet is mixed with abrasive particles to enhance the material removal rate. The properties of the abrasive particles, such as size, shape, and hardness, together with the heterogeneity of the mix, can affect the material removal process and the resulting kerf geometry, adding an additional level of complexity to the modelling process.
- **Experimental validation:** Modelling the water jet generated kerfs requires accurate data on the jet properties, workpiece material properties, and other parameters. However, obtaining such data can be challenging, and experimental validation of the models is essential to ensure their accuracy.

Overall, the complex and multifaceted nature of the water jet cutting process presents numerous challenges to accurately model the generated kerfs, and researchers must take a multi-disciplinary approach to address them.

2.5.1. History of PWJ removal mathematical models

This technology was firstly patented in the 1930s as a low-pressure water jet system that was proved to be effective to cut paper and afterwards with the addition of abrasives was developed for mining industry [65]. Nowadays, WJ technology has been developed up to obtain a cutting accuracy of ± 0.01 mm and a positioning accuracy of ± 0.003 mm. This manufacturing technique does not apply almost cutting forces to the workpiece and the produced thermal influence is negligible [57].

With the addition of abrasive particles, a high machining versatility is obtain as well as simplicity and cutting flexibility to cut in almost any direction and any kind of material, such as cutting small pockets in composite material with no lamination if the right parameters are used [66]. Furthermore, it is also an economical process, usually no post-processing is needed and virtually it is able to cut almost any material [57], [67]. Whereas abrasive waterjet is widely used to cut almost any kind of material plain waterjet is ideal to cut soft material, remove coatings or clean surfaces [68] without damaging the substrate or polish surfaces [69]. Prediction of the waterjet made trench is essential to control the process. Hence, based on this, there is a research area that focuses on understanding high pressure plain water jet coating removal [70]. This section summarized the various attempts and improvements that have been done in this field.

The very first research where based on making simulation of the interaction between the jet and the target [59]. However, these simulations are too computationally consuming in order to make advanced calculation, so it was concluded that the best way to analyse the trenches was by developing an analytical mathematical model. The simplest case to start the mathematical model is a straight trench with a 90 º of jet impact angle and a straight path, the angle that maximum erosion occurs in brittle materials [71]. Figure 17 shows the geometry of the model.

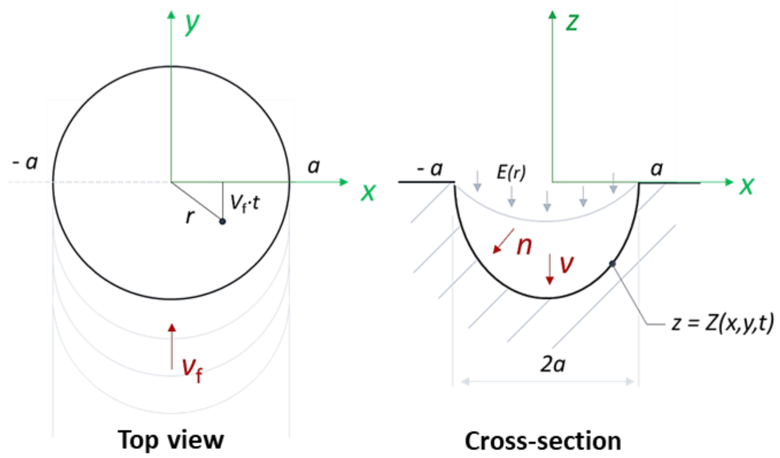

Figure 17: *Scheme of the trench generated by the AWJ machining process and the forces that are interacting in the process. a) front view, b) top view* [72].

The jet footprint function is given as z = Z (x, y, t) and after developing the mathematics of the geometry, where the jet footprint is dependent on the etching rate: $E(r) = C(V \cdot n)^k$ [72]. This rate is based on the materials properties and to avoid calibration processes the equation is transformed to non-dimensional by dividing its components by the nozzle diameter “a”. Non-dimensional parameters are represented with a dash on the top. The obtained result is non-linear and impossible to solve, so is integrated and linearized [72].

The program is suitable to predict abrasive water jet cutting as well as plain water jet milling and laser ablation process as shown by G. B. J. Gadot et al. [73], due to the fact that the program works by including a calibration data trench for further analysis. These data are obtained by scanning a machined trench with the 3D surface scanner. The trench must have small slopes for accuracy purposes and so it must be machined at high-speed rates: in the case of AWJ a cutting speed of v_f = 50 mm/s while only the cutting speed was changed maintaining the rest of the parameters constant [74]. Then, the specific etching rate is obtained using computer procedures. Finally, to predict the profile at any kerf is integrated using the Newtonian method. The model can also be calculated considering the SoD [72]. This model can be implemented in a MATLAB code and is able to predict the kerf curve with less than a 5 % of error in comparison to the experimental data [72].

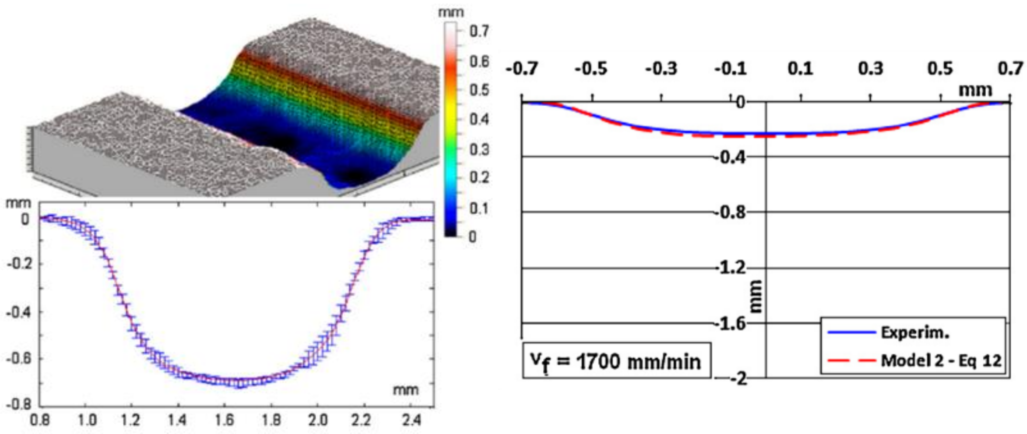

Figure 18: *Example of the prediction of a trench milled, with an abrasive water jet at 1700 mm/min on an Inconel target, with less than a 5 % of error* [72].

J. Billingham et al. upgrade afterwards the mathematical model to overlapping straight trenches and trenches considering different impact angles between the AWJ and the workpiece [75], [76]. More advanced models that analyse an inverse machining problem [77]in where the user is able to define the desired trench and the model returns the ideal parameters to do so [77], [78].

Along all the mathematical models that are able to predict the machined trenches studies has also been made to analyse their accuracy, as the one A. Rabani et al. [79] and D. Axinte et al. [80] about acoustic emission energy transfer to monitor abrasive waterjet milling. Moreover, the study of the obtained surface texture and its residual stresses has also been developed [81].

In the current research the aim is to remove a full aerospace coating. In the previous models, a needle nozzle was considered as the cutting tool. However, a needle nozzle would be unproductive to remove the area of a full cover of aerospace coatings from an engine part. J. Reichman et al. have proposed an oscillating needle nozzle in order to cut a wither trench while cutting big rock blocks in two [82]. Based on the idea of optimising the material removal process a rotational four jet nozzle was propose for the application. G. Chomka et al. have already analysed the kinetics of a two jet rotary nozzle [83], but the study just develops the calculation of the position of the jets when it rotates without further development.

Moreover, the coatings to be removed will be made by multi material layer. Removing layer of more than one material and ensuring no damage to another material below is an issue that has not been faced in the previous models.

2.5.2. *Development of high velocity impact study: effect of the impact of a single droplet*

Once understood the microstructure of the TBCs as well as the need of replacing them the next step is to understand the effect of the water droplets shocking the YSZ coating with the purpose of destroying it. K. Kong et al. had registered the impact of a single droplet released at high pressure while analysis the milling mechanism of gamma titanium aluminide [50], as shown in Figure 19. In this research, they explain the process of the droplets while shocking the surface however the main research if focused on the effect that the whole jet creates.

In abrasive waterjet milling, the water droplets are released at around 300 MPa, which makes that they collide against the target at supersonic speed. C. Visser et al. analysed the droplet impact [84] and K. Kondo and K. Ando performed similar research by simulating the droplet impact [85]. However, they velocities vary from 100 m/s and 30 m/s to 50 m/s respectively, more focused for liquid jet cleaning applications. Although they show a detailed analysis, their studies are made in a too low speed and so they do not pay attention to the effect of the droplet impact in the target material.

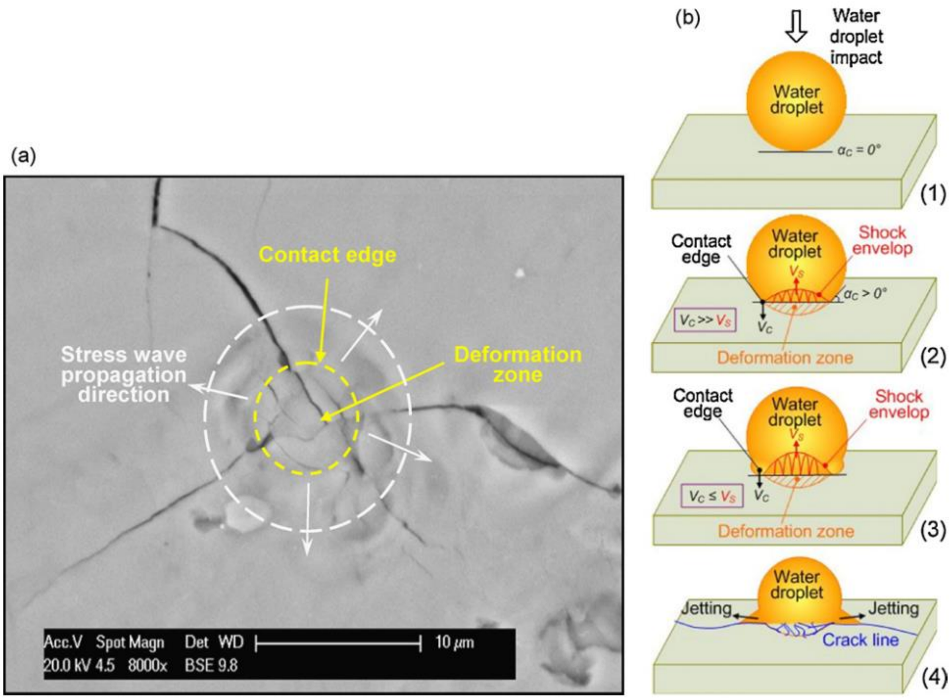

Figure 19: *a) crater and crack formed after the impact of a single water droplet in gamma titanium aluminide; b) Sequence of the water droplet when impacting a hard solid surface at a supersonic speed* [50].

C. Tang et al. also make a study on droplets that hit the target at low velocity but as an upgrade they analyse the effect of the droplet shock while hitting target with different surface roughness’s [86] and G. Cossali et al. analysed the evolution of a droplet and its splats during a time slot [87].

F. Heymann has studied the impact of supersonic liquid droplet against a solid surface [88]. However, in this case they focus the study in the instant when the droplet touches the target at a supersonic speed. They observed that in the first instant no lateral flow or splats will occur and that the base of the droplet will be compressed, as shown in Figure 20 a. If compression was not happening the pressure at the contact instant will be infinite as the touching area will be infinitesimal, as this is not possible Haller assumes that compression actually occurs. This stage will continue until the shock wave, generated in the contact point, breaks the outer perimeter of the droplet, the representation of the propagation of the shock wave is appreciated in Figure 20 c. Once the shock wave passes the droplet perimeter frontier lateral flow and splats will be generated. The pressure of the droplet impact will be distributed ensuring maximum pressure at the centre of the impact and one that the droplet breaks and splats this pressure will be transfer to the target surface [88].

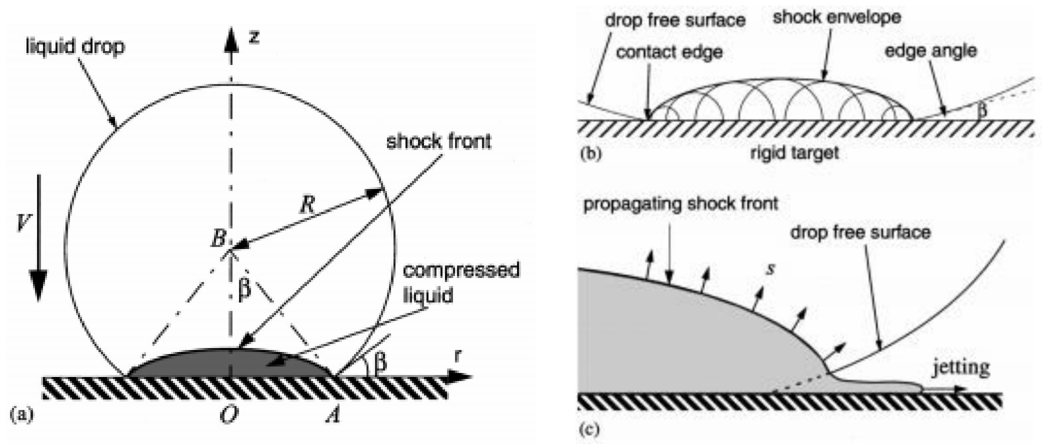

Figure 20: *a) Schematic representation of a droplet when impacting at supersonic speed; b) Magnification of the impact area; c) Schematic representation of the propagation of the shock wave and the spreading of the jet after breaking the droplet perimeter* [89].

Afterwards K. Haller et al. make a computational study supporting F. Heymanns ideas [89]. However, these studies are focused again on the droplet and none of them analyse what is the effect in the target material.

In order to analyse what is going in the target material Y. Xie et al. has propose to make single point scratches performed by a nanoindenter [90]. However, with this mechanism the shock effect is not analysed.

Moreover, it must be considered that the APS coating shows an uneven microstructure in where the grains can vary in shape and size in the same millimetre square. M. Mieszala et al. made a comparison of the effect of the impact of the abrasives of the abrasive water jet machining process in single crystal, microcrystal and nanocrystal nickel alloy samples [91]. In this research, as shown in Figure 21, microcrystal structure turns into nanocrystal, nanocrystal maintain unchanged and single crystal structure suffers a nanocrystallization in the very edge accompanied by dislocation concentration around the area demonstrating the importance of the microstructure in the machining effect.

Based on the research conducted up to this point, the project's methodology will be to examine the impact made by a single droplet when it impacts a substrate at supersonic speed, but with an emphasis on the impact made on the material rather than the droplet itself.

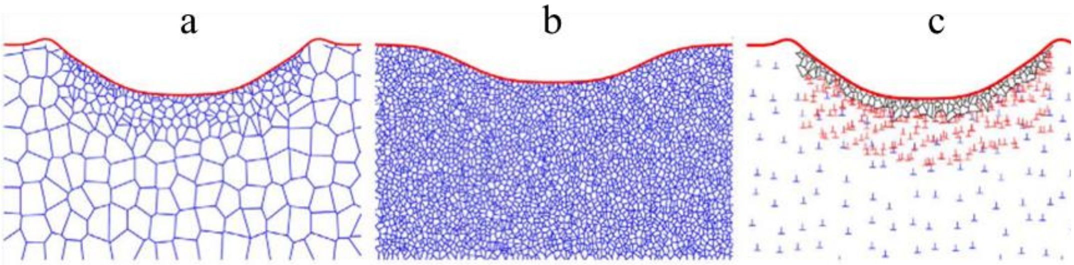

Figure 21: *a) Microcrystal nickel alloy that is transformed in nanocrystals after abrasive waterjet impact; b) Nanocrystal nickel allow that is maintained unchanged after abrasive waterjet impact; c) Single crystal nickel alloy that suffers a nanoscale crystallization and a packing of dislocation in the abrasive waterjet impact area. This demonstrates that the microstructure generates a great influence in the water jet machining process* [91].

2.5.3. Research gaps on this field

Despite the significant progress made in the modelling and simulation of water jet generated kerfs, there are still several research gaps that need to be addressed. This section summarizes the research gap areas identified along the literature review:

- **Multi-scale modelling:** As seen in the literature most current modelling focuses on the macroscopic behaviour of the water jet and the workpiece, neglecting the micro-scale material removal mechanisms. However, this approach leaves out the interactions at a microscopic scale that can lead to structural damage when a material removal process is going on and hence contribute to the removal mechanisms that are nowadays under-regarded. Multi-scale modelling approaches that incorporate both macroscopic and microscopic material removal mechanisms are needed to help improve the kerf geometry and surface quality prediction accuracy.

- **Accurate material models:** Accurate material as well as multi material interaction case study models that can capture the complex behaviour of different types of materials under the extreme conditions of water jet cutting are still lacking. Developing such material models is essential for accurately simulating the material removal process and predicting the kerf geometry, especially in cases with multiple layers.
- **In situ simulation:** In-situ simulations can play an important role in the control and optimization of the water jet milling processes. It enables the adjustment and refinement of parameters based on real-life tests run in the moment, allowing for the modelling of new parameter sets before conducting further experimental tests. To facilitate this iterative process, it is essential to employ simulation models that are fast and efficient in their calculations or execution. Such models enable real-time simulation and empower the ability to change and correct parameters promptly while tests are being conducted in the industrial environment.
- **Optimization algorithms:** Water jet cutting involves numerous process parameters, such as pressure, flow rate, and stand-off distance, which can affect the material removal rate and the quality of the kerf. Optimization algorithms that can identify the optimal process parameters for a given material and cutting application are needed to improve the efficiency and quality of the cutting process.
- **Experimental validation:** Despite the significant progress made in modelling and simulation, experimental validation of the models is still essential for ensuring their accuracy and reliability. Further experimental studies that provide detailed data on the jet and workpiece properties are needed to validate and improve the accuracy of the models.

Overall, addressing these research gaps is crucial for improving the accuracy and efficiency of water jet cutting, and for advancing the state-of-the-art in this field. Water jet cutting has been found to be a versatile and efficient cutting technology that is widely used in industries such as aerospace, automotive, and manufacturing. It offers several advantages over traditional cutting methods, including the ability to cut a wide range of materials with high precision and minimal material wastage. Accurately modelling and simulating the water jet cutting process is essential for improving the efficiency and quality of the cutting process and for advancing the state-of-the-art in this field. By accurately predicting the kerf geometry and surface quality, researchers can optimize the cutting parameters and identify the optimal cutting conditions for a given material and application. This can lead to significant improvements in efficiency and cost-effectiveness, as well as improvements in the quality and accuracy of the cut parts. Furthermore, modelling and simulation can also help to minimize material wastage, reduce production time, and improve the safety of the cutting process. Overall, accurate modelling and simulation of water jet cutting is critical for improving the efficiency and quality of the cutting process and for advancing the use of this technology in a wide range of industries.

2.6. Surface integrity analysis techniques

After modelling the water jet milled trenches is essential to contrast it with experimental validation to prof if the simulated calculations meet the reality. For this surface integrity analysis techniques will be applied. The surface layer of a material will be affected by the water jet milling process, hence the microstructure, residual stresses, hardness, and other surface properties will be altered. These techniques are a group of methods used to examine and evaluate the quality and properties of a material's surface layer. This analysis techniques will evaluate, characterizes and measure such properties and assess their impact on the material's performance and durability.

In this project various surface analysis techniques will be use to study the mechanical properties of the milled trenches after the tests that will be classified by the following criteria: surface analysis, surface integrity and material property analysis techniques.

2.6.1. Surface analysis

Surface analysis is a technique used to examine the surface of a material to determine its composition, structure, and properties. Surface analysis can provide detailed information about the composition and structure of a material's surface, including the presence of impurities, defects, and surface treatments.

Some of the most common techniques for this analysis include optical 3D surface metrology systems (see Figure 22) [64], [77], [92], [93], optical profilometers [94], scanning electron microscopy (SEM), atomic force microscopy (AFM), X-ray diffraction (XRD), X-ray photoelectron spectroscopy (XPS) and secondary ion mass spectrometry (SIMS).

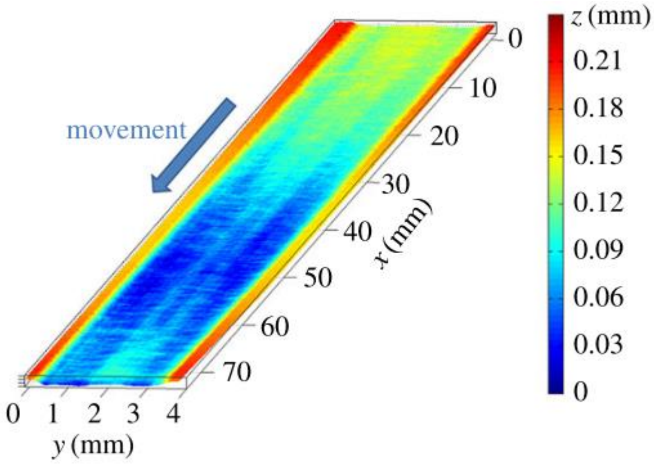

Figure 22: *Example of a 3D view of a water jet milled trench and scanned by a 3D surface metrology machine* [77].

2.6.2. Surface integrity

On the other hand, surface integrity is the condition of the top layer of the material after being transformed by some kind of manufacturing process. With this technique the roughness, hardness, residual stresses, cracks and microstructural changes are the properties that are being studied. This is used to evaluate the impact of the manufacturing process (i.e. in this case high pressure plain water jet milling) of the surface quality.

Some of the most common techniques for this analysis include scanning electron microscopy (SEM) [95], [96] (se Figure 23), X-ray diffraction (XRD), Raman spectroscopy [27], [97], transmission electron microscopy (TEM), Electron Backscatter Diffraction (EBSD) [95], [96], transmission Kikuchi diffraction (TKD) [95], just to mention some.

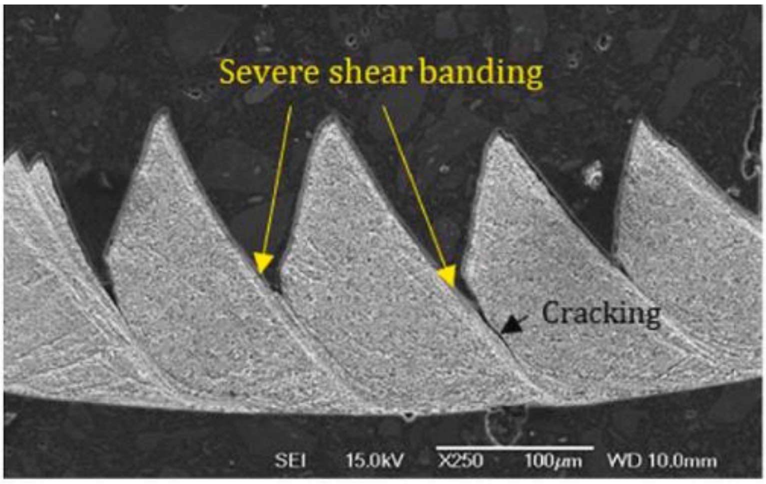

Figure 23: *Example of a how an SEM can be used to identify cracking and grain structure changes affecting the surface integrity, in this case the surface of a machining a Ni-superalloy chip* [96].

2.6.3. Material property analysis

Finally, the material property analysis techniques are used to determine the mechanical, thermal, electrical, and other properties of a material. The aim is to determine the properties of a material itself, regardless of its surface condition or manufacturing history. This is important for understanding how a material will perform in a given application under different conditions.

There are several ways to assess the mechanical properties of a material both in a non-destructive (NDT) and destructive testing (DT) ways. NDTs are set of techniques used to evaluate the properties of a material, component or system without causing any permanent damage to it. Among them the most extended ones are visual inspection, microscopy, radiography, ultrasound, eddy currents for metals, magnetic particles and acoustic emission [98]–[100]. As for the DTs, both because the part has to be altered or because samples need to be taken for analysis, predominate tensile and compression testing, fracture toughness analysis, impact tests (i.e. Charpy test), fatigue analysis, hardness testing (i.e. material indentations).

In this project a nanoindenter was used to understand the materials properties after high pressure water jet impact in 8YSZ at a relatively low strain rate (i.e. compared to the strain rates generates with high pressure water jet impact [63]) [101]–[104]. Nanoindentation is a technique used to measure the mechanical properties of materials at the nanoscale, by indenting a small probe into the surface of the material and measuring the force and displacement. The technique is commonly used in materials science and engineering, and can provide valuable information about the hardness, elastic modulus, and other mechanical properties of materials [103].

The basic principle of nanoindentation is to use a small probe, typically a diamond tip with a radius of a few nanometres, to indent the surface of the material. The depth of the indent is typically in the range of a few nanometres to a few microns, and the force required to make the indent is measured by a load cell. By measuring the force and displacement as the probe is indented into the material, it is possible to obtain a load-displacement curve that can be used to determine the mechanical properties of the material [105].

One of the key advantages of nanoindentation is its ability to measure the mechanical properties of materials at small length scales. This is important for understanding the mechanical behaviour of materials in micro- and nanoscale devices, and for developing new materials with specific mechanical properties. Or as in the case of this project to understand the strain rate impact behaviour of the material [106].

Chapter 3

Methodology

The following chapter describes the necessary materials and equipment used to develop this project. This includes a detailed explanation of the Water Jet machines together with the types of nozzles available. Furthermore, all the different test materials as well as all the used tools and the sample preparation processes for the experimental process for the model validation and the materials analysis are defined. Finally, the material analysis techniques and the machines used for those purposes are carefully exposed.

3.1. Plain Water jet milling machines

A water jet (WJ) machine is a complex equipment that involves several components working together to generate and direct the high-pressure water jet. The main parts of the machine include:

- **High-pressure pump:** in where the high-pressure water required for cutting is generated.
- **Intensifier:** amplifies the pressure of the water to even higher values, it uses a hydraulic piston to increase the pressure of the water to the required level.
- **Cutting head:** this directs the high-pressure water jet towards the material to be cut which includes a nozzle and a mixing chamber, which mixes water with abrasive particles (in case of using particles, if not the water would just pass by).
- **CNC control system:** this is the part of the machine that controls the cutting process and ensures precision and accuracy. It uses computer programming to direct the cutting head along the desired path.
- **Abrasive delivery system:** this element delivers the abrasive particles to the mixing chamber, where they are mixed with water before being directed towards the material to be cut. In case of not using abrasives, this inlet will just be closed.
- **Catch tank:** here the water and the abrasive particles are collected after they have been used in the machining process.
- **Water filtration system:** this filters and recirculates the water used in the cutting process, reducing water consumption.
- **Motion system:** moves the cutting head along the desired path. It includes a gantry or a robotic arm, which may be driven by stepper motors, servomotors, or linear motors.

All these components, represented in Figure 24, work together to produce a high-pressure water jet that is capable of cutting through a variety of materials or able to mill with accuracy and precision. Subsequently, the specific WJ machines used in this project as well as the parameter ranges at which they work are described.

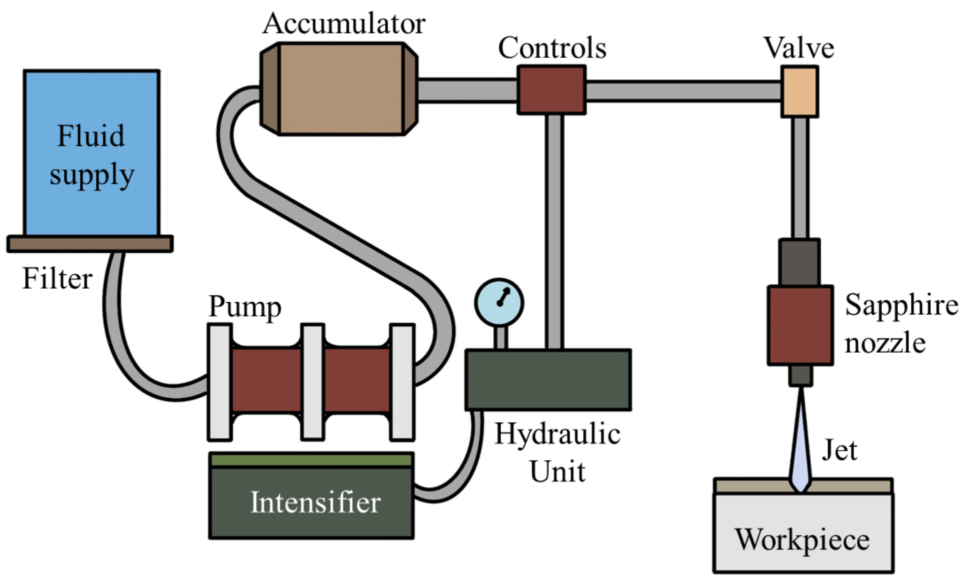

Figure 24: *Schematic of a water jet machine system* [*Adapted from* [107]].

3.1.1. University of Nottingham waterjet machines and their specifications

d) <u>**Three axis micro waterjet machine**</u>

The abrasive water jet (WJ) machine has been the main machine used for the study of the removal of aerospace coating. For this the micro waterjet F4 three-axis machine, manufactured by the Swiss company WATERjet AG and located at the University of Nottingham was used, see Figure 25 a. This machine is a prototype from the company and is characterized by its high accuracy while cutting, it has a translational speed that ranges from 0 to 4000 mm/min. WJ machines mainly work by pumping water at a high pressure and realising it from a narrow aperture called nozzle. When the pressurised water is released, its energy is turned into kinetic energy and erodes the material below. As for the pump, the University of Nottingham three-axis WJ machine uses a KMT Waterjet systems SL-V100D Plus ultra-high pressure pump. This pump, showed in Figure 25 b, generates a pressure from 500 bar to 4000 bar (from 50 MPa to 400 MPa). Table 1 shows a summary of the components and parameters of the machine.

Table 1: *Summary of the 3-axis water jet machine components and its respective parameters.*

AWJ components	Parameters
Working area	1 × 0.55 m
Catcher depth	1 m
Pump pressure	50 – 400 MPa
Traverse speed	0 – 4K mm/min
Nozzle head movement	X-Y-Z axis
Machine post process SW	Internal SW and MasterCAM 9.0

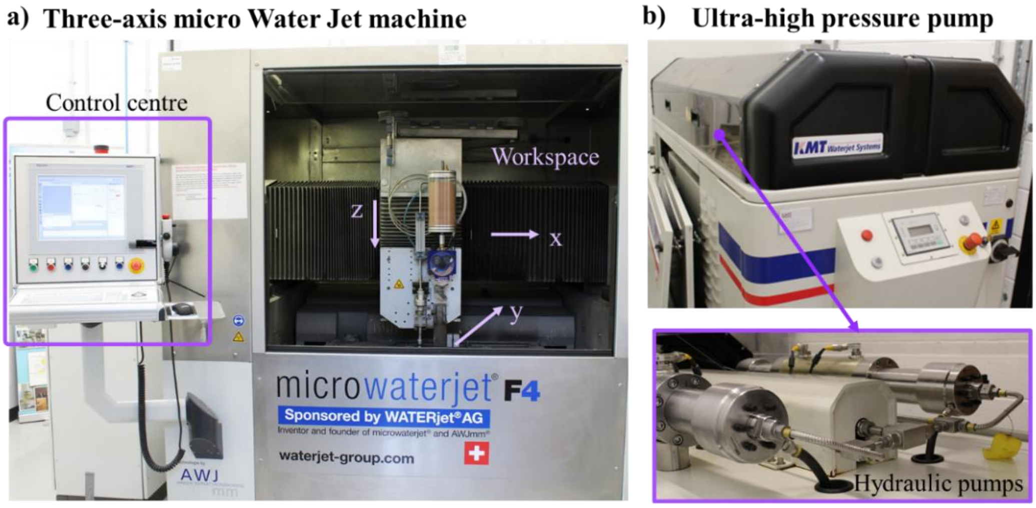

Figure 25: *a) Three-axis micro water jet machine from* micro waterjet. *b) Ultra-high pressure pump* KMT Waterjet systems SL-V100D Plus *connected to the WJ machine to pressurise the water.*

e) <u>Five axis waterjet</u>

Although the three-axis WJ machine is excellent for precision manufacturing, an Ormond five-axis WJ machine was also used because it is easier to adapt to curved surfaces and is also available at the University of Nottingham.

This CNC controlled waterjet machine consists of the following main sub-systems: CNC controlled (FAGOR 8055) five-axis manipulator and turntable, KMT streamline SL-V100D ultra-high pressure (UHP) pump, a mast mounted abrasive hopper, catcher tank filled with water to absorb the jet energy and muffle the sound of the jet, AWJ mixing chamber and nozzle. The working area for waterjet operation is within 1.2 x 0.65 m and there are several transversal bars attached horizontally across the 1.7 m depth catcher. The nozzle head can be programmed to move on five-axes (linear X-Y-Z, and rotary B and C axis) but the C axis at the moment cannot make a continuous 360° movement which can be limiting for some machining procedures, the machine is shown in Figure 25. The pump pressure, as it uses the same pump as in the 3-axis water jet machine it works in the same range: between 50 and 400 MPa. The maximum traverse speed that can be reached depends on the machine acceleration and the travel length, but it is defined in ~ 20.000 mm/min. As for the software, the machine does not use a commercial software, so the MasterCAM 9.0 has been used as the software for the path generation. Table 2 shows a summary of the components and parameters of the machine.

Table 2: *Summary of the 5-axis water jet machine components and its respective parameters.*

AWJ components	Parameters
Working area	1.2 × 0.65 m
Catcher depth	1.7 m
Pump pressure	50 – 400 MPa
Traverse speed	0 – 20.000 mm/min
Nozzle head movement	X-Y-Z axis; B axis (-90° to 90°); C axis (0°-359°)
Machine post process SW	MasterCAM 9.0

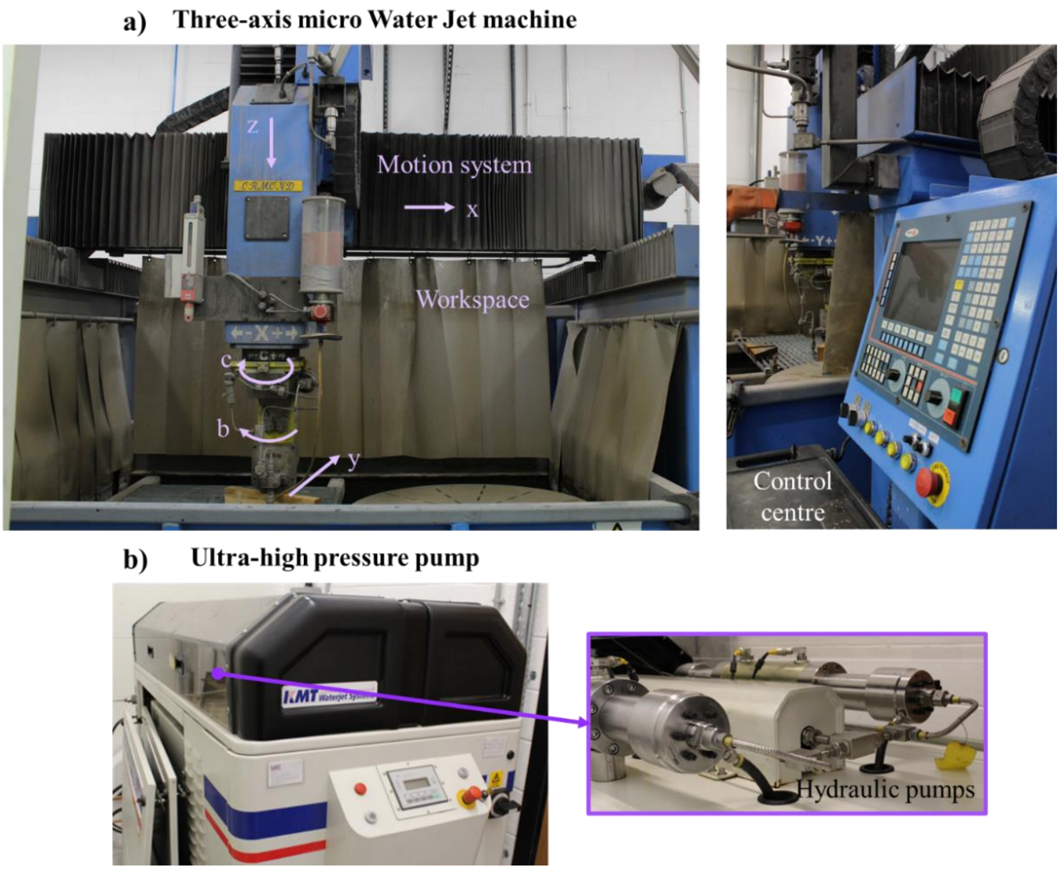

Figure 26: *a) Five-axis water jet machine from Omicron. b) Ultra-high pressure pump* KMT Waterjet systems SL-V100D Plus *connected to the WJ machine to pressurise the water.*

f) <u>Water jet machine modes</u>

- <u>WJ for cutting: Abrasive Water Jet (AWJ) machining</u>

In order to use both of the WJ machines for cutting abrasives are fed in the water slurry. These abrasives are Si particles with a 220# mesh size fed at an 80 g/s rate. As for the nozzle, for cutting purposes, a needle nozzle, shown in Figure 27, is used in the tree-axis micro WJ machine and the one shown in Figure 27 b in the five-axis machine. UoN machines are capable of accommodating orifices with diameters of 0.05 to 0.4 mm while the range of the nozzle diameters depends on the tool supplier which in this case ranges between 0.3 to 1.5 mm diameters mixing tube. The orifice to nozzle diameter has usually a 1:3 ratio [57].

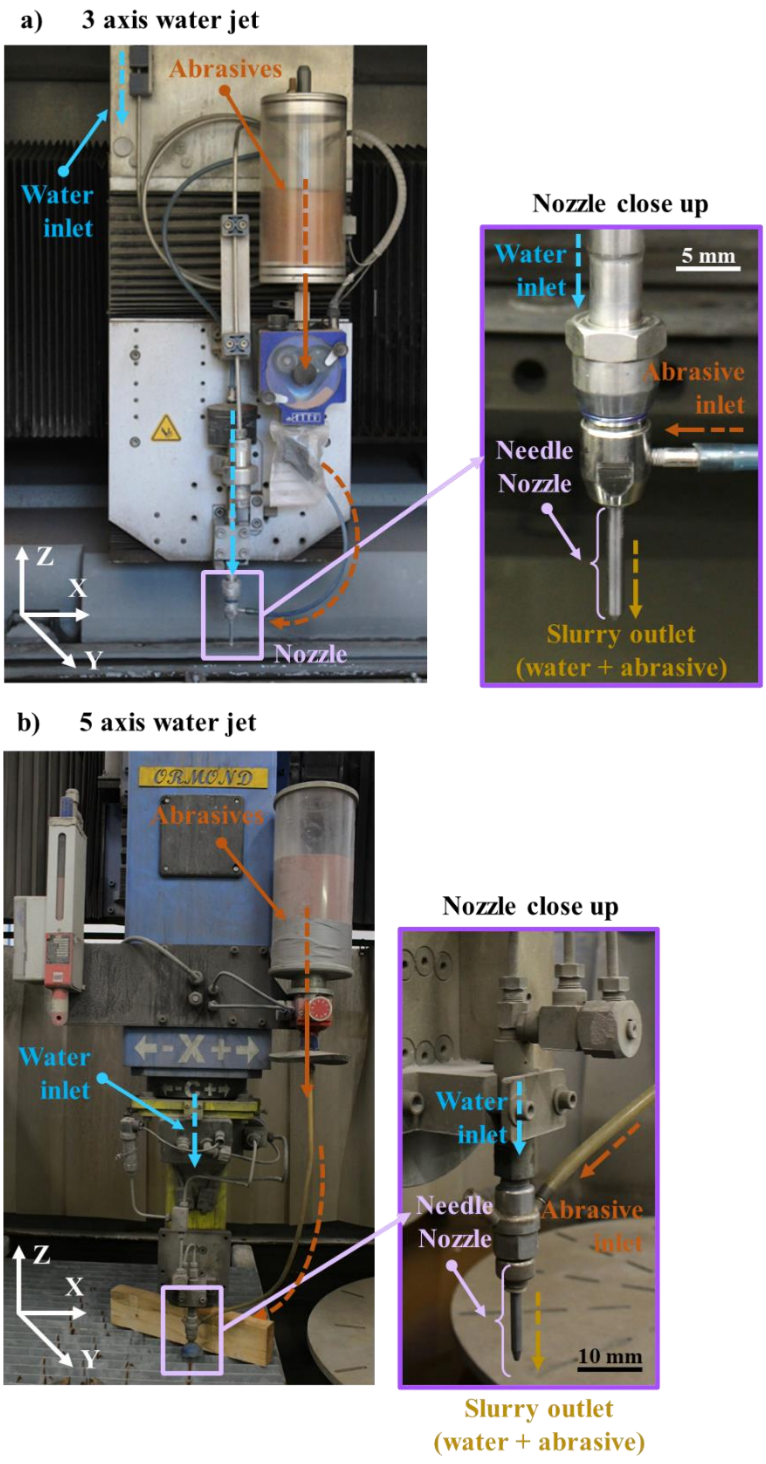

Figure 27: *Close up of the distribution system of the AWJ machine in where the abrasive and water inlet as well as the slurry outlet through the needle nozzle for: a) the three-axis WJ machine, b) five-axis WJ machine.*

- <u>WJ for milling: Plain Water Jet (PWJ) milling</u>

On the other hand, the WJ machines can be used without abrasives for milling purposes. As in AWJ machining, pressurised water is forced through a small orifice and nozzle, creating a narrow and high-velocity jet of water, but without the abrasives it is not powerful enough to cut through the materials by releasing high pressure water, hence, it can be used for milling if the machining depth is controlled.

However a needle nozzle, due to its nature, is not the most ideal tool to remove large surface areas. As a result a collaboration was made with the French company AQUARESE to implement a rotational head in the WJ machines. The AQUARESE equipment was installed after making a design study of the actual WJ system. First an adaptation panel was designed as coupling device between the WJ machine and the rotational head, for both UoN WJ machines. The head is detachable so the WJ machines can be use for cutting and milling and the head can be interchanged between both machines. This addition is controlled with an external controlling panel that enables the control of the rotational speed.

g) Water Jet Machining nozzles

The nozzle head is an essential part of the machining head assembly in a water jet machine. It is responsible for creating the high-velocity water jet that is used to cut through the material. The nozzle to be use must be chosen depending on the application. During this project a needle shape, a four jet and a fan nozzle have been used in both machines. The main parts of a nozzle head include:

- **Nozzle body:** The nozzle body is the main body of the nozzle and is typically made of a hard material like carbide or diamond. It is designed to withstand the high-pressure water flowing through it and to accurately direct the jet towards the material to be cut.
- **Orifice:** The orifice is the small opening in the nozzle body through which the high-pressure water flows. The size and shape of the orifice can vary depending on the application, and it is critical to ensure the water jet's accuracy and cutting performance.
- **Mixing chamber:** The mixing chamber is located just behind the orifice and is responsible for mixing the abrasive particles with the water before the jet is directed towards the material to be cut. The mixing chamber may be a separate part of the nozzle head or be integrated into the nozzle

body. In the case of water-only machining the water just passes through this section as if it was part of the tubing.

- **Mixing tube:** The mixing tube is a small tube that connects the abrasive supply line to the mixing chamber. It is typically made of a hard material like tungsten carbide and is designed to withstand the abrasive particles' high velocity.
- **Abrasive inlet:** The abrasive inlet is the part of the nozzle head where the abrasive particles are introduced into the water stream. It is typically a small port located near the mixing chamber.

In the nozzles that can be used with and without abrasives (e.g. needle nozzle) the mixing chamber, tube and abrasive inlet are present but when using it as a plain water jet system the water just passes through the chamber and the tube, and the abrasive inlet is closed. As for the nozzle heads that can only be used as water-only machining (e.g. 4 jet and fan rotational nozzle heads) these parts are just not present. Overall, the design and quality of the nozzle head are critical to ensure the water jet's accuracy, precision, and cutting performance.

- <u>Needle nozzle</u>

As described in Figure 27 a and b the needle nozzle is 30 mm long, and a 0.3 to 1.5 mm orifice nozzle is typically used for cutting purposes if it is combined with abrasives. With a thinner nozzle the achieved cut will be more precise with less material waste from the cutting line but with a shorter cutting length. However, when used without abrasives and the optimal set of parameters it can also be used for milling.

- <u>Four jet rotational nozzle head</u>

This nozzle is a four orifice rotational nozzle head from Aquarese (Figure 28a). It is always used without abrasives, hence is just used for milling purposes. The head contains four 1 mm outlets which are distributed at each of the quarters (i.e. every 90º) at a different radius (i.e. 9 mm, 2 × 7.8 mm and 6 mm) and the released water is equally distributed. This head has a wide milling area that ranges from 15 to 25 mm and quite gentle with the target material which makes it ideal to remove soft coatings such as abradable, rubbers and paint.

- Fan jet rotational nozzle head

The rotational fan jet nozzle (Figure 28b) has a narrow slot (10 mm long, 1 mm wide) with a 1 mm orifice in the middle of the cavity. When the water is released this fills the slot cavity, and as a result the water is released creating a fan shape. As the four jet nozzle, this is also used just for milling purposes and always without abrasives. This head has a narrower interaction area for a single pass (i.e. from 12 to 20 mm) but in comparison to the four jet nozzle it releases more energy per area. It is ideal to mill harder materials that the four jet nozzle is not even able to scratch, such as the titanium aluminide coatings, but it needs more care when defining the milling parameters as it is easier to damage the substrate material with this nozzle.

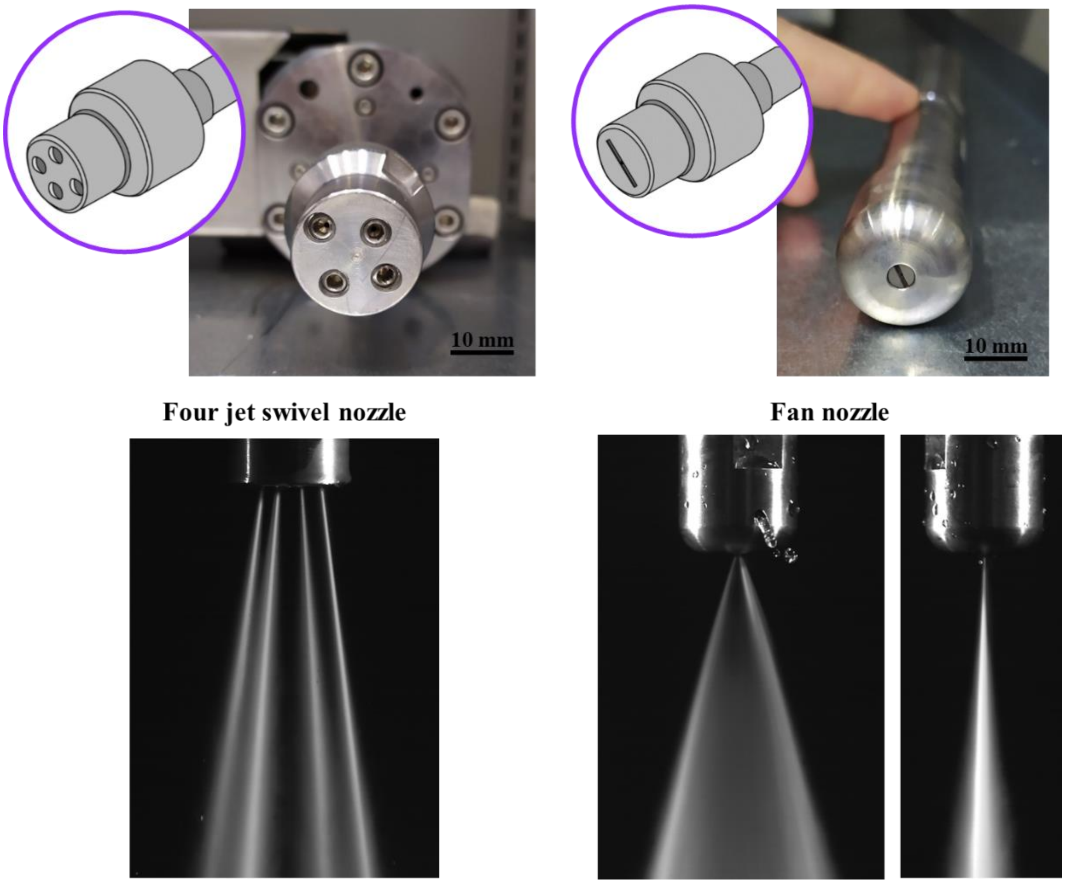

Figure 28: ***Rotational*** *a) Four jet and b) Fan nozzles.*

3.1.2. PWJ in industrial environment - Rolls-Royce water jet machine

The main goal of this thesis is to develop a mathematical model to predict PWJ milled trenches. Once the model has been developed, it was put to the test in an industrial setting with the aim of demonstrating its veracity. The PWJ machine, which is located at the Rolls-Royce corporate office in Derby, was employed for this. This machine is a walk in WJ machine that is designed to be used just with water (i.e. without abrasive particles). In this machine a cylindrical part (e.g. a casing from the engine) is attached to a rotating base that makes a +360° spin and the 5 axis robot arm is finished with the nozzle head. This head can be programmed to follow the trajectory that is desired, which in this case is: a motion that follows the profile of the part section while keeping a constant SoD. In contrast to the UoN pump the RR one can reach a pump pressure (P) of up to 600 MPa and a translational sped (v_t) of 7000 mm/min.

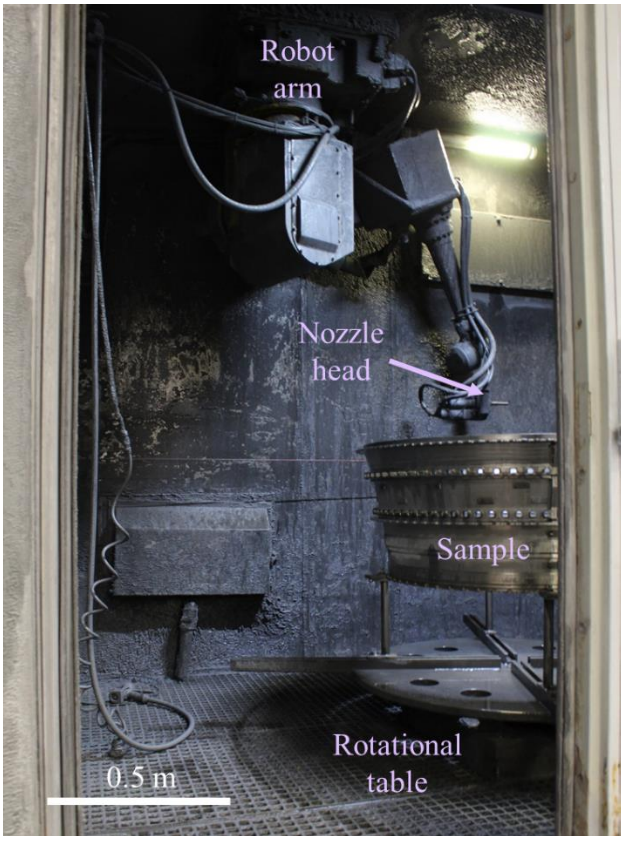

Figure 29: *Rolls-Royce PWJ machine.*

3.2. Sample preparation process

Since micromechanical testing was employed in this research, it was ensured that sample grinding and polishing as well as carbon coating of the sample surfaces was performed and applied in line with the appropriate standards for micro-testing [108].

The grinding and polishing set of steps were done in the Struers Tegra Force 5 (Figure 30) in various steps as described in Table 3.

Table 3: *Polishing steps for sample preparation for material characterization and understanding of material removal mechanisms, steps recommended from STRUERS.*

Step	Pad	Coolant suspension (µm)	Force (N)	Time (min)
Coarse grinding	MD-Piano	Diamond 9	15	2
Fine polishing	Dac	Diamond 3	10	5
Fine polishing	Dac	Diamond 1	10	10
Finishing	Chem	Coloidal silica 0.01	20	2
Cleaning	Chem	Plain water	20	2

Figure 30: *Struers Tegra Force 5 UoN UTC polishing machine.*

For any sample (polished or not), before getting it into any microscope that works with an electron beam, sample surfaces have been carbon coated as the ceramic materials analysed are not conductive enough, hence, charging is accumulated in the less conductive regions disenabling the possibility for analysis. The samples are positioned within the chamber on a rotating tray, and once the chamber is vacuumed, a carbon filament is lit to produce regulated sparks. The vaporized carbon is deposited in the surface of the samples evenly, creating an approximately a 15 nm coating layer. For this a Quorum Q150 R ES from the nmRC (Figure 31) was used.

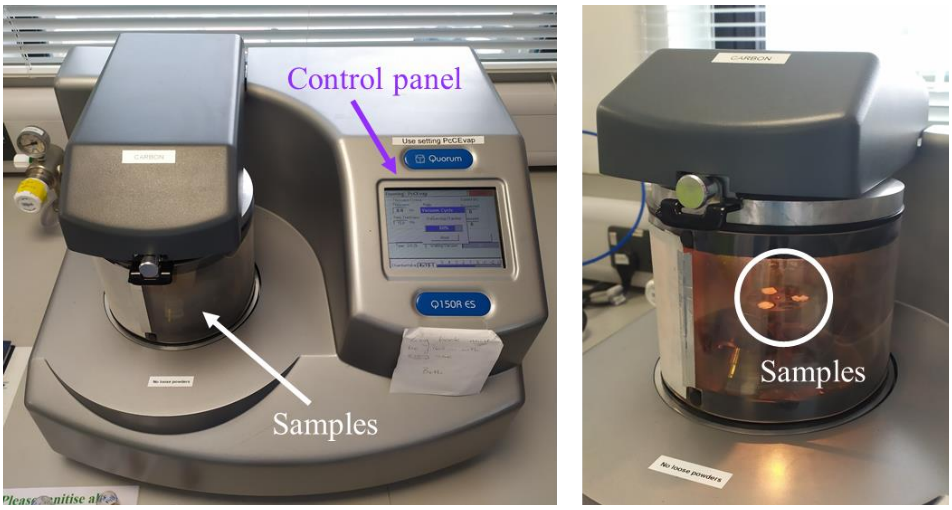

Figure 31: *Carbon coater Quorum Q150 R ES from the nmRC.*

3.3. Water jet analysis

a) <u>High speed camera</u>

An IDT Y4-S2 Motion Pro high-speed camera (Integrated Design Tools Inc.) was used for recording the jet released from both four and fan jet rotational nozzles in order to analyse the water distribution at different pressures. The acquisition rate was set up at 5 kHz and Motion Studio was used to process the data, in where the brightness, contrast, playback speed and zoom-in area of the recorded videos were adjusted. The camera was connected to its own power supply and one set of led lights was used to illuminate the section of interest. Meaningful frames were saved from the recording and, finally, these were post-processed in Mountains Map SW in where the brightness scale of the images was correlated with the water density in each section.

3.4. Material analysis techniques

3.4.1. Surface analysis

b) <u>High-resolution optical 3D measurement system</u>

The Alicona Infinite Focus G4 (Figure 32) is a high-resolution optical 3D surface metrology system that is used for the characterization and analysis of surfaces. It uses a technique called Focus Variation (FV) to obtain high-resolution 3D images of surfaces. The FV technique uses a combination of vertical scanning and focus variation to measure surface topography, providing high-resolution images of surface features with sub-micron accuracy. The system can measure surface features such as roughness, step heights, and surface defects, and can provide detailed information on surface texture, wear, and other surface properties. It includes a variety of objectives (i.e. 5x, 10x, 20x, 50x, 100x and 1000x) that allow it to measure surfaces with a wide range of feature sizes and geometries.

In this project the magnification lens of 10x was employed to create 3D reconstructions of the surface of the machined trenches to compare the modelled kerfs to the machined ones with a vertical and lateral resolution ranging from 2.3 μm to 10 nm. The analysis of the collected measurements was carried out in Mountains Map software and translated for plotting with custom MATALB code.

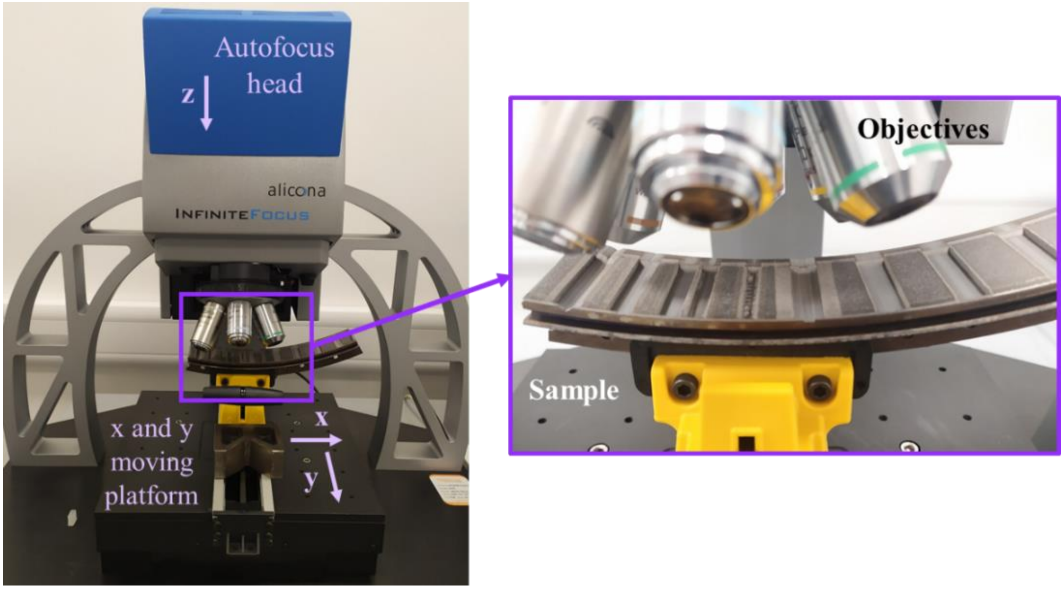

Figure 32: *Alicona G4 infinite focus and an example of the obtained results.*

3.4.2. Surface integrity

a) <u>Scanning electron microscopy (SEM)</u>

Scanning electron microscopy (SEM) is a type of microscopy used to study the surface of a material in high resolution. It allows for a much higher resolution than optical microscopes as it can reach up to 1 nm. This is due to the shorter wavelength of highly charged electrons compared to light photons.

The basic components of an SEM include an electron source, a series of electromagnetic lenses, and a detector system. The electron source typically uses a heated tungsten filament or a field-emission electron gun to generate a beam of electrons that is focused onto the surface of the material by a series of lenses.

The technique works by scanning a beam of electrons over the surface of the material. When the high-energy electrons from the electron source strike the surface of the sample, they interact with the atoms in the topmost layer, this interaction is responsible for the formation of different signals in a region called the interaction volume (as illustrated in Figure 33). The detection of this signals, collected by specialized detectors provides information about the material and is used to construct images of the surface.

The primary interaction that takes place is elastic scattering, known as the primary electron beam-sample interaction. In this process, the incident electrons undergo elastic collisions with the atoms in the sample, causing some electrons to scatter back (backscattered electrons or BSE) while others pass through with minimal energy loss (transmitted electrons).

Additionally, inelastic scattering occurs, leading to the generation of secondary electrons (SE) and characteristic X-rays. Secondary electrons are low-energy electrons emitted from the surface of the sample due to the excitation and ejection of electrons from the sample's atoms. These secondary electrons carry valuable information about the topography and surface morphology of the material and are primarily used for generating high-resolution images.

Backscattered electrons, on the other hand, have higher energies and can penetrate deeper into the sample, providing information about the composition and crystal structure of the material. By detecting the intensity and energy distribution of backscattered electrons, SEM can distinguish regions with different atomic compositions, allowing researchers to obtain compositional contrast in their images.

The resolution is determined by the size of the interaction volume. A smaller interaction volume leads to better spatial resolution. The size of the interaction volume is influenced by the energy of the incident electron beam, the atomic number of the sample, and the angle at which the beam strikes the surface [109].

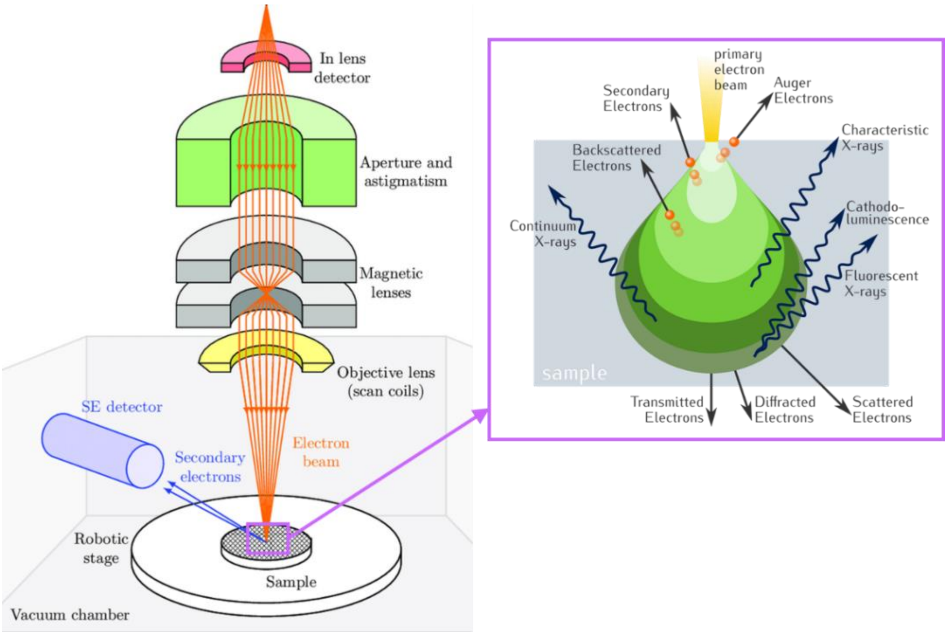

Figure 33: *Schematic representation of the internal structure of an SEM and the description of the interaction volume of the beam with the material (adapted from* [110]*).*

The SEM has been used for visual inspection of the material removal mechanisms of the water jet (i.e. to study the coating layer removal zones and the crack generation through the impacted coating layers). A FEI Quanta 600 SEM has been used (Figure 34a). Furthermore, in order to obtain more detailed pictures of the high speed water droplet impacts discussed in chapter 7 a Field Emission Gun SEM (FEG-SEM) Jeol 7000F has been used to reach higher magnifications, thanks to the higher voltages permitted compared to the tungsten filament of a regular SEM (Figure 34b). Both equipment's are available at the Nanoscale and Microscale Research Centre (nmRC) from the University of Nottingham.

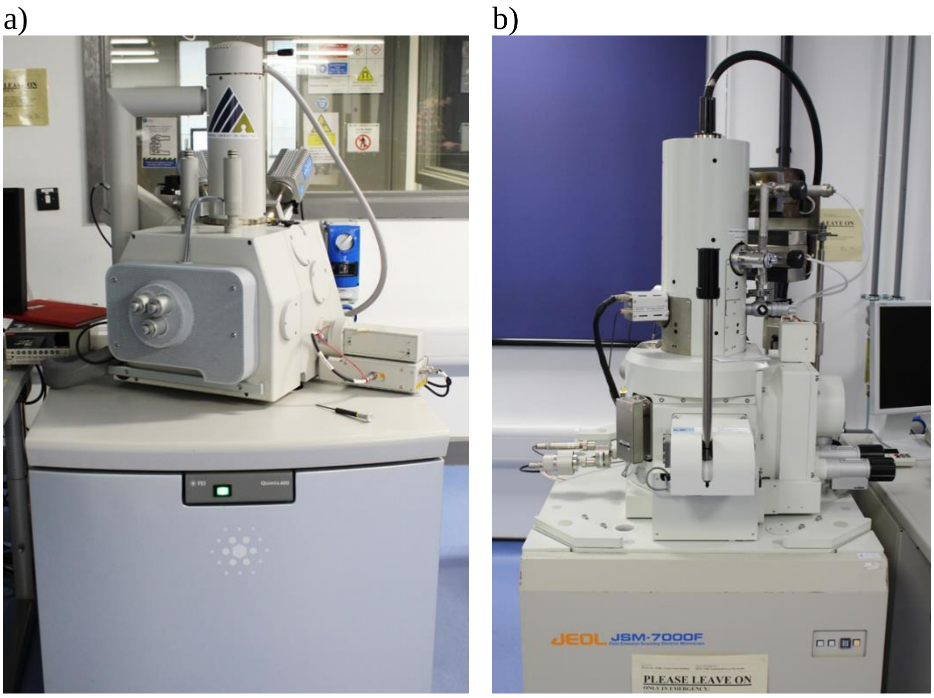

Figure 34: *a) FEI Quanta 600 SEM and b) SEM (FEG-SEM) Jeol 7000F both from the nmRC.*

b) <u>Energy-dispersive X-ray spectroscopy (EDX)</u>

Energy-dispersive X-ray spectroscopy (EDX) is a technique used in conjunction with the SEM to analyse the elemental composition of materials. The technique works by detecting the characteristic X-rays that are emitted when high-energy electrons interact with the sample. The sample is bombarded with a focused beam of electrons, causing the atoms in the sample to emit X-rays of characteristic energies. These X-rays are then collected and separated by energy using a detector, such as a silicon drift detector or a high-purity germanium detector. The energy of the X-rays is proportional to the atomic number of the element, so the signal can be used to identify the elements present in the sample.

EDX provides a rapid, non-destructive way to determine the elemental composition of materials, and it is particularly useful for identifying the distribution of elements within a material, as the X-rays can be detected with high spatial resolution in the SEM. Moreover, it enables the measurement of the relative abundance of each element, and to map the distribution of elements in the sample.

The technique can also be used to detect light elements such as carbon, nitrogen, and oxygen, which are not easily detected by other techniques such as X-ray diffraction.

In this case, it has been employed to identify if the coating layers have been fully removed from the substrate by using high pressure waster jet techniques and compare the results with the simulations. For this the FEI Quanta 600 SEM in EDX mode has been used.

c) <u>Raman spectroscopy</u>

The Raman effect, discovered by Sir Chandrashekhara Venkata Raman in 1928, occurs when light is scattered by a material and its frequency is shifted due to interaction with the vibrational modes of the material. The resulting Raman spectrum contains information about the vibrational modes of the material. This makes it a powerful analytical technique to study the vibrational modes of molecules and materials.

In Raman spectroscopy, a laser beam is typically used as the excitation source, and the scattered light is analysed using a spectrometer to obtain the Raman spectrum. The Raman spectrum typically consists of a series of peaks corresponding to the different vibrational modes of the material. The positions and intensities of these peaks can be used to identify the chemical composition of the material, residual stress analysis and phase study as well as to obtain information about its molecular structure and physical properties. It is non-destructive, meaning that samples can be analysed without altering their chemical or physical properties.

Raman spectroscopy is a well stablished technique in the study of phase transformation of YSZ [18]. Consequently, a Horiba LabRAM HR confocal Raman spectroscopy microscope with a Synapse CCD detector, from the UoN nmRC, has been used to characterise the phase state of the analysed YSZ samples and study the high strain impact of high pressure water jet droplets in the affected material (Figure 35). The microscope is equipped with a x50 lens (0.55 numerical aperture) and was set up with λ 532 nm wavelength (i.e., green) laser, operating at a power of ~2 mW

(100%), a spot size of approximately 1.2 µm (calculated based on the Rayleigh criterion) and a grating of 1800 lines/mm. The confocal nature of the employed setup allows to obtain measurements from a small volume of material near to the top surface. Measurements were collected for 2 seconds, and the average of two measurements was kept as the final result.

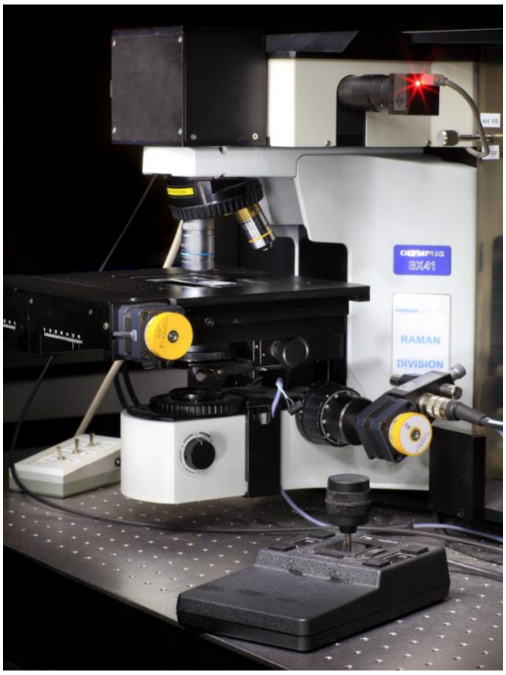

Figure 35: *Horiba LabRAM HR confocal Raman spectroscopy microscope from the nmRC.*

d) <u>Focused ion beam (FIB)</u>

Focused ion beam (FIB) is a technique that uses a beam of ions to remove material from a sample or to modify its surface with high precision. The technique is widely used in materials science, semiconductor fabrication, and other fields that require high-resolution imaging, precision machining, or sample preparation.

The basic components of a FIB system include an ion source, a series of electromagnetic lenses, and a detector system. The ion source typically uses a gas such as gallium, which is ionized and accelerated to produce a beam of ions that can be focused onto the sample by a series of lenses. The ions can be controlled in terms of energy, current, and spot size, allowing for precise removal or modification of material.

One of the key advantages of FIB is its ability to create precise, three-dimensional structures at the nanoscale. In this project the EI Quanta 200 3D Dual Beam FIB-SEM from the nmRC has been used for manufacturing lamellas for material characterization in the TEM. First the area of interest has been covered in 15 × 1 μm a gallium layer and then the 15 × 7 × 1 μm rectangles were milled with the ion beam. Afterwards, the lamella has been extracted and positioned in a holder and finally, its thickness has been reduced from 1 μm to ~ 100 nm. This machine is shown in Figure 36.

Figure 36: *EI Quanta 200 3D Dual Beam FIB-SEM from the nmRC.*

e) <u>Transmission electron microscopy (TEM)</u>

Transmission electron microscopy (TEM) is a type of microscopy used to study the internal structure of materials with very high resolution, typically at the scale of a few micrometres or less. The technique works by passing a beam of electrons through a very thin section of a material and measuring the resulting signals. Thanks to its high resolution and contrast image analysis it allows the study of crystal structures, defects, and interfaces within materials.

The basic components of a TEM include an electron source, a series of electromagnetic lenses, and a detector system. The electron source typically uses a heated tungsten filament or a field-emission electron gun to generate a beam of electrons that is focused onto the sample by a series of lenses. As the electrons pass through the sample, they can be scattered, diffracted, or absorbed, producing various signals that can be detected by specialized detectors.

For this project a Jeol 2100F TEM (Figure 37) has been used. There are different models of TEM analysis techniques, the ones applied have been: i) HAAD STEM that gives a general view of the lamellas. This technique works by transmitted electron signal, in where the electrons pass through the sample without being scattered or absorbed, then these electrons are focused onto a detector placed below the sample, and their signals can be used to produce high-resolution images of the material's internal structure. ii) BF TEM in where atomic resolution can be obtained (i.e. defects below 5 nm have been observed) and iii) SADP TEM that gives information as diffraction patterns.

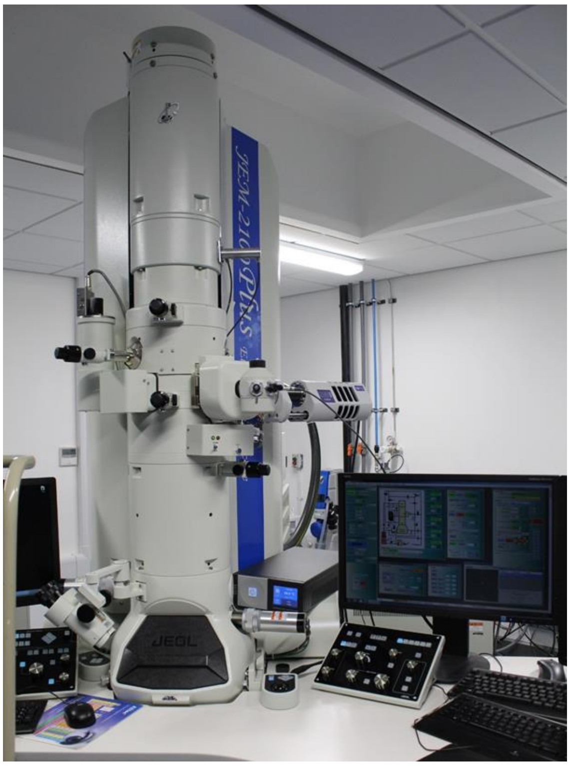

Figure 37: *Jeol 2100F TEM from the nmRC.*

3.4.3. *Material property analysis*

a) <u>Nanoindenter</u>

In this project an SEM with an in-situ Alemnis nanoindenter has been used. This was equipped with a spherical tip (diamond Ø40 µm) to mimic the shape of the water droplet as much as possible but to access lower values of strain rate. The indentations have been analysed by studying the relationship between the indentation depth (h) and the load/unload (P) forces that equals to the indentation energies, which are calculated from the area underneath the load and unload curve. The setup is shown in Figure 38.

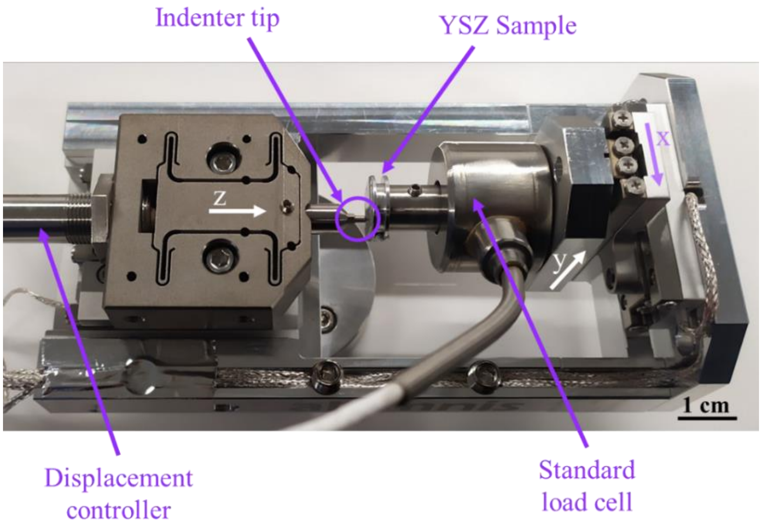

Figure 38: *Alemnis nanoindenter from the UTC installed inside the FEI Quanta 600 SEM from the nmRC equipped with a 40 µm Ø spherical tip.*

Chapter 4

Development of the mathematical model for multi material coating removal with PWJ

This chapter describes the development of the mathematical model designed to calculate the jet footprint to remove multi-material coatings. First, the importance of the nozzle choice is analysed in addition to the calculation of their kinematics. Soon after, the model itself is defined: this is based on the understanding of the etching rate considering the mechanical properties of each individual material layer that compounds a coating and the energy of a PWJ system. This interaction has been obtained for any specific pressure, considering the energy variations along the height of the jet, for one or multiple jets, which follows a defined arbitrary trajectory in a 3D space, during a period of time. Finally, a particular case in reference to the coating removal of pocket edges has also been analysed.

4.1. Introduction

Aerospace coatings, which are meant to work in harsh environments, are usually made of various material layers: i) a top coat (e.g. thermally sprayed AlSi alloy) that complements the mechanical/thermal properties of the substrate; ii) a bond coat that enhances the adhesion of the top coat and the substrate (e.g. thermally sprayed Ni alloy) and finally iii) the substrate (e.g. Ti alloy). These coatings get worn and need to be replaced to prolong the aeroengine service life and for this, PWJ milling process is proposed [111]. Both the distinct mechanical properties of each of the layers, and the characteristic of time dependency of the WJ machining process, makes the operation difficult to predict (e.g. jet penetration). Therefore, the process is hard to perform accurately, especially when the aim is to remove the top layers without damaging the substrate material.

Previously, Finite Element Models (FEM) have been proposed for coating removal processes with high velocity PWJ milling systems and a non-stationary jet [112] as well as AWJ milling trenches [59]. However, particularly for large-scale simulations, the computing cost of solving FEM models can be very high. In order to handle the computations effectively, this can result in lengthier processing times and need powerful hardware and resources. Hence, FEM models are not the most competitive option for an industrial environment specially when the aim is to test new relevant machining parameters in situ and expect a fast response. Additionally, these models demand for specialised software that is reliant on external licencing, which is typically expensive, requires upkeep and upgrades, and is challenging to transfer the knowledge from one plant to another.

Taking this into consideration, a mathematical framework based on the calculation of the etching rate to predict the depth of the removed material for nonstationary jets has been previously suggested [72]. This model has been upgraded for straight trenches, tilted angles [71] as well as overlapping trenches [75] and free forms [113]. Even if they have demonstrated accurate water jet milling predictions in these conditions, the application of this model in a multi-layered system (i.e. components with coatings) is a challenge. In this model the etching rate is obtained by post processing a calibration data, hence the etching rate curve is obtained for the entire trench. Having several materials in layers requires a distinct etching rate for each layer because this parameter depends on the material, SoD, and coating thickness. This complicates the boundary conditions needed to transit from one layer to another [72]. To avoid this issue a model that considers the etching rate in a punctual way rather than considering it for the full trench is proposed.

The scope of this chapter (summarized in Fig. 1), is to propose a functional mathematical model that predicts the water jet milled trenches produced by a different water jet removal nozzles heads (e.g. a four jet rotary and a fan nozzle), which presents the novelty of considering the individual properties of the each of the multi-material layers (i.e. aerospace coating), based on the analysis of the energy distribution of the multiple jets. This model covers any pump pressure, stand off distance (SoD), arbitrary trajectory and the overlapping of the multiple jets' footprints in curved and flat surfaces. Moreover, it allows to control the depth of the jet penetration on multi-material systems to enable the damage prevention of the substrate material, while optimising the PWJ milling process to maximise the material removal rate.

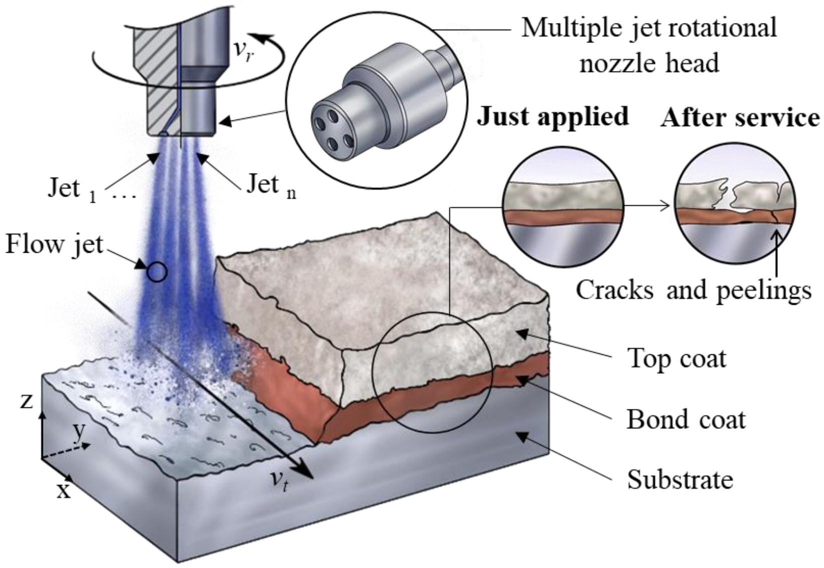

Figure 39: *Schematic representation of an example of a multi-layer coating being stripped using high pressure waterjet technology with a rotational multiple plain water jet nozzle.*

4.2. Study of the material removing nozzles

4.2.1. Key parameters to be considered in PWJ milling

As previously stated, Plain Water Jet milling is a non-conventional machining technique that releases plain water (i.e. without any abrasives), from a small nozzle, with a high kinetic energy in order to abrade the target material. This process depends on multiple variables that involve the control of the water jet pump, the variables from the water jet machine and material properties that are meant to be removed [114].

The key parameters and features that the user needs to define the PWJ milling process from a machining point of view are as follows (see Figure 40):

- **Water Pressure (P / MPa)**: This parameter is defined by the water pump of the machine. A higher pressure of the water being released from the nozzle will produce a higher abrasive energy of the jet. Hence, the material removal rate increases proportionally.
- **Stand of Distance (SoD / mm):** The distance from the top of the sample to the end tip of the nozzle, in positive z direction. Based on this distance

the jet energy will be more focused or disperse. Therefore, the material removal rate of the target will vary from a deeper trench with a lower SoD, to a wider when increasing this distance.

- **Speed of the nozzle head, translational speed (v_t / mm/min):** The speed at which the nozzle head advances. The higher the translational speed, the lower the trench depth will be.
- **Nozzle:** The nozzle choice will define the geometry of the jet and thus the energy distribution at the target. At the same pressure and speeds, different nozzle heads will generate a variety of trenches.

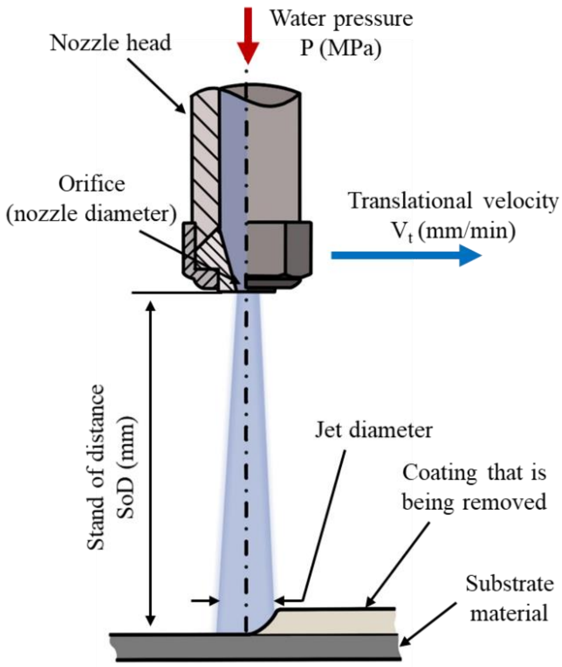

Figure 40: *Schematic representation a jet indicating the key parameters to consider in order to model its performance (adapted from* [115]*).*

4.2.2. *Types of nozzles considered for the study and the analysis of their jet flow*

There are many nozzle types in the market and each of them is designed for a different application. The aim of this project is to remove (i.e. clean) surface coatings without damaging the substrate material. For this application a nozzle that provides a wide diameter is preferred in contrast to a focused nozzle (e.g. a needle nozzle) as it will be faster due to its larger material removal area and in addition, the jet energy will be more distributed in the target surface. Considering these points, for this project, a four jet rotational nozzle and fan nozzle have been analysed.

The four jet nozzle, presented in Figure 28a, is a rotational head with four individual needle nozzles located at different radiuses from the centre at each quarter (i.e. every 90º). The total jet radius of this nozzle will be as wide as the outer radius of the jet furthest from the centre.

The fan jet, shown in Figure 28b, on the other hand, is a nozzle with a thin slot in where the outlet orifice is located inside. When the water is released, the thin slot gets filled redirecting the water to get out creating a curtain/fan shape (i.e. a wide jet from the front and a needle shape when looked from the side). When this nozzle rotates the total jet radius becomes as wide as the fan shape width.

Due to the wide radiuses both nozzles are ideal to mill large areas of material in a reasonable time. However, due to the energy distributions of the jets the 4 jet nozzle is gentler than the fan nozzle which makes it more suitable to remove soft coatings whereas the fan nozzle is more efficient with harder material coatings.

To comprehensively understand the jet flow of both nozzles (i.e., the four jet and fan nozzle) and mathematically model their behaviour, a close analysis was conducted using a high-speed camera (IDT Y4-S2 Motion Pro) recording at 4500 frames per second. From the recorded videos, specific frames were extracted for further analysis. The extracted data was then subjected to examination in Mountains Map® to determine the water density of each jet. To evaluate the jet behaviour under different conditions, four representative pressures were chosen for the tests: 100 MPa, 200 MPa, 300 MPa, and 400 MPa. These selected pressure values allowed for an in-depth analysis of the jet evolution at a range of water speeds.

By correlating the high-speed camera observations with the pressure-dependent water density data, researchers can gain a comprehensive understanding of the nozzle's performance and optimize their industrial applications accordingly.

a) <u>Four jet nozzle</u>

The high speed camera pictures for the four jet nozzle, Figure 41, show that each of the four water jets are clearly defined and divided, independent to each other. The study reveals the water density and the jet diameter (see Figure 40) increase with the raise of the water pressure.

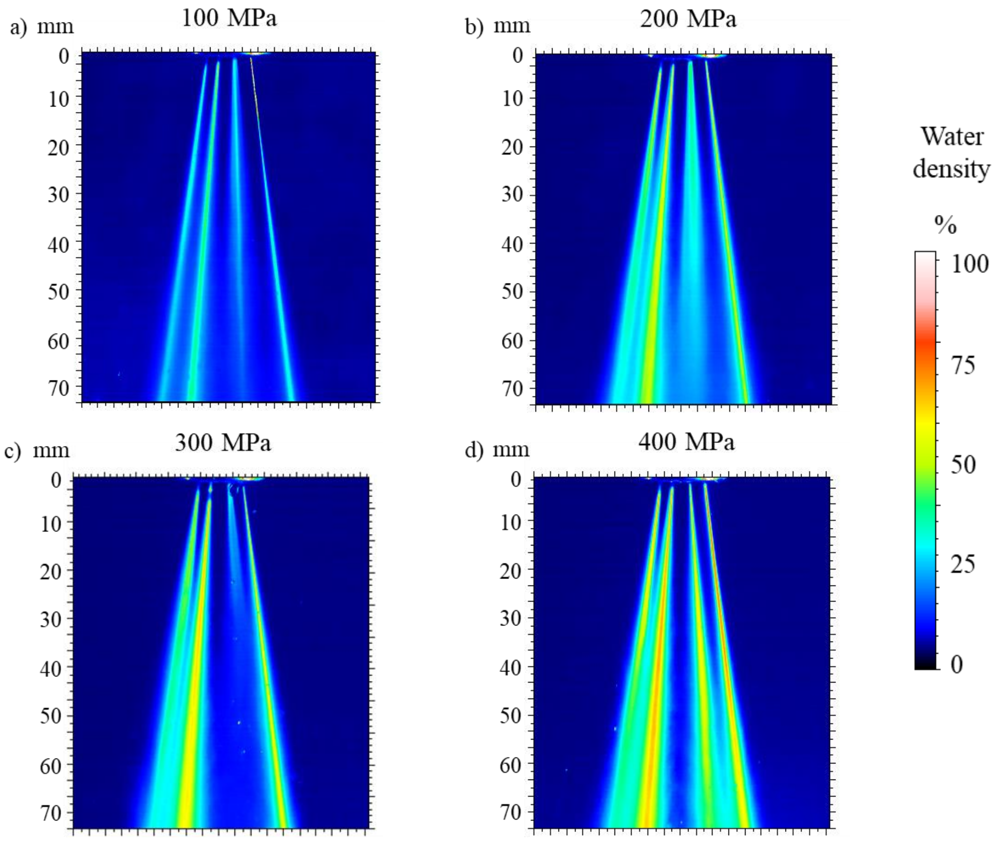

Figure 41: *High speed camera (IDT Y4-S2 Motion Pro) plus MM water density distribution analysis of the four jet nozzle flow at a) 100 MPa, b) 200 MPa, c) 300 MPa and 400 MPa.*

Moreover, the snapshots also demonstrate that the water density distribution of each jet follows a specific pattern. According to the literature, in the case of the needle nozzles the distribution of the jet is considered to have a normal distribution (i.e. Gaussian distribution) [116], [117].

To grasp a clearer understanding of these images, let us carry a more meticulous examination (see Figure 42). Each of the jets is positioned at a different distance from the camera due to the cylindrical shape of the nozzle head. The camera is focused on the nearest nozzle to it (e.g. jet 4), which exhibits the most distinct water distribution pattern. Upon analysing the colour code representing the water density distribution of this particular jet, we can discern a Gaussian distribution, supporting the claim made earlier in the literature. Furthermore, the jet's energy distribution will also follow a gaussian distribution since it has the same pattern as the water density.

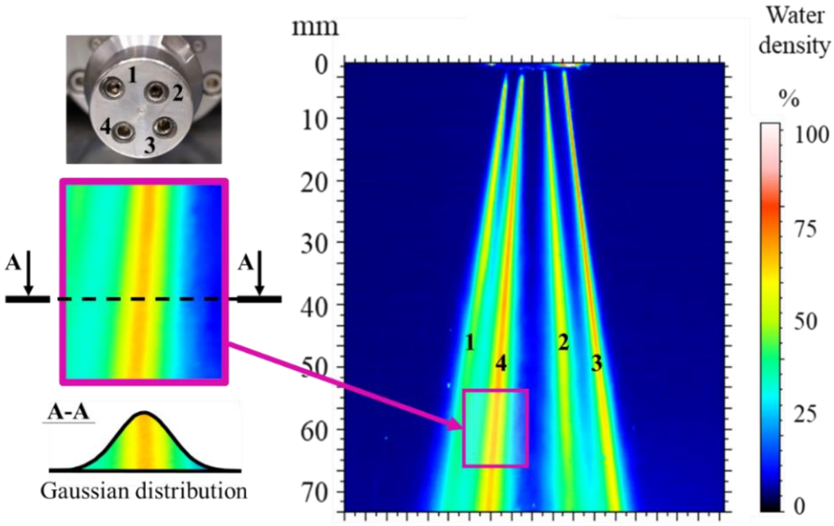

Figure 42: *A close-up high-speed camera image of a fan jet nozzle displaying the locations of each jet and the gaussian distribution of the water flow while taking into account the water density % colour scale.*

b) <u>Fan jet nozzle</u>

The same study was also conducted with the fan nozzle as it is shown in Figure 43. In this case the front and side views of the jet are show as the jet is not radially symmetric. The images for this nozzle show that this nozzle does not follow a Gaussian distribution as in the case of the four jet, but still follow a distinct patter among each other. The water density on the fan nozzle does not seem to have a uniform composition, thus it shows what looks like two opposite streams and a curtain of water between them. When raising the pressure, the density of these side jets increases while the middle curtain does not show a clear pattern. Furthermore, no information was found in the literature about the water distribution for this type of nozzle.

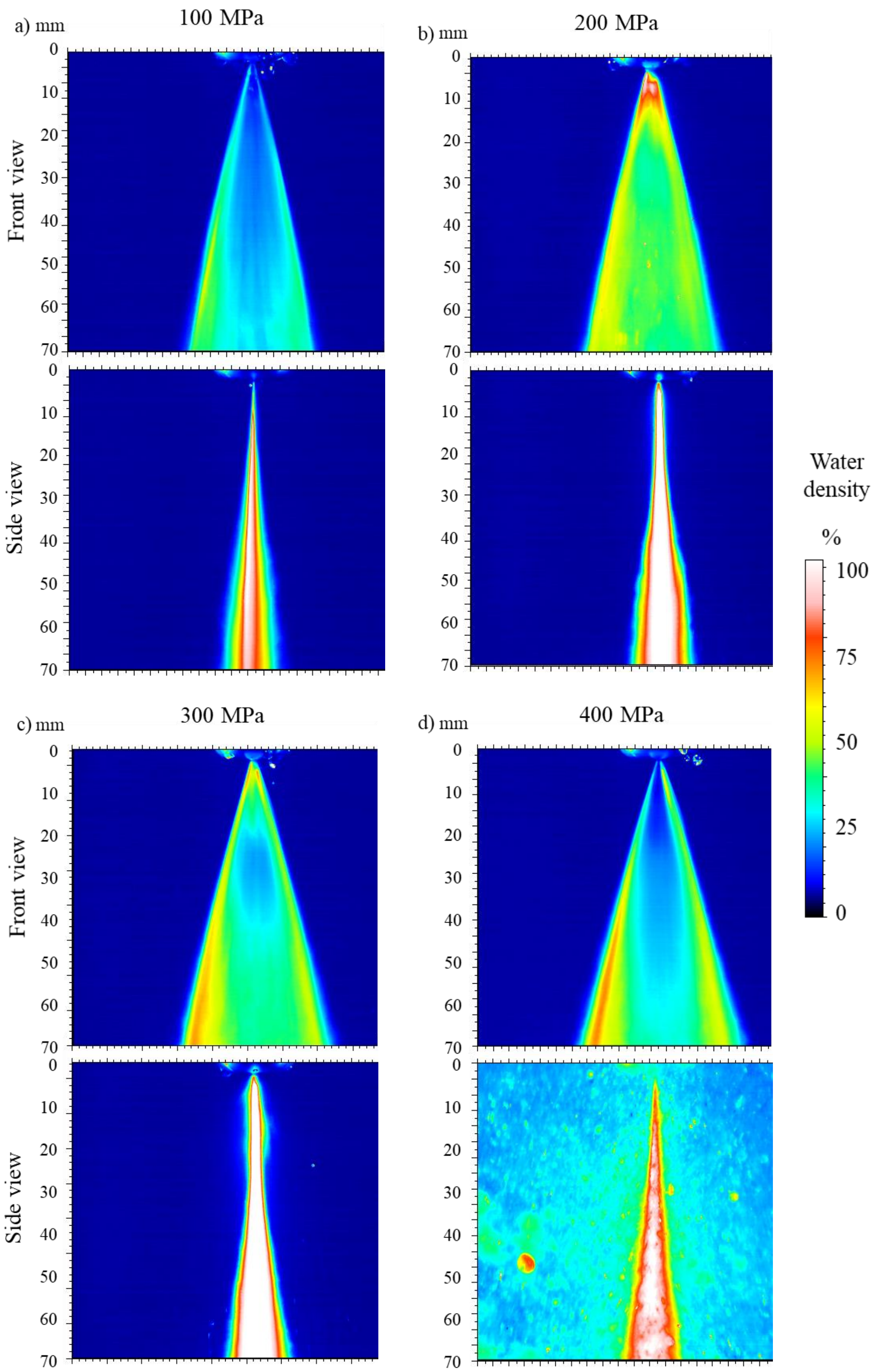

Figure 43: *High speed camera (IDT Y4-S2 Motion Pro) plus MM water density distribution analysis of the fan jet nozzle flow, both from the front and side, at a) 100 MPa, b) 200 MPa, c) 300 MPa and 400 MPa.*

The water distribution for the fan nozzle could not be identified from the high speed camera pictures. An attempt was done by taking a slice across the direction perpendicular to the flow, but due to the quality of the images, in this case it was hard to obtain an identifiable mathematical distribution, hence, the attempt was not successful. Thus, in order to get the fan nozzle's jet distribution, a trench was therefore machined, and the resulting curve was measured, as shown in Figure 44:

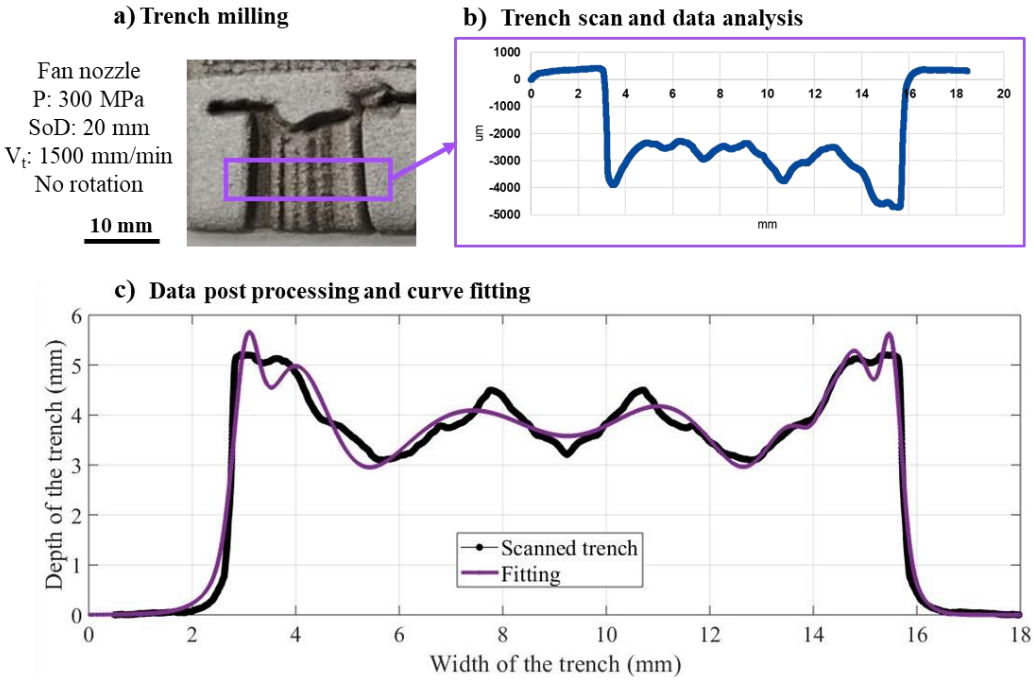

Figure 44: *Process followed to calculate the water density distribution of the fan jet nozzle: a) first by milling the trench (3 axis WJ from UoN) in a soft material, b) then scanning (high-resolution optical 3D surface metrology system) and data analysis in MM and finally c) data post processing and fitting curve calculation in MATLAB.*

First a trench was milled by using the 3 axis water jet from the University of Nottingham in a soft material (i.e. 5 mm abradable coating) so the indentation left by the jet can be easily scanned (Figure 44a). Then the trench was scanned in a surface scanner (high-resolution optical 3D surface metrology system) and post processed in Mountains Map, here an area of the trench was considered to create a mean trench that was exported as a point cloud (Figure 44b). Finally, after smoothing the data just enough to remove the background noise a curve fitting was obtained in MATLAB (Figure 44c). This fitting was then introduced in the model as the energy distribution shape of the fan jet nozzle.

It is worth mentioning that even if a considerable effort was made trying to obtain a faithful approximation of the energy distribution, in the case of this type of nozzle in where the jet is quite uniform, the exact shape of the energy is not crucial. The aim has been to capture the essential characteristics of the system, rather than dwelling on fine-tuned energy details that might have marginal impact on the model.

4.2.3. Kinematics study of the nozzle heads for an optimal coating removal

After understanding the distribution of water density of both nozzles the movement in space of the jets needs to be considered for an optimum coating removal. As stated before, nozzle heads that spin were chosen to optimise the coating removal area, this means that the resultant velocity of the nozzle heads will be a combination of a rotational as well as a translational velocity. The kinematics of the nozzle head is based on the particular geometry, so in the following section the relative velocity of each point the jets will be calculated. The mathematical model has been presented parametrically.

a) <u>Four jet nozzle</u>

In the case of the four jet nozzle (n = 4) each of the jets (j_n) are located at a different radius (r_n) from the centre at each cardinal point (γ = 90º) and all of them rotate at the same time around the z axis at a constant rotational speed (v_r). Meanwhile the rotational nozzle head advances forward in a constant translational speed (v_t) as represented in Figure 45.

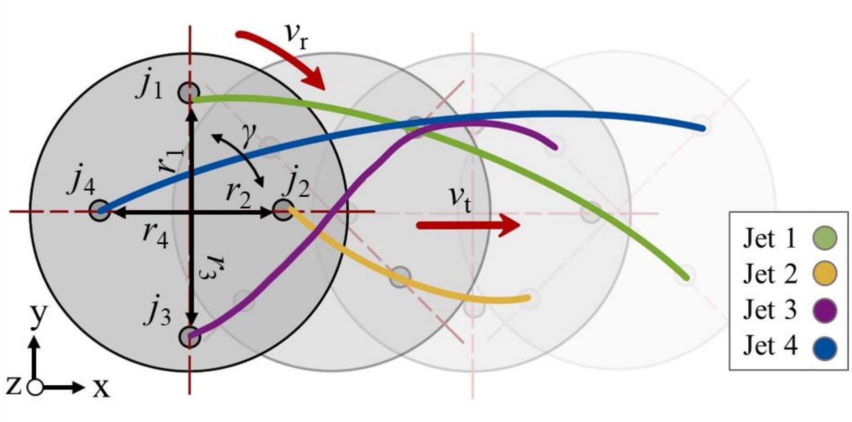

Figure 45: *Schematic representation of the trajectory of each individual jet of the four jet rotary nozzle and the definition of the parameters as well as the reference system in order to understand the kinematics of the nozzle head when rotating and advancing transversally.*

First, the equation (2) and (3) defines the translational (d_{j1t}) and rotational velocity (d_{j1r}) vectors of the first nozzle (j_1). In where the angular velocity is calculated as in the equation (4) considering the v_r and the time (t).

$$d_{j1t} = \begin{Bmatrix} v_t \times t \\ 0 \end{Bmatrix} = \begin{Bmatrix} x \\ y \end{Bmatrix} \tag{2}$$

$$d_{j1r} = \begin{Bmatrix} r_1 \times cos\,\alpha \\ r_1 \times sin\,\alpha \end{Bmatrix} = \begin{Bmatrix} x \\ y \end{Bmatrix} \tag{3}$$

$$\alpha = v_r \times t. \tag{4}$$

The absolute position of the m_1 (d_{total_m1}) is calculated by the sum of both relative motion vectors as represented in equation (5).

$$d_{total\_j1} = d_{j1t} + d_{j1r} = \begin{Bmatrix} r_1 \times cos\,\alpha \\ r_1 \times sin\,\alpha \end{Bmatrix} + \begin{Bmatrix} v_t \times t \\ 0 \end{Bmatrix} \tag{5}$$

Finally, considering that is possible to have more than one jet (m_n) in the same manifold, the position of the each of the jets has been calculated relatively considering the angle that they make with the first nozzle (β_n), as shown in equations (6), (7).

$$\beta_n = \alpha + j_n \times {}^{2\pi}/_{n_{total}} \tag{6}$$

$$d_{total\_jn} = \begin{Bmatrix} fx_{4J} \\ fy_{4J} \end{Bmatrix} = \begin{Bmatrix} r_n \times cos\,\beta_n \\ r_n \times sin\,\beta_n \end{Bmatrix} + \begin{Bmatrix} v_t \times t \\ 0 \end{Bmatrix} \tag{7}$$

Subsequently, the absolute velocity (v_{total}) of the nozzle jets has been calculated by deriving the position, as shown in equation (8) and (9).

$$\begin{matrix} v_{fx} \\ v_{fy} \end{matrix} = \begin{matrix} \frac{d(fx(t))}{dt} \\ \frac{d(fy(t))}{dt} \end{matrix} = \begin{Bmatrix} -(v_r \times r_n \times sin(v_r \times t)\ ) + (v_t) \\ v_r \times r_n \times cos(v_r \times t) \end{Bmatrix} \tag{8}$$

$$v_{total} = \sqrt{{v_{fx}}^2 + {v_{fy}}^2} \tag{9}$$

The positioning of the jet represents the coordinate point of the centre of each jet in the nozzle head, the nozzle diameter and the taper effect of it is not considered yet. The understanding of the position of the jets overtime is highly important as it directly affects the pattern that the jet will follow and thus the coating removal efficiency. This pattern will determine if the surface will be totally cleaned or if any spot will be left untouched, hence with coating unremoved.

b) <u>Fan jet nozzle</u>

The kinematic pattern of the fan jet nozzle head is similar to the four jets, both are nozzle heads that rotate in their z axis while moving forward in positive x at a constant transversal speed. In both cases the particular points will follow a sinusoidal path along the trench.

However, in the case of the fan nozzle there are not multiple jet distributed but there is a single nozzle inside a slot (see Figure 46), that when the water is released from it, the slot gets filled and it is released creating a water curtain (i.e. very narrow looking it from the side, but with a fan shape looking from the front). Due to this the kinematic analysis will be studied using a random number of infinitesimal points (in this example n = 7) along the width of the slot (n_{width}) and their position in time will be analysed. The plots will only represent the edges and some points along the fan, but it needs to be considered that infinite points would exist along the width of the slot.

Equation (10) and (11) defines the translational (d_{pnt}) and rotational velocity (d_{pnr}) vectors of the points along the width of the fan nozzle. The angular velocity is calculated in the same way as for the four jet nozzle (equation (4)).

$$d_{pnt} = \begin{Bmatrix} v_t \times t \\ 0 \end{Bmatrix} \rightarrow \begin{Bmatrix} x \\ y \end{Bmatrix} \tag{10}$$

$$d_{pnr} = \begin{Bmatrix} r_n \times cos\,\alpha \\ r_n \times sin\,\alpha \end{Bmatrix} \rightarrow \begin{Bmatrix} x \\ y \end{Bmatrix} \tag{11}$$

Finally, the equation (12) describes the position for any given time for any given point along the width of the fan jet nozzle slot.

$$d_{total\_pn} = d_{pnt} + d_{pnr} = \begin{Bmatrix} fx_{fan} \\ fy_{fan} \end{Bmatrix} = \begin{Bmatrix} r_n \times cos\,\alpha \\ r_n \times sin\,\alpha \end{Bmatrix} + \begin{Bmatrix} v_t \times t \\ 0 \end{Bmatrix} \rightarrow \begin{Bmatrix} x \\ y \end{Bmatrix} \tag{12}$$

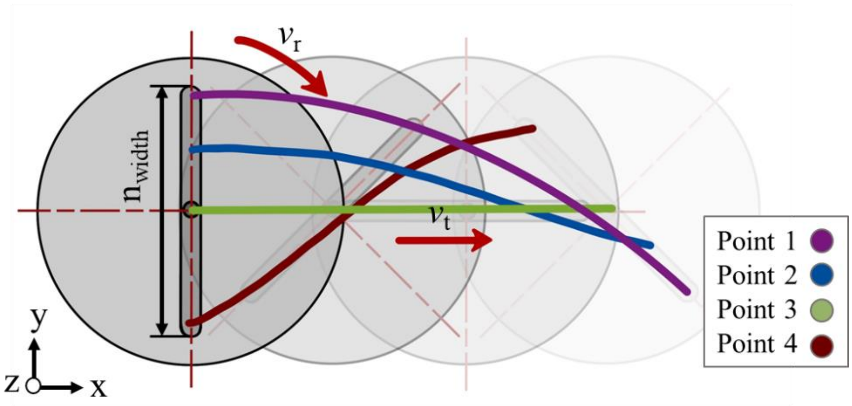

Figure 46: *Schematic representation of the trajectory of four different points through the width of the fan nozzle slot and the definition of the parameters as well as the reference system in order to understand the kinematics of the nozzle head when rotating and advancing transversally.*

Figure 47 and Figure 48 represent four MATLAB graphs from the four jet and fan jet nozzle respectively at different parameter combinations. All the configurations maintain a constant v_r (-2π rad/s) and a variable v_t (1 m/s, 5 m/s, 25 m/s, 100 m/s) to visually understand the effect of the speed in the coverage of the jets. The studied length for the calculation is the same for all the plots (150 mm), which means that the necessary time (t) to cover the same distance changes for each considered v_t. In each case the resultant pattern varies from a full removal to very low removal points. The results can be used to calculate the optimum translational speed without compromising the total processing time.

Figure 47a and b present patterns that fully covers the area of study, even passing several times over the same spots. The difference between both passes is that the parameters involved in Figure 47a are too conservative that most certainly will take longer than necessary. The plot in Figure 47b keeps the coverage, as the four jets pass over every point, with many overlapping and along both edges of the trench.

On the other hand, Figure 47c and d exhibit clear gaps between the jet rotations and that the edges of the trench do not follow a linear pattern. These are examples of how a trench where the jet moves at just over critical speed would look like. These patterns will never remove all the necessary material.

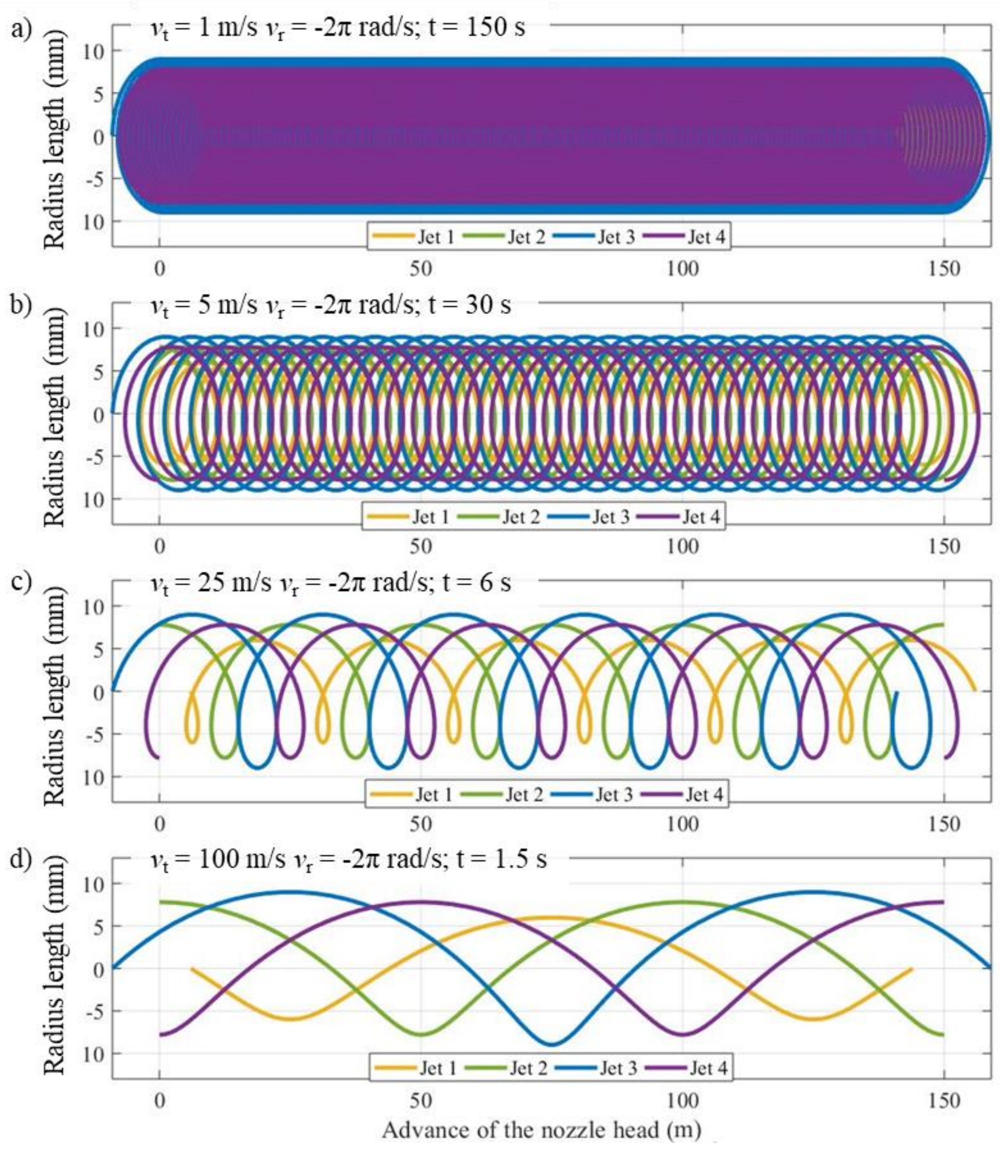

Figure 47: *MTATLAB graph representation of the effect that the difference in v_t (and hence the change in the absolute jet speed) provokes in the jet positioning patterns, in the four jet nozzle, while keeping the rest of the parameters constant (v_r = -2π): a) 1 m/s, b) 5 m/s, c) 25 m/s, d) 100 m/s.*

Figure 48 represent the same case scenarios respectively in each a, b, c and d version but for the fan jet nozzle head.

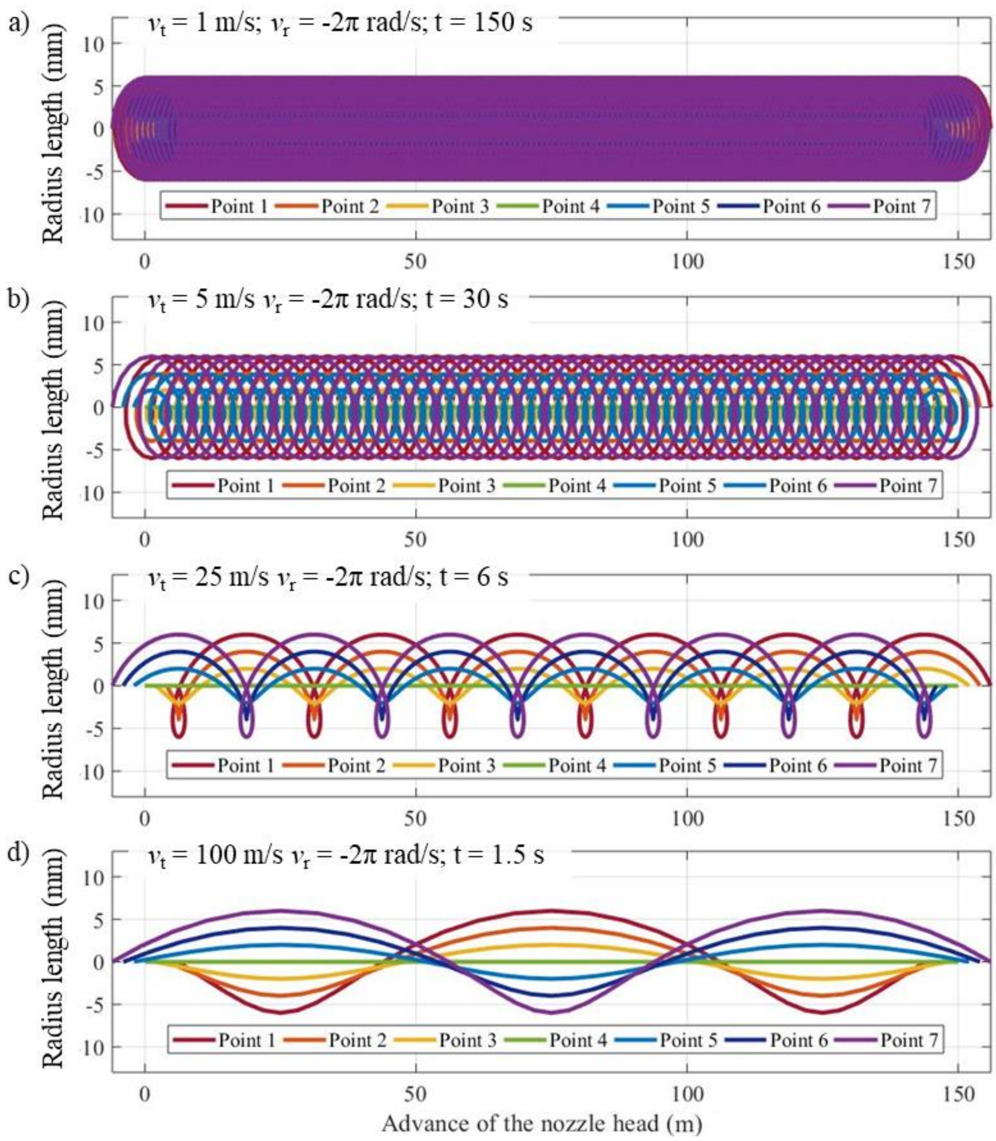

Figure 48: *MATLAB graph representation of the effect that the difference in v_t (and hence the change in the absolute jet speed) provokes considering different points along the jet width in the fan jet nozzle, while keeping the rest of the parameters constant ($v_r = -2\pi$): a) 1 m/s, b) 5 m/s, c) 25 m/s, d) 100 m/s.*

4.3. Mathematical model based on the calculation of the jet energy

4.3.1. Introduction: description of previous models and its limitations

Originally, the prediction calculations where organized to be based on the model defined by Axinte et al. in 2010 [72], in where the material removal is calculated using the material specific erosion (i.e. etching) rate. The etching rate in this context is dependent on the properties of the workpiece material and other process parameters (e.g. pressure, mass flow of abrasives). It is treated as a function that needs to be calibrated using experimental data and in the 2010 model it follows a linear geometry and jet motion, with no variation in the y-direction [72]. The idea in the current project is to combine the absolute velocity of the speed of the jet (which is variable at each point dependant on the trajectory) with this etching rate to obtain the material removal mathematical model. As shown in Figure 49 the result of the addition between the kinematics of the jet (Figure 49a) with the calculation of the material specific etching rate (Figure 49b) results in variable depth trench (Figure 49c), that follows the jet trajectory, that depends on the nozzle absolute velocity (i.e. slower the nozzle deeper the trench).

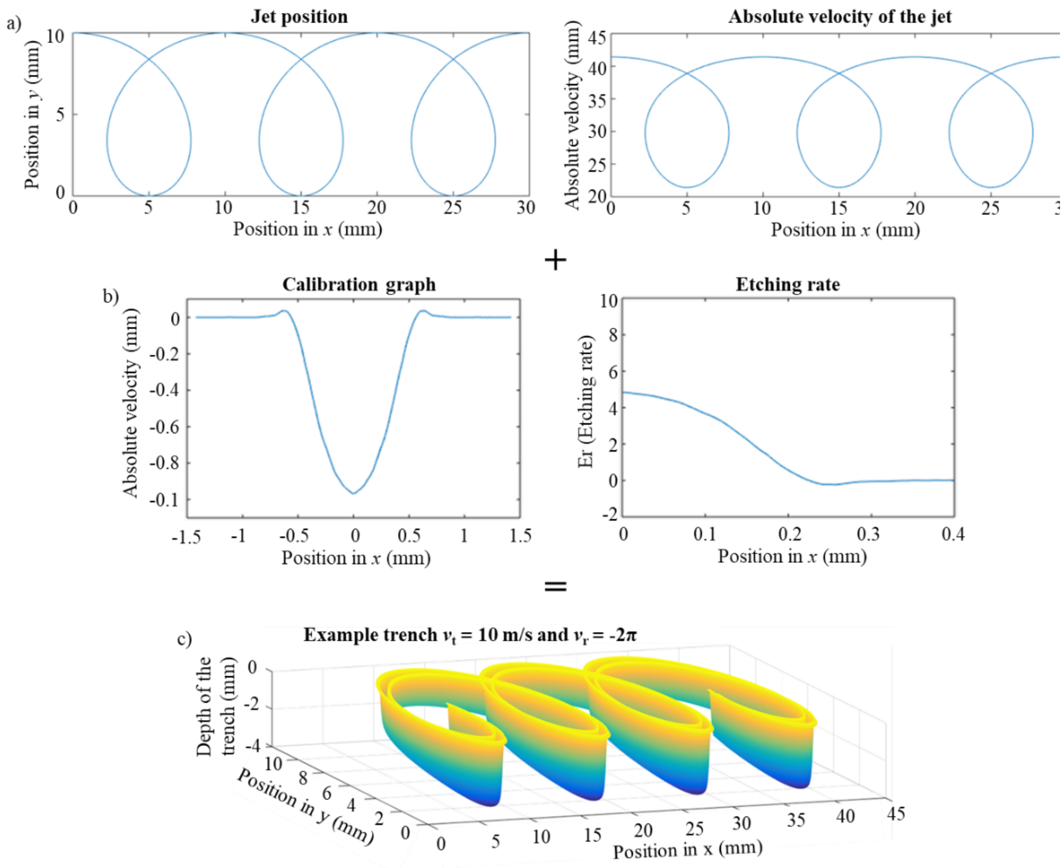

Figure 49: *The combination of both a) the kinematics of the jet and the b) calculation of the material specific etching rate (defined by Axinte et al. in 2010 [72]) c) results in variable depth trench that follows the jet trajectory that depends on the nozzle absolute velocity.*

The main point of this project is to remove coatings with multiple material layers on top of each other. This implies considering that in each application the layers might have different thicknesses and material properties. Depending on the material properties the depth of the trench will vary as depicted in Figure 50.

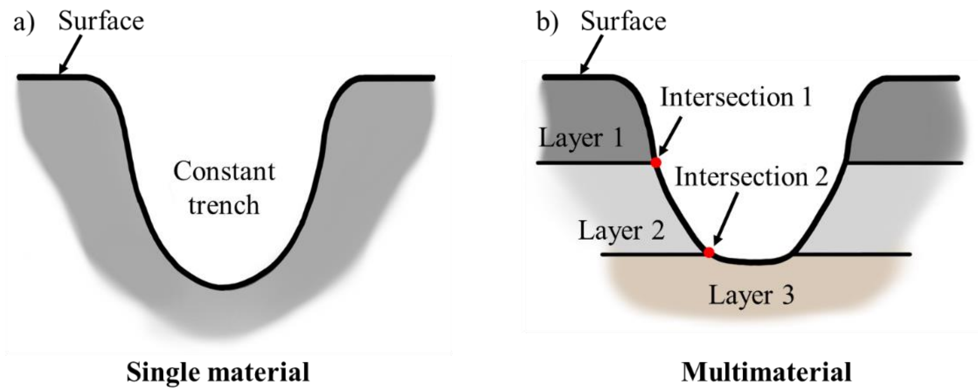

Figure 50: *Comparison of the trench shape between a) a single material target that creates a continuous outline vs b) a trench made in a multimaterial target that has clear intersection between layers due to the fact that the trench shape depends in the jet as well as the material properties of the target.*

The previous model from 2010 [72] is limited for this type of prediction, as the etching rate is obtained from a calibration data that considers the geometry of the trench curve. If more than one layer needs to be considered, the etching rate will still be calculated from the full trench, so it will not separate the properties of each material layer. Furthermore, if the thickness or the materials of the layers change, new calibration data will need to be measured to readjust the trench geometry and a new etching rate calculated for every variation of the sample.

The novel model proposed in this project is based on the understanding of the etching rate (i.e. depth of material removed) by modelling the kinetics and the energy of a Plain Water Jet (PWJ) system, this way the model will be able to consider the mechanical properties of each individual material layer that compounds the coating. This interaction is obtained for any specific pressure, considering the energy variations along the height of the jet, for one or multiple jets, which follows a defined arbitrary trajectory in a 3D space, during a period of time. It will still be needed a calibration data to include the individual mechanical properties. But the same calibration data will be enough for that material no matter what the thickness, coating order or machining parameters. The calibration data will be just linked to the material itself.

4.3.2. *Definition of the energy distribution of a rotary jet for an arbitrary trajectory in a 3D space*

The flow is modelled based on the energy that is released from the jet (E_{nozzle}), which is defined by the pump pressure (P), the position in space (x, y, z) and the geometry of the nozzle (g_n), such as the diameters and length.

$$E_{nozzle} = f(P, x, y, z, g_n) \quad (13)$$

The jet has been particularised as a cone shape to define the energy distribution as it is one of the most common jet types used in WJ systems. However, the model could be adjusted for any nozzle geometry and therefore for any energy distribution. As explained in section 4.2.2 in this project a four jet and a fan jet rotary nozzle will be used. For the energy model explanation a single jet of the four jet nozzle, which is basically a usual needle nozzle with a cone shaped jet, will be used as an example. In the case of the fan nozzle the energy distribution through the jet width will follow equation (13).

For a cone shape nozzle, the following assumptions have been defined: i) the jet follows a Gaussian distribution along the z axis and ii) energy conservation is assumed along the z direction of the jet, as described in Figure 51.

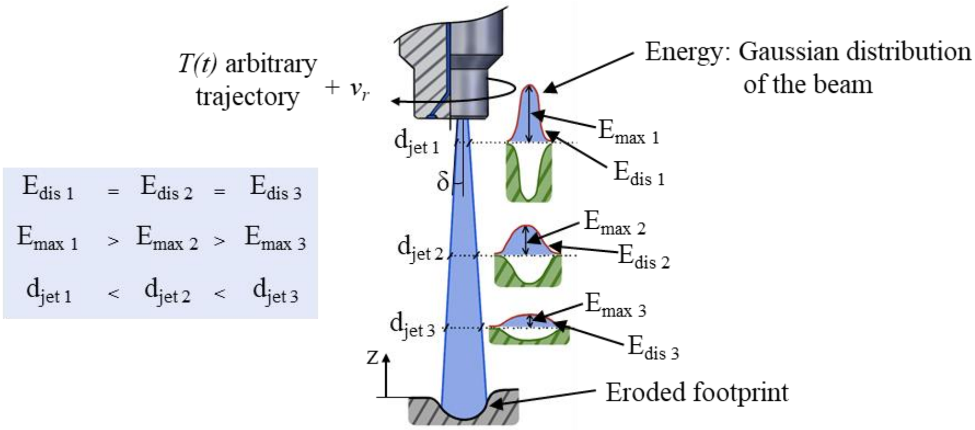

Figure 51: *Energy distribution of a cone shape nozzle (i.e. needle nozzle) following a Gaussian energy distribution along the jet z axis.*

The energy distribution calculation of a cone shape nozzle that follows a Gaussian distribution has been previously studied [116]. Here, the jet velocity is obtained applying Bernoulli's principle and the kinetic energy of the jet is calculated. In this case, it has been considered that there is no air on the jet as it is just plain water. The maximum energy (E_{max}) is calculated for any pump pressure (P), water density (ρ), any nozzle diameter (d_{nozzle}), jet cone angle (δ) and distance to the nozzle in z positive direction. In this study, the energy distribution along the radius ($E_{dis}(r)$) is defined based on the maximum energy at each height of the z axis of the jet and the variation of the jet diameter expressed with (σ).

$$E_{dis}(r,z) = E_{max}(z)e^{-\left(\frac{r^2}{2\sigma^2}\right)} \tag{14}$$

In where for PWJ:

$$E_{max} = f(P,\rho,z) \tag{15}$$

$$\sigma = f(d_{nozzle},z,\delta) \tag{16}$$

Thus, the energy distribution is a property of the jet, independent to the trajectory that follows. The trajectory (T) of a rotary jet can be defined by a homogeneous transformation matrix which consists of a rotation and a translation in 3D space in a defined period of time: $T(t)$. Hence, the jet energy that follows the defined trajectory is described as E_{space}.

$$E_{space}(r,z,t) = \begin{bmatrix} E_{dis}(r,z) \\ E_{dis}(r,z) \\ -z \end{bmatrix} \times T(t) \tag{17}$$

4.3.3. *Definition of the target material considering an arbitrary number of coating layers*

The depth (z) of the target material consists of a defined number of material layers (m) and a freeform surface (S), each one with different mechanical properties and in where each of the layers is set in parallel on top of the previous one, see equation (18). In the model S is created in a simple way: The size of x and y defines the size of the part that is going to be calculated and the spacing between values of x and y determines the mesh size. The calculations of how much material is removed depending on the energy that reaches the surface is defined in the numerical value of the x and y components (z). Being zero the initial value defining that the target was not yet modified by any jet and going towards negative values defining the depth at which the material has been removed while the surface is being impacted by the jet energy.

The size of the jet, the time length that wants to be simulated, the resolutions that is needed for reliable results and the computers computational time have to be considered when defining these parameters. Figure 52 shows a comparison between different mesh sizes that have been tested to find the optimal discretisation, hence the one with the best resolution and least computational time valance. Spatial meshes from 1 (M = 30) to 20 points per mm (M = 600) have been simulated. The inflexion point can be identified around the 10 point per mm (M = 300) discretisation, as in this resolution a good continuity of the trench is found (specially at the curves). Below this resolution, the shape of the trench loses its accuracy, so the resolution is not suitable to provide confident results. Above 10 points per mm, even if the resolution increases, it does not improve the predictability of the model and furthermore, there is an increase in computational cost.

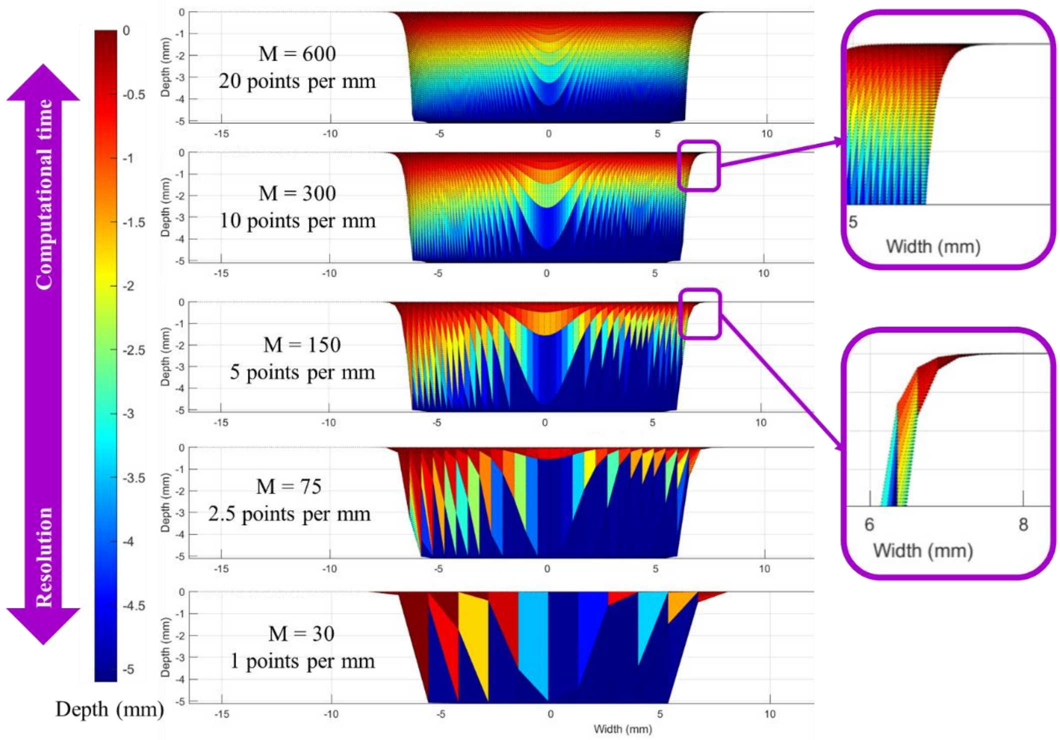

Figure 52: *Comparison of different spatial mesh sizes to define the optimal discretisation showing examples at the following points per mm: 20, 10, 5, 2.5 and 1. The mesh size of M=300 with 10 points per mm offers a good enough resolution with least compromise on the computational time.*

$$z = S_m(x, y) \tag{18}$$

In previous WJ trench milling mathematical models [72], an etching rate is described to calculate the depth of the removed material at each jet radius (r) and for a specific exposure time.

In this case, an etching rate (U) is also calculated to define the depth of the removed material for adimensional (expressed with suffix a) arbitrary energy in space ($E_{space}(r, z, t)_a$), see equation (19). Due to this, no calibration data is needed to express the machining parameters (e.g. pressure, height) as the energy has already been modelled considering these parameters, and hence, they are easily controllable. However, the material properties (i.e. resistance to jet impingement) need to be considered by the relationship between the maximum cutting depth point defined by the energy at which this point is obtained (C) and the jet cutting sensitivity of the target material (k) constants, which will be obtained by calibration data. As calibration data is used the proposed model will be considered a mathematical model that considers empirical data. The process in order to calibrate the model is explained in section 5.5.2.

$$U = C\, E_{space}(r, z, t)_a{}^k \tag{19}$$

Moreover, each of the material layers (m) can have a unique thickness (h_m) that is defined as the distance between S_1 and S_{m+1}, along the normal of S_m. Throughout this thickness, the material will have its own homogeneous properties represented by C_m and k_m.

As described in equation (20) the material properties C_m and k_m (i.e. the subindex $_m$ indicates that each particular layer (m) will have its own particular C and K values) will have to be defined for every material layer for every element in x and y that belongs to all the layers from the first to the last one plus the substrate (hence the $m+1$) both edges inclusive.

$$C_m, k_m \;\; \forall (x, y) \in [S_1, S_{m+1}] \tag{20}$$

4.3.4. The interaction between the jet and the target material

The distance between the nozzle head to the material is defined as the SoD. Once the nozzle is set to a specific SoD, equation (17) is used to calculate the energy (E_{space}) at each point of the material surface, for which, in a freeform target (S_m) will vary at each point. Additionally, reordering the equation (19) and knowing the values of the material coefficients, the necessary energy to remove each layer with their corresponding thickness is easily obtained. The points where the jets overlap, the energy that the surface will receive is a sum of each pass, exemplified in Figure 53.

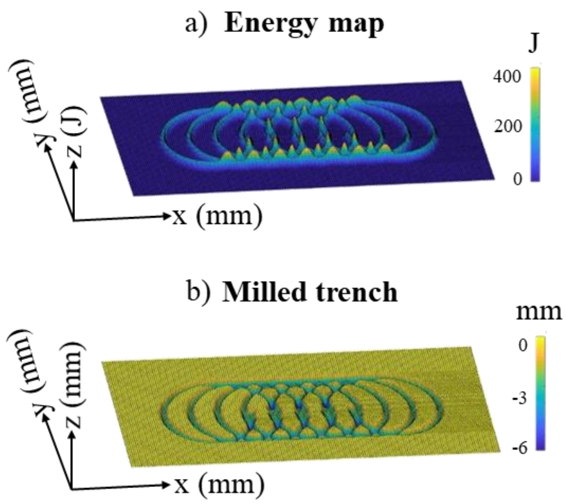

Figure 53: *Example of a) the energy distributed at every x, y target points of a single rotational jet nozzle that follows a linear trajectory and b) the resulting milled trench generated by such nozzle.*

Based on the energy map, a comparison between the received energy and the one needed to entirely remove a coating layer is compared at each target point (x, y). To calculate the removed depth (Z) the quantity of energy is correlated with the energy needed to remove the corresponding material layer. If the energy is high enough, the entire energy needed to remove the layer is deducted, and the rest is used for the calculation of the trench geometry in the following layer, as mathematically described in equation (21). What is to say, the material removed in depth (Z) along the defined area (x, y) is obtained by the multiplication of the material coefficient C_m and the received energy E (through x and y, considering the SoD to the power of K_m) plus the summatory of the thicknesses of the previously removed layers $h_{(m-1)}$. In the case when the energy was high enough to remove the previous layer fully, this value will be the entire thickness of the layer. In conclusion, the eroded trench footprint will be the sum of the eroded trenches of each material layer, as shown in Figure 54.

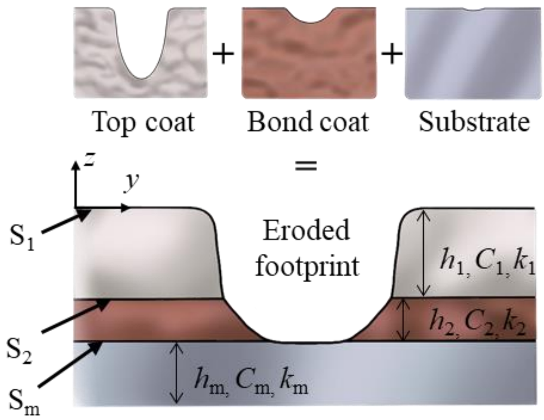

Figure 54: *Generic representation of a cross section of a single jet multi-material trench with the definition of the coefficients (Ci, ki, i=1 ... m) of the surfaces of each material layers.*

$$Z(x,y) = C_m E(x,y,SOD)_a{}^{k_m} + \sum_{1}^{m} h_{(m-1)} \tag{21}$$

4.3.5. Application of the concept in realistic parts: Overlapping trenches, curved surfaces and calculation of the milling time

In order to be able to apply the model to a virtually any kind of part the following considerations have been implemented: a) curved and flat surfaces, b) Overlapping trenches and c) calculation of the overall cleaning time of a part.

a) <u>Modelling of flat and curved surfaces</u>

The developed model is prepared to work with flat surfaces as well as concave and convex surfaces of any radius. In a rounded surface the SoD of the jet will differ along the jet radius as shown in Figure 55a. An example of a usual real life application for cleaning a curved part is shown in Figure 55b: a rounded engine casing with an inner coating located as strips inside pockets that needs to be removed.

In this case, the casing will rotate while the nozzle head moves vertically from the top to the bottom; the rotation of the casing is the equivalent of the transversal speed and the downwards movement along each revolution creates the overlapping.

The velocity of this movement will define the overlapping separation percentage. In this application it is key to accurately adjust the cleaning parameters as the casing has some exposed areas between coating strips that cannot be damaged, thus having a mathematical model that predicts the surface effect is indispensable.

To implement this geometry feature in the model, the shape of the workpiece has been implemented onto the initial state of the calculation, hence is independent to the jet energy calculation and its kinematics, the definition of the target material and their interaction. Thanks to this it is easy to implement a curvature to the model in the following way: i) positive radius will imply a convex surface, ii) a negative one a concave and iii) an infinite radius will simulate a flat surface. Due to how this has been coded, it is possible to modify this section and generate any kind of surface geometry including freeforms to the model in the future.

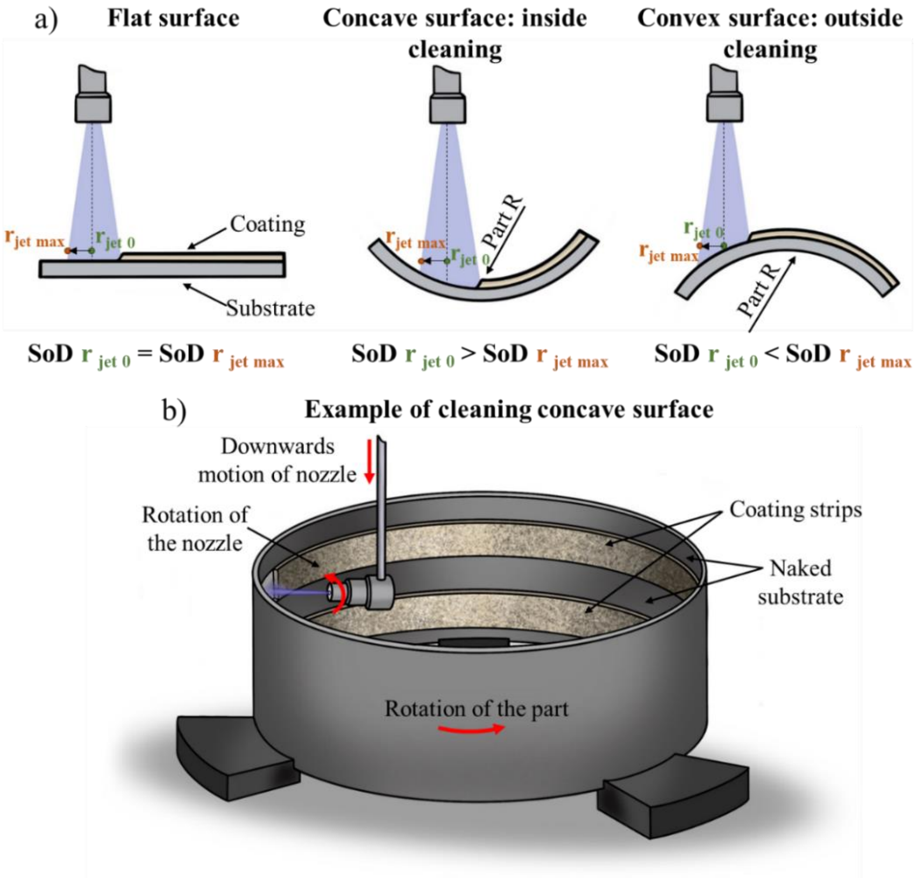

Figure 55: *a) Effect on the difference of the SoD along the jet radius and b) a representation of a usual of real life application of coating removal in the interior of a jet casing.*

a) <u>Simulation of overlapping trenches</u>

To achieve an optimal cleaned surface (i.e. full coating removal and no damage to the substrate) sometimes it is necessary to pass the WJ more than once over the same area. This interaction is called overlapping and understanding its effect is fundamental for the model. When a second trench overlaps the target surface, the state of the coating is different to the initial conditions as some material has already been removed, so the model must take this into consideration. Overlapping can increase the possibility of damaging the substrate material, although sometimes it is necessary to have a full cleaning, so it is essential to be well predicted.

Figure 56 shows an example how overlapping's are modelled in the SW. In order to define overlapping's two parameters are considered: the number of trenches (Figure 56a) that will be simulated and the percentage of separation between the centres of the trenches (Figure 56c). For this variable, 0% means that the trenches will be one on top of the other and 100% means that they will be one next to the other. A higher value than that will result in a gap between trenches (Figure 56b). Furthermore, in order to maintain a low computational effort it has been decided that simulating a segment of the workpiece and a maximum of five trenches would be enough to measure the viability of the chosen milling parameters.

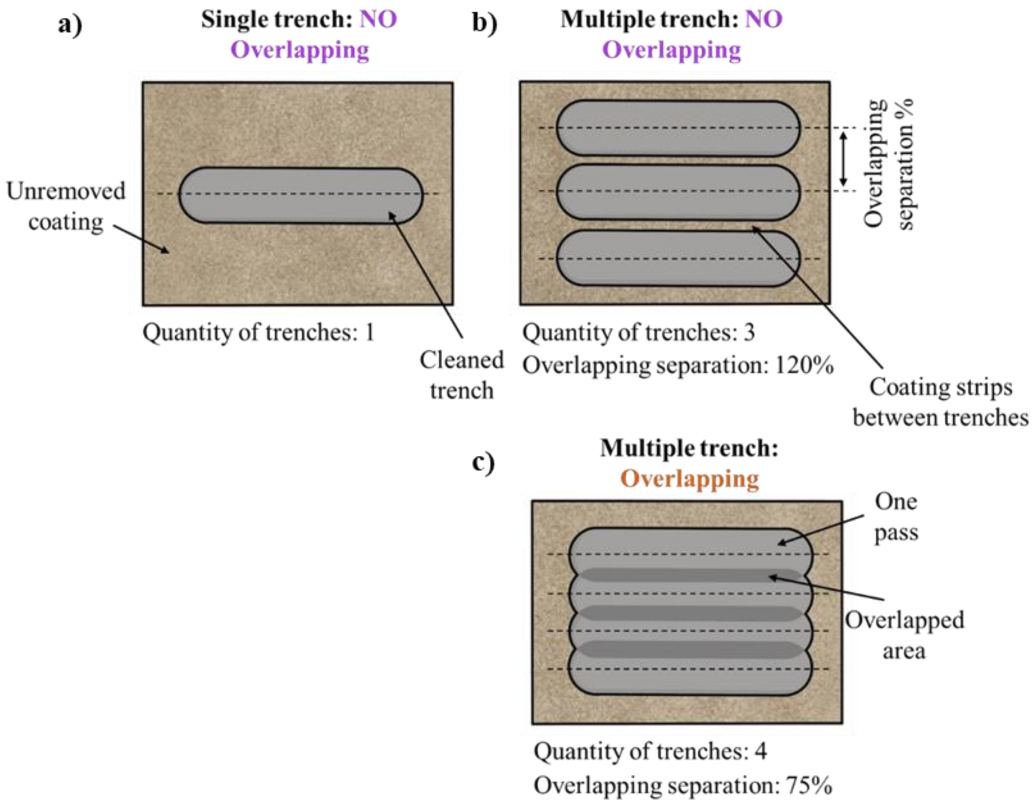

Figure 56: *Representation of overlapping trenches showing a) a single trench, b) multiple trenches with 120% of overlapping separation that results in no overlap and having unremoved coating stripes between trenches and c) example with multiple trenches with a 75% of overlapping separation resulting in areas with more than one pass.*

b) Calculation of the milling time of a whole part

Finally, the milling time of the part has been calculated. On the one part, the model has a feature that calculates the total cleaning time of the part considering the full surface area that needs to be cleaned and the machining parameters. On the other hand, the model calculates the estimated time that takes to clean a 1 x 1 m plate. This way it is very simple to compare the cleaning speed of any parameter combination that is being tried.

4.4. Particular case: geometry of a pocket, the edge of a trench

The mathematical model described until now, although being very versatile regarding machining parameters, coating layer design and surface creation is only considered for a uniform coating applied parallel to the substrate. However, in the particular case of a casing pocket depicted in the Figure 57, which is a very common application for this model, the coating layer is not parallel to the substrate at every point. The kinetics of the nozzle head (section 4.2.3), the energy distribution of the jet (section 4.3.2) and the way that the jet will interact with the target material (section 4.3.4) will still be as already explained. However, the geometry of target material has to be defined differently. This section will develop how this was done.

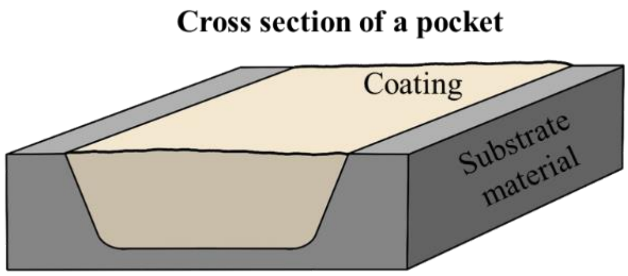

Figure 57: *Schematic drawing of a cross section of a pocket with protective coating*

It is important to understand that when cleaning a surface with pockets the jet will pass over all the sections, no matter if it is just substrate or a pocket (see Figure 55b). This is because stabilizing the jet at the desired pressure takes time and it cannot be switched on and off while in the run. Considering that the optimal coating removal parameters can damage the naked substrate, the jet speed can be changed in each section of the pocket geometry. The definition of the pocket sections is shown in Figure 58:

- **Section A:** Just substrate. This is just the naked material of the part and the damage by water jet must be from minimum to zero.
- **Section B:** The slope of the pocket. This section begins at the start of the pocket slope (P_1). Deeper in the section the thickness of the coating will constantly increase up to P_2.
- **Section C:** Curved section of the pocket. Starting in P_2 this section is a continuation of the section B but instead of the coating layer increasing at a constant rate it increases following the curvature of the pocket.

- **Section D:** Flat area. Starting in P3 this last section is the same as in the original program defined in 4.3 where the thickness is constant. The coating layers here are parallel to the substrate.

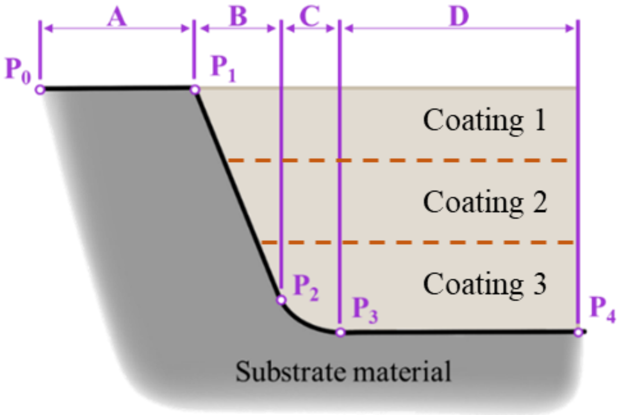

Figure 58: *Schematic drawing of the different sections that compound the transition from exposed substrate (A) material to fully coated area (D).*

This pocket geometry has been parametrized (see Figure 59) and hence the x and y position for each point of the substrate surface has been defined. This will allow to consider the target material: just substrate (section A), a different variable coating thickness depending on the (x) position along the workpiece (sections B and C) and total coating thickness plus substrate underneath (section D).

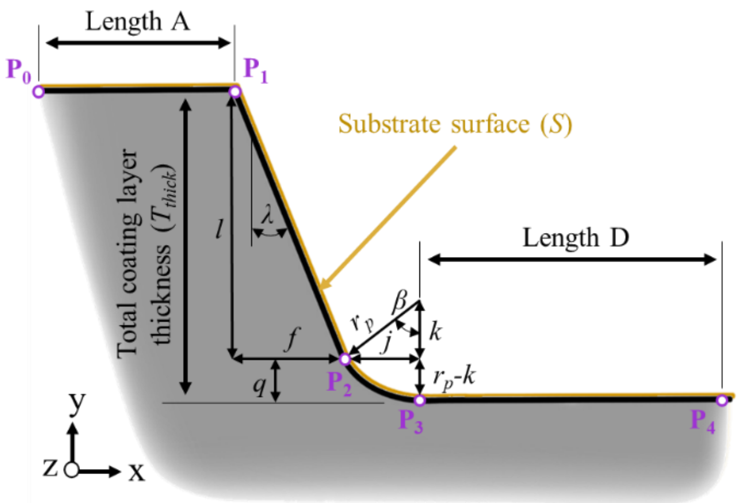

Figure 59: *Definition of the parameters that determine the geometry and dimensions of the sections of the edge of a pocket.*

The total thickness (T_{thick}) is defined by the sum of all the coating thicknesses (i.e. this particularization it is also modelled for any number of defined coating layers as in the model developed in section 874.3) and the slope angle (λ) as well as the curvature radius (r_p) are both known geometry. Then, the geometry points are defined by equation (22) and the section points are defined in equation (23).

$$\beta = 90 - \lambda \qquad q = r_p - k$$
$$j = r_p \times \sin\beta \qquad l = T - q \qquad (22)$$
$$k = r_p \times \cos\beta \qquad f = l \times \tan\lambda$$

$$P_0 = 0 \qquad P_2 = P_1 + f$$
$$P_1 = Length\ A \qquad P_3 = P_2 + j \qquad P_4 = P_3 + Length\ D \qquad (23)$$

The surface mesh generated is then included as the free form surface (S) in equation (18) and the rest of the model continues as previously described from that point on.

4.5. Presentation of the results: street light system

On their own the model results presented in Figure 53b are difficult to understand at first glance. In order to make them more readable and require a lower knowledge level, a street light system has been designed to represent the results. The resultant material has been divided in four groups: i) untouched surface (i.e. surface that did not receive any jet energy) is represented in blue, ii) the target material that has been milled but not enough to have a full coating removal is shown in yellow, iii) the areas that have a full coating removal and undamaged substrate are presented in green and finally iv) the substrate areas that have been damaged are demonstrated in red. When a resultant graph shows any red pixel, the parameters used for the machining are considered too aggressive. If the resultant graph shows a mainly green area with independent yellow or blue islands it means that the removal has been unsuccessful as there is still unremoved coating material, hence the parameters need to be further tuned. Finally, if the graph shows a full green area with just yellow areas in the edges (i.e. taper angle effect) it represents that a full removal of the coating is achieved, so the used conditions are valid. An example with the four jet rotational nozzle, 5 trenches and 75% of overlapping separation at different parameters can be: with a good removal result in Figure 60a and too much removal Figure 60b.

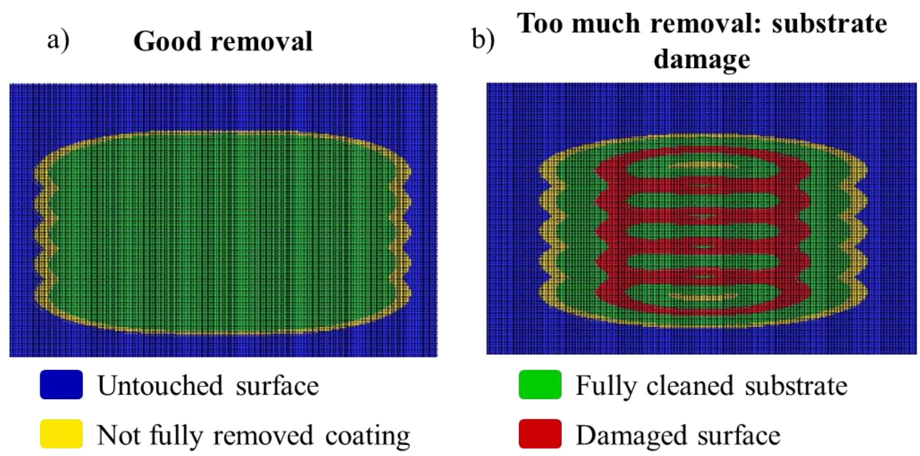

Figure 60: *Example of street light system result representation made with the four jet rotary nozzle, 5 trenches and 75% of overlapping separation a) showing a good material removal and b) too much removal and substrate damage.*

The same has been done with the particular case of the pocket edge. This is depicted in the Figure 61, an example milled with a four jet rotary nozzle, simulating 5 trenches at a 75% overlapping separation. The points (P_n) marked in the figure represent the same sections defined previously in Figure 58.

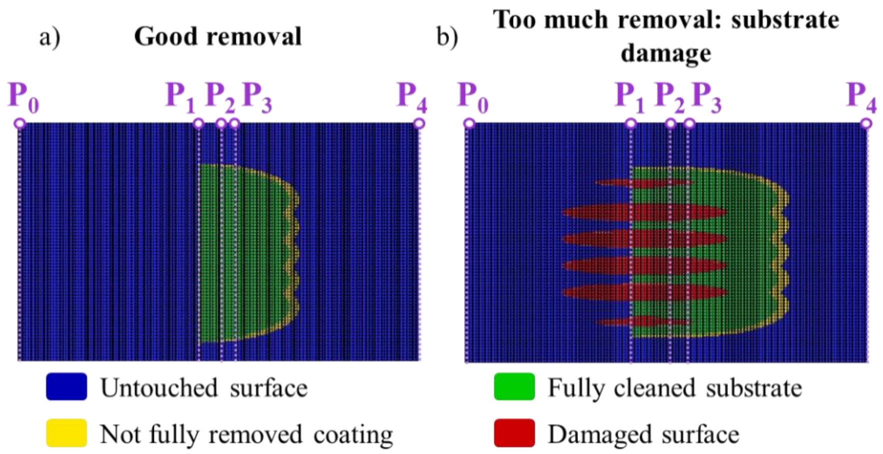

Figure 61: *Example of street light system result representation made with the four jet rotary nozzle, 5 trenches and 75% of overlapping separation in the particular case of the edge of a pocket a) showing a good material removal and b) too much removal and substrate damage.*

4.6. Concluding remarks

This chapter proposes a highly versatile model that predicts the eroded patches (i.e. overlapped jet footprints) produced by rotational plain water jet nozzle heads. This enables a controlled removal of coating used in aerospace systems in a robust manner (i.e. no damage to the substrate and a full removal of the coating). The innovation lays on the fact that this model, unlike previous ones, considering multiple layer coatings and the mechanical properties of each of the individual layers. Mathematically it is based on the understanding of the etching rate (i.e. calculation of the depth of material that has been removed).

First, the flows of both considered nozzle heads (i.e. four jet rotational and fan jet nozzles) as well as their kinetics have been calculated, followed by the definition of the energy model of a Plain Water Jet (PWJ) system. The energy model is defined by the energy distribution of a rotary jet for an arbitrary trajectory in a 3D space, pursued by the characterization of the target material considering an arbitrary number of coating layers. Finally, the interaction between the jet and the target material has been defined. This interaction is obtained for any specific pressure, considering the energy variations along the height of the jet, for one or multiple jets, which follows a defined arbitrary trajectory, during a defined period of time. However, a calibration data will still be needed to include the individual material mechanical properties.

Afterwards, the model has been upgraded for calculating single and multiple trenches that are able to overlap, flat and curved surfaces and calculation of the milling time for flat and rounded parts. Finally, the particular case of the edge of a pocket section has also been studied considering that in this example the coating is not always parallel to the substrate layer.

Chapter 5

Development of the Software to apply the mathematical model in an industrial environment

In order to viably use the model in an industrial application a functional and easy to use interface is necessary. This chapter explains the construction of the designed software (SW) application developed in MATLAB AppDesigner with this aim. For this section a set of parameters has been selected as an example and the program has been simulated so the reader will be guided step by step through the parameter setting, calculation process and results analysis while using the program.

5.1. Introduction

With the aim of implementing the model in an industrial environment an application has been developed in the AppDesigner of MATLAB with a user friendly interface. It is not only easy to set the modelling parameters, but the results are clearly presented. At the end of the program a document is generated in order to have a simulation record. The application can be installed in any computer with an installation package and an executable file is created.

The App is organized in six tabs organized by usage order (Figure 62): (1) Input parameters, (2) Calibration coefficient calculation, (3) Results: Energy map and milled trench, (4) Results: Understanding coating removal, (5) Results: (Pockets) Milled trench and coating removal, (6) Unit converter. Due to the page width limitations some of the details of the tab figures are not easily readable, Annex A shows them in a full page size.

To showcase the model in this chapter an example run has been made in a flat sample with a two layer coating on top of a substrate. It simulates the milling with a four jet rotary nozzle with four 1.5 mm nozzles each located at an 8, 10, 9 and 8.5 mm radius from the centre with the parameters defined in Table 4:

Table 4: *Definition of the parameters used in the run to show the app as an example.*

Parameter	Value	Unit
P	300	MPa
SoD	20	mm
V_t	1500	rpm
V_r	600	Mm/min
Running time	12	s
	Overlapping trenches	
Quantity	5	-
Separation	75	%
	Top coat	
Thickness	5	mm
	Bond Coat	
Thickness	0.1	mm
	Substrate	
Thickness	5	mm

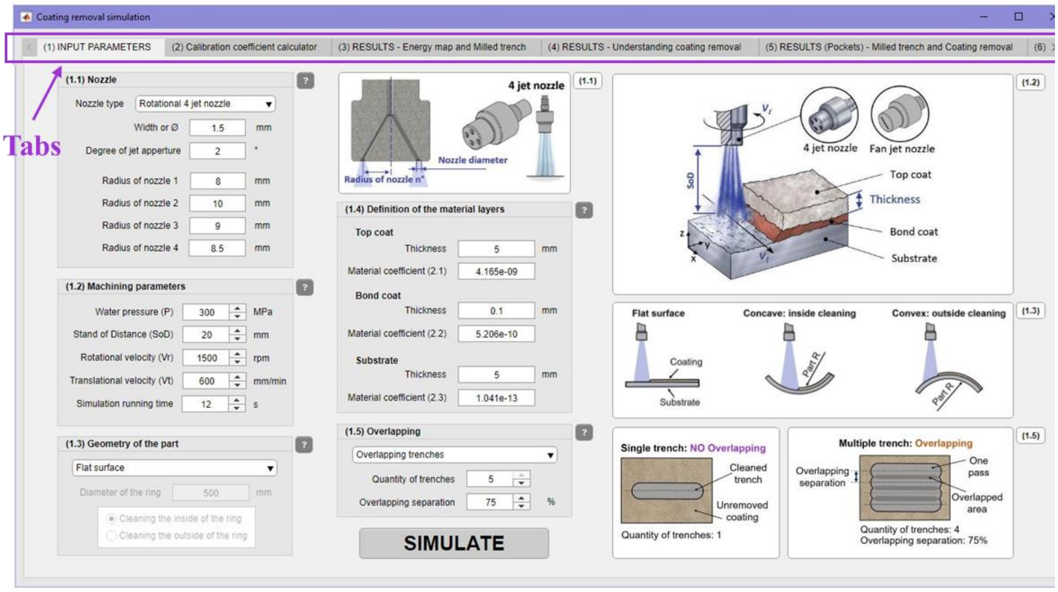

Figure 62: *View of the first tab "Input parameters" of the software and the presentation of the navigation panel to move from tab to tab.*

5.2. Structure of the designed application

5.2.1. (1) Input parameters

The "Input parameters" tab (Figure 62) can be considered the main page of the software (SW) as it is where all the conditions for the simulation are defined. It is the starting point for all the software and an indispensable step to be able to use the rest of the app. The window is divided in five sections depending on the aspect that needs to be characterized: nozzle, machining parameters, part geometry, overlapping and material layers.

The nozzle segment (Figure 63) has all the necessary parameters to completely define the geometry of the nozzle and the jets. It is possible to select between two types of nozzles (rotational four jet or fan nozzle, both defined at section 4.2.2), and the required input parameters are adapted accordingly. For the four jet nozzle (Figure 63a), the diameter of the jets and their aperture angle needs to be assigned, together with the positional radius of each jet respective to the nozzle rotation axis. On the other hand, for the fan nozzle (Figure 63b) only the width of the fan and the aperture need to be specified. A figure has also been added next to the parameter definition area to help with the understanding of the meaning of each parameter.

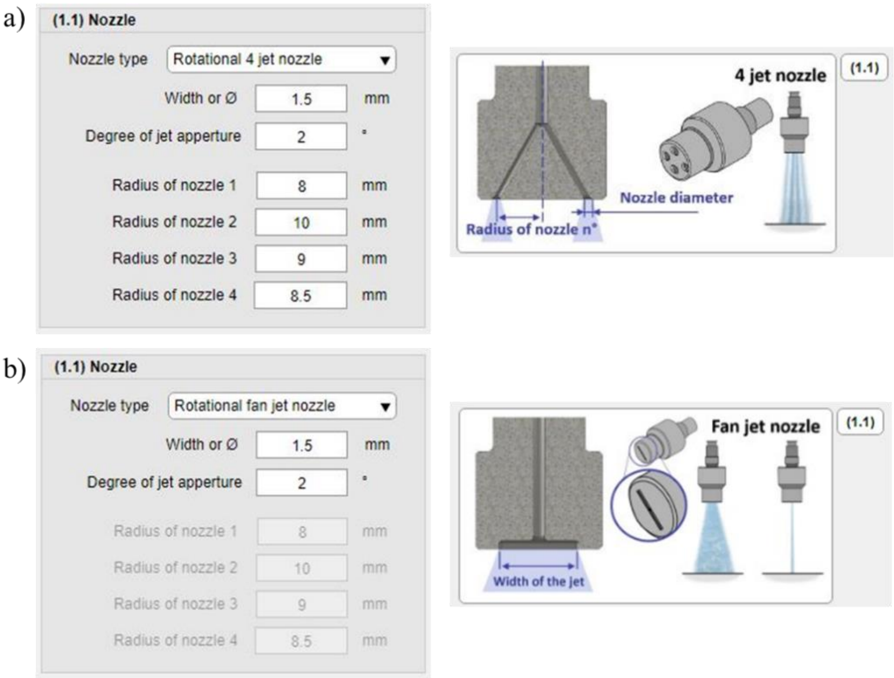

Figure 63: *Nozzle definition segment of the Input parameters window showing the necessary parameters to characterise a) the rotational 4 jet nozzle and b) the fan jet nozzle, with their respective figures showing the meaning of each parameter.*

Having selected the nozzle parameters, the next step is to define the machining conditions (Figure 64). These are the variables that represent the machine that is being emulated and the conditions that want to be simulated to obtain an estimation of the material removal. On the one hand, there is the water pressure which is defined (and also limited) by the pressure range of the water pump of the machine. On the other hand, there are the parameters determining the relative position of the jet and the workpiece which are the usually tuned variables to simulate different conditions as well as the SoD and both translational (V_t) and the rotational velocities (V_r) of the rotary nozzle heads. Finally, the simulation running time is defined to control the length of the simulation. If the translational speed is high, the jet will travel a further distance, so less simulation time will be necessary, while for low speeds the time will need to be increased to achieve a considerable trench. It is key to control this parameter and just simulate the necessary t in order to have meaningful simulations as it increases the computational time considerably.

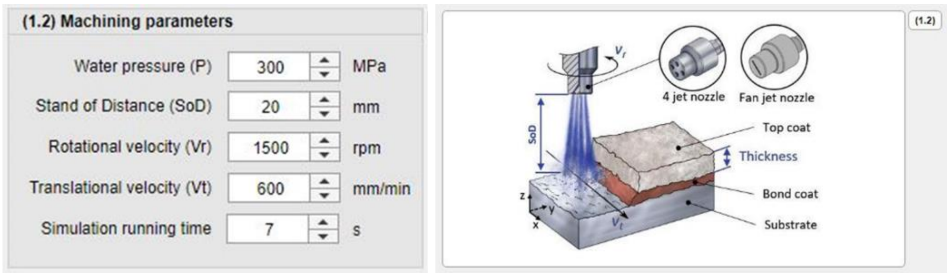

Figure 64: *View of the "Machining parameters" section for defining the machining conditions for the simulation, with a representative image of the variables.*

Next in line is the determination of the workpiece and its geometry (Figure 65). Two geometrical options are available for selection, flat workpiece and curved workpiece, which can be used to represent three machining conditions depending on the surface where the coating is placed on the curved part. For a flat workpiece (Figure 65a), no other variable is necessary, whereas for the curved (Figure 65b) a selection must be made to define if the coating is in the inside or outside of the curvature, and the diameter of the part needs to be entered. Once again, an example of each type of workpiece is visually represented next to the variable input boxes. If there is the need to analyse other type of geometries or free forms this needs to be addressed in the code itself.

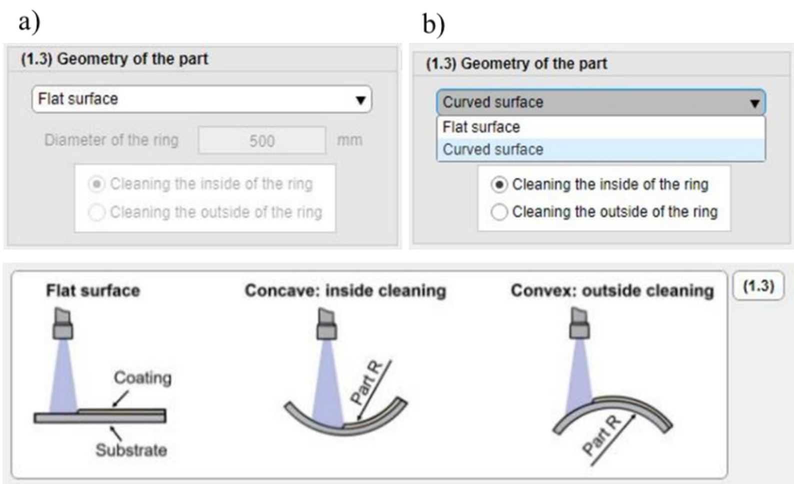

Figure 65: *Section of the "Input parameters" tab to define the type, geometry and position of the coating for the workpiece together with figures representing a) a flat surface and b) a curved surface with both options of cleaning inside or outside the ring.*

Apart from the parameters that previously defined the speed of the jet, another consideration must be done depending on how many trenches want to be simulated (Figure 66). Having a single trench (Figure 66a) will generate an individual line that will represent the material removal with a single pass of the jet. On the other hand, having multiple trenches (Figure 66b) it is possible to simulate the effect of passing the jet multiple times on top of the same workpiece area (i.e. effect of jet overlapping). The quantity of trenches can be tuned, with a maximum of five, as it is considered that increasing that number further will not give additional information but can be increase the computational demand. Furthermore, the overlapping separation is given in percentage as the width of the jet will depend on the previously set parameters. An overlapping of 0% will result on the jet passing exactly on the same line, while a 100% or higher separation will generate two parallel trenches not touching each other.

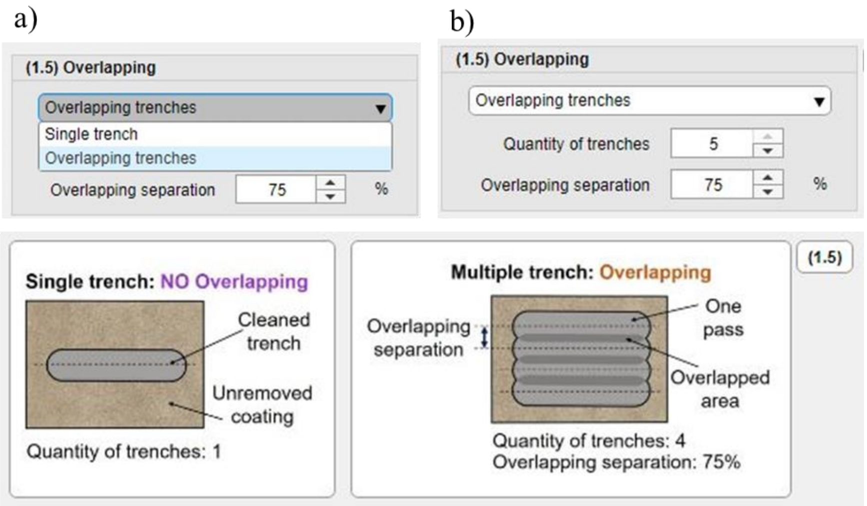

Figure 66: *Segment with the required variables to define the quantity of trenches to simulate a a) single trench and b) multiple trenches and their overlapping percentage. The two images visually represent the difference between having a single or multiple trenches and the meaning of the variables.*

Finally, the last parameters to be defined are the material properties, the thicknesses of the workpiece and the coating layers that need to be simulated. Three sections are divided to consider each material of three layers of the workpiece independently (coating layers are defined in Figure 64): the top coat, the bond coat and the substrate. The thicknesses will be given by the part that is being emulated while the material coefficients will be specific for each material.

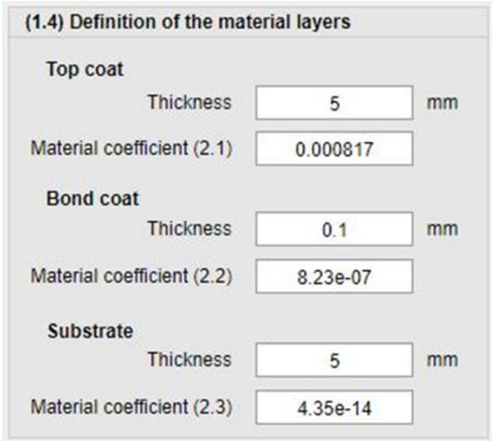

Figure 67: *Definition of the thicknesses in mm and the material coefficient value for each of the coating layers, in where the material coefficient is calculated from calibration data.*

The material coefficients can be calculated using the calculator on tab (2) Calibration coefficient calculator. These need to be calculated using calibration data the first time a material is used, as it is material dependent, but once the coefficient is known for a particular material it will be the same for any other simulation and any other set of parameters.

5.2.2. (2) Calibration coefficient calculator

The Calibration coefficient calculator is a tool that needs to be used the first time a new material must be simulated. By using some calibration data obtained from simple experiments, it provides a coefficient that represents the mechanical properties of the material. This coefficient is a unitless metric that determines the relation between the energy that is focused against the material and the removal rate achieved, so it is independent of machining parameters and type of jet (e.g. single, four jet, fan jet nozzle etc.), and will be representative for any conditions. Furthermore, as each material has its own independent coefficient, it will allow to consider coatings with many layers, and calculate the material removal depending on the energy arriving to each layer and their coefficient.

To calculate the “material dependent calibration coefficient” the following steps will need to be followed in order to generate the required information for the calculator:

1. To begin with, a straight single jet trench with known machining parameters needs to be milled in the material to be analysed with PWJ machine. It is important to ensure that the full depth of the trench is performed in a uniform area throughout the thickness of the material.

2. The parameters used to carry out the trench need to be introduced in the "machining parameters" section of the software: water jet pressure (P), Stand of Distance (SoD), translational velocity of the jet (V_t) and the diameter of the nozzle.

3. The "trench depth" of each material needs to be measured by direct measurement, (i.e. by preparing a micrograph and measuring in a microscope or by scanning the surface with a surface scanner), and the value of the deepest point of the trench has to be set in the "measured value" section (see Figure 67).

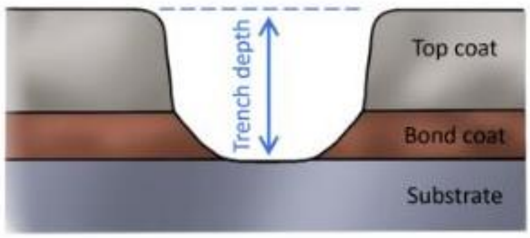

Figure 68: *Definition of the trench depth that needs to be measured for the calibration.*

4. Finally, clicking on the "Calculate" button of each coating layer the "material dependent coefficient" is calculated. When doing this the value will be automatically saved in the corresponding square of the "(1.4) Definition of the material layers" section from the "(1) Input parameters" tab.

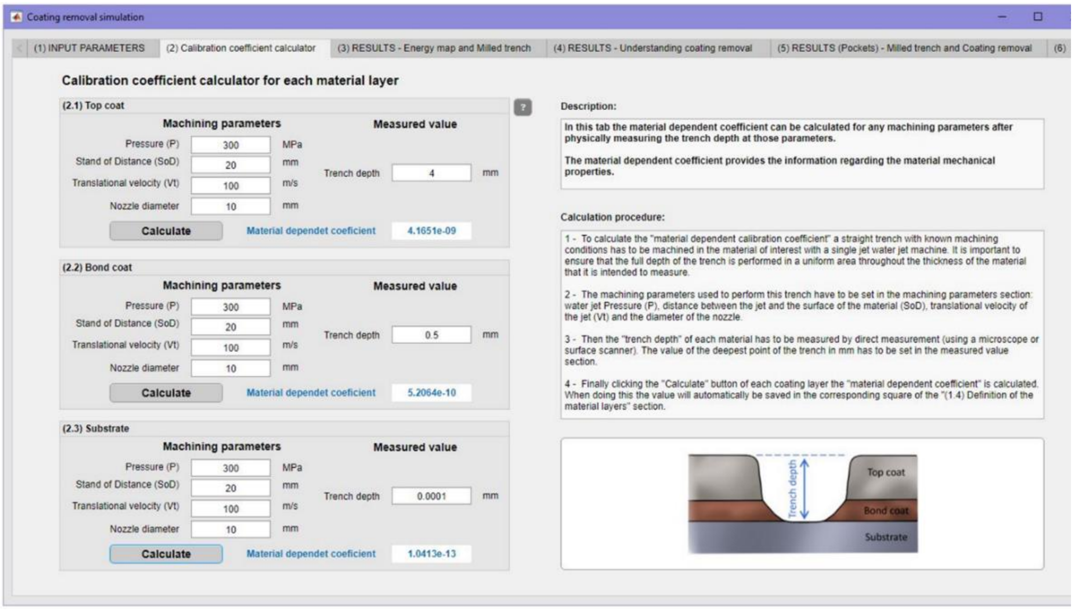

Figure 69: *Representation of tab number 2: Calibration coefficient calculator to calculate the material dependent coefficient for each layer from calibration data obtained from a single jet trench. The procedure for the calculation is also presented, together with a representative picture of the layers and the trench.*

By using this tool, a library could be created containing the coefficients of all the used coating materials. If these values are recorded, in the future no more calibration tests will be needed for known materials and they could be used for any machining conditions.

To make the software more accessible to new users, information pop-ups (Figure 70) have been implemented that appear when a figure is clicked so it explains the meaning of the image.

Figure 70: *Example of a pop-up that appears when the user clicks on an image, with an explanatory description of what is shown in the figure.*

Furthermore, a small button with a question mark (Figure 71) has also been added next to the variables, this will open a pop-up with the description of the required parameter.

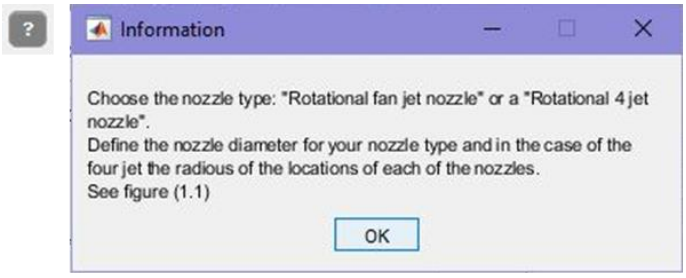

Figure 71: *Example of a button with the question mark that is located next to the variable input boxes, and the pop-up that appears with a description of the parameter.*

Finally, once all the parameters have been introduced to the software, at the bottom of the "(1) Input parameters" page the "Simulate" button can be found (Figure 72). Pressing this button will start the calculation process which will take some time. To avoid pressing the button many times and show the user that the software is working, this button has been set to grey out and the text changed to "Calculating…" when pressed.

Figure 72: *Simulate button at the bottom of the "Input parameter" tab to run the calculation, and the alternative version to show when the program is running.*

5.2.3. (3) RESULTS – Energy map and milled trench

The third tab of the software is the first window showing the actual results of the simulation and until the simulation is run it does not present any graph. As it can be seen in Figure 73 it has two main plots: one for the energy map results on the left, and the other for the resultant milled trench.

The energy map graph presents the raw output from the energy calculations that explain the total energy where the jets have passed. It considers the path that the waterjet has taken and the resultant energy in Joules (J) that reached each point (x, y) of the target surface is calculated. The x and y directions of the plot represent the length and width of the sample, while the z axis is the energy value. In this example it can be seen that the energy in the middle sections of the trench is higher due to the overlapping of the trenches, but this does not yet mean anything (i.e.

regarding the effect on the material) as the material properties have not been considered.

The milled trench graph shows the result of applying the energy of the jet onto the material properties of the coating and substrate. By using the material coefficients and the geometry of the workpiece, it calculates the quantity of material removed and the resultant footprint left on the workpiece. This can be considered the raw result of the simulation which already represents the behaviour of the workpiece with the defined machining conditions, but the readability is very limited. In this particular case, it seems that the jet has removed all the material where it passed, but it is very hard to assess at first glance if the substrate has been damaged or if small thin patches are left.

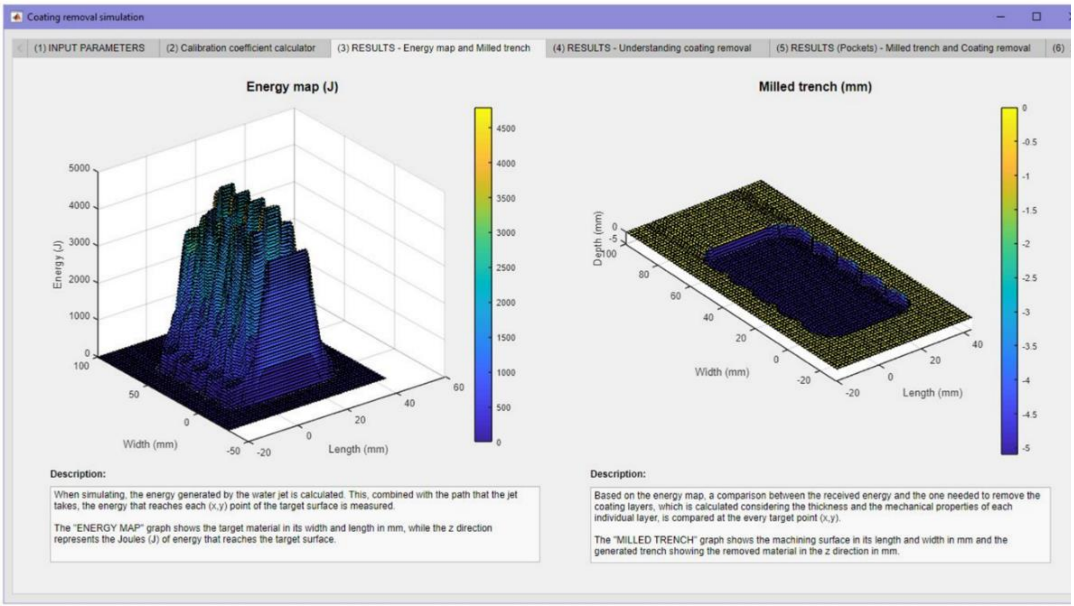

Figure 73: *Representation of tab 3: Resultant preliminary graphs from the total energy calculation on the left and the resultant milled trench on the right, with a description of the meaning of both plots under them.*

5.2.4. (4) RESULTS – Understanding coating removal

In order to have a better understanding of the energy map and milled trench results a *street light system* graph (explained in the section 4.5.) it is calculated. This will allow to clearly represent and easily understand the depth of the resultant workpiece surfaces. As it is shown in Figure 74, the same data from the previous milled trench has been used but this time the top view has been selected and the colour system has been adapted. The blue colour represents the untouched surface, so every point around the trench that has not been affected by the water jet has this colour. The yellow parts show areas where the coating has not been fully removed. In this case it can only be seen at the edges of the trench due to the taper effect so it can be considered as valid. Marked in green is the area that has had all the coating well removed, and furthermore, as no red segments are seen it can be concluded that the substrate has not been damaged. Apart from this, a header on top of the image that has considered the values from the graph, also shows a text saying that the parameters have given a "Good removal", confirming what can be seen with the colour code. Furthermore, the error allowance for over-removal of the substrate material (set by Rolls-Royce) is also shown, which is not changeable as it comes from quality limitations but is a necessary piece of information.

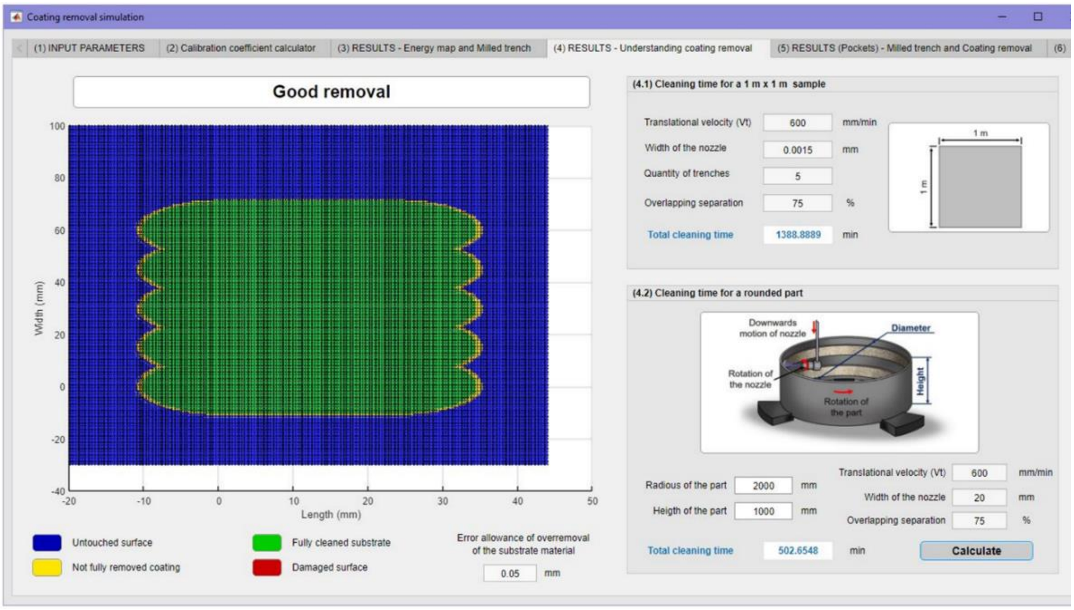

Figure 74: *Representation of tab 4: Material removal results represented with the street light method to clearly identify untouched surface (blue), not fully removed coating (yellow), fully cleaned substrate (green) and damaged surface (red). The calculators to estimate the time needed to remove the coating from the two most common coated parts are also shown.*

Additionally, this tab also has two more calculation tools that estimate the approximate time needed to clean the most common types of workpieces with the selected parameters: a one square meter flat workpiece, and a rounded part with dimensions defined by the user.

5.2.5. (5) RESULTS (Pockets) – Milled trench and coating removal

To consider the particular case of the coating removal on the edge of a pocket, where the geometry of the workpiece is different and the coating layers thicknesses change, an additional tab has been added (Figure 75). This tab requires some more inputs to define the sections that determine the geometry of the pocket to be analysed: length of section A, slope of section B, radius of section C and the length of section D. As the jet will be passing over uncoated parts of the workpiece (section A), the velocity at each section can also be adapted to avoid damaging the substrate. This page has its own "Simulate" button as it might not be necessary to run it every time, but it still considers the parameters from the "Input parameters" tab. For the parameters used in the example run see Table 4 and Table 5.

Table 5: *Definition of the parameters used in the calculation of the pocket section in the run to show the app as an example.*

Parameter	Value	Unit
Length A	15	mm
Slop section B	30	°
Radios section C	2.5	mm
Length D	15	mm
	Continuous velocity	
V_t	600	Mm/min

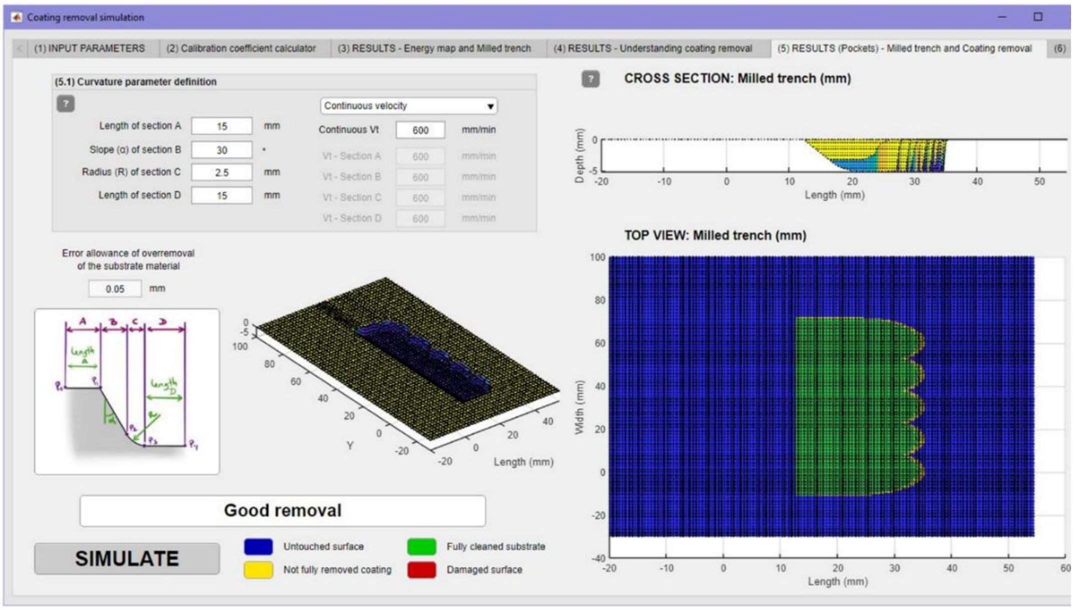

Figure 75: *Representation of tab 5, calculation and results of the particular case in where the edge of the pocket is studied.*

The results in this page are shown in three ways: an isometric view of the raw trench as a preliminary graph, a cross section of the trench to see the geometry of the substrate and the coating removal, and finally a top view with the street light system together with the text box where the assessment of the removal quality is given. In this case the results show that the removal has been well done along the pocket, and no damage has been induced to the substrate in either coated or uncoated sections.

5.2.6. (6) Unit converter

The final tab shown in Figure 76 presents a basic unit converter with the main units relevant to the model. This tab is organized in four simple sections: pressure, translational speed, length and angle and rotational speed. To convert the value has to be written in the relevant section and then proceed to calculate.

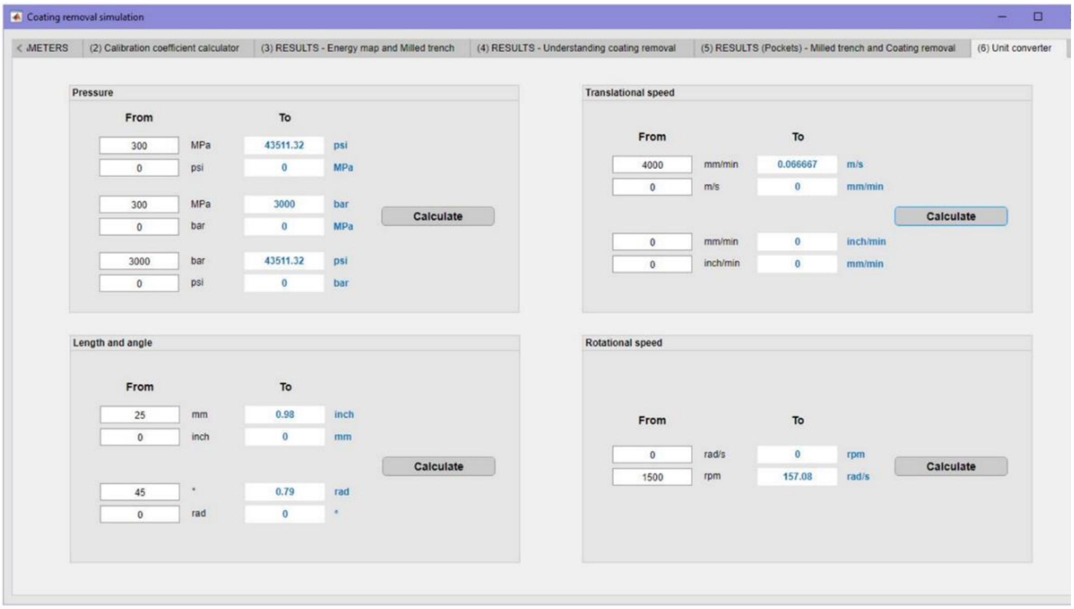

Figure 76: *Tab (6) Unit converter with the units relevant to the model organized in four sections: pressure, translational speed, length and angles and rotational speed unit converters.*

Finally, once that the simulation is finished the SW will generate a pdf report summarizing the used parameters and the obtained results, so it is easy to keep track of all the calculations made.

5.3. Installation of the software

To install the SW "MATLAB runtime" is needed which is an official for free SW from MATLAB that is specially designed to be able to run MATLAB executables without having a MATLAB licence.

To install the SW an executable with an internal launcher has been created so the first time that the SW is executed the MATLAB runtime is installed automatically.

5.4. Discussion on the software's functionality

Having an interactive UI provides the user with a tool that is both easy to instal and use making the program more approachable for an industrial environment. This makes it ready to be used by non-experts that do not need to know the details of the coding in order to be able to use the program and understand the results.

The model has been tested in a small scale by Rolls Royce users in a factory environment and the feedback was positive. The small changes suggested by the technicians such as the implementation of a case study for the pocket areas, a possibility print or save the results in a pdf document and have a unit conversion table where all successfully included. Nonetheless, the model even if it has plans to be used in the future in further applications in the company by the time of publishing this document it does not have a launch date yet.

However, while the implementation of a user interface (UI) brings significant advantages, it also comes with certain inherent limitations that deserve consideration:

- **Limited nozzle addition flexibility:** the current UI design does not permit the seamless addition of new nozzles directly from the interface itself. In the event that a new nozzle type is required, the conventional approach involves manual coding of each unique nozzle into the raw codebase.
- **Control over part and mesh sizes:** Although adjustments to both part size and mesh size are straightforward when directly modifying the raw code, these essential parameters are not conveniently accessible through the UI. Inadequate selection of these parameters within the UI could potentially lead to errors or even an undesirable increase in computational processing time.
- **Capped coating layers:** The UI imposes a constraint on the number of coating layers that can be applied, limiting the options to a maximum of three layers. While this may be enough for many scenarios, certain applications might necessitate additional coating layers that, unfortunately, cannot be accommodated within the current UI framework.
- **Predefined nozzle path restrictions:** The UI's capabilities in defining nozzle paths are limited to parallel lines, which is the optimal cleaning path for the type of applications addressed in this thesis. However, if future use cases demand alternative nozzle path strategies (e.g. zig-zag, spiral milling,

etc.) their implementation would have to be made by custom coding within the application's codebase.

- **Overlapping trench limitation:** To ensure efficient computational processing, the UI has been engineered to accommodate a maximum of five overlapping trenches. This restriction is essential for maintaining acceptable performance levels within reasonable timeframes.
- **Geometric constraints:** The geometries available in the UI are a flat plate and a concave or convex surface. If a different shape needs to be analysed (e.g. spherical, parabola, slope or even a free form) it would require to be included from the raw code.

As part of a proposal of future work, conducting a user conformability test is encouraged, ensuring that any necessary improvements to the UI features are identified and addressed.

5.5. Concluding remarks

This chapter describes the implementation of a user’s friendly interface to the model developed in Chapter 4. This is necessary in order to be able to use the model in an efficient way in an industrial environment. The highlights of the applications are described as follow:

- The app is design to be able to choose between a four jet and fan rotational nozzle head, flat or curved samples that could be cleaned from the inside or outside and to choose if a single trench or multiple trenches will be simulated with different degrees of overlapping.
- The software has an attractive design that guides the user step by step through the tabs that are organized in a sequential order: the input parameters are required in the first place, followed by the presentation of the results and the particular case is shown at the end.

- Elements that help the user navigate the application have also been implemented in the SW such as the descriptions in the questions marks and further details when clicking the images. These elements help make the interface more accessible.
- The overall results of the simulation (i.e. the energy map as well as the milled trench) are showed in the UI app. However, for an easier interpretation of the results, these are shown with a four colour system that indicates if the coating has been fully or partially removed or if the substrate has been damaged. Moreover, a feature that calculates the time to clean a 1 m^2 plate as well as defined dimension rounded part has also been included.
- The option to generate an automatic pdf report is asked. Thanks to this is easy to keep track of the performed simulations over the time.
- Finally, while the UI implementation offers numerous benefits, it presents certain limitations too: new nozzle addition requires manual coding, part and mesh size adjustments are only feasible through raw code modification, a maximum of three coating layers are allowed, nozzle path options are restricted to parallel lines, five overlapping trenches is the computational limit, and the UI confines analysis to specific geometric shapes, necessitating manual code inclusion for more diverse shapes. As future work, user conformability test is encouraged, ensuring that any necessary improvements to the UI features are identified and addressed.

Chapter 6

Assessment of material removal capabilities of the developed mathematical model

A model is only valid if it is proven to be representative of what is observed in the real life tests. In this chapter the validation of the mathematical model is demonstrated using both nozzle heads in test samples. Afterwards, to prove it in a real case application in an industrial environment, a test that consists in successfully cleaning a combustion chamber with coating strips in Rolls-Royce facilities is described. Finally, a study in order to further understand the material removal mechanism is discussed.

6.1. Mathematical model validation in a controlled sample

To ensure an accurate simulation of the model a small scale validation has been done for both rotational nozzles (i.e. rotational four jet and fan nozzles) in controlled samples. For this the simulated data from the model and trenches performed in the University of Nottingham 3 axis micro waterjet from WATERjet AG have been compared.

6.1.1. Four jet rotational nozzle head model validation

In the particular case of the four head rotary nozzle, the chosen workpiece material for the model validation is a square piece of 150×150 mm with a 100 mm curvature radius. It is covered in a coating formed by two different material layers plus the substrate, shown in Figure 77. The aim of the procedure is to remove the coating layers without damaging the substrate. In this case, as no abrasives have been used k (i.e. sensitivity of the target material to the erosion tool, equation (19)) is assumed to be 1.

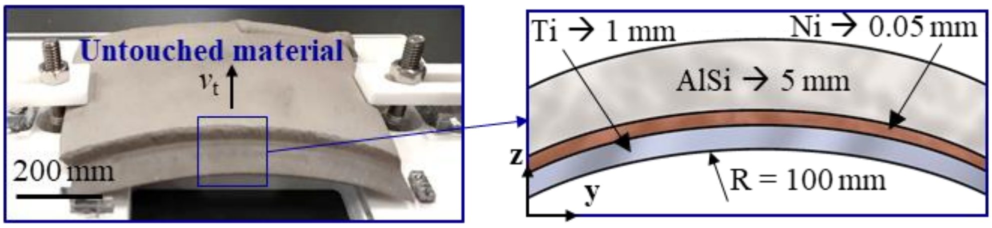

Figure 77: *Experimental setup and description of the geometry and material details of the coating and the substrate of the trial material.*

The relationship between the maximum eroded depth and the energy at this point (C) (see (24)), has been calibrated for each material by milling a single straight trench at a constant P of 300 MPa and 20 mm SoD and a fast v_t of 1020 mm/min.

$$C = {E_{space}(r)_a}^{1} / U(r) \qquad (24)$$

For which: $r = 0 \rightarrow U = U_{max}$

Knowing the maximum energy and depth at these conditions, which for a straight trench will be at the centre, the material dependent C value is obtained for each material layer of the coating system. As it is a PW system the value will be constant for any speed. The characteristics of the material coating layers and its coefficients are presented in Table 6.

Table 6: *Description of the properties of each of the materials used in the model validation example.*

Layer	Material	Thickness (mm)	C
Top coat	Thermally sprayed AlSi	6	0.27
Bond coat	Thermally sprayed Ni ally	0.15	0.02
Substrate	Ti alloy	2	4.3×10^{-6}

The four jet rotational nozzle head rotates around its z axis (rotational position defined by (β) and is based on the angular velocity (α) and is moving at a translational speed (v_t) in x direction. The combination between the translational (v_t) and rotational (v_r) speeds will define the resulting trajectory (equation (25)), but also the overlapping points (see Figure 78) generated by crossing the jet paths, which is a key indicator to ensure the desired removal ratio (e.g. if the relation is not correct, unremoved material will be present).

$$\begin{Bmatrix} X_i \\ Y_i \\ Z_i \end{Bmatrix} = \begin{Bmatrix} \mathrm{R}_i \cos\beta \\ \mathrm{R}_i \sin\beta \\ 0 \end{Bmatrix} + \begin{Bmatrix} v_t\, t \\ 0 \\ SOD \end{Bmatrix} \quad (25)$$

For which: $\beta = \alpha + n_i\gamma \qquad \alpha = v_r\, t \qquad \gamma = {}^{2\pi}/_{n}$

As for the experiments, the milled trenches have been carried out at a pump pressure (P) of 300 MPa, a rotational speed (v_r) 1500 rpm and a SoD of 20 mm as the minimum height. The tests had been carried up out in a three-axis micro waterjet machine (Waterjet AG, Switzerland) equipped with a high pressure pump (P_{max} 400 MPa). The tests included a sweep of transversal velocities (v_t), from 60 mm/min to 1020 mm/min, in 16 equidistant steps of 5 mm. Moreover, a rotational multiple plain water jet nozzle (AQUARESE) has been used with the set up and nozzle geometry specified in the Figure 78. The simulated trenches have been modelled in MATLAB while the milled trenches were analysed on a surface scanner

(Alicona G4). Energy Dispersive X-Ray (EDX) analysis has been performed in a Scanning Electron Microscope (FEI Quanta600 MLA SEM).

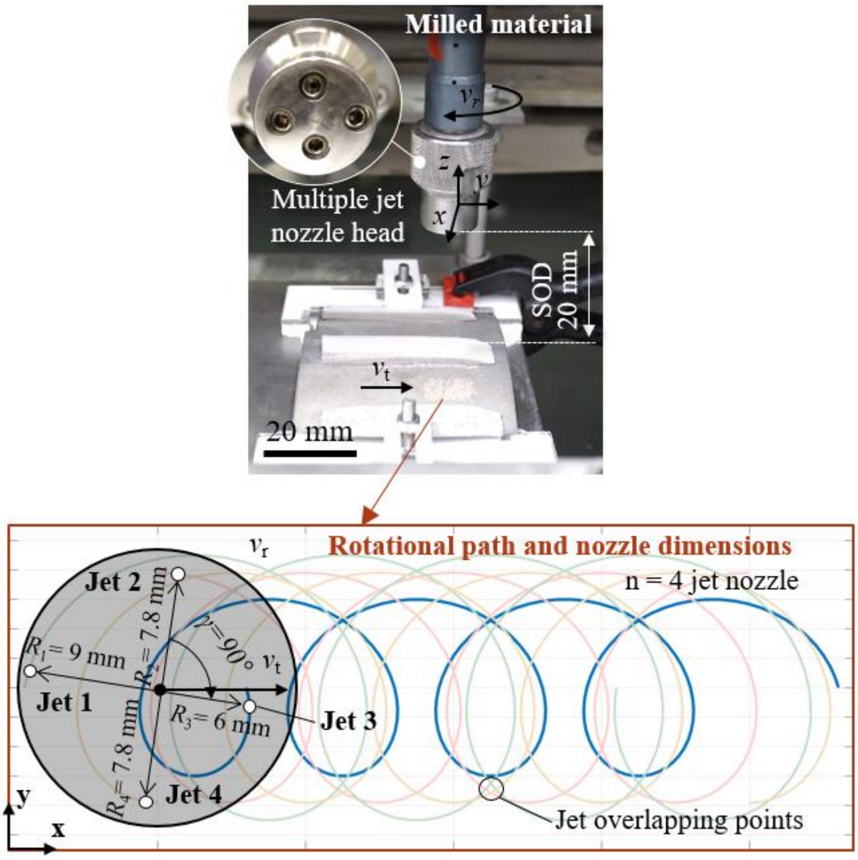

Figure 78: *Experimental setup showing the four jets nozzle head, the two layers coated annular component and the trajectories of the centres of the four rotational nozzles caused by a linear movement of the head.*

To compare and validate the proposed model with the milled trenches, three distinct speeds have been selected. These velocities include a deliberately slow speed (v_t = 60 mm/min), known for excessive milling, a moderate speed (v_t = 660 mm/min) anticipated for optimal milling, and a notably fast speed (v_t = 1200 mm/min) expected to result in not enough material removal for optimal milling. These choices ensure that the proposed model's performance can be thoroughly compared and validated against milled trenches, offering a full representation of potential outcomes.

On the one hand, the mathematical model has been run using the UI described in chapter 5. As a new material has been milled the "material dependent calibration coefficient" had to be calculated first (i.e. C_m and K_m described in chapter 4), which is to say, the calibration of the model with the material of interest was performed. Firstly, a precisely fabricated single jet trench was generated within the material of interest using the three axis Water Jet uniformly across the material's thickness. The distinct parameters utilized for the trench, encompassing water jet pressure (P), Stand of Distance (SoD), translational jet velocity (v_t), and nozzle diameter, are considered as well as the depth of the trench is directly measured using the surface scanner to obtain the utmost depth point of the trench. These parameters are used to calculate the etching rate (U), described in equation (19). In the UI these parameters are recorded in the “machining parameters” and “measured values” tab and ultimately obtained upon activating the "Calculate" function for each coating layer. This resulting value is then automatically recorded in the corresponding location within the segment designated as "Definition of the material layers" under the "Input parameters" category.

On the other hand the plot for the real trench is obtained from an averaging of 200 profiles obtained from a 5 mm trench, and both the maximum and minimum values are considered (i.e. it encompasses the whole experimental area). Both the modelled and experimental trenched are compared in Figure 79.

Considering that water jet milling is a time dependent process, a faster speed means that less energy will reach the surface of the target and hence the etching rate will be lower. The comparison between a simulated and experimental trench at v_t = 60 mm/min is carried out in Figure 79a. At this milling speed the coating layers have not been fully removed from the substrate. The unremoved coating in the centre is caused by the fast milling transversal velocity that prevents to have enough overlapping points to remove all the coating, which the model is able to predict with a 0.28 mm (4.5 %) of error maximum on the unremoved coating areas and 0.07 mm (1.2 %) in the cleaned ones. On the other hand, the unremoved coating in the corners is due to the lack of energy to remove the coating but also caused by the additional removal mechanism (e.g. crack growth); at this point the error gets up to 27 %. At

v_t = 660 mm/min (Figure 79b) there are no residues in the centre of the trench but still some in the corners; as the model also suggests. In the areas where the coating is fully removed the maximum error is as in v_t = 1020 mm/min whereas in the unremoved coating areas the prediction error decreases to 0.19 mm (3.1 %). Finally, the comparison of the profiles at lowest speed is shown at Figure 79c and at these conditions the coating layers are fully removed without damaging the substrate with a maximum error of 0.08 mm (1.3 %).

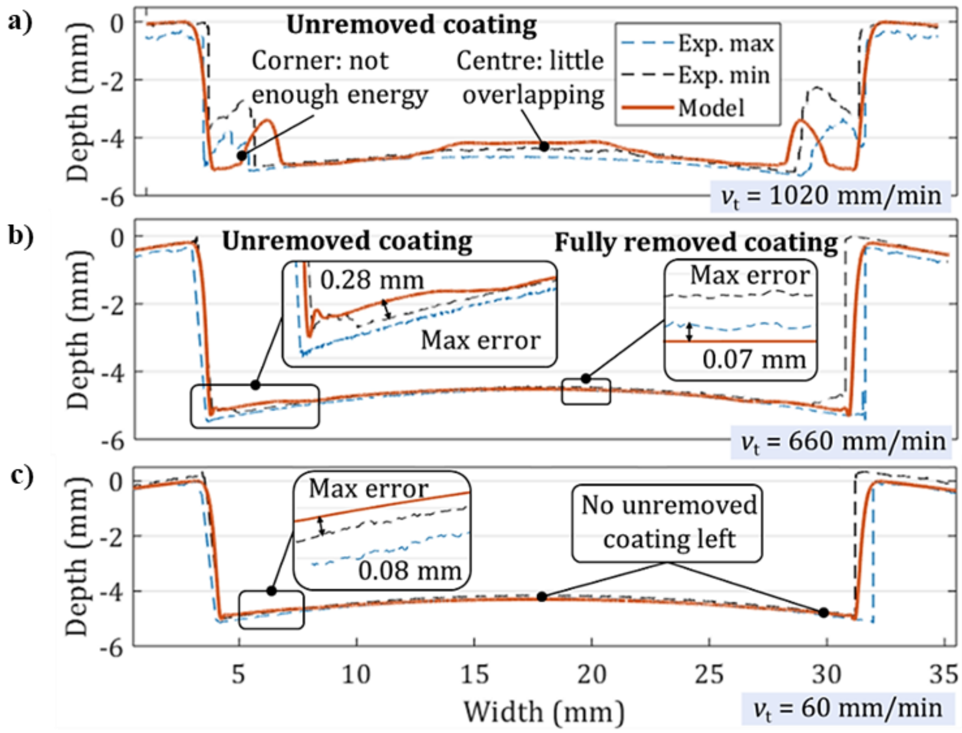

Figure 79: *Comparison of the simulated and the milled trench at a range of transversal velocities (vt): a) 1020 mm/min, b) 660 mm/min c) 60 mm/min.*

For a better identification of the unremoved coating and to ensure no damage of the substrate, the 3D scanned and predicted surface of the slowest trench at v_t = 60 mm/min and the fastest one at v_t = 1020 mm/min are compared (Figure 80). The first one (i.e. left) shows a perfectly cleaned surface with a clear division between the untouched coating and the substrate as seen in the EDX. For the v_t = 1020 mm/min milled trenches (i.e. right) bond coat residues are not fully removed. In the EDX map is demonstrated that on the edges of the trench, as predicted in the model, a 0.48 μm band bond coat is unremoved whereas in the centre bond coat islands are still present.

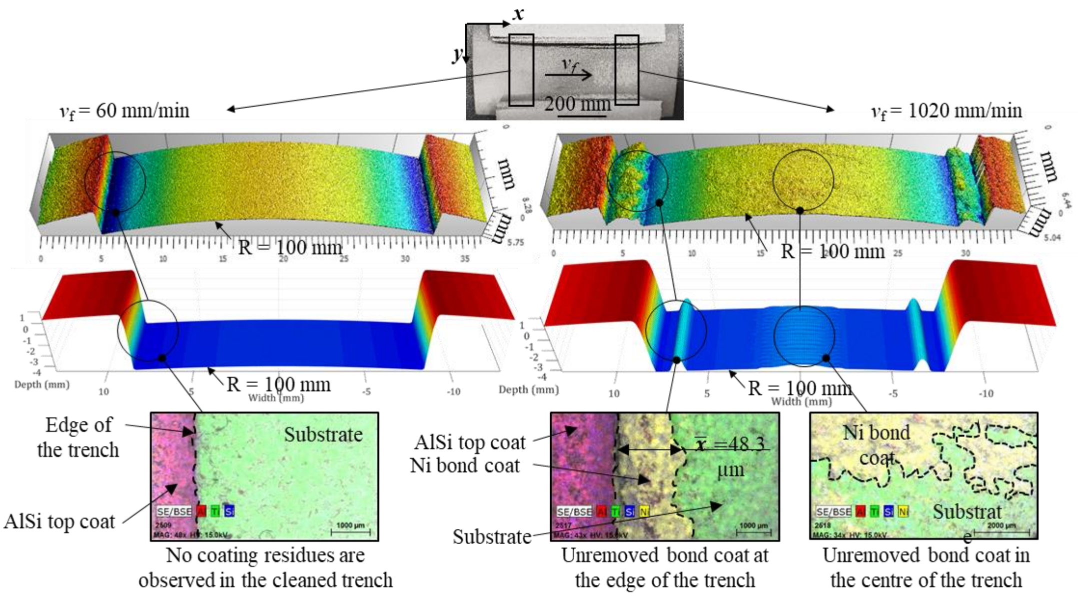

Figure 80: *Comparison between two example trenches one at vt = 60 mm/min, in order to ensure a full cleaning of the trench and the other at vt = 1020 mm/min to show the accuracy of the model when predicting preserved coating bits along the trench. The experimental and simulated trenches are shown, as well as EDX analysis to identify the coating layer and zones where it has not been removed.*

6.1.2. Fan jet nozzle model validation

For the validation of the fan rotary nozzle head a different approach has been considered in order to prove other aspects of the model. In contrast to the validation of the four jet nozzle in this case the sample chosen for analysis it has been the edge of a pocket in where at the beginning of the trench there is just substrate and then, due to the nature of the geometry, it evolves into a coated surface, with the layers parallel to the surface. This samples were obtained from a 1 m diameter ring from the rotor casing, but as the aim was to validate the model with as much parameter combinations as possible the milled trenches have been performed in the in the axial direction, hence it is considered to be a straight trench, see Figure 81. As the materials involved are the same as the ones shown in Table 6 the material coefficients do not need to be calculated again.

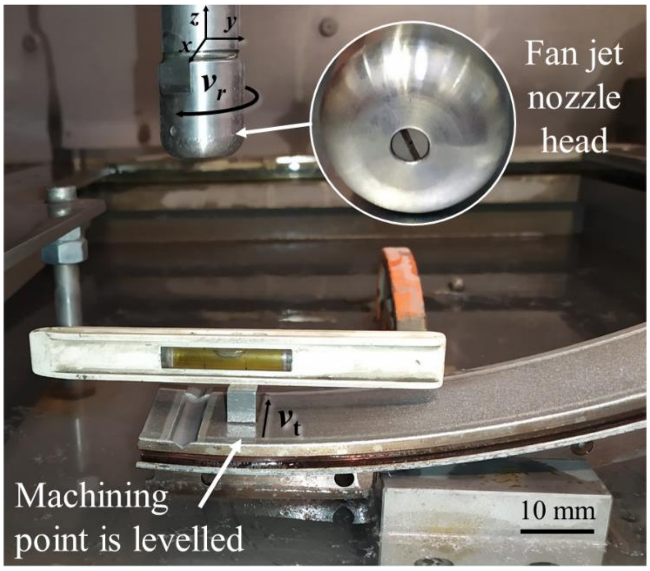

Figure 81: *Definition of the geometry of the tests samples as well as the tests set up for the small scale validation of the fan jet rotational nozzle head in pocket samples.*

The test results are shows in three different ways:

1) **Scan of the milled trench:** this is the surface scan obtained with the multi focus scanner (Alicona G4) and post processed in Mountains Map from the real milled sample. To understand this graph close attention has to be put to the geometry. These pictures show a trench milled in the edge of a pocket. Untouched material can be appreciated in the edges but the middle section is clear. In this area, where the coating material has been removed, the pocket geometry is clearly identified, with the naked substrate at the back, and then towards the front, the pocket with its characteristic geometry: a slope, radius and finally a flat area in where the coating used to be sitting parallel to the substrate before being removed. Depending on the milling parameters good and bad removals can be identified by considering the surface quality. If marks are identified in the centre of the trench, then damage has been induced to the substrate whereas if coating blotches are left in the edge of the trench then the coating has not been fully removed.

2) **Modelled trench:** this graph shows the resultant milled trench calculated by the model which is explained in section 4.3.4. This is the actual result of the simulation, however, in some cases, due to the representation of the mesh sizing, the small variations along the trench, hence the damage in the substrate, are hard to visualize.

3) **Model interpretation (top view):** this graph, obtained by simulation, is the interpretation of the "*modelled trench*" by using an easy to understand colour code based on the street light system explained in section 4.5. This helps to better understand the results of the "*modelled trench*" as the discontinuities along the milled trench are highlighted. The colours in the plot mean the following: i) blue untouched surface, ii) yellow not fully removed coating, iii) red damaged substrate, iv) blue good removal.

Overall, the analysis has been focused in three different machining parameters in order to study their separate effect: the translational velocity, the pump pressure and the overlapping separation when milling multiple trenches.

a) <u>Effect of the translational velocity</u>

First of all, the influence of the translational velocity in the milling result has been studied by milling trenches at three different v_t: 100, 1000 and 4000 mm/min. For these tests the following parameters have been kept constant: P 3500 bar, v_r 1500 rpm, SoD 20 mm in a single trench. The obtained results are shown in Figure 82.

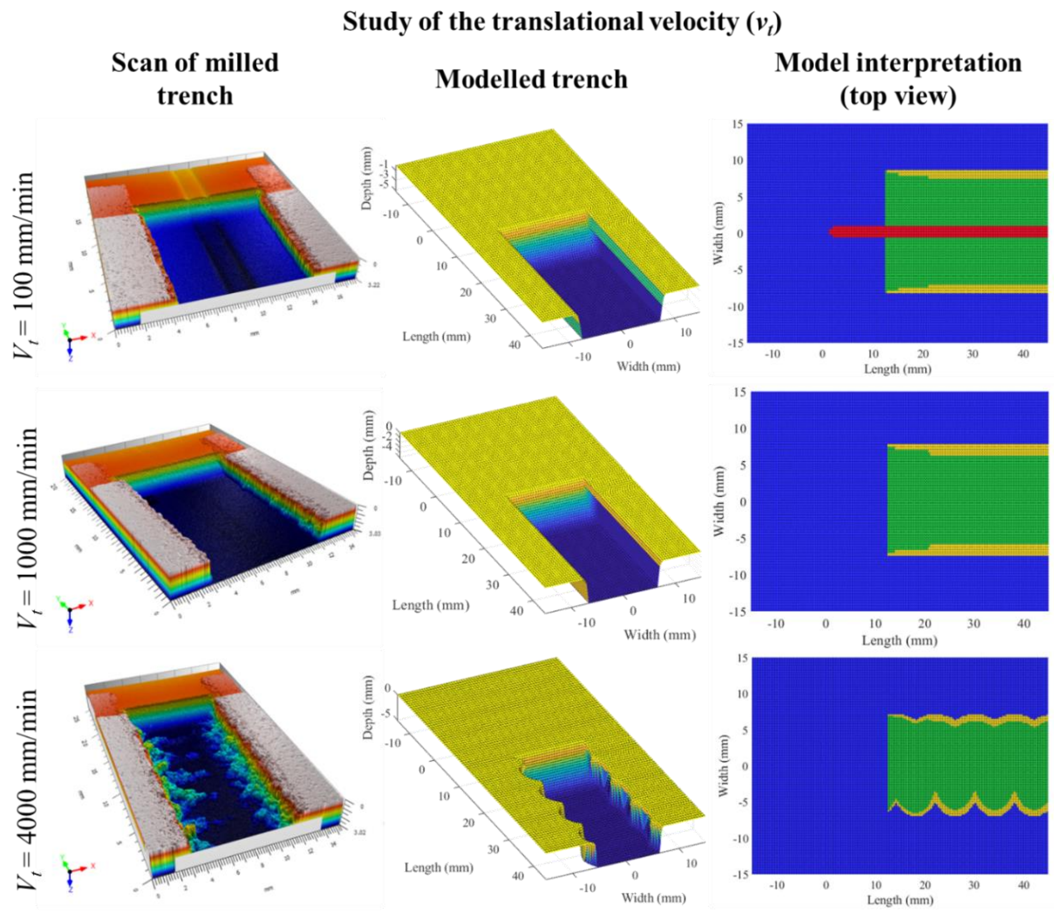

Figure 82: *Study of the translational velocity comparing 100, 1000 and 4000 mm/min trenches in where the results are presented as a scan of the milled trench, modelled trench and model interpretation shown from the top view with the street light system.*

First, a pass at v_t = 100 mm/min trench (i.e. the slowest trench) was milled in the sample material while a simulation was run with the same parameters. In the *scan of milled trench*, which corresponds to the surface scan of the actual machined sample a clear substrate damage can be appreciated. The damage is present in all the sections of the pocket: in the section A, which corresponds to naked substrate, as well as in the D section which was coated previous to the water jet pass (for further terminology clarification visit Figure 58) in where a deep straight cut can be seen in the centre of the trench. On the other hand, the *modelled trench* that was obtained from the mathematical model simulation shows the same damage. However, these discontinuities are very hard to see in this type of graph, even if they are there, as out of the SW context problematic areas cannot be zoomed in to see them more clearly. In these cases is where the *model interpretation* graph comes in handy. This plot represents the *top view* of the model trench highlighting the relative height between what the geometry of the substrate should be, compared to the actual substrate and the damage after the process. The *model representation* shows the same results as the *milled trench scan*: damage in the substrate along all the sections (i.e. red areas), hence incorrect set of parameters. This happens because of receiving too much jet energy, so it can be concluded that the jet should pass at a slower general translational speed.

As for the v_t = 1000 mm/min (i.e. mid speed) slight marks can be seen in the *scan of milled trench* in all the section but these discontinuities are inside the deviations allowed by Rolls-Royce: 0.05 mm. Due to this both the *modelled trench* as well as *its interpretation* represent the parameters as good removal (i.e. no red areas). These conditions are okay for a single trench as the substrate, even inside the allowed parameters, is starting to wear out, but it should be taken with care if used in overlapping trenches in where the jet will pass more than once from the same area.

Finally the v_t = 4000 mm/min (i.e. fastest trench) is shown as both milled and modelled trench. In the *scan milled trench* areas in where the coating has not been fully removed are clearly interpreted specially at the edge of the trench. As for the *modelled trench* and *its interpretation* graph this edge discontinuities are also visualized. This is since the machining conditions do not cover all the trench width so they will be edges with not enough jet energy received for all the coating to be removed. An important aspect seen in this case is that even if the coating has not been fully removed, no damage has been induced to the substrate. In conclusion, these parameters are valid as they should allow to have multiple passes and overlapping to remove all the coating without damaging the workpiece.

b) <u>Effect of the pressure</u>

Second, the influence of the pressure in the milling result has been studied by milling trenches at four different *P*: 200, 250, 300 and 350 MPa. For these tests the following parameters have been kept constant: v_t: 4000 mm/min, v_r 1500 rpm, SoD 20 mm in a single trench. The obtained results are shown in Figure 83.

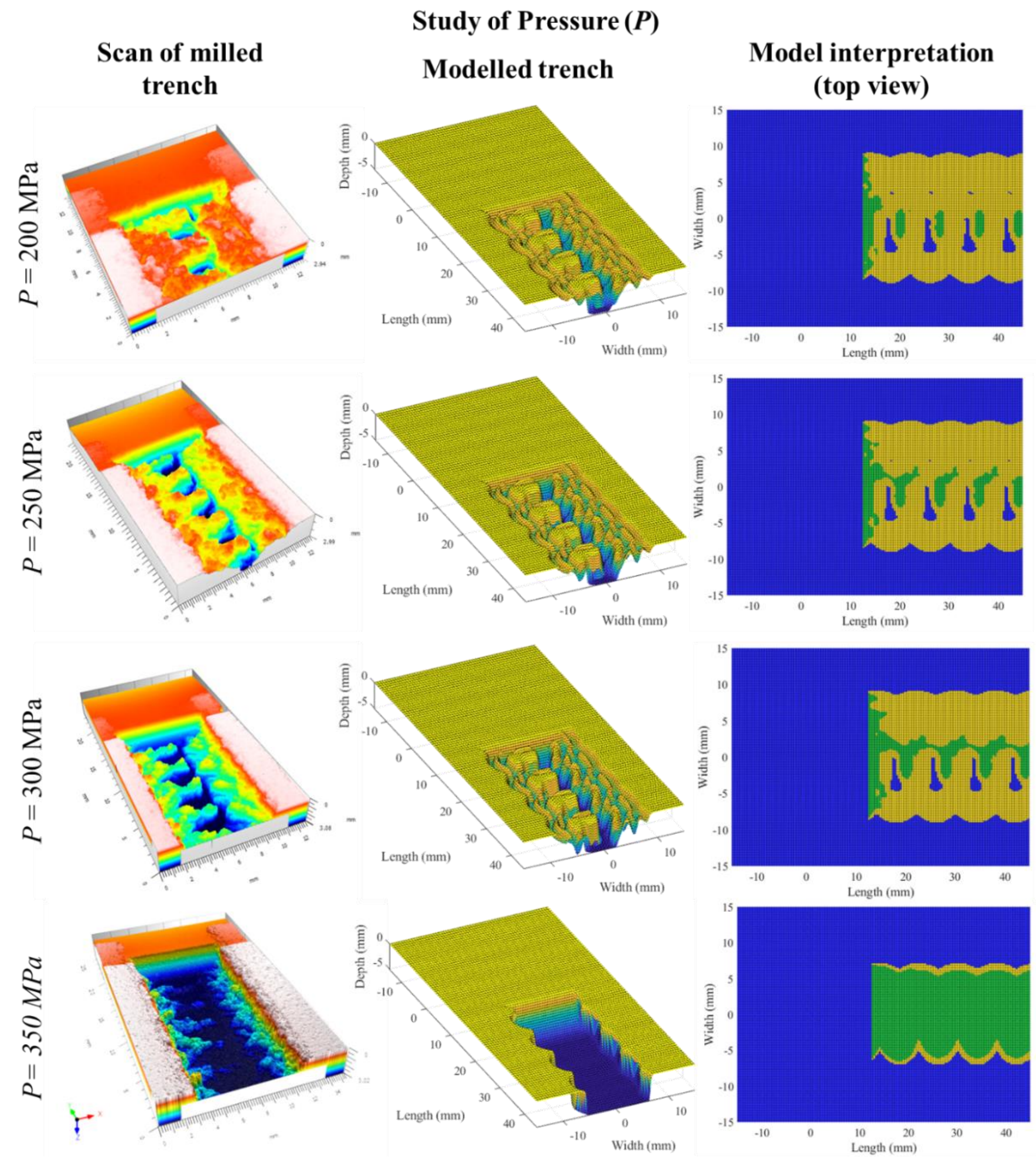

Figure 83: *Study of the pump pressure comparing 200, 250, 300 and 350 MPa trenches in where the results are presented as a scan of the milled trench, modelled trench and model interpretation shown from the top view with the street light system.*

In the WJ machine in where the tests were performed the pump pressure ranges from 50 to 400 MPa. However, the machine cannot be run at 400 MPa for large periods of time for safety reasons so 350 MPa is considered the maximum viable pressure of the machine. Ideally, considering that the aim is to remove the coatings in the shortest amount of time maximum pump capacity is desired as the energy received by the workpiece would be greater, hence higher removal rate would be achieved.

There is a clear similarity between the *scan milled trenches* and the *modelled trench* and its *interpretation,* demonstrating the validation of the model. In this case a greater removal can be seen at the increment of pump pressure, observing an increase in the fully removed good areas at each interval. The jump between 300 and 350 MPa is considerable, so it can be considered that at this step the influence of the material removal mechanisms comes to play, which will be further discussed in section 6.4.

c) <u>Effect of the overlapping separation</u>

Finally, the effect of the overlapping separation is studied as it has been learned that the optimal set of parameters not to damage the substrate has been to go gentle and have multiple passes: 80 % and 55 % of overlapping separation. For these tests the following parameters have been kept constant: *P*: 350 MPa, v_t: 4000 mm/min, v_r 1500 rpm and SoD 20 mm. The obtained results are shown in Figure 84.

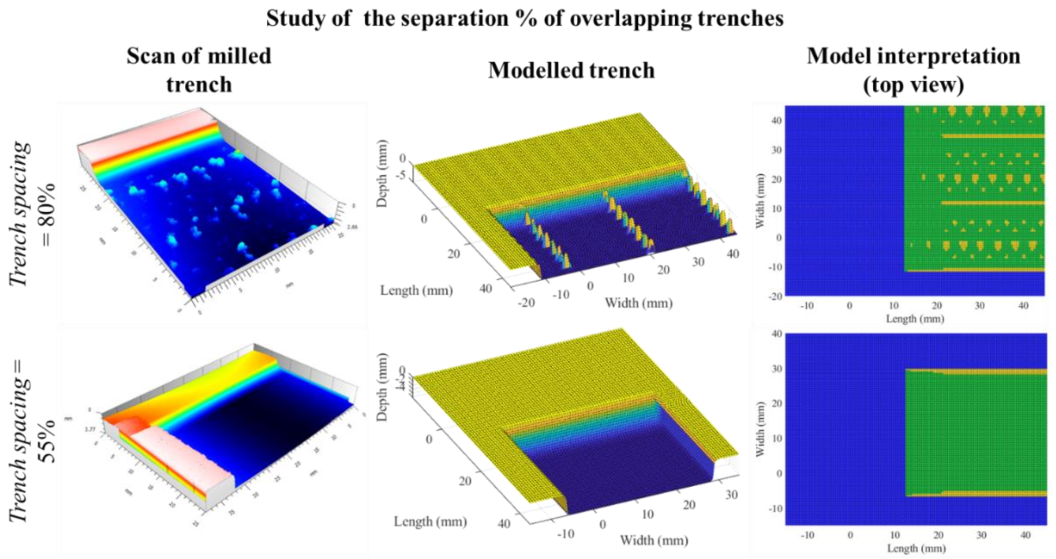

Figure 84: *Study of the separation percentage of the overlapping trenches comparing 80 and 55 % in where the results are presented as a scan of the milled trench, modelled trench and model interpretation shown from the top view with the street light system.*

After having studied the impact of different translational velocities and the pressures, the most interesting parameter values have been selected for this analysis:

v_t = 4000 mm/min and P = 350 MPa. Even if a full removal is not obtained, it gives promising results with a considerate coating removal and with no substrate damage, which makes this configuration interesting to be analysed in overlapping conditions.

In order to analyse different overlapping separations, simulations were done at a range. From those, the two most representative settings were machined to compare the model with the real case: at 80% (sample in Figure 85a) and 55% (sample in Figure 85b) separation. As for the 80% of overlapping separation it can be observed in both the *milled trench scan* and in the simulated models that the separation is too wide to ensure a full coating removal and that traces are left all over the area. However, when reducing the separation to the 55 %, a clean surface with no damage can be observed in all the cases demonstrating the ideal coating removal parameters as well as proving the validity of the model to predict the coating removal accurately.

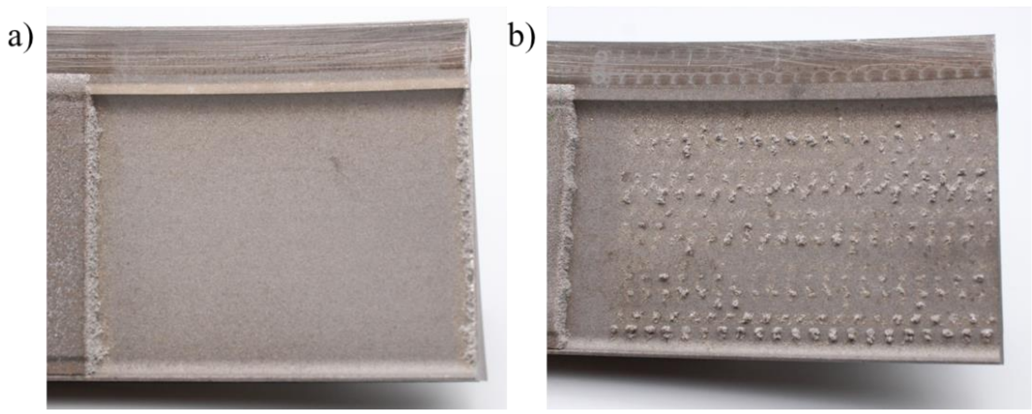

Figure 85: *Photograph of the samples after coating removal at P: 350 MPa, vt: 4000 mm/min, vr 1500 rpm, SoD 20 mm and a) 55 % of overlapping separation between trenches and b) at 80 %.*

6.2. Proposal of the most suitable parameters for the studied materials

After analysing the multiple milled and simulated trenches the following statements are concluded about the effect of the machining parameters in the trench generation. Overall, more than one set of parameters are valid for coating removal with no damage to the substrate. This is because when multiple parameters are on the play a balance between them should be achieved. This said, the ideal set of parameters will be those which fulfil the objective in the fastest way possible considering the limitations of the available equipment.

- **Nozzle:** Both nozzles have demonstrated to be accurately represented by the developed mathematical model. The four jet rotary nozzle works better for softer materials as it is gentler, and it ensures a full removal with no substrate damage whereas the fan nozzle is more aggressive which will be too harsh in soft coatings but achieves a good removal in harder ones.
- **Pressure (P):** The pump pressure affects to the trench depth; more pressure leads to higher energy reaching the workpiece which ends with a higher material removal. This is also the most unstable parameter; the pump needs time to stabilize before the beginning of each test, so this needs to be kept constant during all the machining process. In the UoN WJ machine the highest pressure set (350 MPa) was still not enough for substrate damage if the rest of the parameters are adequately tuned for the studied materials.
- **Stand of distance (SoD):** Higher the SoD wider the trench will be as the taper effect will be more noticeable, hence faster removal rate. However, when going too far the jet becomes unstable and the removal more unpredictable. After analysing the high speed camera recordings of the nozzle heads this parameter was set in 20 mm as it shows a good valance in this area (see section 4.2.2).
- **Rotational velocity (V_r):** This was selected after the manufacturer recommendation and it was set at 1500 rpm for all the tests. The balance between v_r and v_t for trench coverage was achieved by adapting the v_t.
- **Translational velocity (V_t):** This is a key parameter as is the value that influences the outcome result the most. Slower the v_t, higher the energy that the workpiece will receive resulting in a greater removal rate but demanding a longer machining time for the same area. For this the fastest translational velocity as possible is desired. After the performed tests it has been observed that 4000 mm/min for the analysed material, in combination

with the rest of the already set parameters, works the best for the UoN WJ machine.

- **Overlapping separation:** This set will also greatly influence in the final machining time as it has a direct effect in how many passes are needed to cover the full surface. Too many or too little overlapping separation in the same area with set machining parameters will lead to over or under cleaning.

6.3. Industrial validation in the Rolls-Royce PWJ machine

Finally, the model has been tested in situ in Rolls-Royce installation in Derby. For the test a compressor casing has been chosen. Considering the limited material and time access to the machine there were performed three trench at various machining conditions:

- **Trench 1:** Usual Rolls-Royce parameters chosen by experience and proven to work fine over the years.
- **Trench 2:** Parameters defined by the model in where a good removal is expected.
- **Trench 3:** Parameters defined by the model in where too much material is removed and the substrate is predicted to be damaged.

The parameters used in each of the trench are described in Table 7 and the coating materials are the ones described in Table 6.

Table 7: *Definition of the parameters used at Rolls-Royce WJ machine in order to prove the material removal prediction capabilities of the developed model.*

Trench	P (MPa)	V_t (mm/min)	V_r (rpm)	Overlapping separation (%)	SoD (mm)
1	241	6220	1500	75 %	12
2	350	4000	1500	55 %	20
3	300	500	1500	80 %	20

Figure 86 shows the set up used in the Rolls-Royce Derby water jet machine as well as the workpiece material used in the tests. This WJ machine is a full cabin in where parts are entirely introduced and are fixed to the rotary base of the machine with a pump pressure that reaches 600 MPa in contrast to the 400 MPa of the UoN WJ machine. In this case the part itself is the one that rotates and the water jet head with the nozzle, that is equipped with a fan jet constantly kept at a 20 mm SoD, stays stationary in x and y while it goes from the top of the part to the bottom in the z axis. The combination of these two movements creates a spiral that will ensure the full coverage of the inside of the part. The combination of the rotational speed of the part and the z axis speed of the head will be equivalent to the combination of the translational speed and overlapping separation in the model, the number of rounds will be equivalent to the number of passes. In this document everything will be presented in the model nomenclature to maintain the consistency.

The objectives of these tests are, to evaluate how accurately the model can predict the coating removal of a real case scenario, as well as to assess how well the jet can do the machining depending on the parameters considered. These studies will be done by comparing the three sets of configurations previously explained to generate three different trenches.

The first experiment was done with the parameters that Rolls-Royce generally uses to remove the coatings. These values come from previous experience and only have experimental results for their justification.

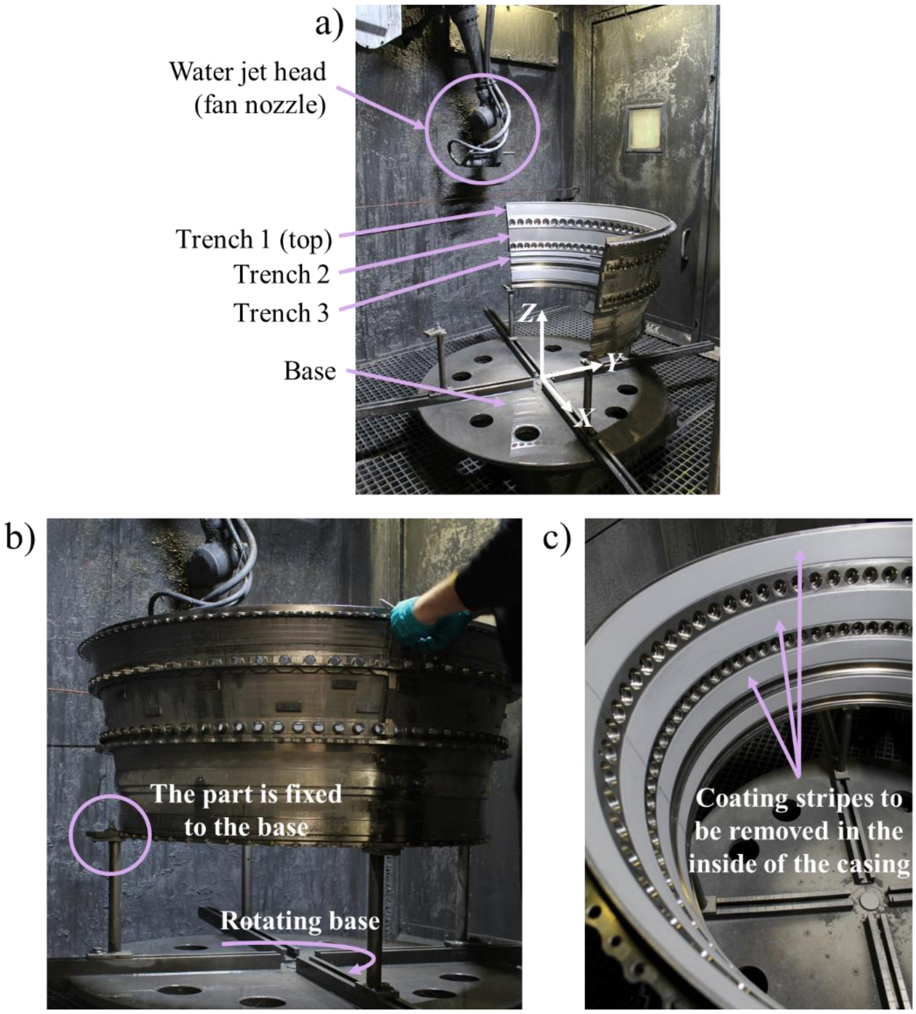

Figure 86: *Description of the Rolls-Royce water jet machine tests set up in where a) the mounted casing inside the machine is showcased as well as the WJ nozzle head, b) the attachment of the casing to the rotary base and c) the representation of the coating steeps to be removed are shown.*

As it can be seen in Figure 87, both the mathematical simulations and the measured results show that at these machining conditions the coating is fully removed. However, if close attention is paid to Figure 87, some stripping lines can be identified. These are not problematic as they fit within the allowances for the process, but still mean that the substrate is being affected and the parameters are harsh. Furthermore, if these parameters are used several times in the lifetime of a part, it cannot be ensured that the substrate will not be affected in the long term. Nevertheless, the model can accurately predict the result of the machined surface with an average error of 2.2%, and the parameters achieve the fastest processing time.

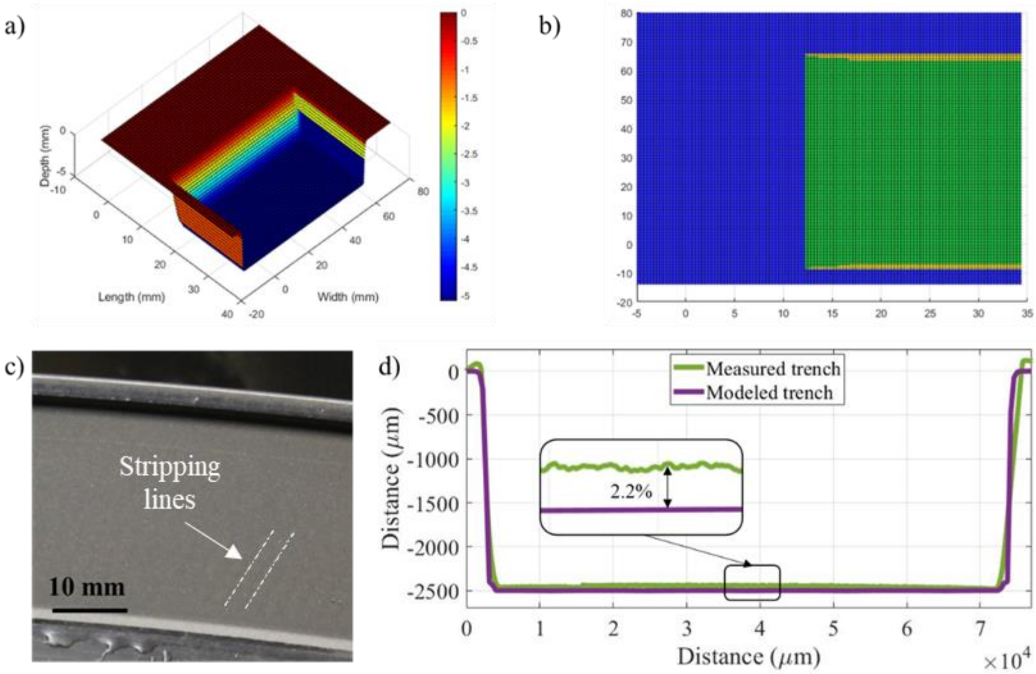

Figure 87: *Study of the milling of the workpiece using the original parameters that Rolls-Royce uses for the process: a) modelled trench obtained from the mathematical model, b) top view representation of the modelled surface, c) picture of the cleaned surface showing the stripping lines, d) comparison of the measured and the modelled trenches with the error between them.*

The parameters selected for the second experiment were taken from the simulations done with the software which had also been validated at the UoN WJ. The machine from Rolls-Royce being slightly different, these might not be the ideal parameters for this WJ, as having a higher pump pressure would enable a faster approach. However, these parameters will still allow to prove if the predictions of the model match the real machining results.

As shown in Figure 88, the results from the mathematical model and the measurements show a full cleaning of the part with no apparent discontinuities. Even if the configuration is slower than the previous, no stripping marks can be identified which ensures that the substrate has not been damaged. Furthermore, this should allow having more iterations in the re-coating of the workpiece without compromising its quality. The results of the model are able to predict the geometry of the trench with an accuracy of 4% at the edges and 2.8% in the middle, as when the full coating is removed the difference is minimum.

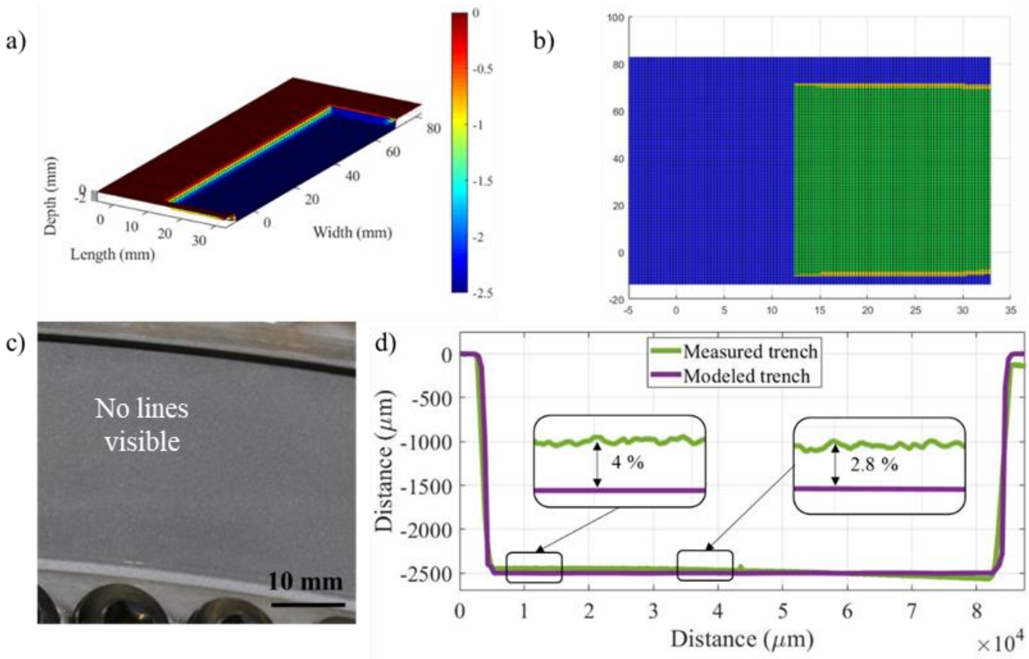

Figure 88: *Study of the milling of the workpiece using the new proposed parameters for a controlled milling and reduce the damage of the substrate: a) modelled trench obtained from the mathematical model, b) top view representation of the modelled surface, c) picture of the cleaned surface, d) comparison of the measured and the modelled trenches with the error between them.*

Finally, the third test was done selecting parameters that according to the model should give a bad removal (i.e. damaged substrate) as a result. This was done to validate that the model can predict when the machining conditions are too harsh, and to prove the accuracy of it against a real case.

The results presented in Figure 89 clearly show a segment of the trench which goes deeper than the required to remove the coating. In both the model and the real measurements, this happens at the middle section, which could be a result of the overlapping between passes. Having too much energy because of the low translational speed, passing more than once over the same area removes too much material damaging the substrate and creating that geometry. Moreover, the accuracy of the model has been further validated, as it shows the full removal of the coating at the edges with an accuracy of 0.26%, while the prediction at the middle, where the damage has been done, the error increases to a 0.8%.

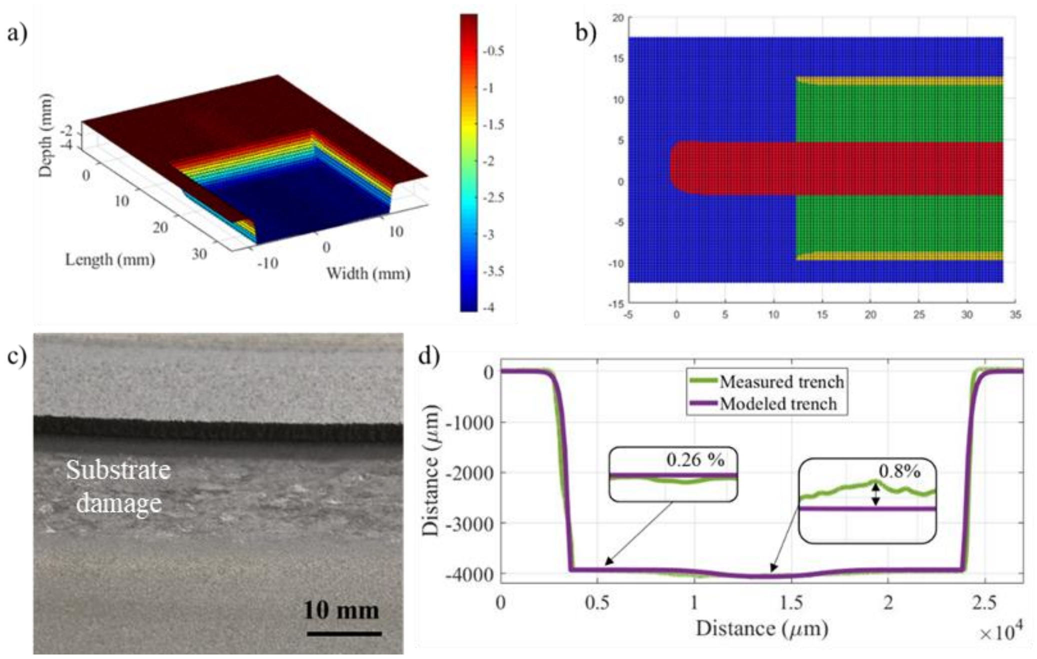

Figure 89: *Study of the milling of the workpiece using parameters that should damage the workpiece to validate the predictability achieved using the model: a) modelled trench obtained from the mathematical model, b) top view representation of the modelled surface with the damage in red, c) picture of the cleaned surface with the damage induced, d) comparison of the measured and the modelled trenches, showing the damage and with the error between them.*

6.4. Understanding of the material removal mechanisms

One of the topics that arises from the validation of mathematical model was: How is the material removed from the samples to generate the trench? In this thesis, the author proposes a hypothesis suggesting that under high pressure, water infiltrates the cracks within an imperfect material's structure. This infiltration plays a role in unforeseen crack propagation, ultimately culminating in the failure of specific material zones.

As coatings are generally applied using methods such as air plasma spray, this generates a very heterogeneous material with a variety of discontinuities throughout the structure (e.g. voids, cracks, pores…) [118]. These imperfections in material can act as stress concentration points. Under mechanical loading, stress tends to concentrate around these imperfections, potentially initiating crack formation. Another weak point in coatings is the union between layers, as the bonding between materials is usually more fragile than the material on its own, making it another very natural place for cracks to grow. When high pressure water goes into these features, it opens them even more propagating the cracks and breaking the material. Moreover, high pressure can have significant effects on materials, it can alter the physical properties and their behaviour (e.g. phase transformation), potentially making them more susceptible to cracking and failure [119]. The presence of water can affect material properties by causing swelling, corrosion, or promoting chemical reactions.

The stochastic nature of materials introduces a level of unpredictability and variability in their behaviour. Considering the presented hypothesis, this stochasticity can contribute to a discrepancy between the theoretical predictions of the model and the actual characteristics observed in real-world milled trenches.

While the model attempts to predict the material removal behaviour when being milled with a high pressure water jet and considers the physical interactions between the jet and the material in a level that it has been proved that the model works, there are still many factors (e.g water infiltration, and crack propagation on material failure, etc.) that have not been considered. The complexity of real materials introduces numerous factors that may not be fully captured by the theoretical framework and hence, the model does not accurately represent the intricate interplay between the material's microstructure, the unique distribution of imperfections within it, and the diverse ways in which water can infiltrate and interact with these imperfections. A visual representation of the proposed hypothesis is shown in the Figure 90.

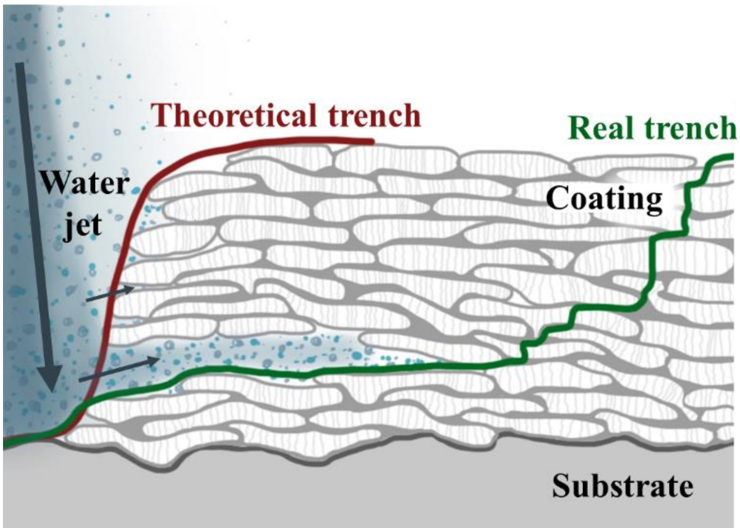

Figure 90: *Visual representation of the theory of how the edge of the trenches after passing a milling trench are expected to be removed vs how it actually gets removed.*

To prove this hypothesis, some trenches have been milled in air plasma sprayed TBCs as the nature of the structure of these coating makes it easier to identify the previously described phenomena. The cross section of the microstructure of the samples have been analysed in an SEM (Figure 91) after cutting, mounting and polishing the samples.

As suggested, the figures showcase the effect of the cracks can be seen in the material removal mechanisms. In Figure 91a, the effect of the growth of a crack can be identified, which lead to the breakage of the material creating a straight vertical fracture. Furthermore, Figure 91b visualizes a crack being generated between the substrate and the bond coat, while the top coat is missing. The top of the trench having a flat geometry suggests that the top coating has been removed due to a crack as it does not follow the shape of the trench. The image on Figure 91c also proves that the material removal mechanism depends on the cracks, as a gap that does not follow the trench geometry can be identified, whereas it follows the direction of a crack.

Finally, Figure 91d shows clear cracks between layers (bond coat-top coat and substrate-bond coat), which are a visible consequence of the milling process with the high pressure water jet. In conclusion, the study done with the SEM at the cross section of the samples explains why sometimes the model and the real trenches mismatch at the very edges, reducing the accuracy of the mathematical model as this effect is unpredictable.

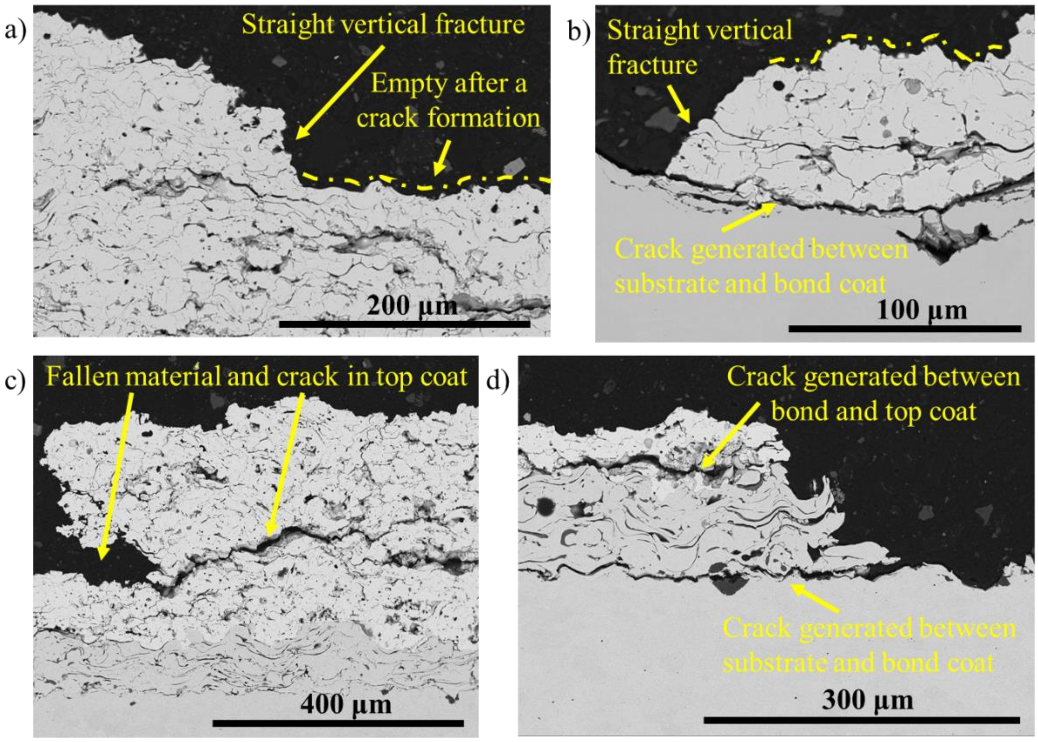

Figure 91: *SEM pictures showing the different cracks generated on the sample after the waterjet milling: a) material removal due to a crack formation, b) example of a crack between the substrate and the bond coat, c) gap generated on the top coat of the sample due to crack and d) cracks generated between layers at the substrate-bond coat, and top coat-bond coat.*

Finally, a comparison has been done to see the difference between a sample processed using adequate milling parameters and another that had been damaged by the waterjet. As seen in Figure 92a, the damage induced to the substrate can be clearly identified in the middle of the trench using both an EDX and SEM analysis. On the other hand, Figure 92b shows how a not full removal looks with coating material being left on top of the substrate.

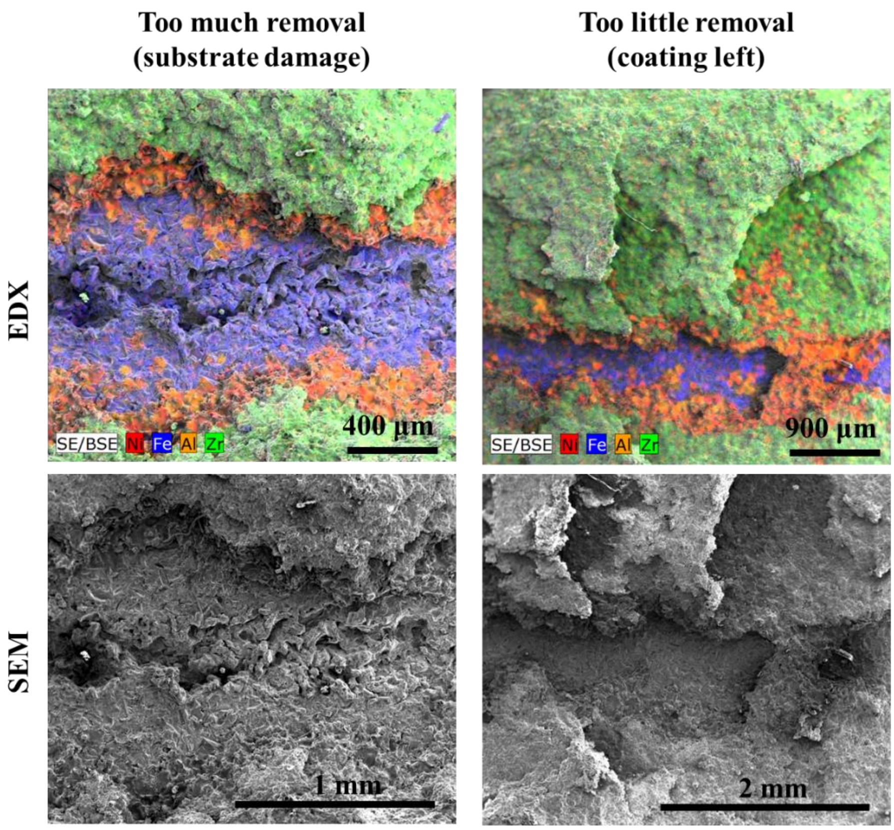

Figure 92: *Pictures from the SEM and EDX analysis to compare machining parameters that leads to too much removal and as a consequence substrate damage and too little removal which implies coating left behind.*

6.5. Concluding remarks

This chapter presents the validation the mathematical model presented by comparing the predictions with the results of real milling of coated samples. Two types of nozzles will be tested at different parameters (i.e. translational speed, pressure and overlapping separation) to evaluate and understand the effect of each in the material removal. The main conclusions drawn from this work are as follow:

- The tests done with the four jet rotational nozzle proved that the density of the overlapped jet footprints depends on the kinematic of the process (i.e. ratio between the rotational and translational speeds) which could result in a non-uniform eroded patch. The model can predict such discrepancies (i.e. unremoved coatings) at good accuracy, max. 4.5% in the middle and 27% at the edges of the trenches respectively; increased error in the latter case is related to secondary effects of the process (e.g.

secondary material cracking). Nevertheless, non-uniform eroded patches is not the scope of the coating removal process, hence, it is considered that model predictions are acceptable in this working scenario.

- The consistency of the coating removal has been demonstrated by the use of SEM and EDX material analysis proving that the kinematics and the multiple jet footprints can be optimized by the model, so that components with no coating residual on the substrate are obtained.
- From the experiments done with the fan nozzle it can be concluded that in some cases, it is preferable to use a lower pressure and higher translational speed, even if not all the coating is removed, to ensure that no damage is done to the substrate. By controlling the overlapping separation, a good removal of the coating can be achieved while the pressure and translational speed are far from critical values that could ruin the sample.
- The importance of the model interpretation using the street light system has also been validated, as in some cases it is not possible to visualize the damage in the original modelled due to the scale of the graph. By separating the depths into contrasting colours, the different segments of the trench are highlighted and easily identified.
- The experiments performed at Rolls-Royce showed that the parameters they used are valid, but still generate some stripping on the workpiece, which even if it is in the allowed damage range, could potentially be detrimental in the long term. For that reason, some new parameters obtained from the mathematical model have been proposed and tested, showing a better result without any damage on the workpiece. Furthermore, the model has been validated to be able to predict when some parameters will not be valid, by relating the model with real case experiments with a maximum error of 4%.

- Finally, a theory for the material removal mechanism has been proposed and proven via EDX and SEM analysis. By studying the results of the trenches done with the waterjet, it has been confirmed that due to the heterogeneities of the coating material, cracks grow at the edges breaking the material from there. That explains why in some cases the model and the real trenches have differences, as this behaviour is not predictable, and hence cannot be implemented into the mathematical model.

Chapter 7

Comparison between high (PWJ) and low (nanoindentation) strain impact in YSZ: Case study

This chapter describes a case study to understand the material removal mechanisms generated by the jet of a WJ machine when impacting the target material at high pressure. For this, one of the most used materials in aerospace coatings has been chosen: Yttria Stabilized Zirconia (YSZ) is generally used as the top coat on the so called Thermal Barrier Coatings (TBC). To carry out this analysis, Raman spectroscopy, TEM analysis and different strain rate nanoindentations have been performed.

7.1. Introduction

After developing the mathematical model for coating removal, with the aim of understanding the differences observed between the model and the machined surfaces, a material removal mechanism analysis has been done in the previous chapter. Based on this, and with the aim of further developing the understanding of the material removal mechanisms that are involved in the direct impact of the jet on the workpiece, the following case study has been proposed: the effect of high strain rate impact in Yttria Stabilized Zirconia.

On the one hand, the first instinct would be to examine the substrate material following its interaction with the waterjet, as it constitutes the resulting entity. However, this is just a simple metal with no relative interest. On the other hand, the literature review has revealed that YSZ can have a phase transformation when impacted at high speeds, which is an interesting topic for study. Considering that this could have repercussion on the material removal mechanism, it would fill the research gap opened in the previous chapter. For this reason, the study has been focused on the top layer of the workpiece.

Yttria stabilized zirconia (6-8YSZ) is widely used as a top coat in Thermal Barrier Coatings (TBCs) to protect metallic substrates. These coatings are exposed to severe high strain rate fields along their life, for example during the impact of debris happening in service or during coating removal in repair processes. In this work we use a water jet and high strain rate nanoindentation to understand how the behaviour at a small scale of 8YSZ depends on the strain rate (from 10^{-3} to 10^{8} s^{-1}). We observe how at extremely high strain rates (10^{6} - 10^{8} s^{-1}) the material suffers from a brittle-dominated failure which induces localized phase transformation. At lower strain rates (10^{-3} - 1 s^{-1}), plasticity dominates, and phase transformation is not observed.

For future approaches, it would hold significant appeal to continue studying the impact of the waterjet at high speeds on different coating materials and especially on substrates generally used in aerospace. This would aim towards the goal of having a full understanding of the impact of the waterjet at high velocities into the target material, and its effect in the material removal mechanisms.

7.1.1. Understanding of YSZ and its response to high strain impact

Zirconia is a remarkable material for high temperature or harsh environment applications. This is due to its high melting point (2680°C), low thermal conductivity and high resistance to chemical attacks. There are three polymorphic modifications of zirconia oxide (ZrO_2): monoclinic (*m*), tetragonal (*t*) and cubic (*c*). The usual transformation of these phases goes from monoclinic at room temperature and atmospheric pressure, to tetragonal by martensitic transformation (T_m) at 1170°C and to cubic at 2370°C until its melting point at 2690°C [120], [121].

The polymorphic transformation of ZrO_2 from tetragonal to monoclinic, when cooling below ~ 950°C, comes with a volume change of ~4% due to a diffusionless martensitic transformation to accommodate the Zr ions from an 8 to 7 fold coordination system [26], [122]. When cooling this creates a strain of ~1.5%, that occurs below the ductile to brittle transformation temperature [23], which leads to cracking, and consequently, to premature failure of the material [123]

On the other hand, the compressive stresses generated by the volume change when the zirconia undergoes the $t \rightarrow m$ martensitic transformation, can be used as transformation toughening if this is done in a controlled manner [124]. If the material has undergone transformation toughening, and cracks are generated under mechanical load, the compressive forces will close them, preventing their propagation and avoiding material failure. Due to this phenomena a material with high toughness, which is capable of dissipating energy under stress, and with a high fracture resistance is created [125].

One way of controlling the behaviour of Zirconia to achieve the required properties for each application is to add small quantities of oxides (e.g. Y_2O_3, CaO, MgO) [18] to partially or fully stabilize it [126]. Yttria (Y_2O_3) is one of the most effective stabilizers to avoid the transformation to a monoclinic (*m*) state [127] which enables the high temperature tetragonal (*t*) or cubic (*c*) phases to be stable at room temperature [29]. In the process, Zr^{4+} ions are randomly replaced by Y^{3+} ions which are slightly larger (i.e. 0.96 Å Y^{3+} and 0.84 Å Zr^{4+}) while the trivalent Y^{3+} ions induces O^{2-} oxygen vacancies in the ZrO_2 structure that is built up by Zr^{4+} tetravalent ions. The introduction of oxygen vacancies reduces the fold coordination number of the zirconia from 8 to <8 at high temperature, hence preventing it from undergoing a $t \rightarrow m$ transformation when cooling down [26].

Adding different percentages of yttria produces materials with distinct properties, making them appropriate for specific applications. Yttria Stabilized Zirconia (YSZ) with a 6-8 wt% of Y_2O_3 is widely used as a top layer in Thermal Barrier Coatings (TBCs) to enhance the performance of metallic components of jet engines at temperatures well above their melting point [128], [129]. 8 wt% of Yttria is considered a metastable phase with a tetragonal structure [102]. It would take 9 wt% Yttria to be fully stabilized, whose crystallographic structure is normally presented as cubic [121]. Having the right proportion of Y_2O_3 is key to obtain the high thermal expansion coefficient, good thermal shock resistance and good chemical stability required for TBCs. Increasing the amount of Y_2O_3 to obtain a fully stabilized YSZ would help with the thermal stability but would make the material more brittle and prone to cracking under mechanical stress [130]. With 8YSZ a good balance of desired properties is achieved, but its fracture toughness tends to be on the lower side, approaching values similar to the monoclinic phase, which results in a limited amount of expected transformation toughening [121].

Despite the numerous studies conducted on YSZ regarding its properties at high temperatures or in harsh environments, there is limited information on how mechanical loads affect its failure mechanisms. These mechanical loads can be easily originated either during in-service (e.g. impact by high-velocity small debris) or during processing (e.g. Water Jet machining) both in the range of high strain rate (HSR) impact. This transformation, beneficial or not, changes the mechanical properties of the material so they need to be known and under control. In this work, we use Plain Water Jet (PWJ) to investigate the effect of mechanical loads, at a small scale, on the properties of YSZ which has relevance not only to manufacturing methods but also in-service like conditions of the surfaces coated with YSZ [50].

7.2. Experimental procedure: methodology and materials

In Water Jet, the plume can be divided into three sections characterized by different water densities that decrease while the jet loses its focus: continuous, open and diffused jet regions as depicted in Figure 93a and b. The PWJ milling process of the coating is performed at the open jet section mainly by the main core (that presents a high density and kinetic energy of the water droplets) while in the mist zone of this section (characterized by a lower density/kinetic energy than the main core) only secondary material removal occurs [131].

The aim of this research work is to investigate how 8YSZ behaves at small scale when being exposed to impacts at high and low strain rates. The tests will be conducted by using a PWJ and a controlled nanoindenter respectively and subsequently the influence of the mechanical response of the material will be analysed. As such, this thesis reports how in 8YSZ $t \rightarrow m$ transformations only happen at high strain rate (HSR) ($>10^6$ s^{-1}) but not low strain rate LSR (<1 s^{-1}).

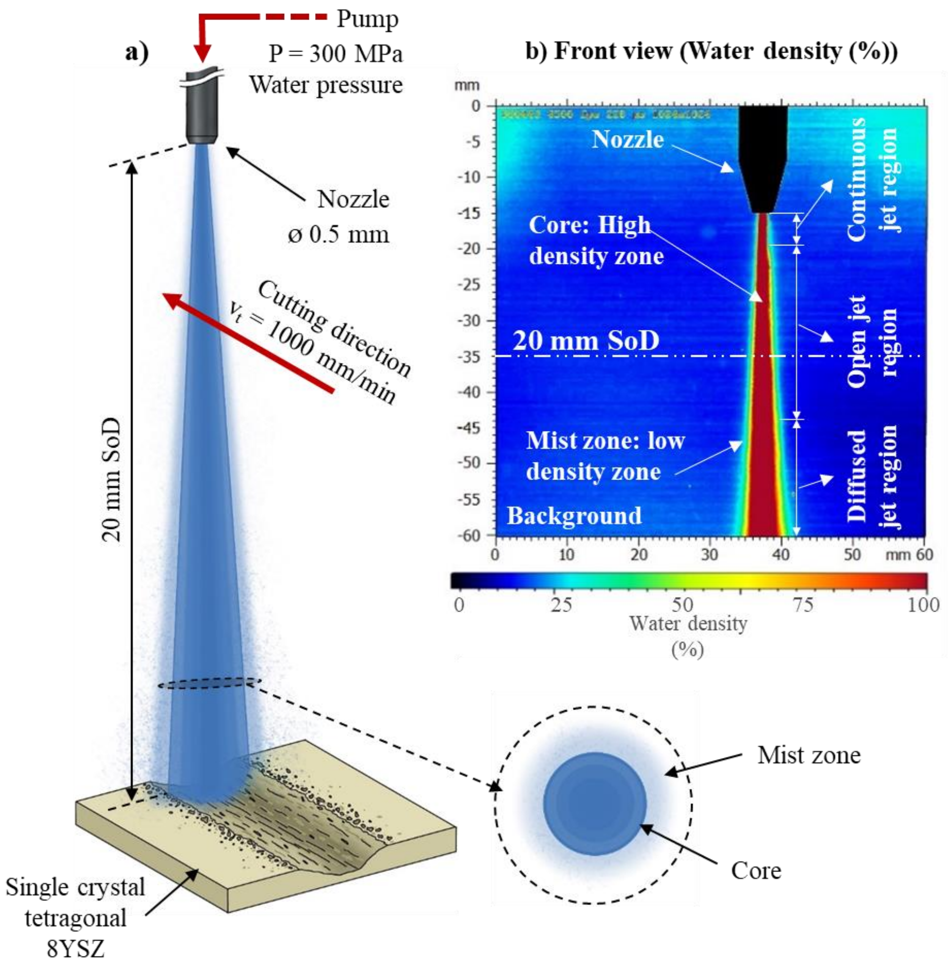

Figure 93: *a) Schematic representation of a PWJ trench indicating the process parameters in the performed tests b) Waterjet density distribution along the jet – experimental results.*

For the present study a straight trench has been milled with a Plain Water Jet machine (i.e. without abrasives) as described in Figure 93. A 0.5 mm orifice needle nozzle at a pressure of 300 MPa, 1000 mm/min feed rate and 20 mm stand of distance (SoD) that impacts the surface at HSR (calculated to be above 10^6 s^{-1} [132]) was used in a 10 mm x 10 mm x 2 mm single crystal 8YSZ sample. At these conditions the jet plume generates an impact on the target surface causing a strain rate between 10^6 to 10^8 s^{-1} [133].

Determining the precise strain rate resulting from a water jet proves to be an exceptionally challenging task. Consequently, an approach focused on establishing a range of values has been adopted instead. To obtain an exact value is not so crucial, especially due to the fluctuations of the jet (as explained in section 2.4). Drawing from existing literature [133], the anticipated strain rate within the specified conditions is well-defined within a certain range. Moreover, the precise numerical value is not so significant, as exceeding a certain strain rate threshold is already on the threshold of causing a change in the material that's being affected.

Considering that the energy (*E*) released by the PWJ follows a Gaussian distribution along the width of the jet [134], the analysis areas have been selected as illustrated in Figure 94 and are shown by using a Scanning Electron Microscope (SEM) (JEOL 7000F FEG-SEM):

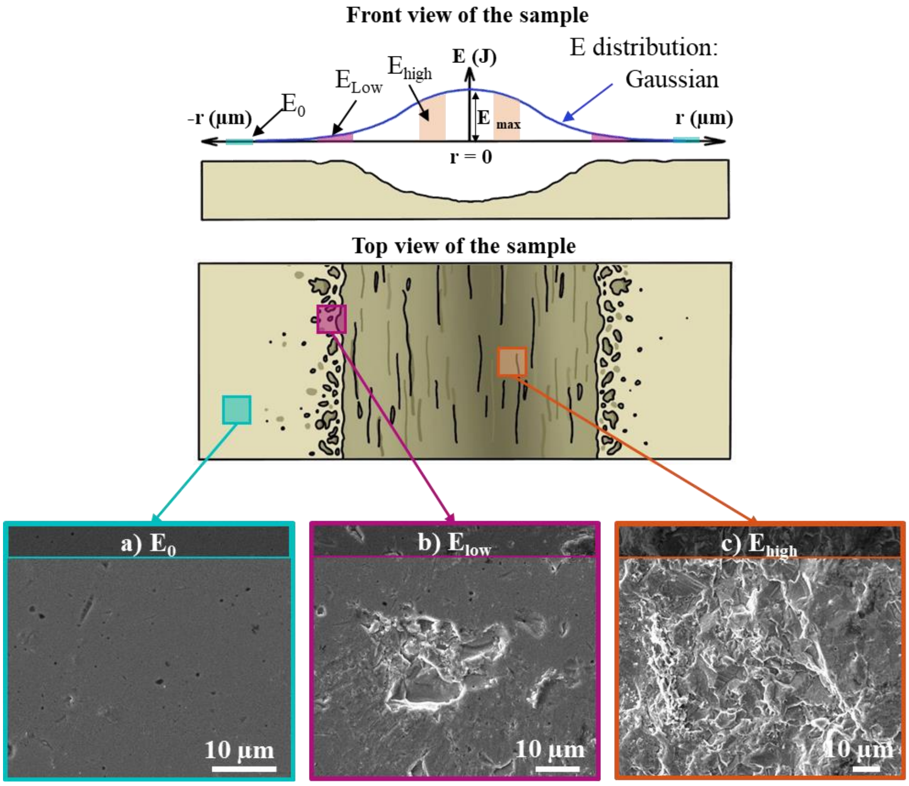

Figure 94: *Schematic representation of the front and top view of the PWJ milled trench indicating Gaussian energy distribution (E) of the jet and the location of the three regions of interest. Finally, SEM images of the selected surface areas: a) E_0, b) E_{low}, c) E_{high} indicating the surface damage under mechanical impact.*

- **E_0:** control region where no jet energy has interacted with the sample (Figure 94a). This area was analysed as reference material.
- **E_{low}:** area whereby the sample has been impinged by low water density mist zone of the jet and hence single droplet impacts can be identified; this is defined as low energy impact region (Figure 94b).

- **E_{high}:** region whereby the surface has been milled by the high density droplets of the main core of the plume and as a result a trench is generated; the main core is the jet region that contains most of the jet's energy (Figure 94c).

7.3. Results on the case study

7.3.1. High strain rate (HSR) impact study in YSZ

Raman spectroscopy is a well stablished technique in the study of phase transformation of YSZ [135]. Consequently, a Horiba LabRAM HR confocal Raman spectroscopy microscope (x50 lens; 0.55 numerical aperture) with λ 532 nm wavelength (i.e., green) laser, operating at a power of ~2 mW (100%) and a spot size of approximately 1.2 µm (calculated based on the Rayleigh criterion), has been used for identifying a $t \rightarrow m$ transformation in the three regions of the sample due to the impact energy of the PWJ.

Figure 95 presents an example of many (>30) Raman spectra from the three regions (E_0, E_{low}, E_{high}) of interest that received different levels of energy from the jet while identifying the peaks related to tetragonal (continuous line) and monoclinic (dotted line) phases. The raw data was then post processed by normalizing the intensity and applying a baseline correction based on the model developed by Schulze et al. [136] for a clearer identification of the peaks.

The Raman spectra of the measurements from E_0 (i.e. control/untouched region) shows prominent vibration modes at 149 cm^{-1}, 247 cm^{-1}, 344 cm^{-1}, 479 cm^{-1} and 626 cm^{-1}. The 149 cm^{-1}, 247 cm^{-1}, 344cm^{-1} and 479cm^{-1} vibration modes match with the literature values of typical *t* bands of 8YS [123], [124], [127]. However, the 626 cm^{-1} peak broadening to the left suggests the existence of additional peaks, (i.e. 612 cm^{-1} and 640 cm^{-1}) reported in the literature related to YSZ tetragonal phase and which have been merged creating an asymmetric peak (626 cm^{-1}). Furthermore, the Raman spectra obtained from E_{high} present the same vibrational modes as the E_0 regions where no monoclinic *(m)* bands are observed confirming the state of the material as fully tetragonal *(t)*. However, the Raman spectra measured in the E_{low} region, where single droplet impact occurs, shows two major changes: *i)* the appearance of two new peaks (i.e. 502 cm^{-1}, 554 cm^{-1}) that are related to $t \rightarrow m$ transformation, *ii)* and a clear variation in the vibration modes (i.e. ~200 cm^{-1} and 500 – 550 cm^{-1} domain) *m* as well as an increase in the intensity of the vibration mode at~350 cm^{-1} which are both characteristic indicators of *m* YSZ. Hence, both changes in the Raman spectra are indicators of a partial $t \rightarrow m$ diffusionless phase transformation after a single high strain impact caused, in our case, by high velocity droplet impact (HSR) at room temperature. This interesting phenomenon reveals the materials modification mechanism of 8YSZ under high strain rate impact.

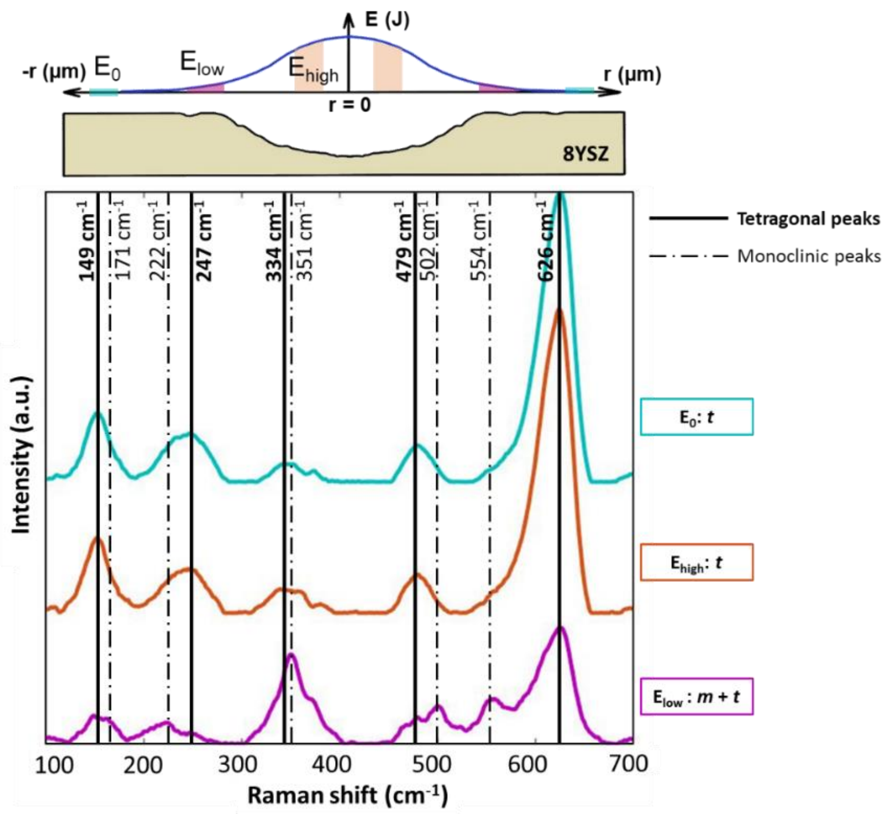

Figure 95: *Raman spectra from each of the three regions of interest: E_0, E_{low} and E_{high}. The analysis demonstrates $t \rightarrow m$ phase transformation phenomena in the zone of single droplet impact which is manifested by the appearance of new peaks (500-550 cm^{-1}), while in the trench, i.e. eroded, area and untouched surfaces show typical tetragonal spectra values.*

As defined in chapter 3, Raman spectroscopy analysis was conducted using a confocal Horiba LabRAM HR Raman microscope equipped with a 532 nm wavelength (WL) green laser and a 600 grating. Each measurement comprised two acquisitions, each lasting 10 seconds for accumulation. The microscopy was performed at a magnification of x50, employing a microscope objective with a numerical aperture (NA) of 0.55. Considering the wavelength of the laser used, the resulting spot size was calculated to be approximately 1.18 µm, following the formula for spot size determination shown in equation (26).

$$Spot\ Size = \frac{1.22 \times WL}{NA} \quad (26)$$

Considering that the used confocal Raman spectrometer just penetrates 1.18 µm in the material, which is a relatively low depth, it implies that the monoclinic 8YSZ has been transformed at the very surface in a much localized manner. In contrast, in the sample zone characterized by E_{high}, $t \rightarrow m$ phase change has not been registered; note that in this zone the high energy of the jet creates cracks on the material inducing a brittle fracture and removing the upper regions. Hence, due to the occurrence of material removal, in this region, new material is continuously exposed to the PWJ, situation that leads to “loss of history” of possible $t \rightarrow m$ transformations. Due to this the E_{low} area was used to understand the high strain rate microscale deformation and fracture.

Nonetheless, to reveal how the martensitic $t \rightarrow m$ transformation is happening at a nanoscale level in the E_{low} region, lamellas were extracted and prepared from a single droplet impacted 8YSZ surface using a Focused Ion Beam (FEI Quanta200 3D FIB-SEM). As shown in Figure 96, Transmission Electron Microscopy (TEM) analysis has been further conducted to reveal how the shock affected the local microstructure.

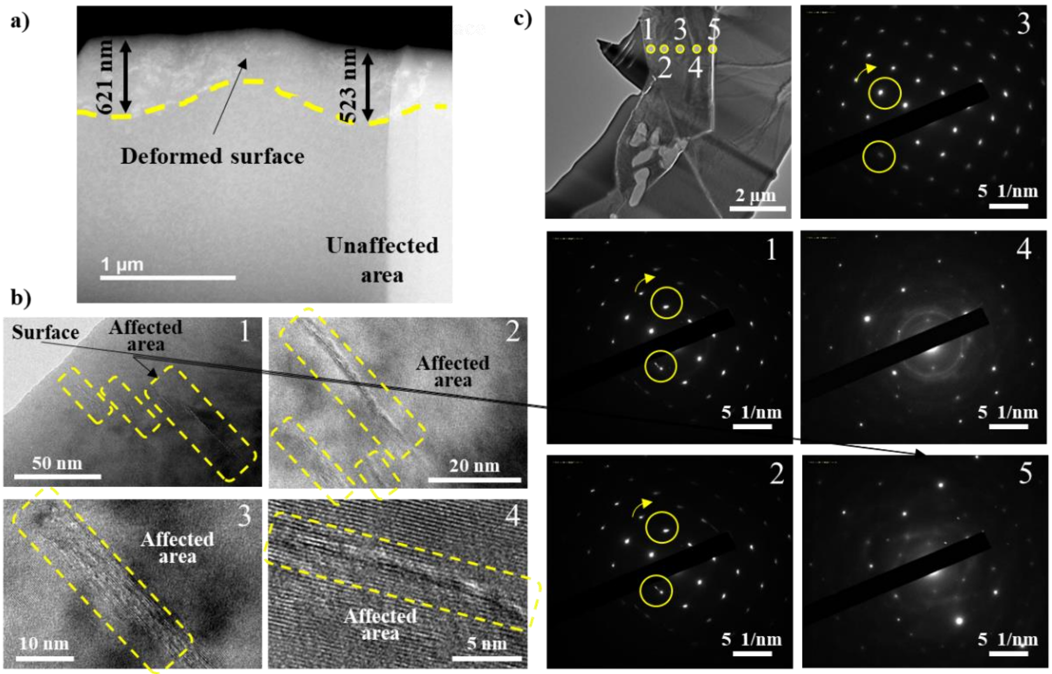

Figure 96: *a) General view of the lamella in the HAADF STEM in where defects created by the process can clearly be seen in the first 500 – 600 nm from the surface. b) BF TEM images showing an acicular dislocation build up that leads to the initial phases of a defect. c) SADP TEM diffraction patterns obtained from a STEM image of a HSR water droplet impact lamella (E_{low}) shows residual strain in the top being released while getting deeper beneath the surface while indicating a phase change when reaching the crack.*

Figure 96a shows a TEM study of an E_{low} region. It can be observed that the damage induced by a high strain impact is concentrated within the first 500 - 600 nm. The diffraction contrast observed within that area suggested the formation of a highly deformed region. Figure 96b shows high-resolution images of the defect present in the deformed area. These show acidulated discontinuities at the atomic scale that could act as defect initiators (e.g. crack initiation zones). Figure 96c shows another E_{low} region where cracks have propagated. Diffraction patterns from the surface inwards show the localised residual strain in the surface that gets relaxed in the bulk. All this evidenced point out that the propagation of cracks leads to a localised $t \rightarrow m$ transformation that induces a transformation toughening procedure. This happens when a crack starts to form in YSZ due to an applied force, the material around the crack tip undergoes a transformation that effectively "closes" the crack or prevents it from propagating further. This process absorbs some of the energy that would have otherwise caused the crack to grow, making the material more resistant to fracture. As a result, the material becomes tougher and less prone to catastrophic failure (see Figure 97) [137], [138]. This observations match with the previously observed with Raman spectroscopy results.

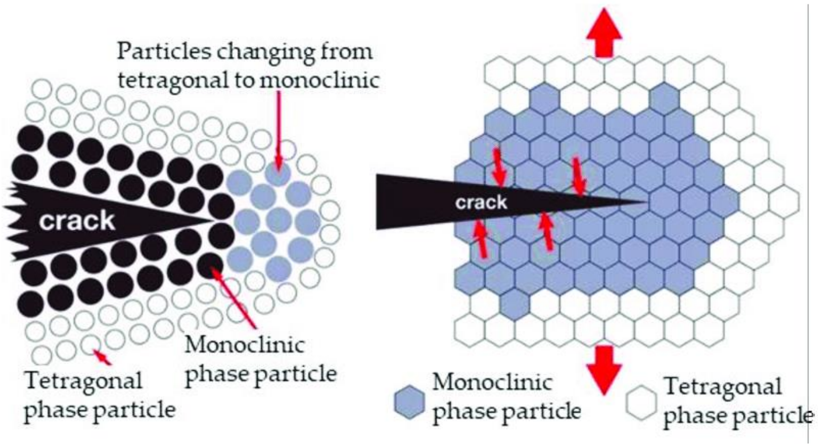

Figure 97: *Transformation toughening process induced by crack propagation* [137].

7.3.2. Low strain rate (LSR) impact analysis in YSZ

However, with the aim of observing the effect of the strain rate in 8YSZ nanoindentation tests have been performed in the region of 10^{-3} s^{-1} to 10 s^{-1}, which are considerably lower than the ones generated with the PWJ milling process that go over 10^{6} s^{-1}. This situation offered the opportunity to explore the effect and differences that the strain rate can cause in the $t \rightarrow m$ transition phenomena by a single impact in a single crystal 8YSZ.

For this study, an SEM in-situ nanoindenter equipped with a diamond spherical tip (Ø40 µm) was used to mimic the shape of the water droplet as much as possible and access lower values of strain rate. The indentations have been analysed by studying the relationship between the indentation depth (h) and the loading/unloading (P) forces that relate to the indentation energies and which are calculated from the area underneath the load and unload curve (Figure 98a and b) [139]. Figure 98c shows that the elastic/plastic ratio, often referred to as the "elastic/plastic slope" or the ratio of elastic modulus to yield strength (i.e. m) grows logarithmically while increasing the strain rate from 10^{-3} to 1 s^{-1}. This ratio is a measure of a material's ability to undergo elastic deformation before transitioning into plastic (permanent) deformation. A higher elastic-plastic ratio indicates that a material can withstand more elastic deformation before undergoing plastic deformation. When comparing it to its strain rate sensitivity, if the elastic-plastic ratio increases as the strain rate increases, it generally suggests that the material is becoming more resistant to plastic deformation at higher strain rates. Moreover, Figure 98d shows how the hardness is also strain rate dependent suggesting a strain hardening phenomena at room temperature generated by the creation of defects in the lattice structure, similar to the findings of D. Xiao et al. [140] in pure zirconia.

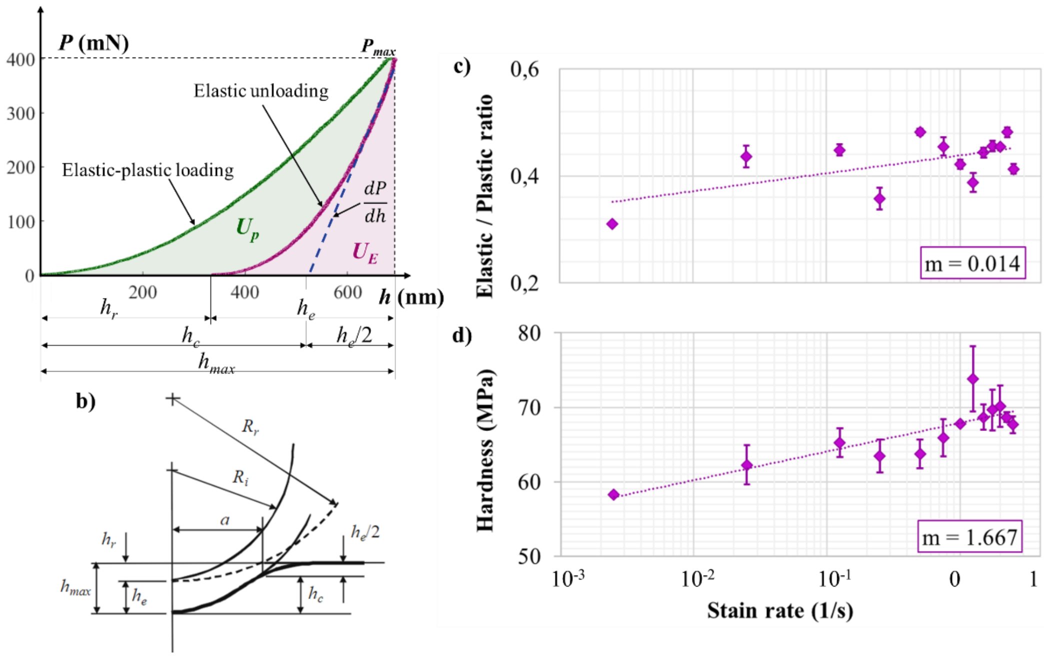

Figure 98: *a) Exemplary P-h diagram obtained at 10 mN/s loading and 5 mN/s unloading and a 10 s hold time that describes the diagrams parameters and the schematic representation of the deformation under a spherical tip and b) the description of the relevant.*

Brittleness is a measure of a material's tendency to fracture without undergoing significant plastic deformation. An increase of this property implies a higher chance of fracturing with minimal plastic deformation. While the relationship between strain rate sensitivity, elastic-plastic ratio, hardness and brittleness is intricate and influenced by multiple factors, results from Raman and TEM observations suggest that an elevated elastic-plastic ratio concerning the material's strain rate suggests a shift towards a more brittle behaviour in 8YSZ.

7.4. Discussion

The comparison of the SEM images of the low strain rate (LSR) indentations performed with the nanoindenter (Figure 99a) with those obtained at high strain rate (E_{low} in Figure 93e) support the analysis shown in Figure 98c. While the craters generated at high strain (>10^6 s^{-1}) show evidence of brittle fracture, the indentations at low strain rates (10^{-3} to 1 s^{-1}) show material pile up at the edge, indicating a more ductile behaviour. However, there are also differences between the results obtained at the low range (i.e. 10^{-3} s^{-1} and 1 s^{-1}), as cracking increases with the strain rate (see Figure 99a).

Moreover, it is also important to acknowledge that even if the setups of high and low strain rate have been compared to tests the material properties, there are fundamental differences between them. PWJ droplets can be deformed and redistribute residual stresses when indenting the surface (at high strain) while for the diamond indentation the tip is considered non deformable [103]. However, this still demonstrates that a ductile to brittle transition at the micron scale can be achieved in 8YSZ when reaching high enough strain rates.

In contrast with the high strain rate (HSR) results (>10^6 s^{-1} in Figure 95) the Raman spectra for the LSR tests (from 10^{-3} to 1 s^{-1} in Figure 99b) show that there is no $t \rightarrow m$ phase transformation. This suggests that the low strain rates are not enough to trigger this change (i.e. the elastic/plastic ratio is too low) and hence that this transformation is linked to the speed required to propagate the discontinuities in zirconia or that at LSR not enough defects are generated to trigger any transformation.

With the results presented above, it can be concluded that the LSR deformation applied with a non-deformable tool induces a ductile deformation mechanism and no phase transformation. The fact that a phase transformation can be seen at HSR (>10^6 s^{-1}) whereas in the LSR indentations (10^{-3} to 1 s^{-1}) this is not observed suggests that the phenomenon is strongly related to the strain rate and the ductile-to-brittle transition at the micron scale. That might also explain why this has not previously been reported. Furthermore, in order to fully identify what happens at different strain rates it would be of considerable interest to complete the range of strain rates missing in the presented results (i.e. from 1 s^{-1} to 10^6 s^{-1}) in a future work.

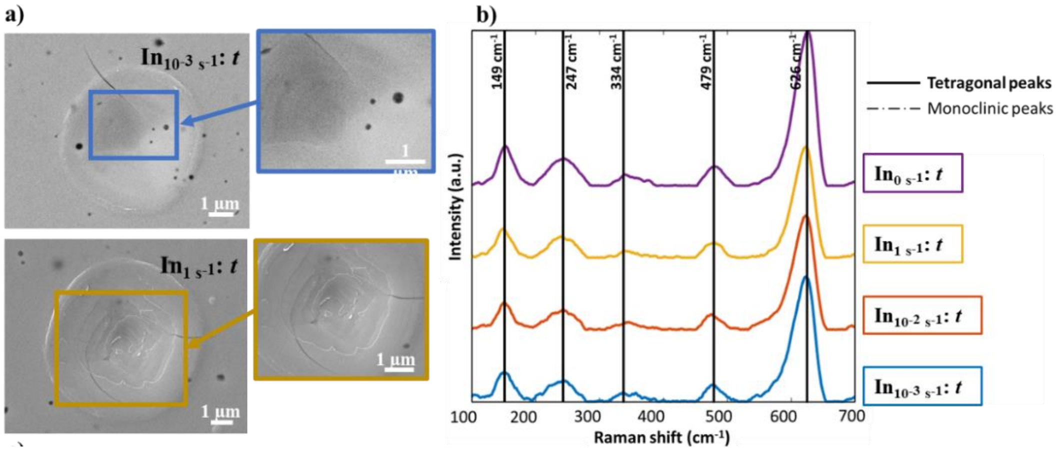

Figure 99: *a) SEM images of the indentations at 10^{-3} s-1 and 1 s^{-1} order of magnitude stain rates, b) Raman spectroscopy results of the indentation at all the analysed strain rates showing the absence of monoclinic phase.*

7.5. Concluding remarks

Following the objective of investigating how 8YSZ behaves at small scale when being exposed to impacts at high and low strain rates, it has been seen that 8YSZ $t \rightarrow m$ transformations only happen at high strain rates (>10^6 s^{-1}) but not at low (<1 s^{-1}). Hence, this arises the question if there is a threshold that could trigger this $t \rightarrow m$ transformation.

- With the impact tests at HSR a $t \rightarrow m$ phase transformation has been reported after Raman spectroscopy analysis at the E_{low} region. This phenomenon happens in 8YSZ at the very surface and at a localized manner (in this case induced by PWJ impact). However, there is no transformation registered in the E_{high} zone as the high energy of the jet creates cracks on the material inducing a brittle fracture and removing the upper regions. Due to this occurrence of material removal, new material is continuously exposed to the PWJ, situation that leads to “loss of history” of possible $t \rightarrow m$ transformations.

- Moreover, the high-resolution TEM analysis in high strain rate impact areas show needle shape discontinuities oriented in a preferential direction, affecting the first ~ 600 nm from the surface and which could act as crack induction points. Multiple cracks have also been observed in those regions and it is believed that they could act as nucleation points for the phase transformation measured with Raman Spectroscopy.
- On the other hand, micro indentations in 8YSZ, using a spherical indenter, at an interval of 10^{-3} s^{-1} to 1 s^{-1} strain rate shows that the elastic/plastic ratio and hardness grows logarithmically while increasing the strain rate. This demonstrates that the material behaving in a ductile or brittle manner is influenced by the strain rate.
- Finally, for the indentations performed at the strain rates ranging between 10^{-3} s^{-1} and 1 s^{-1} there was no indication of $t \rightarrow m$ transformation. It is believed that this lack of phase transformation is linked to the absence of cracks dominating the failure mechanism.

Chapter 8

Conclusions of the research and future work evaluation

After the development of the project, this final chapter presents a summary of the project focusing on the final conclusions along with the research gaps left for future analysis.

8.1. Conclusions

Overall, PWJ technology is a versatile and increasingly popular manufacturing process that has a wide range of applications across various industries. With the ability to cut a variety of materials to precise specifications without causing thermal damage, PWJ technology has become a preferred method for many manufacturing and production operations. The aim of the PhD research project is to implement the plain waterjet technology to remove the aerospace coatings in an effective, fast and economical way, ensuring no damage to the substrate underneath the coatings. Ideally, these parts should be ready to be recoated and be installed in the engine again after ensuring their mechanical properties are still adequate after being cleaned.

Chapter 1 describes how Plain Water Jet machining is one of the most promising technologies to do so. The main goal is to identify the main challenges when applying this technology and develop a model to predict how the coatings are going to be removed as well as analysing what happens structurally in the process to the water impacted material. Chapter 2 develops the basis of WJ milling technology. It, presents a comprehensive literature review analysing the development that this technology has overcome as well as the mathematical tools that have evolve to support it. Chapter 3 describes the necessary materials and equipment used in order to develop this project. This includes a detailed explanation of the Water Jet machines used in this project, including the types of nozzles. Moreover, all the different test materials as well as all the used tolls and the sample preparation processes for the experimental process for the model validation and the materials analysis are defined as well as the material analysis techniques and the machines used for those purposes. Chapter 4 describes the development of the mathematical model design to calculate the jet footprint to remove multi-material coatings. First, the importance of the nozzle choice is analysed in addition to the calculation of their kinematics. Soon after, the model itself is defined: this is based on the understanding of the etching rate considering the mechanical properties of each individual material layer that compounds a coating and the energy of a PWJ system. This interaction has been obtained for any specific pressure, considering the energy variations along the height of the jet, for one or multiple jets, which follows a defined arbitrary trajectory in a 3D space, during a period of time. Finally, a particular case in reference to the coating removal of pocket edges has also been analysed. Chapter 5 explains the construction of the designed software (SW) application developed in MATLAB AppDesigner with this aim. For this section a set of parameters has been selected as an example and the program has been simulated so the reader will be guided step by step through the parameter setting, calculation process and results analysis while using the program. Chapter 6 validates the developed mathematical model for both nozzle heads in test samples. Afterwards, to prove it in a real case application in an industrial environment, a test that consists in successfully cleaning a combustion chamber with coating strips in Rolls-Royce facilities is described. Finally, a study in order to further understand the material removal mechanism is discussed. Chapter 7 describes a case study to understand the material removal mechanisms generated by the jet of a WJ machine when impacting the target material at high pressure. For this, one of the most used materials in aerospace coatings has been chosen: Yttria Stabilized Zirconia (YSZ) is generally used as the top coat on the so called Thermal Barrier Coatings (TBC). To carry out this analysis, Raman spectroscopy, TEM analysis and different strain rate nanoindentations have been performed. Finally, this 8^{th} Chapter summarises the project as well as presenting its conclusions and the ideas for future works.

8.1.1. Chapter 4: Development of the mathematical model for multi material coating removal with WJ milling

Overall, a highly versatile model that predicts the eroded patches (i.e. overlapped jet footprints) produced by rotational plain water jet nozzle heads has been developed. This enables a controlled removal of coating used in aerospace systems in a robust manner (i.e. no damage to the substrate and a full removal of the coating). The innovation consists on this model, unlike previous ones, considering multiple layer coatings and the mechanical properties of each of the individual layers. Mathematically it is based on the understanding of the etching rate (i.e. calculation of the depth of material that has been removed).

- First, the flows of both of the considered nozzle heads (i.e. four jet rotational and fan jet nozzles) as well as their kinetics have been calculated, followed by the definition of the energy model of a Plain Water Jet (PWJ) system. The energy model is defined by the energy distribution of a rotary jet for an arbitrary trajectory in a 3D space, pursued by the characterization of the target material considering an arbitrary number of coating layers. Finally, the interaction between the jet and the target material has been defined. This interaction is obtained for any specific pressure, considering the energy variations along the height of the jet, for one or multiple jets, which follows a defined arbitrary trajectory, during a defined period of time. However, a calibration data will still be needed to include the individual material mechanical properties.
- The model has been upgraded for calculating single and multiple trenches that are able to overlap, flat and curved surfaces and calculation of the milling time for flat and rounded parts. Finally, the particular case of the edge of a pocket section has also been studied considering that in this example the coating is not always parallel to the substrate layer.

8.1.2. Chapter 5: Development of the Software to apply the mathematical model in an industrial environment

This chapter describes the implementation of a user's friendly interface to the model developed in Chapter 4. This is necessary in order to be able to use the model in an efficient way in an industrial environment. The highlights of the applications are described as follow:

- The app is design to be able to choose between a four jet and fan rotational nozzle head, flat or curved samples that could be cleaned from the inside or outside and to choose if a single trench or multiple trenches will be simulated with different degrees of overlapping.
- The software has an attractive design that guides the user step by step through the tabs that are organized in a sequential order: the input parameters are required in the first place, followed by the presentation of the results and the particular case is shown at the end.
- Elements that help the user navigate the application have also been implemented in the SW such as the descriptions in the questions marks and further details when clicking the images. These elements help make the interface more accessible.
- The overall results of the simulation (i.e. the energy map as well as the milled trench) are showed in the UI app. However, for an easier interpretation of the results, these are shown with a four colour system that indicates if the coating has been fully or partially removed or if the substrate has been damaged. Moreover, a feature that calculates the time to clean a 1 m^2 plate as well as defined dimension rounded part has also been included.
- The option to generate an automatic pdf report is asked. Thanks to this is easy to keep track of the performed simulations over the time.
- Finally, while the UI implementation offers numerous benefits, it presents certain limitations too: new nozzle addition requires manual coding, part and mesh size adjustments are only feasible through raw code modification, a maximum of three coating layers are allowed, nozzle path options are restricted to parallel lines, five overlapping trenches is the computational limit, and the UI confines analysis to specific geometric shapes, necessitating manual code inclusion for more diverse shapes. As future work, user

conformability test is encouraged, ensuring that any necessary improvements to the UI features are identified and addressed.

8.1.3. Chapter 6: Assessment of material removal capabilities of the developed mathematical model

Overall, the validation of the mathematical model presented by comparing the predictions with the results of real milling of coated samples are presented in this section. Two types of nozzles will be tested at different parameters (i.e. translational speed, pressure and overlapping separation) to evaluate and understand the effect of each in the material removal. The main conclusions drawn from this work are as follows:

- The tests done with the four jet rotational nozzle proved that the density of the overlapped jet footprints depends on the kinematic of the process (i.e. ratio between the rotational and translational speeds) which could result in a non-uniform eroded patch. The model is able to predict such discrepancies (i.e. unremoved coatings) at good accuracy, max. 4.5% in the middle and 27% at the edges of the trenches respectively; increased error in the latter case is related to secondary effects of the process (e.g. secondary material cracking). Nevertheless, non-uniform eroded patches is not the scope of the coating removal process, hence, it is considered that model predictions are acceptable in this working scenario.
- The consistency of the coating removal has been demonstrated by the use of SEM and EDX material analysis proving that the kinematics and the multiple jet footprints can be optimized by the model, so that components with no coating residual on the substrate are obtained.
- From the experiments done with the fan nozzle it can be concluded that in some cases, it is preferable to use a lower pressure and higher translational speed, even if not all the coating is removed, to ensure that no damage is done

to the substrate. By controlling the overlapping separation, a good removal of the coating can be achieved while the pressure and translational speed are far from critical values that could ruin the sample.

- The importance of the model interpretation using the street light system has also been validated, as in some cases it is not possible to visualize the damage in the original modelled due to the scale of the graph. By separating the depths into contrasting colours, the different segments of the trench are highlighted and easily identified.
- The experiments performed at Rolls-Royce showed that the parameters they used are valid, but still generate some stripping on the workpiece, which even if it is in the allowed damage range, could potentially be detrimental in the long term. For that reason, some new parameters obtained from the mathematical model have been proposed and tested, showing a better result without any damage on the workpiece. Furthermore, the model has been validated to be able to predict when some parameters will not be valid, by relating the model with real case experiments with a maximum error of 4%.
- Finally, a theory for the material removal mechanism has been proposed and proven via EDX and SEM analysis. By studying the results of the trenches done with the waterjet, it has been confirmed that due to the heterogeneities of the coating material, cracks grow at the edges breaking the material from there. That explains why in some cases the model and the real trenches have differences, as this behaviour is not predictable, and hence cannot be implemented into the mathematical model.

8.1.4. Chapter 7: Study of the effect of the material removal mechanism of the PWJ milling in YSZ: Case study

Following the objective of investigating how 8YSZ behaves at small scale when being exposed to impacts at high and low strain rates, it has been seen that

8YSZ $t \rightarrow m$ transformations only happen at high strain rates (>10^6 s^{-1}) but not at low (<1 s^{-1}). Hence, this arises the question if there is a threshold that could trigger this $t \rightarrow m$ transformation.

- With the impact tests at HSR a $t \rightarrow m$ phase transformation has been reported after Raman spectroscopy analysis at the E_{low} region. This phenomenon happens in 8YSZ at the very surface and at a localized manner (in this case induced by PWJ impact). However, there is no transformation registered in the E_{high} zone as the high energy of the jet creates cracks on the material inducing a brittle fracture and removing the upper regions. Due to this occurrence of material removal, new material is continuously exposed to the PWJ, situation that leads to "loss of history" of possible $t \rightarrow m$ transformations.
- Moreover, the high-resolution TEM analysis in high strain rate impact areas shows needle shape discontinuities oriented in a preferential direction, affecting the first ~ 600 nm from the surface and which could act as crack induction points. Multiple cracks have also been observed in those regions and it is believed that they could act as nucleation points for the phase transformation measured with Raman Spectroscopy.
- On the other hand, micro indentations in 8YSZ, using a spherical indenter, at an interval of 10^{-3} s^{-1} to 1 s^{-1} strain rate shows that the elastic/plastic ratio and hardness grows logarithmically while increasing the strain rate. This demonstrates that the material behaving in a ductile or brittle manner is influenced by the strain rate.
- Finally, for the indentations performed at the strain rates ranging between 10^{-3} s^{-1} and 1 s^{-1} there was no indication of $t \rightarrow m$ transformation. It is believed that this lack of phase transformation is linked to the absence of cracks dominating the failure mechanism

8.2. Future work

Despite the significant advances in PWJ technology, there is still much to be done in terms of optimizing the process and expanding its applications. Future research could focus on developing more accurate and efficient models to predict the behaviour of water jets and optimize process parameters for different materials and cutting geometries. Moreover, there is an increasing demand for environmentally sustainable manufacturing processes, and future work could investigate ways to reduce the energy consumption of only-water high pressure WJ technology or to explore new WJ milling techniques that utilize renewable energy sources. By addressing these challenges and opportunities, future research can help to advance its capabilities and drive further innovation in manufacturing and production industries. The following section discusses ideas that could be developed regarding the developed project:

8.2.1. Chapter 4: Development of the mathematical model for multi material coating removal with WJ milling

One of the key research points of this project has been the development of the mathematical model to predict full 3D kerfs of water jet milled trenches in multi material coatings. Hence, even if the model has been proven to do its job it still has improvements that can be implemented to upgrade it.

- The developed model could have an option integrated to upload freeforms (i.e. complex geometries) and the SW could consider them as the milling surface that the high pressure jet will follow to simulate the created kerfs for optimal surface cleaning.
- The four and fan jet rotational nozzles, even though they were the most interesting ones for the current applications, are not the only ones in the market. Other nozzles suitable for milling large areas could be considered to study them mathematically and implement them as options in the model.

Even more, pros and cons of the studied nozzles can be considered to design and develop an optimal coating removal nozzle.

- As in the case of the nozzles there are many more coating layers and substrate materials implemented in the aero engines. The model could be proven in other materials. Based on this, if enough materials are tested a library could be created that recorded different material coefficients so calibration tests will not be necessary every time that new parameters are needed to be tested.
- In order to calculate the material removed for an amount of energy that reaches the substrate the involved material is considered continuous and homogeneous. However, this is never going to be the case as due to the manufacturing processes and the damage induced during service the coating materials will always present irregularities. As the next step of improving the accuracy of the model this could also be considered.

8.2.2. Chapter 5: Development of the Software to apply the mathematical model in an industrial environment

After developing the model, this has been implemented into a SW to ease the use. In this aspect there are also some future actions that could be taken for improvement.

- Although the application is fully functional, the script of the code could be optimized to make the simulations faster. This would both reduce the time needed to define the best parameters, and also decrease the hardware specification requirements for the computer.
- The user's interface could also be improved to implement any new features implemented to the model. Furthermore, the data collected from real user's experience would also be useful to determine the most useful characteristics to enhance them or any necessary refinement.

8.2.3. Chapter 6: Assessment of material removal capabilities of the developed mathematical model

In this chapter the material model has been proved comparing simulated kerfs with real life milled trenches. Moreover, the material removal mechanism of coating layer removal has been studied. Here are some future line ideas:

- To demonstrate the model's predictive power in different configurations, simulations and experiments in other materials would be intriguing. To demonstrate the model's predictive power in different configurations, simulations and experiments in other materials would be intriguing. By milling trenches in a wide variety of materials and geometries the model could be improved to make it more accurate for future applications.
- Alternativelly, further studies could be done for better understanding the material removal mechanism. By doing it, the behaviour could be predicted and thus it would be possible to implement it in the model to achieve better predictions of the trench geometries.

8.2.4. Chapter 7: Study of the effect of the material removal mechanism of the PWJ milling in YSZ: Case study

In this chapter a water jet and a high strain rate nanoindentation were used to understand how the behaviour of fully stabilized zirconia changes upon different strain rates (from 10^{-3} to 10^{8} s^{-1}). It was observed that at extremely high strain rates (10^{6} - 10^{8} s^{-1}) the material suffers from a brittle-dominated failure which induces localized phase transformation even if the materials is in its fully stabilized form. On the other hand, at lower strain rates, plasticity dominates, and phase transformation is not observed. However, this work left some open aspects that could be further studied:

- The strain rate study done with the water jet and the nanoindenter could be followed by doing more experiments at the missing strain rate values. By filling the gaps between the low and high strain rate tests, the evolution of the material could be studied and the phenomena further understood.

- It would be of great interest to continue studying the impact of the waterjet at high speeds on different coating materials and especially on substrates generally used in aerospace. This would aim towards the goal of having a full understanding of the impact of the waterjet impact at high velocities into the target material, and its effect in the material removal mechanisms.

References

[1] T. Sharp and K. Hickok, "The world's first commercial airline," *Space*, Mar. 2022.

[2] Airbus, "Global market forecast 2017–2036.," 2016.

[3] Boeing, "Current market outlook 2017–2036," 2016.

[4] S. Foster, V., Dim, J., Zhang, F., & Vollmer, "How can we explain the rise in transport emissions... and what can we do about it?," *Transport for Development*, 2021. https://blogs.worldbank.org/transport/how-can-we-explain-rise-transport-emissions-and-what-can-we-do-about-it (accessed Jan. 26, 2023).

[5] M. Masiol and R. M. Harrison, "Aircraft engine exhaust emissions and other airport-related contributions to ambient air pollution: A review," *Atmos Environ*, vol. 95, pp. 409–455, 2014, doi: 10.1016/j.atmosenv.2014.05.070.

[6] W. Song *et al.*, "Impact interaction of in-flight high-energy molten volcanic ash droplets with jet engines," *Acta Mater*, vol. 171, pp. 119–131, 2019, doi: 10.1016/j.actamat.2019.04.011.

[7] R. McPherson, "A review of microstructure and properties of plasma sprayed ceramic coatings," *Surf Coat Technol*, vol. 39–40, no. C, pp. 173–181, 1989, doi: 10.1016/0257-8972(89)90052-2.

[8] D. R. Clarke and S. R. Phillpot, "Thermal barrier coating materials," *Materials Today*, vol. 8, no. 6, pp. 22–29, Jun. 2005, doi: 10.1016/S1369-7021(05)70934-2.

[9] N. P. Padture, M. Gell, and E. H. Jordan, "Thermal barrier coatings for gas-turbine engine applications," *Science (1979)*, vol. 296, no. 5566, pp. 280–284, 2002, doi: 10.1126/science.1068609.

[10] M. Legrand, A. Batailly, and C. Pierre, “Numerical investigation of abradable coating removal in aircraft engines through plastic constitutive law,” *J Comput Nonlinear Dyn*, vol. 7, no. 1, 2012, doi: 10.1115/1.4004951.

[11] N. Salvat, A. Batailly, and M. Legrand, “Modeling of abradable coating removal in aircraft engines through delay differential equations,” *J Eng Gas Turbine Power*, vol. 135, no. 10, 2013, doi: 10.1115/1.4024959.

[12] M. O. Jarligo, T. Steinke, D. E. Mack, and D. Stöver, “Overview on advanced thermal barrier coatings,” *Surf Coat Technol*, vol. 205, no. 4, pp. 938–942, Nov. 2010, doi: 10.1016/J.SURFCOAT.2010.08.151.

[13] Y. Tamarin, *Protective coatings for turbine blades*. United Staters of America: ASM International, 2002.

[14] E. O. Ezugwu, “Key improvements in the machining of difficult-to-cut aerospace superalloys,” *Int J Mach Tools Manuf*, vol. 45, no. 12–13, pp. 1353–1367, Oct. 2005, doi: 10.1016/J.IJMACHTOOLS.2005.02.003.

[15] P. Caron and T. Khan, “Evolution of Ni-based superalloys for single crystal gas turbine blade applications,” *Aerosp Sci Technol*, vol. 3, no. 8, pp. 513–5233, Dec. 1999, doi: 10.1016/S1270-9638(99)00108-X.

[16] T. Ford, “Single crystal blades,” *Aircraft Engineering and Aerospace Technology*, vol. 69, no. 6, pp. 564–566, 1997, doi: 10.1108/00022669710186589.

[17] P. Purushothaman, “Assignment: Design of Machine Element and Manufacturing Processes,” no. February 2012, 2012, doi: 10.13140/2.1.2551.9366.

[18] N. P. Padture, “Thermal Barrier Coatings for Gas-Turbine Engine Applications,” *Science (1979)*, vol. 296, no. 5566, pp. 280–284, Apr. 2002, doi: 10.1126/science.1068609.

[19] Y.-S. Song, I.-G. L. A, D. Y. Lee, D.-J. Kim, S. Kim, and K. Lee, "High-temperature properties of plasma-sprayed coatings of YSZ/NiCrAlY on Inconel substrate Yo-Seung," *Materials Science and Engineering*, vol. 332, pp. 129–133, 2002, doi: 10.1109/IEEEGCC.2015.7060017.

[20] C. J. Munez, P. Poza, and J. Go, ez-Garcia, "TEM analysis of the microstructure of thermal barrier coatings after isothermal oxidation," vol. 60, pp. 7197–7206, 2012, doi: 10.1016/j.actamat.2012.09.028.

[21] S. Dhomne and A. M. Mahalle, "Thermal barrier coating materials for SI engine," *Journal of Materials Research and Technology*, no. x x, pp. 6–11, 2018, doi: 10.1016/j.jmrt.2018.08.002.

[22] H. Zhao, F. Yu, T. D. Bennett, and H. N. G. Wadley, "Morphology and thermal conductivity of yttria-stabilized zirconia coatings," *Acta Mater*, vol. 54, no. 19, pp. 5195–5207, Nov. 2006, doi: 10.1016/j.actamat.2006.06.028.

[23] N. T. Paper, "Overview of Zirconia With Respect to Gas Turhine Applications," 2019.

[24] G. Witz, V. Shklover, W. Steurer, S. Bachegowda, and H. P. Bossmann, "Phase evolution in yttria-stabilized zirconia thermal barrier coatings studied by rietveld refinement of X-ray powder diffraction patterns," *Journal of the American Ceramic Society*, vol. 90, no. 9, pp. 2935–2940, 2007, doi: 10.1111/j.1551-2916.2007.01785.x.

[25] Y. Dong, L. Qi, J. Li, and I. Chen, "A computational study of yttria-stabilized zirconia: II. Cation diffusion," *Acta Mater*, vol. 126, pp. 438–450, Mar. 2017, doi: 10.1016/j.actamat.2017.01.008.

[26] Y. Hemberger, C. Berthold, and K. G. Nickel, "Simultaneous phase and chemistry analysis in YSZ by Raman spectroscopy," *14th Biennial Worldwide Congress on Unified International Technical Conference on Refractories,*

UNITECR 2015, in conjunction with the 58th International Colloquium on Refractories, no. November 2016, 2015.

[27] G. Pezzotti and A. A. Porporati, “Raman spectroscopic analysis of phase-transformation and stress patterns in zirconia hip joints,” *J Biomed Opt*, vol. 9, no. 2, p. 372, 2004, doi: 10.1117/1.1647547.

[28] K. Yasuda, M. Itoh, S. Arai, T. Suzuki, and M. Nakahashi, “Phase transformation of yttria-stabilized zirconia plasma-sprayed coatings in a humid atmosphere,” *J Mater Sci*, vol. 32, no. 23, pp. 6291–6297, 1997, doi: 10.1023/A:1018649530154.

[29] G. M. WOLTEN, “Diffusionless Phase Transformations in Zirconia and Hafnia,” *Journal of the American Ceramic Society*, vol. 46, no. 9, pp. 418–422, 1963, doi: 10.1111/j.1151-2916.1963.tb11768.x.

[30] D. Tejero-Martin, M. R. Rad, A. McDonald, and T. Hussain, “Beyond traditional coatings, a review on thermal sprayed functional and smart coatings,” vol. 1289, no. 4, pp. 78–84, 2013.

[31] J. Singh and D. E. Wolfe, “Nanostructured component fabrication by electron beam-physical vapor deposition,” *J Mater Eng Perform*, vol. 14, no. 4, pp. 448–459, 2005, doi: 10.1361/105994905X56223.

[32] S. N. Kane, A. Mishra, and A. K. Dutta, “Simulation of the prticle melting degree in air plasma spraying,” *J Phys Conf Ser*, vol. 755, no. 1, pp. 1–13, Oct. 2016, doi: 10.1088/1742-6596/755/1/011001.

[33] K. Von Niessen and M. Gindrat, “Plasma spray-PVD: A new thermal spray process to deposit out of the vapor phase,” *Journal of Thermal Spray Technology*, vol. 20, no. 4, pp. 736–743, 2011, doi: 10.1007/s11666-011-9654-9.

[34] M. Dorfman, U. Erning, and J. Mallon, “Gas turbines use ‘abradable’ coatings for clearance-control seals,” *Sealing Technology*, no. 97, pp. 7–8, 2002, doi: 10.1016/s1350-4789(02)80002-2.

[35] F. Mohammad, M. Mudasar, and A. Kashif, “Criteria for Abradable Coatings to Enhance the Performance of Gas Turbine Engines,” *Journal of Material Science and Metallurgy*, vol. 2, no. 1, pp. 1–7, 2021.

[36] J. Stringer and M. B. Marshall, “High speed wear testing of an abradable coating,” *Wear*, vol. 294–295, pp. 257–263, 2012, doi: 10.1016/j.wear.2012.07.009.

[37] H. Wang, “Criteria for analysis of abradable coatings,” *Surf Coat Technol*, vol. 79, no. 1–3, pp. 71–75, Feb. 1996, doi: 10.1016/0257-8972(95)02443-3.

[38] H. I. Faraoun *et al.*, “Improvement of thermally sprayed abradable coating by microstructure control,” *Surf Coat Technol*, vol. 201, no. 6, pp. 2303–2312, 2006, doi: 10.1016/j.surfcoat.2006.03.047.

[39] Y. Cui, M. Guo, C. Wang, J. Jiao, and L. Cheng, “Zirconia-based abradable coatings fabricated on single-crystal superalloy: Microstructure, residual stress and mechanical properties,” *J Alloys Compd*, vol. 907, p. 164537, 2022, doi: 10.1016/j.jallcom.2022.164537.

[40] Y. Fu, C. Shao, C. Cai, Y. Wang, Y. Zhou, and G. Zhou, “Temperature induced structure degradation of yttria-stabilized zirconia thermal barrier coatings,” *Surf Coat Technol*, vol. 351, no. July, pp. 21–28, 2018, doi: 10.1016/j.surfcoat.2018.07.057.

[41] K. Chen, D. Seo, and P. Canteenwalla, “The effect of high-temperature water vapour on degradation and failure of hot section components of gas turbine engines,” *Coatings*, vol. 11, no. 9, pp. 1–26, 2021, doi: 10.3390/coatings11091061.

[42] K. J.-P. Bridges and D. R. Mumm, “Degradation Mechanisms in Ceramic Abradable Coatings for Hot Section Turbine Components,” *ProQuest Dissertations and Theses*, p. 119, 2018.

[43] C. Persson and P. O. Persson, “Evaluation of service-induced damage and restoration of cast turbine blades,” *J Mater Eng Perform*, vol. 2, no. 4, pp. 565–569, 1993, doi: 10.1007/BF02661742.

[44] I. R. Crystal and C. A. Schuh, “Grain-size effect on cracking accumulation in yttria-doped zirconia ceramics during cyclic martensitic transformations,” *Acta Mater*, vol. 209, pp. 1–10, 2021, doi: 10.1016/j.actamat.2021.116789.

[45] T. A. Tejedor, R. Singh, and P. Pilidis, *Maintenance and repair of gas turbine components*. 2013. doi: 10.1533/9780857096067.3.565.

[46] D. L. Monette, “Coating removal techniques in the aerospace industry,” in *Corrosion Control in the Aerospace Industry*, Elsevier, 2009, pp. 225–247. doi: 10.1533/9781845695538.3.225.

[47] X. Yang *et al.*, “Removal and repair techniques for thermal barrier coatings: a review,” *Transactions of the Institute of Metal Finishing*, vol. 98, no. 3, pp. 121–128, 2020, doi: 10.1080/00202967.2020.1750204.

[48] F. Klocke *et al.*, “Abrasive machining of advanced aerospace alloys and composites,” *CIRP Ann Manuf Technol*, vol. 64, no. 2, pp. 581–604, 2015, doi: 10.1016/j.cirp.2015.05.004.

[49] S. Bagherifard, R. Ghelichi, and M. Guagliano, “Numerical and experimental analysis of surface roughness generated by shot peening,” *Appl Surf Sci*, vol. 258, no. 18, pp. 6831–6840, 2012, doi: 10.1016/j.apsusc.2012.03.111.

[50] M. C. Kong, D. Axinte, and W. Voice, “Aspects of material removal mechanism in plain waterjet milling on gamma titanium aluminide,” *J Mater Process Technol*, vol. 210, no. 3, pp. 573–584, 2010, doi: 10.1016/j.jmatprotec.2009.11.009.

[51] Z. Coatings, “Chemical Milling Environmental Improvements, Aerospace is Green and Growing,” *Surface Technology White Papers*, vol. 101, no. February, pp. 1–10, 2014.

[52] B. Gysen and M. Malik, “Selective stripping of high temperature turbine blade coatings and aerospace braze materials,” *Surface Engineering*, vol. 5, no. 3, pp. 208–212, Jan. 1989, doi: 10.1179/sur.1989.5.3.208.

[53] X. Li *et al.*, “Laser paint stripping strategy in engineering application: A systematic review,” *Optik (Stuttg)*, vol. 241, no. April, p. 167036, 2021, doi: 10.1016/j.ijleo.2021.167036.

[54] D. Duke, Y. Kanda, K. Tobita, and R. Yamauchi, “Stripping and splicing polyimide-coated fibers,” May 2011, p. 77535V. doi: 10.1117/12.884940.

[55] A. Merati, M. Yanishevsky, and Y. Bombardier, “Effect of Alternative Paint Stripping Processes on the Fatigue Performance of Aluminium Alloys - Atmospheric Plasma De-painting,” 2020, pp. 589–599. doi: 10.1007/978-3-030-21503-3_47.

[56] M. Hashish, “WaterJet Machining Process,” *Handbook of Manufacturing Engineering Technology*, 2014.

[57] A. W. Momber and R. Kovacevic, *Principle of abrasive water jet machining*. London: Springer-Verlag, 1998.

[58] I. Sanchez, D. Axinte, and R. Smith, “Modelling of rotational multiple plain water jets for controlled removal of multi-material coatings,” *CIRP Annals*, vol. 69, no. 1, pp. 309–312, 2020, doi: 10.1016/j.cirp.2020.04.108.

[59] S. Anwar, D. A. Axinte, and A. A. Becker, “Finite element modelling of overlapping abrasive waterjet milled footprints,” *Wear*, vol. 303, no. 1–2, pp. 426–436, Jun. 2013, doi: 10.1016/J.WEAR.2013.03.018.

[60] M. C. Kong, D. Axinte, and W. Voice, “An innovative method to perform maskless plain waterjet milling for pocket generation: A case study in Ti-

based superalloys," *Int J Mach Tools Manuf*, vol. 51, no. 7–8, pp. 642–648, 2011, doi: 10.1016/j.ijmachtools.2011.04.006.

[61] M. C. Kong, D. Axinte, and W. Voice, "Challenges in using waterjet machining of NiTi shape memory alloys: An analysis of controlled-depth milling," *J Mater Process Technol*, vol. 211, no. 6, pp. 959–971, 2011, doi: 10.1016/j.jmatprotec.2010.12.015.

[62] James M. Sohr and Merle L. Thorpe, *Stripping of Thermal Spray Coatings with Ultra High Pressure Water Jet*. 1992.

[63] D. Ning *et al.*, "Experimental study on the coating removing characteristics of high-pressure water jet by micro jet flow," *Micromachines (Basel)*, vol. 12, no. 2, 2021, doi: 10.3390/mi12020173.

[64] Z. Liao, I. Sanchez, D. Xu, D. Axinte, G. Augustinavicius, and A. Wretland, *Dual−processing by abrasive waterjet machining—A method for machining and surface modification of nickel−based superalloy*, vol. 285, no. May. Elsevier, p. 116768. doi: 10.1016/j.jmatprotec.2020.116768.

[65] R. Melentiev and F. Fang, "Recent advances and challenges of abrasive jet machining," *CIRP J Manuf Sci Technol*, vol. 22, pp. 1–20, 2018, doi: 10.1016/j.cirpj.2018.06.001.

[66] D. S. Srinivasu and D. A. Axinte, "Surface integrity analysis of plain waterjet milled advanced engineering composite materials," *Procedia CIRP*, vol. 13, pp. 371–376, 2014, doi: 10.1016/j.procir.2014.04.063.

[67] J. H. Weber, M. G. Fahrman, and J. R. Crum, "Enciclopaedia of Materials: Science and Technology," in *Science and Technology*, Elsevier, Ed., Chicago, 2001, pp. 6135–6140.

[68] E. S. Geskin, M. C. Leu, F. Li, and L. Tismeneskiy, "An Analytical and Experimental Study of Cleaning With Moving Waterjets," *ASME*, vol. 120, no. March 1996, pp. 580–589, 1998.

[69] Z. Guo, T. Jin, L. Ping, A. Lu, and M. Qu, "Analysis on a deformed removal profile in FJP under high removal rates to achieve deterministic form figuring," *Precis Eng*, vol. 51, no. 1, pp. 160–168, 2018, doi: 10.1016/j.precisioneng.2017.08.006.

[70] P. L. Torrubia, J. Billingham, and D. A. Axinte, "Stochastic simplified modelling of abrasive waterjet footprints," *Proceedings of the Royal Society A: Mathematical, Physical and Engineering Science*, vol. 472, no. 2186, p. 20150836, Feb. 2016, doi: 10.1098/rspa.2015.0836.

[71] M. C. Kong, S. A. A, J. Billingham, and D. A. Axinte, "Mathematical modelling of abrasive waterjet footprints for arbitrarily moving jets: Part I - Single straight paths," *Int J Mach Tools Manuf*, vol. 53, no. 1, pp. 58–68, 2012, doi: 10.1016/j.ijmachtools.2013.01.003.

[72] D. A. Axinte, D. S. Srinivasu, J. Billingham, and M. Cooper, "Geometrical modelling of abrasive waterjet footprints: A study for 90° jet impact angle," *CIRP Ann Manuf Technol*, vol. 59, no. 1, pp. 341–346, 2010, doi: 10.1016/j.cirp.2010.03.112.

[73] G. B. J. Cadot, D. A. Axinte, and J. Billingham, "Continuous trench, pulsed laser ablation for micro-machining applications," *Int J Mach Tools Manuf*, vol. 107, pp. 8–20, 2016, doi: 10.1016/j.ijmachtools.2016.04.011.

[74] M. C. Kong and D. Axinte, "Response of titanium aluminide alloy to abrasive waterjet cutting : geometrical accuracy and surface integrity issues versus process parameters," *Proc Inst Mech Eng B J Eng Manuf*, vol. 223, pp. 19–42, 2009, doi: 10.1243/09544054JEM1226.

[75] J. Billingham, C. B. Miron, D. A. Axinte, and M. C. Kong, "Mathematical modelling of abrasive waterjet footprints for arbitrarily moving jets: Part II—Overlapped single and multiple straight paths," *Int J Mach Tools Manuf*, vol. 68, pp. 30–39, May 2013, doi: 10.1016/j.ijmachtools.2013.01.003.

[76] D. S. Srinivasu, D. A. Axinte, P. H. Shipway, and J. Folkes, "Influence of kinematic operating parameters on kerf geometry in abrasive waterjet machining of silicon carbide ceramics," *Int J Mach Tools Manuf*, vol. 49, no. 14, pp. 1077–1088, 2009, doi: 10.1016/j.ijmachtools.2009.07.007.

[77] A. Bilbao-Guillerna, D. A. Axinte, J. Billingham, and G. B. J. Cadot, "Waterjet and laser etching : the nonlinear inverse problem," *R Soc Open Sci*, vol. 4, p. 161031, 2017, doi: 10.1098/rsos.161031.

[78] A. Bilbao Guillerna, D. Axinte, and J. Billingham, "The linear inverse problem in energy beam processing with an application to abrasive waterjet machining," *Int J Mach Tools Manuf*, vol. 99, pp. 34–42, 2015, doi: 10.1016/j.ijmachtools.2015.09.006.

[79] A. Rabani, I. Marinescu, and D. Axinte, "Acoustic emission energy transfer rate: A method for monitoring abrasive waterjet milling," *Int J Mach Tools Manuf*, vol. 61, pp. 80–89, 2012, doi: 10.1016/j.ijmachtools.2012.05.012.

[80] D. A. Axinte and M. C. Kong, "An integrated monitoring method to supervise waterjet machining," *CIRP Annals*, vol. 58, no. 1, pp. 303–306, 2009, doi: 10.1016/j.cirp.2009.03.022.

[81] L. Huang, P. Kinnell, and P. H. Shipway, "Removal of heat-formed coating from a titanium alloy using high pressure waterjet: Influence of machining parameters on surface texture and residual stress," *J Mater Process Technol*, vol. 223, pp. 129–138, Sep. 2015, doi: 10.1016/j.jmatprotec.2015.03.053.

[82] J. M. Reichman and J. B. Cheung, "An oscillating waterjet deep-kerfing technique," *International Journal of Rock Mechanics and Mining Sciences and*, vol. 15, no. 4, pp. 135–144, 1978, doi: 10.1016/0148-9062(78)91219-6.

[83] G. Chomka and J. Chudy, "Rotary head kinematics during cleaning of flat surfaces," *Acta Mechanica et Automatica*, vol. 6, no. 3, pp. 19–26, 2012.

[84] C. W. Visser, Y. Tagawa, C. Sun, and D. Lohse, "Microdroplet impact at very high velocity," *Soft Matter*, vol. 8, no. 41, pp. 10732–10737, 2012, doi: 10.1039/c2sm26323h.

[85] T. Kondo and K. Ando, "Simulation of high-speed droplet impact against a dry/wet rigid wall for understanding the mechanism of liquid jet cleaning," *Physics of Fluids*, vol. 31, no. 1, 2019, doi: 10.1063/1.5079282.

[86] C. Tang *et al.*, "Dynamics of droplet impact on solid surface with different roughness," *International Journal of Multiphase Flow*, vol. 96, pp. 56–69, 2017, doi: 10.1016/j.ijmultiphaseflow.2017.07.002.

[87] G. E. Cossali, M. Marengo, A. Coghe, and S. Zhdanov, "The role of time in single drop splash on thin film," *Exp Fluids*, vol. 36, no. 6, pp. 888–900, 2004, doi: 10.1007/s00348-003-0772-0.

[88] F. J. Heymann, "High-speed impact between a liquid drop and a solid surface," *J Appl Phys*, vol. 40, no. 13, pp. 5113–5122, 1969, doi: 10.1063/1.1657361.

[89] K. K. Haller, Y. Ventikos, D. Poulikakos, and P. Monkewitz, "Computational study of high-speed liquid droplet impact," *J Appl Phys*, vol. 92, no. 5, pp. 2821–2828, 2002, doi: 10.1063/1.1495533.

[90] Y. Xie and H. M. Hawthorne, "The damage mechanisms of several plasma-sprayed ceramic coatings in controlled scratching," *Wear*, vol. 233, pp. 293–305, 1999.

[91] M. Mieszala *et al.*, "Erosion mechanisms during abrasive waterjet machining: Model microstructures and single particle experiments," *J Mater Process Technol*, vol. 247, no. January, pp. 92–102, 2017, doi: 10.1016/j.jmatprotec.2017.04.003.

[92] M. Merola, A. Ruggiero, J. S. De Mattia, and S. Affatato, "On the tribological behavior of retrieved hip femoral heads affected by metallic debris. A

comparative investigation by stylus and optical profilometer for a new roughness measurement protocol,” *Measurement (Lond)*, vol. 90, pp. 365–371, 2016, doi: 10.1016/j.measurement.2016.05.003.

[93] W. Wei *et al.*, “On modelling coolant penetration into the microchannels at the tool-workpiece interface,” *J Manuf Process*, vol. 84, no. October, pp. 43–54, 2022, doi: 10.1016/j.jmapro.2022.09.044.

[94] E. S. Cadel *et al.*, “A comparison of metal/metal and ceramic/metal taper-trunnion modular connections in explanted total hip replacements,” *J Biomed Mater Res B Appl Biomater*, vol. 110, no. 1, pp. 135–143, 2022, doi: 10.1002/jbm.b.34897.

[95] K. Winter, Z. Liao, R. Ramanathan, D. Axinte, G. Vakil, and C. Gerada, “How non-conventional machining affects the surface integrity and magnetic properties of non-oriented electrical steel,” *Mater Des*, vol. 210, no. August, p. 110051, 2021, doi: 10.1016/j.matdes.2021.110051.

[96] A. la Monaca, D. A. Axinte, Z. Liao, R. M’Saoubi, and M. C. Hardy, “Towards understanding the thermal history of microstructural surface deformation when cutting a next generation powder metallurgy nickel-base superalloy,” *Int J Mach Tools Manuf*, vol. 168, no. PB, p. 103765, 2021, doi: 10.1016/j.ijmachtools.2021.103765.

[97] O. Gavalda Diaz, D. A. Axinte, P. Butler-Smith, and D. Novovic, “On understanding the microstructure of SiC/SiC Ceramic Matrix Composites (CMCs) after a material removal process,” *Materials Science and Engineering A*, vol. 743, no. November 2018, pp. 1–11, 2019, doi: 10.1016/j.msea.2018.11.037.

[98] S. K. Dwivedi, M. Vishwakarma, and P. A. Soni, “Advances and Researches on Non Destructive Testing: A Review,” *Mater Today Proc*, vol. 5, no. 2, pp. 3690–3698, 2018, doi: 10.1016/j.matpr.2017.11.620.

[99] A. Kroworz and A. Katunin, "Non-destructive testing of structures using optical and other methods: A review," *SDHM Structural Durability and Health Monitoring*, vol. 12, no. 1, pp. 1–17, 2018, doi: 10.3970/sdhm.2018.012.001.

[100] Y. K. Zhu, G. Y. Tian, R. S. Lu, and H. Zhang, "A review of optical NDT technologies," *Sensors*, vol. 11, no. 8, pp. 7773–7798, 2011, doi: 10.3390/s110807773.

[101] H. Masuda, K. Morita, and T. Ohmura, "Nanoindentation-induced plasticity in cubic zirconia up to 500 °C," *Acta Mater*, vol. 184, pp. 59–68, 2020, doi: 10.1016/j.actamat.2019.11.028.

[102] G. Bolelli *et al.*, "Damage progression in thermal barrier coating systems during thermal cycling: A nano-mechanical assessment," *Mater Des*, vol. 166, 2019, doi: 10.1016/j.matdes.2019.107615.

[103] D. Axinte, H. Huang, J. Yan, and Z. Liao, "What micro-mechanical testing can reveal about machining processes," *Int J Mach Tools Manuf*, vol. 183, no. October, p. 103964, 2022, doi: 10.1016/j.ijmachtools.2022.103964.

[104] R. Limbach, B. P. Rodrigues, and L. Wondraczek, "Strain-rate sensitivity of glasses," *J Non Cryst Solids*, vol. 404, pp. 124–134, 2014, doi: 10.1016/j.jnoncrysol.2014.08.023.

[105] M. A. Peters *et al.*, *Nanoindentation*. 2011.

[106] S. J. Bull, "Nanoindentation of coatings," *J Phys D Appl Phys*, vol. 38, pp. 393–413, 2005, doi: 10.1088/0022-3727/38/24/R01.

[107] G. Aydin and I. Karakurt, "Abrasive Water Jet Machining (AWJM)," *Advanced Machining Science*, vol. 3, no. 11, pp. 15–35, 2022, doi: 10.1201/9780429160011-2.

[108] "BSI Standards Publication Metallic materials — Instrumented indentation test of hardness and materials parameters Part 1 : Test method," *BS EN ISO 14577-1:2015*, 2015.

[109] David C. Joy and James B. Pawley, "High-resolution scanning electron microscopy," *Ultramicroscopy*, vol. 47, no. 1–3, pp. 80–100, Nov. 1992.

[110] A. Kudryavtsev, "3D Reconstruction in Scanning Electron Microscope : from image acquisition to dense point cloud." [Online]. Available: https://tel.archives-ouvertes.fr/tel-01930234

[111] M. S. Sahith, G. Giridhara, and R. S. Kumar, "Development and analysis of thermal barrier coatings on gas turbine blades - A Review," *Mater Today Proc*, vol. 5, no. 1, pp. 2746–2751, 2018, doi: 10.1016/j.matpr.2018.01.060.

[112] T. Mabrouki, K. Raissi, and A. Cornier, "Numerical simulation and experimental study of the interaction between a pure high-velocity waterjet and targets : contribution to investigate the decoating process," *Wear*, vol. 239, pp. 260–273, 2000.

[113] D. Axinte, J. Billingham, and A. B. Guillerna, "New models for energy beam machining enable accurate generation of free forms," *Sci Adv*, vol. 3, no. 9, pp. 1–8, 2017, doi: 10.1126/sciadv.1701201.

[114] N. K. Jain and V. K. Jain, "Modeling of material removal in mechanical type advanced machining processes: A state-of-art review," *Int J Mach Tools Manuf*, vol. 41, no. 11, pp. 1573–1635, 2001, doi: 10.1016/S0890-6955(01)00010-4.

[115] B. Jurisevic, K. Kuzman, and M. Junkar, "Water jetting technology: An alternative in incremental sheet metal forming," *International Journal of Advanced Manufacturing Technology*, vol. 31, no. 1–2, pp. 18–23, 2006, doi: 10.1007/s00170-005-0176-9.

[116] T. O. G. Cho, “Rock Cutting Depth Model Based on Kinetic Energy of Abrasive Waterjet,” *Rock Mech Rock Eng*, vol. 49, no. 3, pp. 1059–1072, 2016, doi: 10.1007/s00603-015-0778-y.

[117] S. Kulju, L. Riegger, P. Koltay, K. Mattila, and J. Hyväluoma, “Fluid flow simulations meet high-speed video: Computer vision comparison of droplet dynamics,” *J Colloid Interface Sci*, vol. 522, pp. 48–56, 2018, doi: 10.1016/j.jcis.2018.03.053.

[118] M. Bai, “Fabrication and characterization of thermal barrier coatings,” 2015, [Online]. Available: https://www.escholar.manchester.ac.uk/api/datastream?publicationPid=uk-ac-man-scw:237603&datastreamId=FULL-TEXT.PDF

[119] T. Strangman, D. Raybould, A. Jameel, and W. Baker, “Damage mechanisms, life prediction, and development of EB-PVD thermal barrier coatings for turbine airfoils,” *Surf Coat Technol*, vol. 202, no. 4–7, pp. 658–664, 2007, doi: 10.1016/j.surfcoat.2007.06.067.

[120] J. R. Kelly and I. Denry, “Stabilized zirconia as a structural ceramic: An overview,” *Dental Materials*, vol. 24, no. 3, pp. 289–298, 2008, doi: 10.1016/j.dental.2007.05.005.

[121] J. Chevalier, L. Gremillard, A. V. Virkar, and D. R. Clarke, “The tetragonal-monoclinic transformation in zirconia: Lessons learned and future trends,” *Journal of the American Ceramic Society*, vol. 92, no. 9, pp. 1901–1920, 2009, doi: 10.1111/j.1551-2916.2009.03278.x.

[122] R. H. J. Hannink, P. M. Kelly, and B. C. Muddle, “Transformation toughening in zirconia-containing ceramics,” *Journal of the American Ceramic Society*, vol. 83, no. 3, pp. 461–487, 2000, doi: 10.1111/j.1151-2916.2000.tb01221.x.

[123] V. Lughi and D. R. Clarke, "High temperature aging of YSZ coatings and subsequent transformation at low temperature," *Surf Coat Technol*, vol. 200, no. 5–6, pp. 1287–1291, 2005, doi: 10.1016/j.surfcoat.2005.07.089.

[124] V. Kulyk, Z. Duriagina, A. Kostryzhev, B. Vasyliv, V. Vavrukh, and O. Marenych, "The Effect of Yttria Content on Microstructure, Strength, and Fracture Behavior of Yttria-Stabilized Zirconia," *Materials*, vol. 15, no. 15, 2022, doi: 10.3390/ma15155212.

[125] A. Loganathan and A. S. Gandhi, "Effect of phase transformations on the fracture toughness of t' yttria stabilized zirconia," *Materials Science and Engineering A*, vol. 556. pp. 927–935, 2012. doi: 10.1016/j.msea.2012.07.095.

[126] A. Ghosh, A. K. Suri, M. Pandey, S. Thomas, T. R. Rama Mohan, and B. T. Rao, "Nanocrystalline zirconia-yttria system-a Raman study," *Mater Lett*, vol. 60, no. 9–10, pp. 1170–1173, 2006, doi: 10.1016/j.matlet.2005.10.102.

[127] a P. Naumenko, N. I. Berezovska, M. M. Biliy, and O. V Shevchenko, "Vibrational analysis and Raman spectra of tetragonal Zirconia," *Phys. Chem. Solid State*, vol. 9, no. January, pp. 121–125, 2008.

[128] D. Ushmaev, Z. Liao, A. Notron, and D. Axinte, "On the importance of interface stability in cellular automata models: Planar and dendritic solidification in laser melted YSZ," *Mater Des*, vol. 219, p. 110823, 2022, doi: 10.1016/j.matdes.2022.110823.

[129] A. Pakseresht *et al.*, "Failure mechanisms and structure tailoring of YSZ and new candidates for thermal barrier coatings: A systematic review," *Mater Des*, vol. 222, p. 111044, 2022, doi: 10.1016/j.matdes.2022.111044.

[130] H. Masuda, K. Morita, M. Watanabe, T. Hara, H. Yoshida, and T. Ohmura, "Ferroelastic and plastic behaviors in pseudo-single crystal micropillars of

nontransformable tetragonal zirconia," *Acta Mater*, vol. 203, p. 116471, 2021, doi: 10.1016/j.actamat.2020.11.013.

[131] Z. Liao, I. Sanchez, D. Xu, D. Axinte, G. Augustinavicius, and A. Wretland, "Dual-processing by abrasive waterjet machining—A method for machining and surface modification of nickel-based superalloy," *J Mater Process Technol*, vol. 285, no. May, p. 116768, 2020, doi: 10.1016/j.jmatprotec.2020.116768.

[132] W. F. Adler, "Waterdrop impact modeling," *Wear*, vol. 186–187, no. PART 2, pp. 341–351, 1995, doi: 10.1016/0043-1648(95)07176-8.

[133] I. M. Hutchings, "Strain rate effects in microparticle impact," *J Phys D Appl Phys*, vol. 10, no. 14, 1977, doi: 10.1088/0022-3727/10/14/001.

[134] I. Sanchez, D. Axinte, and R. Smith, "Modelling of rotational multiple plain water jets for controlled removal of multi-material coatings," *CIRP Annals*, vol. 69, no. 1, pp. 309–312, 2020, doi: 10.1016/j.cirp.2020.04.108.

[135] A. Portinha *et al.*, "Residual stresses and elastic modulus of thermal barrier coatings graded in porosity," *Surf Coat Technol*, vol. 188–189, no. 1-3 SPEC.ISS., pp. 120–128, 2004, doi: 10.1016/j.surfcoat.2004.08.014.

[136] H. G. Schulze, R. B. Foist, K. Okuda, A. Ivanov, and R. F. B. Turnera, "A small-window moving average-based fully automated baseline estimation method for raman spectra," *Appl Spectrosc*, vol. 66, no. 7, pp. 757–764, 2012, doi: 10.1366/11-06550.

[137] I. Žmak, D. Ćorić, V. Mandić, and L. Ćurković, "Hardness and indentation fracture toughness of slip cast alumina and alumina-zirconia ceramics," *Materials*, vol. 13, no. 1, Jan. 2020, doi: 10.3390/ma13010122.

[138] M. Alkhafagy, A. Iman Jabber Abed, A. Mohammed Talib Alkhafagy, and O. Abed Al-Hussein Al-Badry, "Effect of Adding Nano Alumina on the Grain Size and the Mechanical Properties of Yttria-Stabilized Tetragonal Zirconia

Polycrystals (Y-TZP) Preparation and Characterization of Hydroxyapatite Powder under Various Sintering Temperature View project Biomaterials research View project Effect of Adding Nano Alumina on the Grain Size and the Mechanical Properties of Yttria-Stabilized Tetragonal Zirconia Polycrystals (Y-TZP)," 2017. [Online]. Available: https://www.researchgate.net/publication/322420180

Annex A

With the aim of having a better view of the tabs from the developed App this section shows them in a full page size:

(1) Input parameters

(2) Calibration coefficient calculation

(3) Results: Energy map and milled trench

(4) Results: Understanding coating removal

(5) Results: (Pockets) Milled trench and coating removal

(6) Unit converter

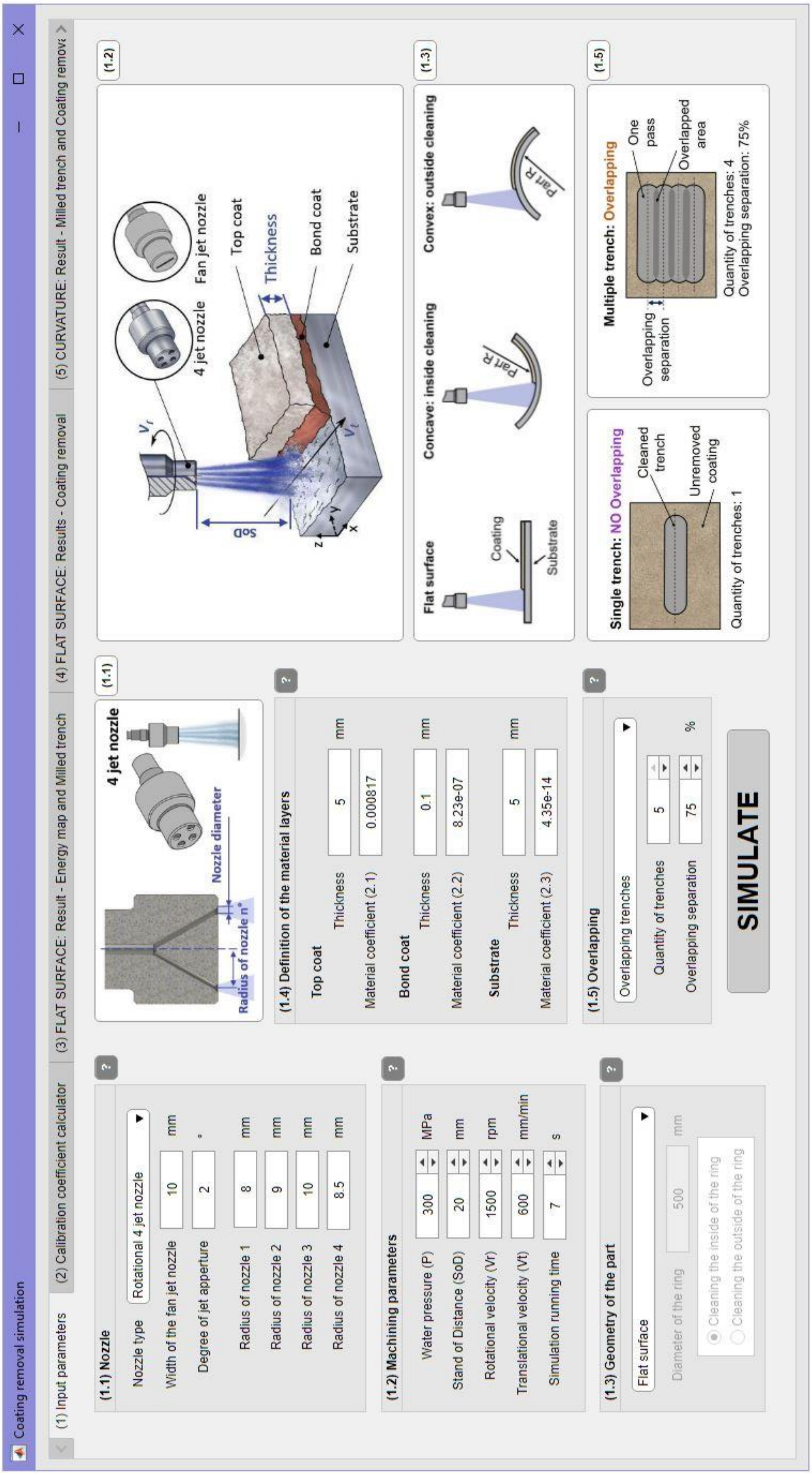
Coating removal simulation
(1) Input parameters
(2) Calibration coefficient calculator
(3) FLAT SURFACE: Result - Energy map and Milled trench
(4) FLAT SURFACE: Results - Coating removal
(5) CURVATURE: Result - Milled trench and Coating remov
(1.1) Nozzle
Nozzle type
Rotational 4 jet nozzle
Width of the fan jet nozzle 10 mm
Degree of jet apperture 2 °
Radius of nozzle 1 8 mm
Radius of nozzle 2 9 mm
Radius of nozzle 3 10 mm
Radius of nozzle 4 8.5 mm
(1.2) Machining parameters
Water pressure (P) 300 MPa
Stand of Distance (SoD) 20 mm
Rotational velocity (Vr) 1500 rpm
Translational velocity (Vt) 600 mm/min
Simulation running time 7 s
(1.3) Geometry of the part
Flat surface
Diameter of the ring 500 mm
Cleaning the inside of the ring
Cleaning the outside of the ring
(1.1)
4 jet nozzle
Nozzle diameter
Radius of nozzle n°
(1.4) Definition of the material layers
Top coat
Thickness 5 mm
Material coefficient (2.1) 0.000817
Bond coat
Thickness 0.1 mm
Material coefficient (2.2) 8.23e-07
Substrate
Thickness 5 mm
Material coefficient (2.3) 4.35e-14
(1.5) Overlapping
Overlapping trenches
Quantity of trenches 5
Overlapping separation 75 %
SIMULATE
(1.2)
4 jet nozzle
Fan jet nozzle
Top coat
Thickness
Bond coat
Substrate
SoD
(1.3)
Flat surface
Coating
Substrate
Concave: inside cleaning
Convex: outside cleaning
Part R
(1.5)
Single trench: NO Overlapping
Cleaned trench
Unremoved coating
Quantity of trenches: 1
Multiple trench: Overlapping
One pass
Overlapped area
Overlapping separation
Quantity of trenches: 4
Overlapping separation: 75%

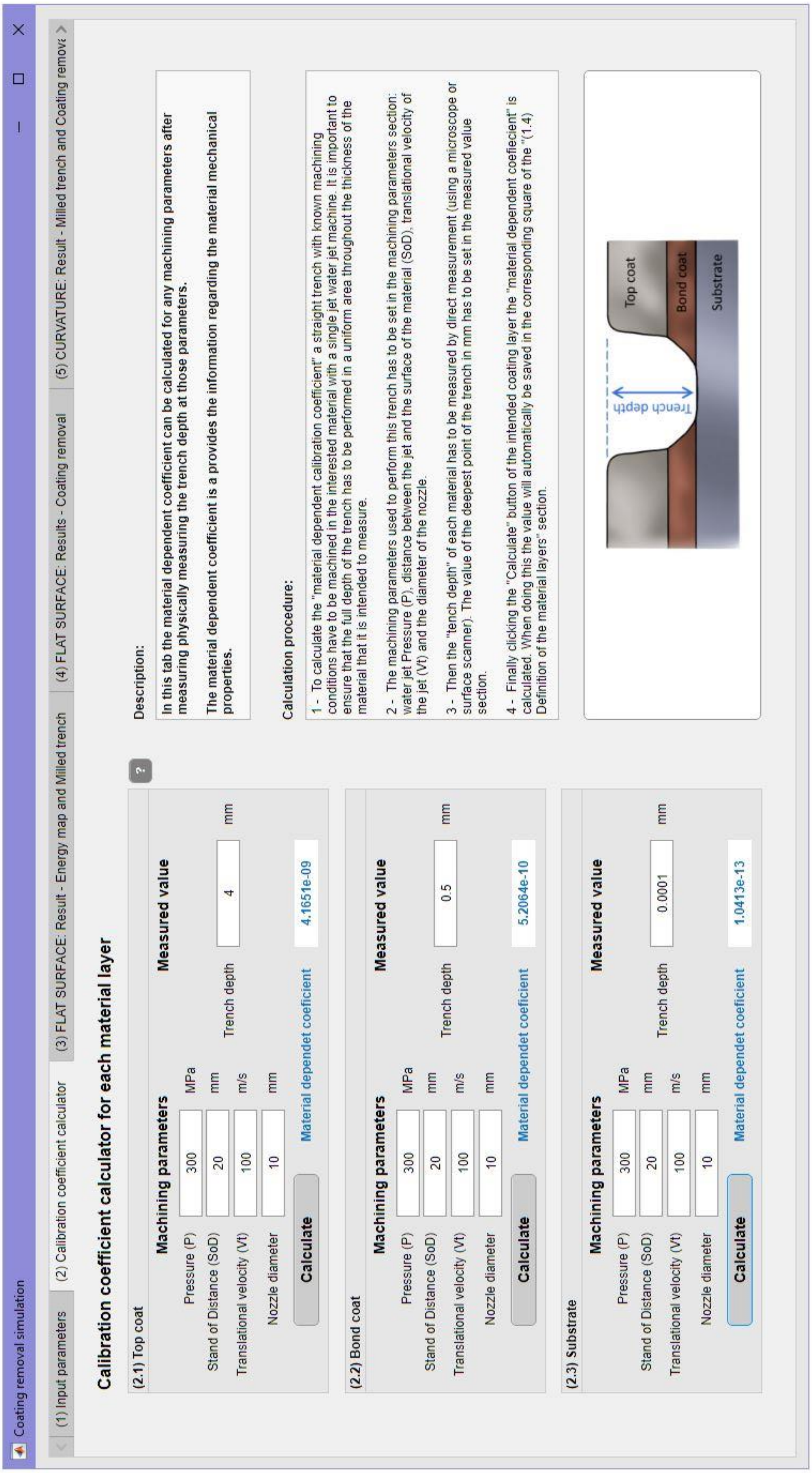
Coating removal simulation
(1) Input parameters
(2) Calibration coefficient calculator
(3) FLAT SURFACE: Result - Energy map and Milled trench
(4) FLAT SURFACE: Results - Coating removal
(5) CURVATURE: Result - Milled trench and Coating remov
Calibration coefficient calculator for each material layer
(2.1) Top coat
Machining parameters
Measured value
Pressure (P)
300
MPa
Stand of Distance (SoD)
20
mm
Translational velocity (Vt)
100
m/s
Nozzle diameter
10
mm
Trench depth
4
mm
Calculate
Material dependet coeficient
4.1651e-09
(2.2) Bond coat
Machining parameters
Measured value
Pressure (P)
300
MPa
Stand of Distance (SoD)
20
mm
Translational velocity (Vt)
100
m/s
Nozzle diameter
10
mm
Trench depth
0.5
mm
Calculate
Material dependet coeficient
5.2064e-10
(2.3) Substrate
Machining parameters
Measured value
Pressure (P)
300
MPa
Stand of Distance (SoD)
20
mm
Translational velocity (Vt)
100
m/s
Nozzle diameter
10
mm
Trench depth
0.0001
mm
Calculate
Material dependet coeficient
1.0413e-13
Description:
In this tab the material dependent coefficient can be calculated for any machining parameters after measuring physically measuring the trench depth at those parameters.
The material dependent coefficient is a provides the information regarding the material mechanical properties.
Calculation procedure:
1 - To calculate the "material dependent calibration coefficient" a straight trench with known machining conditions have to be machined in the interested material with a single jet water jet machine. It is important to ensure that the full depth of the trench has to be performed in a uniform area throughout the thickness of the material that it is intended to measure.
2 - The machining parameters used to perform this trench has to be set in the machining parameters section: water jet Pressure (P), distance between the jet and the surface of the material (SoD), translational velocity of the jet (Vt) and the diameter of the nozzle.
3 - Then the "tench depth" of each material has to be measured by direct measurement (using a microscope or surface scanner). The value of the deepest point of the trench in mm has to be set in the measured value section.
4 - Finally clicking the "Calculate" button of the intended coating layer the "material dependent coefiecient" is calculated. When doing this the value will automatically be saved in the corresponding square of the "(1.4) Definition of the material layers" section.
Trench depth
Top coat
Bond coat
Substrate

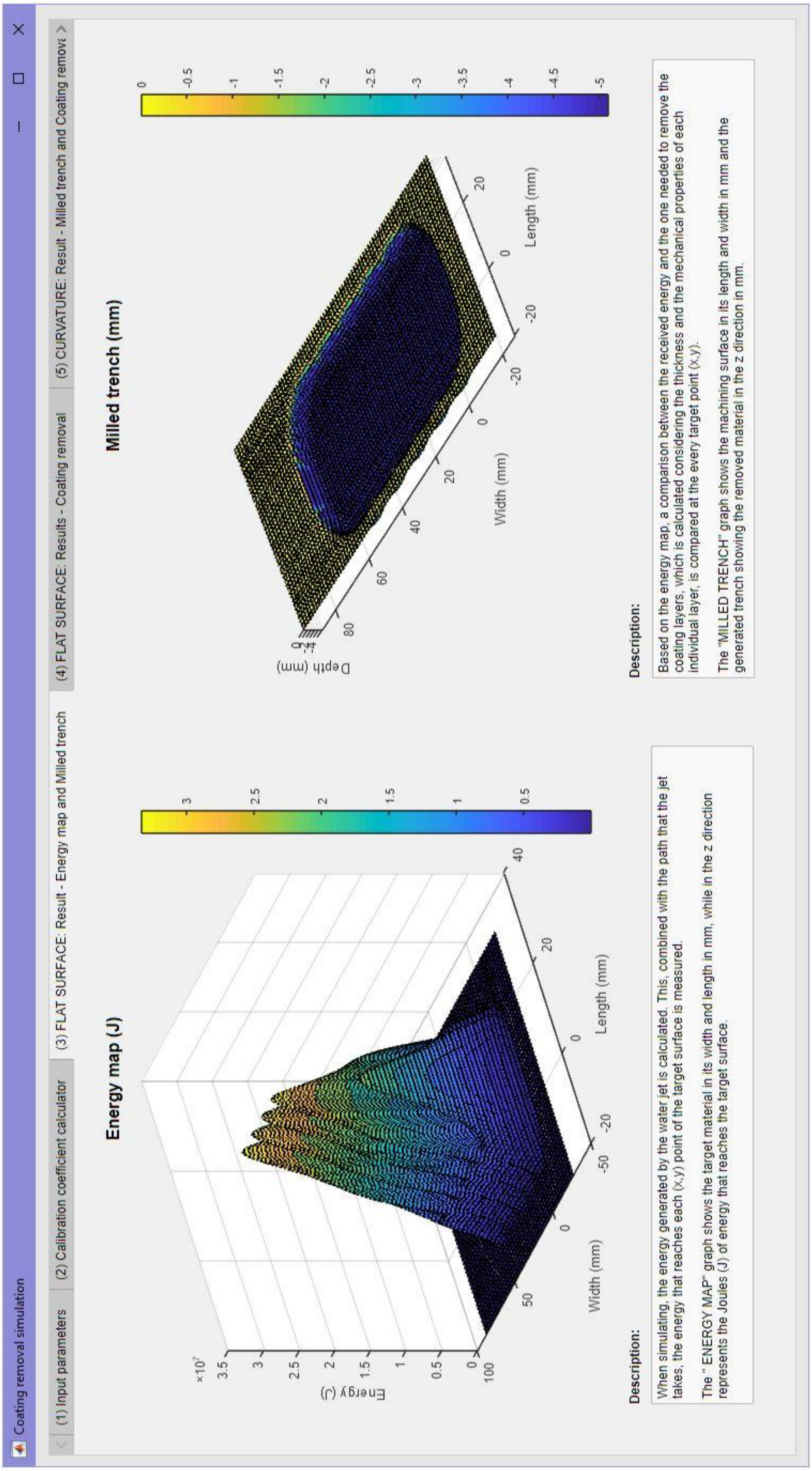
Coating removal simulation
(1) Input parameters
(2) Calibration coefficient calculator
(3) FLAT SURFACE: Result - Energy map and Milled trench
(4) FLAT SURFACE: Results - Coating removal
(5) CURVATURE: Result - Milled trench and Coating remov
Energy map (J)
Energy (J)
Width (mm)
Length (mm)
Milled trench (mm)
Depth (mm)
Width (mm)
Length (mm)
Description:
When simulating, the energy generated by the water jet is calculated. This, combined with the path that the jet takes, the energy that reaches each (x,y) point of the target surface is measured.
The " ENERGY MAP" graph shows the target material in its width and length in mm, while in the z direction represents the Joules (J) of energy that reaches the target surface.
Description:
Based on the energy map, a comparison between the received energy and the one needed to remove the coating layers, which is calculated considering the thickness and the mechanical properties of each individual layer, is compared at the every target point (x,y).
The "MILLED TRENCH" graph shows the machining surface in its length and width in mm and the generated trench showing the removed material in the z direction in mm.

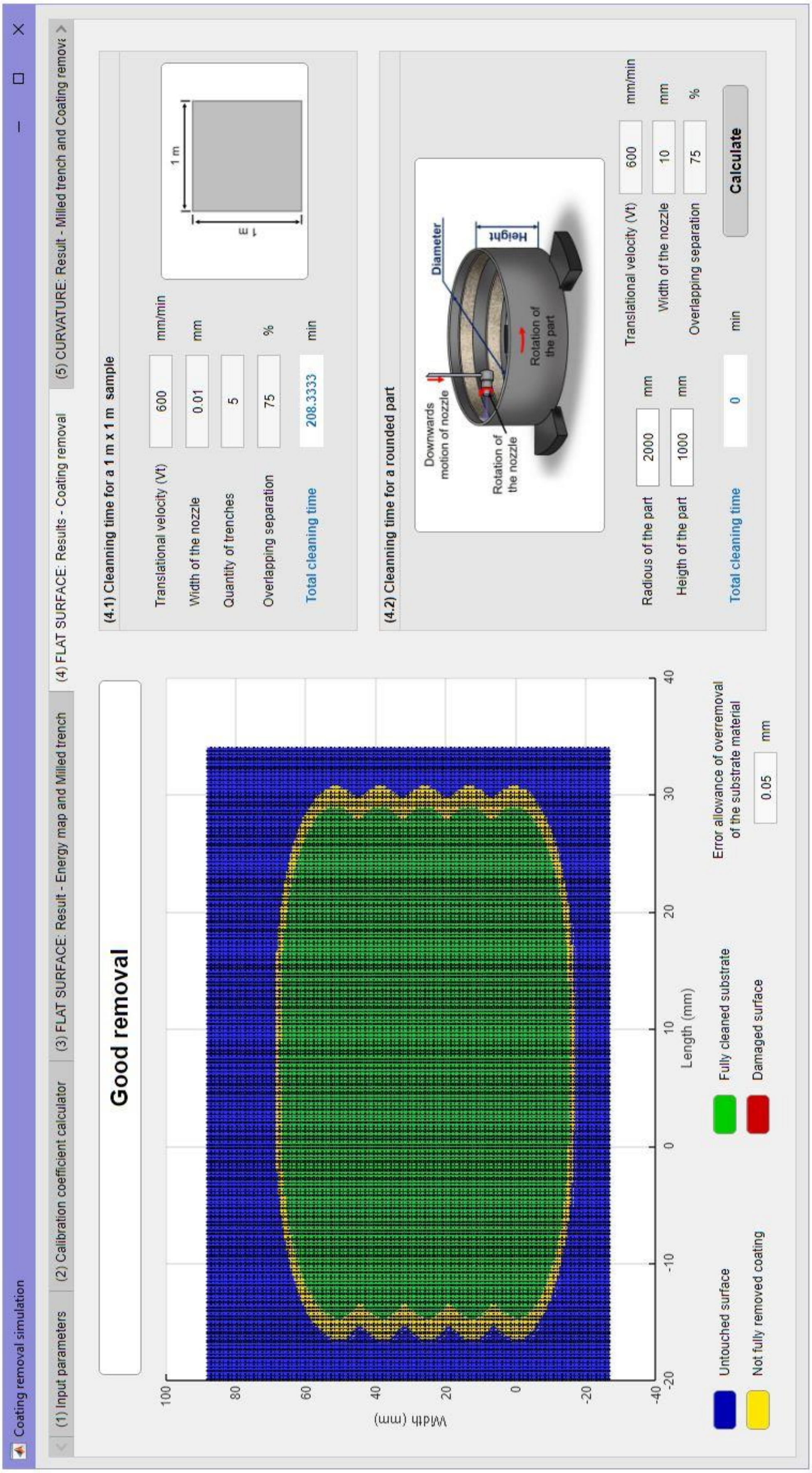
Coating removal simulation
(1) Input parameters
(2) Calibration coefficient calculator
(3) FLAT SURFACE: Result - Energy map and Milled trench
(4) FLAT SURFACE: Results - Coating removal
(5) CURVATURE: Result - Milled trench and Coating remova
Good removal
Width (mm)
Length (mm)
Untouched surface
Not fully removed coating
Fully cleaned substrate
Damaged surface
Error allowance of overremoval of the substrate material
0.05
mm
(4.1) Cleanning time for a 1 m x 1 m sample
Translational velocity (Vt)
600
mm/min
Width of the nozzle
0.01
mm
Quantity of trenches
5
Overlapping separation
75
%
Total cleaning time
208.3333
min
1 m
1 m
(4.2) Cleanning time for a rounded part
Downwards motion of nozzle
Rotation of the nozzle
Rotation of the part
Diameter
Height
Radious of the part
2000
mm
Heigth of the part
1000
mm
Total cleaning time
0
min
Translational velocity (Vt)
600
mm/min
Width of the nozzle
10
mm
Overlapping separation
75
%
Calculate

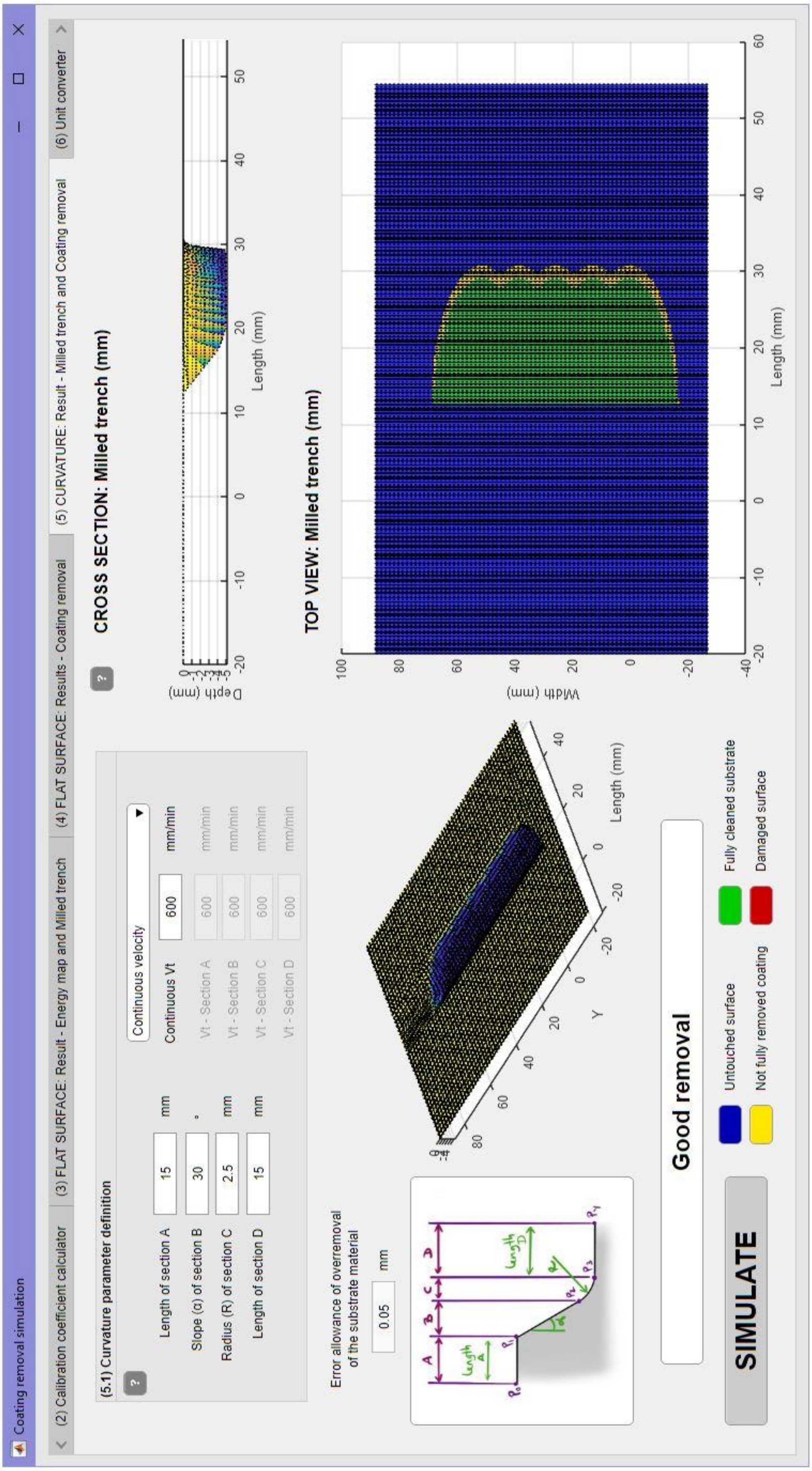
Coating removal simulation
(2) Calibration coefficient calculator
(3) FLAT SURFACE: Result - Energy map and Milled trench
(4) FLAT SURFACE: Results - Coating removal
(5) CURVATURE: Result - Milled trench and Coating removal
(6) Unit converter
(5.1) Curvature parameter definition
Length of section A
15
mm
Slope (α) of section B
30
°
Radius (R) of section C
2.5
mm
Length of section D
15
mm
Continuous velocity
Continuous Vt
600
mm/min
Vt - Section A
Vt - Section B
Vt - Section C
Vt - Section D
Error allowance of overremoval of the substrate material
0.05
mm
Good removal
SIMULATE
Untouched surface
Fully cleaned substrate
Not fully removed coating
Damaged surface
CROSS SECTION: Milled trench (mm)
Depth (mm)
Length (mm)
TOP VIEW: Milled trench (mm)
Width (mm)
Length (mm)

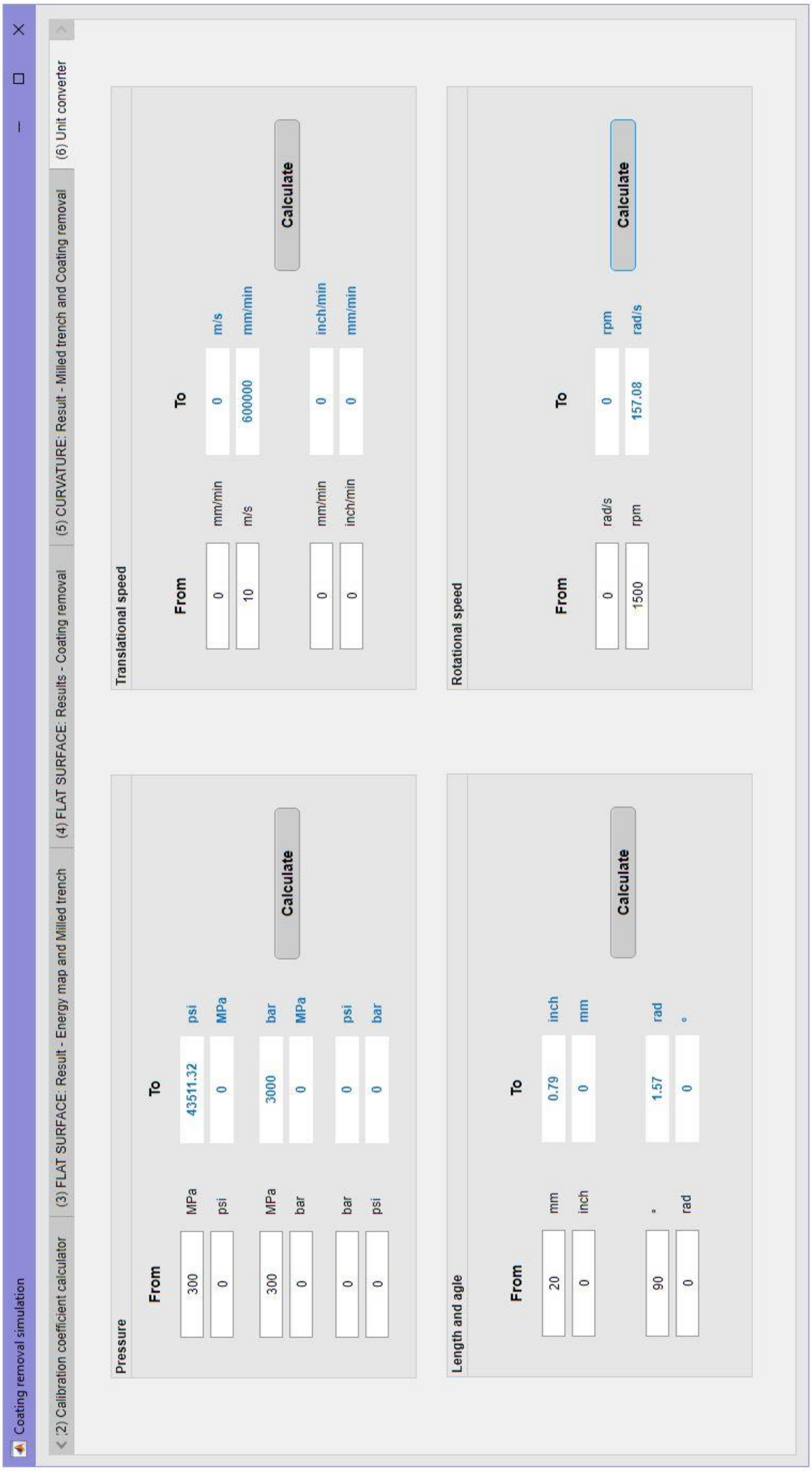
Coating removal simulation
(2) Calibration coefficient calculator
(3) FLAT SURFACE: Result - Energy map and Milled trench
(4) FLAT SURFACE: Results - Coating removal
(5) CURVATURE: Result - Milled trench and Coating removal
(6) Unit converter
Pressure
From
To
300 MPa 43511.32 psi
0 psi 0 MPa
300 MPa 3000 bar
0 bar 0 MPa
0 bar 0 psi
0 psi 0 bar
Calculate
Translational speed
From
To
0 mm/min 0 m/s
10 m/s 600000 mm/min
0 mm/min 0 inch/min
0 inch/min 0 mm/min
Calculate
Length and agle
From
To
20 mm 0.79 inch
0 inch 0 mm
90 ° 1.57 rad
0 rad 0 °
Calculate
Rotational speed
From
To
0 rad/s 0 rpm
1500 rpm 157.08 rad/s
Calculate